SAPIENZA
UNIVERSITÀ DI ROMA

Innovative tools and technologies for orbital angular momentum based Quantum Information protocols

Facoltà di Scienze Matematiche Fisiche e Naturali
Dottorato di Ricerca in Fisica - XXXVI Ciclo

Danilo Zia
ID number 1699281

Advisor
Prof. Fabio Sciarrino

Academic Year 2023/2024

Thesis defended on 23 May 2024
in front of a Board of Examiners composed by:

Prof. Tullio Scopigno (chairman)
Prof. Mehul Malik
Prof. Gian Piero Pepe

Innovative tools and technologies for orbital angular momentum based Quantum Information protocols
Sapienza University of Rome

This thesis has been typeset by LaTeX and the Sapthesis class.

Author’s email: danilo.zia@uniroma1.it

List of works

The following list contains the main works developed during the Ph.D., upon which this thesis is based:

- Alessia Suprano, **Danilo Zia**, Emanuele Polino, Taira Giordani, Luca Innocenti, Mauro Paternostro, Alessandro Ferraro, Nicolò Spagnolo, and Fabio Sciarrino,“Enhanced detection techniques of orbital angular momentum states in the classical and quantum regimes”, *New Journal of Physics*, vol. 23, p. 073014 (2021).
  Author's contribution: DZ took part in building the experimental setup, performed the whole development of the theoretical model and the data analysis using the machine learning-based approach applied in the classical regime, and contributed to the writing of the paper.

- Alessia Suprano, **Danilo Zia**, Emanuele Polino, Taira Giordani, Luca Innocenti, Alessandro Ferraro, Mauro Paternostro, Nicoló Spagnolo, and Fabio Sciarrino,“Dynamical learning of a photonics quantum-state engineering process”, *Advanced Photonics*, vol. 3, p. 066002 (2021).
  Author's contribution: DZ contributed to the design of the experimental setup and its realization, developed the whole code for implementing the RBFOpt black box algorithm in the engineering of light states, took part in the measurement performed in the classical regime and in the data analysis, and contributed to the writing of the paper.

- **Danilo Zia**, Riccardo Checchinato, Alessia Suprano, Taira Giordani, Emanuele Polino, Luca Innocenti, Alessandro Ferraro, Mauro Paternostro, Nicolò Spagnolo, and Fabio Sciarrino, “Regression of high dimensional angular momentum states of light”, *Physical Review Research*, vol. 5, p. 013142 (2023).
  Author's contribution: DZ conceived the experiment and contributed to the realization of the platform, took part in the collection of the experimental data and in the analysis performed using machine learning techniques, and contributed to the writing of the paper.

- Alessia Suprano, **Danilo Zia**, Mathias Pont, Taira Giordani, Giovanni Rodari, Mauro Valeri, Bruno Piccirillo, Gonzalo Carvacho, Nicolò Spagnolo, Pascale Senellart, Lorenzo Marrucci, and Fabio Sciarrino, “Orbital angular momentum based intra-and interparticle entangled states generated via a quantum dot source”, *Advanced Photonics*, vol. 5, p. 046008 (2023).
  Author's contribution: DZ contributed to the design of the experimental setup and the data acquisition, took part in the analysis for the reconstruction of the states density matrix, and contributed to the writing of the paper.

- **Danilo Zia**, Nazanin Dehghan, Alessio D'Errico, Fabio Sciarrino, and Ebrahim Karimi, "Interferometric imaging of amplitude and phase of spatial biphoton states", *Nature Photonics*, vol. 17, p. 1009 (2023).
  Author's contribution: DZ contributed to the design of the experiment, led the building of the platform, performed the data collection for the reconstruction of spatially structured states, fully developed the code used for implementing the digital holography technique, and contributed to the writing of the paper.

- Alessia Suprano, **Danilo Zia**, Luca Innocenti, Salvatore Lorenzo, Valeria Cimini, Taira Giordani, Ivan Palmisano, Emanuele Polino, Nicolò Spagnolo, Fabio Sciarrino, G Massimo Palma, Alessandro Ferraro, and Mauro Paternostro,"Experimental property-reconstruction in a photonic quantum extreme learning machine", *Physical Review Letters*, vol 132, p. 160802 (2024).
  Author's contribution: DZ led the realization of the experimental platform and the collection of data, contributed to analysis for the polarization state reconstruction, and to the writing of the paper.

- Alessia Suprano, **Danilo Zia**, Emanuele Polino, Davide Poderini, Gonzalo Carvacho, Matteo Lugli, Alessandro Bisio, Paolo Perinotti, and Fabio Sciarrino, "Photonic cellular automaton simulation of relativistic quantum fields: observation of Zitterbewegung", arXiv preprint arXiv:2402.07672v1 (2024).
  Author's contribution: DZ led the building of the setup, performed the experimental realization and analysis of the step-by-step simulation of the Dirac evolution, and contributed to the writing of the paper.

Conference papers

The works performed were additionally reported in the following conference proceedings:

- Alessia Suprano, **Danilo Zia**, Mathias Pont, Taira Giordani, Giovanni Rodari, Mauro Valeri, Bruno Piccirillo, Gonzalo Carvacho, Nicolò Spagnolo, Pascale Senellart, Lorenzo Marrucci, and Fabio Sciarrino, "Quantum Dot-based Generation of Orbital Angular Momentum Entangled States", Conference on Lasers and Electro-Optics (2023).

- **Danilo Zia**, Riccardo Checchinato, Alessia Suprano, Taira Giordani, Emanuele Polino, Luca Innocenti, Alessandro Ferraro, Mauro Paternostro, Nicolò Spagnolo, and Fabio Sciarrino, "Regression Approach for the Reconstruction of Orbital Angular Momentum States", Conference on Lasers and Electro-Optics (2023).

Contents

Introduction **1**

I Theoretical Background **6**

1 Quantum Mechanics and Quantum Information **7**
1.1 Basics of Quantum Mechanics 8
1.1.1 Quantum Mechanics Postulates 8
1.1.2 Density Matrix Representation 10
1.1.3 Quantum Measurements 11
1.1.4 Separable and Entangled states 13
1.2 Quantum Information 14
1.2.1 Qubits and qudits 14
1.2.2 Circuit model of quantum computation: Quantum gates . . . 16
1.2.3 Quantum Algorithms and Quantum Walk 17
1.2.4 Fidelity of quantum states 20

2 Photonic Technologies **22**
2.1 Basis of classical and quantum description of light 23
2.2 Angular Momentum of Light 26
2.3 Paraxial Helmotz equation 29
2.3.1 Gaussian mode 30
2.3.2 Hermite-Gaussian mode 31
2.3.3 Laguerre-Gaussian mode 33
2.3.4 Hypergeometric-Gaussian mode 35
2.4 Single photons sources 36
2.4.1 Nonlinear processes 37
2.4.2 Spontaneous Parametric Down Conversion 40
2.4.3 Quantum Dots 45
2.5 Manipulation of photons angular momentum 48
2.5.1 Polarization degree of freedom 48
2.5.2 Orbital angular momentum degree of freedom 51

3 Machine Learning and Optimization Algorithms **57**
3.1 Optimization Algorithms 57
3.1.1 RBFOpt algorithm 58
3.2 Machine Learning 60
3.2.1 Principal Component Analysis 62
3.2.2 Neural Networks 63
3.2.3 Extreme Learning Machine and Reservoir Computing 67

II Experimental engineering of orbital angular momentum states of light 69

4 Generation of High Dimensional Orbital Angular Momentum Entangled States 70
4.1 Spatial correlation in Spontaneous Parametric Down Conversion process 71
4.1.1 Interferometric imaging for state reconstruction 73
4.1.2 Experimental Setup and Results 75
4.2 Entangled OAM states generate via a quantum dot source 79
4.2.1 Characteristics of the quantum dot source 79
4.2.2 Experimental platform for generating intra- and interparticle entangled OAM states 81
4.3 Conclusions 86

5 Photonic Orbital Angular Momentum States Engineering Platform 88
5.1 Engineering protocol and Experimental setup 89
5.2 Black box approach to OAM engineering 92
5.2.1 Theoretical Simulations 94
5.2.2 Experimental results 97
5.3 Conclusions 100

6 Detection of Orbital Angular Momentum States 102
6.1 Refined theoretical model for an enhanced holographic technique: q-plate action 104
6.1.1 Experimental results of the enhanced holographic technique . 106
6.2 Machine learning-based approach to OAM measurement 108
6.2.1 Classification of vector vortex beams via convolutional neural networks 109
6.2.2 Regression of high dimensional light states 112
6.3 Conclusions 120

III Orbital Angular Momentum for Quantum Information Protocols 122

7 Quantum Machine Learning 123
7.1 Quantum extreme learning machine 124
7.2 Experimental Photonic QELM 125
7.3 Conclusions 132

8 Quantum Simulation via Quantum Cellular Automaton 134
8.1 Linear Quantum cellular automaton 135
8.2 Dirac cellular automaton: simulation of relativistic particles 136
8.2.1 Experimental Simulation of the *Zitterbewegung* effect 137
8.3 Conclusion 141

Conclusions 143

Appendices **148**

A EPR Paradox and Bell's inequality **148**
A.1 EPR Paradox: Quantum Mechanics incompleteness 148
A.2 Bell's theorem and quantum nonlocality 149
A.2.1 Loopholes in experimental tests of Bell's inequality 151

B Off-axis Digital Holography: Hermite-Gaussian modes, phase matching function and quantum imaging **153**

C Fresnel integrals for the refined theoretical propagation model **156**

D Fidelity and efficiency results for the refined theoretical HyGG model **158**

E Optimization of the QW in the measurement frames formalism **161**

Acronyms **163**

Bibliography **165**

Introduction

Quantum Mechanics is one of the most consolidated and used theories, enabling a reliable description of the behavior of the microscopic world. Its predictions, verified with great accuracy experimentally, changed our comprehension of nature. Even if there is still an ongoing discussion about the interpretation of its foundations, Quantum Mechanics furnishes a powerful recipe for describing reality. In particular, quantum phenomena such as the Heisenberg uncertainty principle and quantum entanglement are incompatible with a classical representation of the world. Formulated in the early years of the 20th century, during the last decades, Quantum Mechanics has experienced a growing interest in the application of its phenomena to the field of information, inspiring the birth of a research area called Quantum Information [1–3]. Here, quantum resources are exploited to improve the performances achievable with the classical ones, for example by producing algorithms that present a time speed-up for solving a specific task [4–6] or giving an intrinsically secure communication procedure [7]. Within this framework, quantum states are used to store and transmit information. In particular, ideally, every two-level quantum system can be used to encode the Quantum Information unit known as *qubit*, which represents the quantum counterpart of the classical bit. In general, qubits can be in a generic superposition of the two logical states associated with the quantum levels, so having an increased information content with respect to the classical bit they enable more powerful parallel processes. These advantages become extreme when we move to work in a higher d-dimensional Hilbert space, encoding the so-called *qudits*. These, not only enhance the information capacity of single physical carriers, but also make quantum encryption protocols more secure [8–11]. They also find extensive applications ranging from quantum computation, communication, metrology, and simulation [12–20].

For implementing Quantum Information protocols, photons are one of the most used physical systems [21]. Light has always had a central role in Quantum Mechanics, starting from its formulation, triggered by the study of the black body radiation [22], to the experimental validation of the theory, such as the observation of the entanglement between two photons through the first Bell's inequality violation [23]. For what concerns their application inside Quantum Information, photons represent an appealing resource. They have low decoherence with respect to other systems, due to their low interaction with the environment, and propagate fast, making them the ideal candidate for carrying information in quantum communication procedures. Moreover, photons can be detected and manipulated relatively easily and at room temperature, without the need to work at a cryogenic one, enabling for simple information processing schemes. Finally, photons present several degrees of freedom that can be used to codify and store information, such as spatial and temporal modes, polarization and Orbital Angular Momentum (OAM). For all these reasons, in the last years, suitable devices and platforms performing photon-based protocols have been investigated and developed [21].

Among the photons degrees of freedom, the OAM has gained a growing interest due to its several applications both in classical and quantum regimes. The OAM together with the Spin Angular Momentum (SAM) compose the total angular momentum of photons. While the SAM is associate with their polarization, the OAM is instead related to the helical spatial structure of their field [24, 25]. Notably, the OAM lives in an unbounded Hilbert space and it is therefore suitable to encode high dimensional quantum states in single photons. For this reason, it has been used for quantum communication, sensing, simulation and metrology [26–41]. Classically, instead, laser beams carrying OAM have been extensively employed for particle trapping, microscopy, sensing and communication [26, 42–48]. Due to this wide range of applications, great effort was put into the development of reliable platforms and methods to engineer and reconstruct high dimensional OAM states. In experimental scenarios, the first one was mostly investigated by acting on probabilistic generated single photons with bulk optics devices capable of modulating their wavefront such as spatial light modulators [49, 50] and q-plates [51–53], or directly exploiting Spontaneous Parametric Down Conversion (SPDC) sources [54–57]. On the other hand, the most common detection approach is based on projective measurement and consist on performing a full-state tomography, which gives complete information about the state under analysis. The drawback of this method is that it is not flexible, scaling quadratically with the dimension of the state under analysis [58]. Therefore, in this context, highly demanded features are the realization of effective sources capable of producing on demand OAM modes, and the implementation of resource efficient measurement schemes apt to retrieve the information codified in the high dimensional states.

The aim of this Ph.D. thesis is to investigate the OAM degree of freedom analyzing first of all its generation and measurement, by proposing and demonstrating innovative approaches to address the main problems arising in this framework, and then using it for Quantum Information protocols.

We started by analyzing the properties of the widely employed SPDC process. In photonic implementations, the latter is mostly used to generate single photons through the conversion of one pump photon into a pair of emitted photons called *idler* and *signal*, with a procedure that preserves energy and momentum. In particular, the pump OAM is conserved during the process and the emitted photons present intrinsically a high dimensional entanglement in this degree of freedom [54–57]. Moreover, the wavefunction of the two produced photons strongly depends on the spatial structure of the pump, which can be then used to shape the biphoton state and generate the wanted state on which to perform Quantum Information protocols. Therefore, we investigated the generation of OAM high dimensional entangled states via the SPDC process by entering a nonlinear crystal with a spatially structured laser. In particular, we proposed and demonstrated a fast and effective holographic method, that, making use of the source properties, allowed us to obtain a high quality reconstruction of the biphoton state, while requiring fewer resources than commonly used tomographic approaches [59].

Although capable of easily generating entangled states, SPDC sources are probabilistic and suffer from detrimental effects such as the production of multiphoton states that undermine their employment in quantum cryptography schemes [60, 61]. Moreover, there is also a trade-off between the purity of the single photon states produced and the brightness of the source. Hence, we decided to study the application of novel Quantum Dots (QDs) sources to produce OAM modes. QDs are nearly deterministic emitters that excited with pulsed lasers behave as artificial atoms, emitting almost on-demand pure and indistinguishable single photons. We used a commercial QD, assessing his performance and manipulating the photon spatial structure through q-plates, which we used to build a probabilistic entangling gate in the OAM Hilbert space [62].

Besides generating single photons, a central task in Quantum Information is the engineering of target states and proper measurement of them. The capacity to produce a specific state is usually linked to the specific experimental setup, so the development of platform-independent engineering protocols is of great importance. One option is then represented by the Quantum Walk (QW) [63], the quantum counterpart of the random walk, which has been proven an efficient technique in building classical algorithms. The QW dynamics describes the evolution of a *walker* state conditioned to the internal state of a *coin* one, and it has been theoretically proven how properly acting on the coin state, after the right number of steps, it is possible to create the target high dimensional state in the walker space without assumption on an experimental implementation [64]. Among the various photonic realizations, a suitable platform for its compactness and scalability, it is the one that performs a QW on a line exploiting the polarization and OAM degrees of freedom to encode respectively the coin and walker states. Experimentally, this configuration has been proven capable of generating arbitrary qudits in the OAM space [65]. Within this framework, we refined this protocol accounting for experimental imperfections and noises using a fully black-box approach [66]. The latter automatically accounts for them since it modifies the coin operators by relying only on the fidelity between the produced state and the target one, without needing a description of the apparatus. We demonstrated the benefits of this method by studying different target states and observing higher fidelity values when comparing its results with those obtained by directly applying the algorithm proposed in [64] to the experimental setup.

On the other side, to address the practical issues of quantum state tomography in high dimensional Hilbert spaces, various OAM demultiplexing procedures were proposed [67–69], where the number of measurements is reduced by employing interferometers, holograms, and diffractive elements. However, besides effectively recognizing the OAM contents of the states, these approaches introduced detrimental noises and signal losses in the experiments. To overcome these limitations, we studied the implementation of innovative Machine Learning (ML) techniques in the OAM measurement procedure [70, 71]. Following a supervised approach, we recorded images of the OAM modes produced by our setup and cast the measurement problem as an image recognition one by performing both classification [70] and regression [71] tasks. Moreover, to increase the performance of the algorithm with simulated data, we developed a refined model of the beam propagation inside the setup. We also applied it to the standard holographic projective technique, enhancing by about three times the signal coupled to a single mode fiber [70].

Finally, after investigating the principal aspects at the basis of every OAM-based platform, we made use of the OAM and the powerful QW dynamics implementing information processing protocols. First of all, leveraging the benefits produced by applying ML, we decided to utilize the QW apparatus to implement a quantum machine learning setup. A fruitful interconnection between Quantum Information and the field of ML has been established and consolidated through several works, both on the theoretical and experimental side [72–74]. In this context, both ML techniques are employed to obtain a deeper comprehension of quantum phenomena, and quantum protocols are used to optimize the performance of ML paradigms, especially when high dimensional quantum states are used [75, 76]. Following this trend, we realized a quantum extreme learning machine (QELM). The latter works by processing the input data after the evolution through a quantum channel, called *reservoir* and identified with the QW platform. The training is made on the measured occupancy probabilities of the OAM space at the output of the setup, and we used the QELM to perform a quantum state tomography of input qubits encoded in the polarization degree of freedom of single photons [77]. Since the reservoir is completely random, in this approach we don't need a precise characterization of the setup and it represents a promising route for resource-efficient quantum state reconstruction when considering high dimensional or multiphoton input states.

Secondly, we investigate the QW applications as a quantum simulation platform. In particular, we implemented a Dirac Quantum Cellular Automaton (DQCA) [78–81], a special case of the more general quantum cellular automaton [82–86]. This consists of a regular grid of cells made up of finite-dimensional quantum systems that interact locally and it has garnered significant attention because of its potential applications in quantum computation [87–89]. In particular, by relating the time evolution produced by the one-dimensional Dirac Hamiltonian and the discrete-time quantum walk dynamics, one obtains a DQCA [90, 91], which is particularly suitable for the simulation of relativistic effects. By identifying the particle position with the OAM carried by single photons and setting properly the experimental parameters of the implemented QW, we were able to simulate for the first time in a photonic platform the *Zitterbewegung* effect, i.e. the trembling motion that occurs during the free evolution of relativistic particles [92].

The thesis is structured as follows:

- **Part I:** In this part, we introduce the basic concepts needed to understand the working environment and the following experimental implementations. We start in Chapter 1 with the basic notions about Quantum Mechanics and Quantum Information. Then, in Chapter 2 we proceed to describe the photonic technologies and resources employed, from OAM theoretical description to sources of single photons and their manipulation. Finally, in Chapter 3 we give a glance at machine learning basic concepts focusing on the paradigms utilized throughout the thesis.

- **Part II:** This part collects the results obtained in studying the engineering and detection of OAM states. We start with the sources of OAM states, analyzing the spatial entanglement in probabilistic SPDC ones and the generation of entangled states with photons generated in a nearly deterministic fashion by a QD (Chapter 4). Then, we focused also on the study of a QW-based engineering platform capable of producing arbitrary qudits, enanching its performance with a black-box approach (Chapter 5). Finally, we analyze the detection of OAM modes, proposing innovative approaches based on machine learning and improving well-known ones (Chapter 6).

- **Part III:** The last part contains the exploitation of the study on OAM generation and measurement for Quantum Information processing. In particular, the QW apparatus is used to perform both quantum machine learning, implementing a QELM paradigm (Chapter 7), and quantum simulation procedure, realizing a DQCA that reproduces relativistic particle evolutions (Chapter 8).

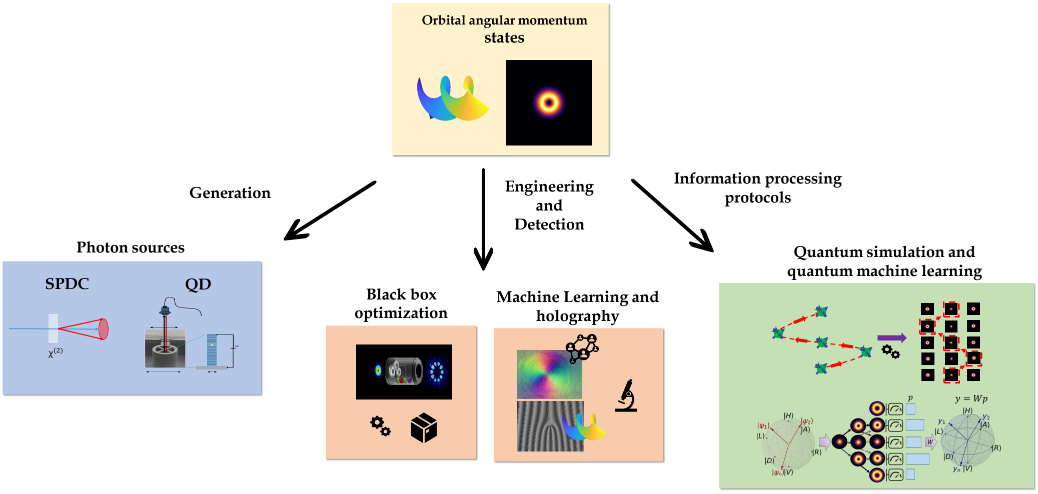

Schematic representation of the thesis. The discussion starts by analyzing the various sources of single photons and how to exploit their properties to generate OAM states. Then we describe manipulation techniques of photons spatial structure and paradigms for engineering and measurement of OAM modes. Finally, we use the expertise acquired and perform information processing protocols.

Part I

Theoretical Background

Chapter 1

Quantum Mechanics and Quantum Information

At the end of the 19th century, the widespread belief that physics was capable of providing a complete description of the world was undermined by the emergence of two new theories: *Relativity*, in its *special* and *general* formulation, and *Quantum Mechanics*. Both of them were developed to explain experimental observations that cannot be understood using the means of classical physics, concerning respectively systems at large and small scales.

The trigger for the development of a quantum theory can be made to coincide with Plank's study and explanation of the radiative behavior of a black body [22], i.e. about the resolution of the so-called *ultraviolet catastrophe*. From its formulation, Quantum Mechanics changed our comprehension of Nature by giving a recipe of rules, collected in the theory postulates, that accurately predicts experimental results, allowing us to describe effects that are not included in the classical formulation. Among these, the most peculiar one is for sure the *quantum entanglement*. The latter is strictly related to the foundational concept of local causality, and was widely debated during the formulation of the *new* Quantum Theory.

Besides being of fundamental importance for the study of Quantum Mechanics foundations, quantum features, such as the entanglement and superposition principle, find several applications in the field of Quantum Information [1–3]. Born from the union of quantum and information theories, the latter is a research area that exploits quantum resources to enhance the information processing performances obtainable using the classical ones, trying to reach the so-called *quantum advantage* [93]. In this context, quantum systems are used to store and carry information, encoding the elementary computational unit: the quantum bit or *qubit*. In recent years, there has been an increasing interest in Quantum Information due to the benefits it offers across several fields, such as quantum communication [21, 94], quantum computation [2, 95, 96], quantum metrology [30, 97] and quantum cryptography [33, 98, 99].

In this chapter, we introduce the structural formalism and notation that will be employed throughout the thesis. In Section 1.1, we start by presenting the basics of Quantum Mechanics and its postulates, giving the tools to describe quantum states, their evolution and measurement. Then, in Section 1.2, we expose their implementation in information theory describing the foundation of Quantum Information, from the encoding of the elementary unit to the retrieval of the computation results.

1.1 Basics of Quantum Mechanics

In this Section, we start by giving the basics of Quantum Mechanics [1–3], describing the postulates that compose the quantum recipe. Then we introduce the density matrix formalism and talk about quantum observables and measurements. Finally, we focus on quantum entanglement.

1.1.1 Quantum Mechanics Postulates

Quantum Mechanics is based on a mathematical framework composed of 5 postulates [1, 2], which are the basic rules for applying Quantum Mechanics in nature description.

Postulate I: *The state of a physical system is completely described by a unit vector* $|\psi\rangle$*, which is called the state vector, or wavefunction, and resides in the Hilbert space* $\mathcal{H}_s$*, i.e. a complex vector space with an inner product, associated with the system.*

It is worth noting that Quantum Mechanics doesn't give any specification about the state vector and the Hilbert space in which it lives. Finding them for a specific system is a complex task that follows intricate rules to apply case by case to give a complete description of the observable physical properties of a system.

Postulate II: *Any physical observable* O *is associated with a Hermitian operator acting in* $\mathcal{H}_s$*. The only possible outcome of a measurement of the observable* O *is one of its eigenvalues.*

Analyzing a quantum system, its state can be expanded in the basis $\{|o\rangle\}$ composed by the eigenvectors of the observable O, for which $O|o\rangle = \lambda_o |o\rangle$, and we have then:

$$|\psi\rangle = \sum_o c_o |o\rangle \tag{1.1}$$

Where $\sum_o |c_o|^2 = 1$ due to the normalization of the unit vector. The expectation value of the physical observable O over the state is computed as:

$$\langle O\rangle = \langle\psi| O |\psi\rangle \tag{1.2}$$

The standard deviation associated with this is given as:

$$\Delta O = \sqrt{\langle O^2\rangle - \langle O\rangle^2} \tag{1.3}$$

If we consider two observables O_1, O_2, they are called *compatible* if they commute, i.e. if holds that $[O_1, O_2] = O_1O_2 - O_2O_1 = 0$. In this case, they have a common basis of eigenstates and can be simultaneously measured with arbitrary precision. Otherwise, the two operators are called *incompatible* and there is a limit over the accuracy on which it is possible to simultaneously measure their expectation values. In particular, the *Heisenberg uncertainty principle* [100] provides a lower bound for their variance:

$$\Delta O_1 \Delta O_2 \geq \frac{1}{2}|\langle[O_1, O_2]\rangle| \tag{1.4}$$

that explains how increasing the precision over one of the two incompatible observables decreases the precision over the other.

Postulate III: *The evolution of a closed quantum system is described by a unitary evolution. The state of a system* $|\psi\rangle$ *at time* t_0 *is linked to the state* $|\psi'\rangle$ *at time* t_1 *by a unitary operator* U *that depends upon only on the times* t_0 *and* t_1*.*

$$|\psi'\rangle = U(t_1, t_0)\,|\psi\rangle \tag{1.5}$$

In the continuous-time framework, this reduces to the famous Schrödinger equation:

$$i\hbar\frac{d}{dt}\,|\psi(t)\rangle = H\,|\psi(t)\rangle \tag{1.6}$$

Where H *is the fixed hermitian operator known as the Hamiltonian of the system and* $\hbar$ *is a physical constant known as reduced Plank constant.*

If the Hamiltonian is time-independent the solution to the Schrŏdinger equation can be written as:

$$|\psi(t_1)\rangle = e^{-\frac{i}{\hbar}H(t_1-t_0)}\,|\psi(t_0)\rangle \longrightarrow U(t_1,t_0) = exp\left[-\frac{i}{\hbar}H(t_1-t_0)\right] \tag{1.7}$$

This gives us a rule to describe the free evolution of an isolated system. However, whenever an experimentalist wants to investigate the properties of a quantum system, he needs to interact in some way with it by performing a measurement. Hence, the system is not closed anymore, we have to introduce a postulate that describes the effect of measurements.

Postulate IV: *Took a quantum system* $|\psi\rangle$*, quantum measurements are described as a collection* $\{M_m\}$ *of measurement operators living in the Hilbert space associated with the system. The indices* m *are associated with the various possible measurement outcomes. The state of the system after the measurement is:*

$$\frac{M_m\,|\psi\rangle}{\sqrt{\langle\psi|\,M_m^\dagger M_m\,|\psi\rangle}} \tag{1.8}$$

and the probability of obtaining such an outcome is:

$$p(m) = \langle\psi|\,M_m^\dagger M_m\,|\psi\rangle \tag{1.9}$$

where we indicate with † *the transpose and complex conjugate operation.*

Since probabilities sum to one, the measurement operators have to respect the *completeness equation*:

$$\mathbb{1} = \sum_m p(m) = \sum_m \langle\psi|\,M_m^\dagger M_m\,|\psi\rangle \longrightarrow \sum_m M_m^\dagger M_m = \mathbb{1} \tag{1.10}$$

Where $\mathbb{1}$ is the Hilbert space identity operator.

The state of Postulate IV is intriguing, it introduces probabilities inside the theory and defines the action of measurements without accounting that the measurement apparatus is a quantum system itself. How to interpret this statement and its consequences that are linked with the way we observe reality, such as the *wave-function collapse*, are still debated [101–103]. For our interests, we can consider Postulate IV as a rule to follow and apply when computing the outcomes probabilities of a measurement, as a tool in our *quantum recipe*.

Finally, we have to deal with the possibility of having a quantum system composed of several subsystems and how to describe it. That is important when we consider interactions between different quantum systems.

Postulate V: *A composite quantum system lives in a Hilbert space obtained as the tensor product of the state spaces of the physical subsystems composing it. Hence, take the systems A living in the Hilbert space $\mathcal{H}_A$ and B living in $\mathcal{H}_B$, the system composed by A and B then lives in $\mathcal{H}_A \otimes \mathcal{H}_B$.*

This formulation will be useful when we introduce the concept of separable and *entangled* quantum states.

Exploiting the superposition principle, which asserts that if $|\psi\rangle$ and $|\phi\rangle$ are possible states of a quantum system also a state of the form $a\,|\psi\rangle + b\,|\phi\rangle$ with $|a|^2 + |b|^2 = 1$ is an allowed description of it. We have that the more general state of the composite system A,B can be written as:

$$|\psi\rangle_{AB} = \sum_{a,b} c_{a,b}\,|a\rangle_A \otimes |b\rangle_B \tag{1.11}$$

where $c_{a,b} \in \mathbb{C}$ with $\sum_{a,b} |c_{a,b}|^2 = 1$ and we explicitly indicated in which space each system lives.

Without going deeper into the meaning of the postulates and their implications, we have now the rules to apply the quantum recipe to each case in which we are interested.

1.1.2 Density Matrix Representation

The postulates we introduced in the previous Section consider that the system we are analyzing is perfectly determined. Hence, we can represent it as a unit complex vector $|\psi\rangle$ which contains all the information on the system. In this case, we say that our quantum state is *pure*.

In practice, the state of a physical system is often not completely known. For example, we can think to know only that our system is in a state taken from the ensemble of pure states $\{|\psi_1\rangle, ..., |\psi_n\rangle\}$ with probabilities $\{p_1, ..., p_n\}$ and $\sum_i p_i = 1$. The state of the system is then in a *statistical mixture* of that states or in a *mixed* state. To describe this situation we can introduce the *density* matrix [1, 3]:

$$\rho = \sum_i p_i\,|\psi_i\rangle\!\langle\psi_i| \tag{1.12}$$

The latter contains information on both the classical probabilities p_i, resulting from our lack of knowledge over the system initial state, and the quantum probabilities, emerging when we perform a measurement over the state $|\psi_i\rangle$ (Postulate IV). Moreover, Eq. 1.12 contains also the pure case, for which the system is in the state $|\psi\rangle$ with probability equal to 1, and so $\rho_{pure} = |\psi\rangle\!\langle\psi|$.

The diagonal elements of ρ are called *population* terms and contain the occupation probability of the states of the ensemble, while the off-diagonal on are related to the interference between states and are called *coherence* terms. The density matrix presents the following properties:

- ρ is Hermitian $\longrightarrow \rho^\dagger = \rho$
- ρ has unit trace $\longrightarrow Tr[\rho] = 1$
- ρ is non-negative $\longrightarrow \langle\phi|\,\rho\,|\phi\rangle \geq 0$ for any $|\phi\rangle$ in the Hilbert space $\mathcal{H}$

Furthermore, a simple criterion to distinguish between pure and mixed states is to analyze the value of $Tr[\rho^2]$, which is why it is called *purity* of ρ. In particular, the density matrix of a pure state presents only one eigenvalue $\lambda_{pure} = 1$ and so $Tr[\rho^2] = 1$, while for a mixed state $Tr[\rho^2] < 1$.

The density matrix formalism is particularly useful when we want to describe a quantum system that is not known and when we are analyzing subsystems of a composite quantum state, All the postulates enunciated in the previous Section can be easily rewritten in this formalism. For instance, if the evolution of the closed system is described by the unitary evolution U and its initial state is $|\psi_i\rangle$ with probability p_i, the final state will be $U\,|\psi_i\rangle$ with the same probability. Hence, we have that:

$$\rho_{t_1} = U(t_0, t_1)\rho_{t_0}U(t_0, t_1)^\dagger \tag{1.13}$$

Moreover, in this formalism, following the definition of Eq. 1.2 we can introduce the expectation value of an observable as follows:

$$\langle O\rangle_\rho = \sum_i p_i \,\langle\psi_i|\,O\,|\psi_i\rangle = \mathrm{Tr}(O\rho) \tag{1.14}$$

Throughout the thesis, we will use both the state vector and the density matrix description depending on the case under study.

1.1.3 Quantum Measurements

As we saw, the measurement procedure is one of the postulates of Quantum Mechanics, describing what happens when we perturb the unitary evolution of a closed quantum system to get information on it. Without going into details about the debated measurement problem [101–103], here we briefly give the standard description of the kinds of measurements and procedures.

Projective Measurements

This is a special case of Postulate IV, for which we ask that in addition to respecting the completeness relation, the operators $\{M_m\}$ have to be Hermitian and orthogonal:

$$M_m^\dagger = M_m \tag{1.15}$$

$$M_i M_j = \delta_{ij} M_j \tag{1.16}$$

From the outcome of the projective measurements the state of the system is known, and if the initial state is pure, the final one, after the measurement, is pure as well. In particular, applying a projector P_m, the quantum state immediately after the measurement is [1–3]:

$$|\psi\rangle_m = \frac{P_m |\psi\rangle}{\sqrt{\langle\psi| P_m |\psi\rangle}} \tag{1.17}$$

The projective measurements present a peculiar property called *repeatability*. Indeed, if we obtain m as the outcome after the measurement and we repeat the measurement procedure we will obtain again m while the quantum state will remain the same since $P_m |\psi\rangle_m = |\psi\rangle_m$.

Positive Operator Valued Measurements

Positive Operator Valued Measurements (POVMs) are especially suited for describing measurement situations in which one is not interested in the state after the measure, for instance when the measured system is destroyed as in the photon detection, but only in the probabilities of the various outcomes. In this case, we can define the measurement operators as:

$$F_k = M_k^\dagger M_k \tag{1.18}$$

In this way, F_k is a positive operator such that $\sum_k F_k = \mathbf{1}$ and $\langle F_k\rangle = \langle\psi| F_k |\psi\rangle = p_k \geq 0$. These operators are sufficient to describe the different measurement outcomes, while the outcome state is not determined by F_k making them a more general approach to describe measurement apparatus.

Projective measurements are included inside the POVM description, in this case $F_k = P_k^\dagger P_k = P_k$ and it is the only instance in which all POVM elements are the same as the measurement operators. In particular, it is possible to show that any POVM can be mapped in a projective measurement scenario in which the measure is performed in an enlarged Hilbert space, obtained by adding ancillary quantum systems to the one of interest [1, 2].

Quantum State Tomography

The objective of the measurement procedure is to obtain information about the properties of a quantum system, a specific case is when we want to completely reconstruct the state or its density matrix from the measurement outcomes. In this case, we talk about *quantum state tomography* [1–3].

Widely used inside the Quantum Information field, quantum state tomography is a method that exploits several copies of a quantum system to retrieve the density matrix entries by estimating suitable observables. For instance, when analyzing bi-dimensional quantum systems the choice is represented by the Pauli matrices (see Section 1.2 for more details), since they represent a basis for the space of 2 × 2 Hermitian matrices. In particular, a technique exploited in this approach to perform the density matrix reconstruction from the measurement outcomes is the *maximum likelihood estimator* [104, 105]. A procedure that finds the density matrix $\hat{\rho}$ that maximizes the likelihood function $\mathcal{L}(\mathbf{x}|\hat{\rho})$, that is the conditional probability of obtaining the outcomes $\{\mathbf{x}\}$ if the density matrix is $\hat{\rho}$. For instance, given a set of POVM measurements $\{F_\nu\}$ and assuming a Gaussian noise in the measured data, the likelihood reads:

$$\mathcal{L}(\mathbf{x}|\rho) = \sum_\nu \frac{\left(\langle F_\nu\rangle_\rho - x_\nu\right)^2}{2\,\langle F_\nu\rangle_\rho} \tag{1.19}$$

Therefore, from Eq. 1.19, we can retrieve the density matrix that better describes the experimental observations. Moreover, with respect to other approaches that directly retrieve the density matrix entries from the measured statistics, the maximum likelihood method ensures to have as a result a meaningful physical state, by properly constraining the solution space. Indeed, we can constrain the reconstruction to give as results only the density matrices that respect the properties reported in Section 1.1.2

1.1.4 Separable and Entangled states

One of the most peculiar manifestations of Quantum Mechanics is for sure the counter-intuitive concept of *entanglement.* In Section 1.1.1 we introduced the Postulate V, which gives us an indication of how to describe the state of a composite system, where the general quantum state of a bipartite system is described by Eq. 1.11. In this framework, we can introduce the concept of entangled states.

If the quantum state of a system can be reduced to the tensor product of a state $|\xi\rangle_A \in \mathcal{H}_A$ with a state $|\phi\rangle_B \in \mathcal{H}_B$, i.e. one has that:

$$|\psi\rangle_{AB} = |\xi\rangle_A \otimes |\phi\rangle_B \tag{1.20}$$

we say that the state is *separable* and we can describe each subsystem independently from the other. Otherwise, it cannot be decomposed and is called *entangled.* The same concept can be given also using the density matrix formalism, for which we have that the total system is described by:

$$\rho_{AB} = |\psi\rangle_{AB} \langle\psi| = \sum_{i,j} \sum_{\alpha,\beta} \rho_{i\alpha,j\beta} |i\rangle_A |\alpha\rangle_B \langle j|_A \langle\beta|_B \tag{1.21}$$

where $\rho_{i\alpha,j\beta} = \langle i|_A \langle\alpha|_B \rho_{AB} |j\rangle_A |\beta\rangle_B$. The density matrix of a separable system is defined, similarly to Eq. 1.20, as:

$$\rho_{AB} = \sum_i p_i \, \rho_{A,i} \otimes \rho_{B,i} \tag{1.22}$$

for some set of states $\{\rho_{A,i}, \rho_{B,i}\}$ belonging respectively to the Hilbert spaces $\mathcal{H}_A$ and $\mathcal{H}_B$, and with $\sum_i p_i = 1$. Also in this formalism, if the decomposition of Eq. 1.22 does not hold, the subsystems are entangled. Furthermore, an entangled state is said to be *maximally entangled* if the reduced matrix of each subsystem, obtained after the partial trace of the other, is proportional to the identity matrix, i.e. the completely mixed state.

An important class of maximally entangled bipartite states is represented by the *Bell states*:

$$\begin{aligned} |\Phi^{\pm}\rangle &= \frac{1}{\sqrt{2}}(|\uparrow\uparrow\rangle \pm |\downarrow\downarrow\rangle) \\ |\Psi^{\pm}\rangle &= \frac{1}{\sqrt{2}}(|\uparrow\downarrow\rangle \pm |\downarrow\uparrow\rangle) \end{aligned} \tag{1.23}$$

which constitute an orthonormal basis for the total Hilbert space $\mathcal{H}_A \otimes \mathcal{H}_B$. The states name derives historically form the violation of Bell's inequality [106], which was deduced during the seminal debates about the *completeness* of the Quantum Theory and was used to rule out the concept of local causality proposed by Einstein, Podolsky and Rosen (EPR) [107]. In particular, the inequality provides a classical limit on the correlation of a measurement outcomes which can be proven to be exceeded by quantum entangled systems (more details can be found in Appendix

A). Therefore, Bell's inequality can be used as a *witness* of entanglement since every state that violates the inequality is nonlocal and entangled. However, even if for pure bipartite state the entanglement and nonlocality are equivalent concepts, that is not the case when we work with mixed ones. In this case, Bell's inequality is not a necessary condition and it is possible to have entangled states that do not violate it [108, 109].

1.2 Quantum Information

In this Section, we give the rudiments of Quantum Information [1–3]. Making use of the properties already introduced in the previous one, such as the superposition principle and the entanglement, Quantum Information connects the two broad branches of quantum and information theories proposing a procedure to overcome the performance obtainable with classical resources. Exploiting quantum features brought benefits to several areas ranging from computation to communication [4–7], producing a speed-up and furnishing more powerful algorithms.

Quantum Information processing is intrinsically probabilistic and quantum algorithms have to be repeated several times to obtain the correct solution with probability as close to one as possible. A generic quantum computation procedure can be divided into three steps:

- Preparation of the initial quantum state
- Implementation of the desired unitary evolution
- Measurement of the output state to obtain the results

We will focus on all of them in the following Sections.

1.2.1 Qubits and qudits

The *qubit* is the elementary unit of Quantum Information. Being the quantum counterpart of the classical bit, the qubit lives in a bi-dimensional Hilbert space. There, taking two orthogonal unit vectors we can define the *computational basis* $\{|0\rangle, |1\rangle\}$ and from the superposition principle the generic state of a qubit is:

$$|\psi\rangle = \alpha |0\rangle + \beta |1\rangle \tag{1.24}$$

where α, β are complex numbers with $|\alpha|^2 + |\beta|^2 = 1$, since $|\psi\rangle$ has to be normalized.

Knowing that a quantum state is always defined up to a global phase, since it doesn't play a role when estimating expectation values and probabilities, we can move to polar coordinates using two real parameters instead of α, β. The Eq. 1.24 can be rewritten as:

$$|\psi\rangle = \cos\frac{\theta}{2} |0\rangle + e^{i\phi} \sin\frac{\theta}{2} |1\rangle \tag{1.25}$$

Where $\theta \in [0, \pi]$ and $\phi \in [0, 2\pi]$. Hence, while the classical bit can assume only values equal to 0 and 1, being parametrized by continuous variables the quantum bit can assume a continuum of states enlarging the possibilities of computation. The polar coordinates formulation is interesting because using that a quantum state can be represented as a point on a unitary sphere called the *Bloch sphere* (reported in Fig. 1.1), and all the transformations applied to the states can be seen as a change of its position inside the sphere.

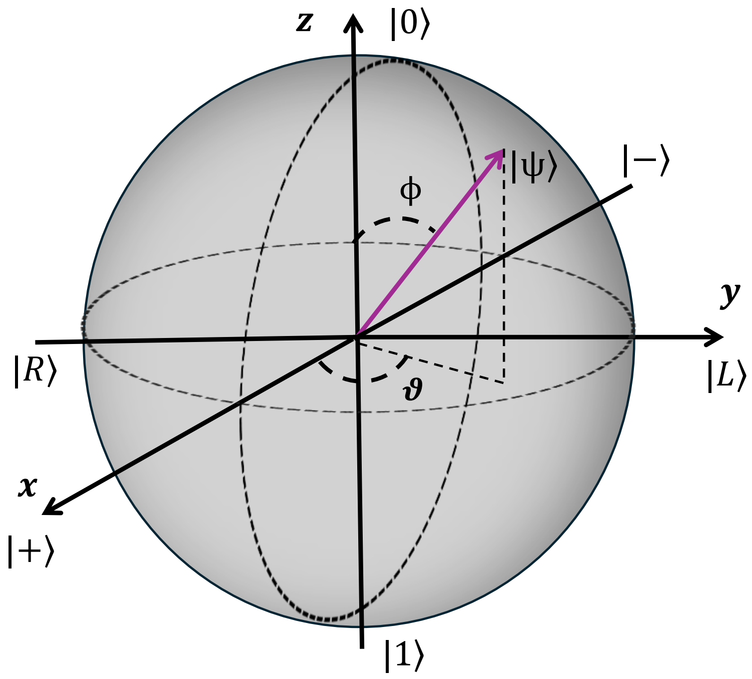

Figure 1.1. Bloch Sphere. Quantum states are represented as geometrical points inside the unitary Bloch sphere. Every pure state is on the surface of the sphere, with the computation state basis $\{|0\rangle, |1\rangle\}$ placed respectively at the north and south poles. Mixed states instead are contained inside the sphere.

Moreover, the density matrix for a qubit can be expressed using the Hermitian matrices basis composed of the three Pauli matrices:

$$\sigma_x = \begin{pmatrix} 0 & 1 \\ 1 & 0 \end{pmatrix}, \quad \sigma_y = \begin{pmatrix} 0 & -i \\ i & 0 \end{pmatrix}, \quad \sigma_z = \begin{pmatrix} 1 & 0 \\ 0 & -1 \end{pmatrix} \tag{1.26}$$

$$\rho = \frac{1}{2}(\mathbb{1} + x\sigma_x + y\sigma_y + z\sigma_z) \tag{1.27}$$

where the real numbers $\{x, y, z\}$ are the expectation values of the three operators $\langle \sigma_i \rangle_\rho = \mathrm{Tr}\,(\sigma_i \rho) = i$ with $i = \{x, y, z\}$, and represent the Cartesian coordinates in the Bloch sphere description. So from 1.27, when performing the quantum state tomography of a qubit the suitable choice of operators to measure is represented by the Pauli matrices.Moreover, defining $\mathbf{r} \equiv (x, y, z)$ it is possible to show that $det\rho = \frac{1}{4}(1 - |\mathbf{r}^2|)$, and recovering the properties of a density matrix we have that $det\rho \geq 0$ if and only if $0 \leq |\mathbf{r}| \leq 1$ for a physical state. Therefore, we can distinguish between pure and mixed states depending on the $|\mathbf{r}|$ value. If $|\mathbf{r}| = 1$ the state is pure, otherwise the state is mixed.

Finally, we can extend the concept of the qubit to d-dimensional Hilbert spaces introducing the *qudit*:

$$|\Psi\rangle = \sum_{i=1}^{d} c_i \, |i\rangle \tag{1.28}$$

where c_i are complex numbers satisfying the normalization condition $\sum_{i=1}^{d} |c_i|^2 = 1$ and $\{|i\rangle\}$ are the d vectors composing the canonical basis of the Hilbert space.

The interest in employing these states, going beyond the qubits, is that they can enhance the performance in quantum communication and cryptography [8, 10, 27] by respectively increasing the information transmitted with a single carrier and the security of the protocols against eavesdroppers.

1.2.2 Circuit model of quantum computation: Quantum gates

A classical computer can be described efficiently by using a n bits register on which we act changing their values in a controlled way. Elementary operations, such as AND and NOT, can be applied to single bits or couples of them and can be combined to produce complex functions. This classical circuit model can be expanded to the case of quantum computation, where, neglecting the interaction between the quantum systems and the environment, unitary operators implementing quantum gates are applied to a quantum register of n qubits. Compared to the classical case, here the superposition principle opens the way for parallel computing with an exponential number of inputs. In any case, for exploiting this power it is necessary to have an architecture that permits to efficiently extract the information stored in the output quantum state.

It is possible to show how every single qubit operation can be decomposed in just two fundamental gates: The *Hadamard* gate H and the phase gate R_z.

$$H = \frac{1}{\sqrt{2}}\begin{pmatrix} 1 & 1 \\ 1 & -1 \end{pmatrix}, \quad R_z(\delta) = \begin{pmatrix} 1 & 0 \\ 0 & e^{i\delta} \end{pmatrix} \tag{1.29}$$

where the first one makes the change of basis:

$$\{|0\rangle, |1\rangle\} \longrightarrow \left\{ |+\rangle = \frac{1}{\sqrt{2}}(|0\rangle + |1\rangle), |-\rangle = \frac{1}{\sqrt{2}}(|0\rangle - |1\rangle) \right\} \tag{1.30}$$

and the second one is a rotation along the z axis of the Bloch sphere (See Fig. 1.1). Employing these two gates it is possible to make arbitrary operations on single-qubit states, for instance starting from $|0\rangle$ we can generate any other state with the following combination of gates:

$$R_z(\pi/2 + \phi)\ H\ R_z(2\theta)\ H\,|0\rangle = e^{i\theta}(\cos\frac{\theta}{2}\,|0\rangle + e^{i\phi}\sin\frac{\theta}{2}\,|1\rangle) \tag{1.31}$$

The two qubits logical gates are instead represented by $2^2 \times 2^2$ matrices. The most interesting ones are the controlled gates, which don't act independently over the two qubits but condition the action over a target one depending on the other. Applying these gates it is possible for example to generate entangled states.

Defining the computational basis on the two-qubit Hilbert space as:

$$|00\rangle = \begin{pmatrix} 1 \\ 0 \\ 0 \\ 0 \end{pmatrix}, \quad |01\rangle = \begin{pmatrix} 0 \\ 1 \\ 0 \\ 0 \end{pmatrix}, \quad |10\rangle = \begin{pmatrix} 0 \\ 0 \\ 1 \\ 0 \end{pmatrix}, \quad |11\rangle = \begin{pmatrix} 0 \\ 0 \\ 0 \\ 1 \end{pmatrix} \tag{1.32}$$

The general definition of a controlled logical gate is:

$$CU = \begin{pmatrix} \mathbb{1} & 0 \\ 0 & U \end{pmatrix} = \begin{pmatrix} 1 & 0 & 0 & 0 \\ 0 & 1 & 0 & 0 \\ 0 & 0 & u_{11} & u_{12} \\ 0 & 0 & u_{21} & u_{22} \end{pmatrix} \tag{1.33}$$

with action:

$$CU \left| i_a \right\rangle \left| i_t \right\rangle = \left| i_a \right\rangle U^{i_a} \left| i_t \right\rangle \tag{1.34}$$

So while the state of the *ancillary* qubit remains unchanged, depending on its initial value, U is applied or not to the target one. Interesting examples are the CNOT and CPHASE for which:

$$U_{CNOT} = \begin{pmatrix} 0 & 1 \\ 1 & 0 \end{pmatrix}, \quad U_{CPHASE}(\phi) = \begin{pmatrix} 1 & 0 \\ 0 & e^{i\phi} \end{pmatrix} \tag{1.35}$$

In particular, CNOT is interesting since it allows us to generate entangled qubits. In fact, by applying an Hadamard gate to the ancillary qubit and a CNOT on both, it is possible to generate the Bell states from the computation basis states:

$$\left|00\right\rangle \longrightarrow \left|\Phi^+\right\rangle, \quad \left|01\right\rangle \longrightarrow \left|\Psi^+\right\rangle, \quad \left|10\right\rangle \longrightarrow \left|\Phi^-\right\rangle, \quad \left|11\right\rangle \longrightarrow \left|\Psi^-\right\rangle \tag{1.36}$$

The reverse of this evolution allows us to measure the Bell states.

Moreover, the CNOT together with the single qubit gates form an universal gate set, that is a set composed of gates with which we can decompose any arbitrary operation [1, 3].

1.2.3 Quantum Algorithms and Quantum Walk

Several quantum algorithms have been developed during the years to exploit the potential of quantum resources over the classical ones. In particular, the studies have been focused on both creating powerful algorithms to speed up the computation and designing clever ways to retrieve the information stored in the final quantum state produced by the calculation. The second one is of particular interest in order to get full access to the power brought by quantum computation. The quantum algorithms can be divided into three classes [1]:

- **Algorithms based upon Fourier transform.** These algorithms follow the classical computation trend of using the discrete Fourier transform to develop an efficient computational model. Using the quantum Fourier transform, these algorithms provide *exponential* speed-ups, such as in the case of the *Shor's algorithm* for finding the prime factors of an integer [4].

- **Searching Algorithms.** These algorithms solve the problem of finding a specific element, satisfying a wanted characteristic, inside a non-structured database. The most famous one is the Grover algorithm which produces a *quadratically* speed-up with respect to the classical algorithms [5].

- **Quantum Simulation.** These algorithms were formulated to address the classical limit in simulating large quantum systems. Indeed, the number of parameters needed for the description increases *exponentially* when adding qubits to the system. Therefore, quantum computers have been proposed to effectively perform these protocols and solve the task at hand, since they can automatically account for such limitations. In this context, the main difficulty is then in the retrieval of the information after the computation. Therefore, a lot of effort is put into the study of how efficiently extract it and obtain the desired results.

In this context, an interesting computational paradigm on which to implement quantum algorithms is represented by the *quantum walk* [63, 110]. This is the quantum counterpart of the classical random walk, which is a powerful classical paradigm widely applied for solving different problems in biology, statistics, and finance [111]. Then it is not surprising that the same model was restated in the quantum domain, looking for a computational speed-up. One of the most interesting result in this ambience is the fact that quantum walks have been proven to be a universal model for quantum computation [112, 113]. In particular, it has been shown that the Grover searching algorithm can be performed with a quantum walk implementation [114, 115]. Moreover, quantum walks find several applications ranging from simulation [116–118] and cryptography [119, 120] to state engineering [65, 66, 121].

Quantum walks are typically divided into two classes: *discrete-time quantum walk* (DTQW) and *continuos-time quantum walk* (CTQW). In the first case, the bipartite system composed of a *coin* and a *walker* evolves per discrete steps, while in the second one, the evolution is described by a unitary operator that acts continuously in time. In this thesis, we will focus only on DTQW and in particular on its one-dimensional case.

Discrete time quantum walks

The one-dimensional DTQW describes the conditional evolution of a quantum state called the walker over a lattice of length d, which has an additional internal degree of freedom called the coin. At each time step, the walker moves on the lattice depending on the state of the coin, creating a rich dynamics that has been exploited to implement many Quantum Information tasks [122].

The walker lives in a d-dimensional Hilbert space $\mathcal{H}_w$, where $d = 2N + 1$ with N the number of steps of the evolution. The coin instead lives in a bi-dimensional Hilbert space $\mathcal{H}_c$ spanned by the basis $\{|\uparrow\rangle, |\downarrow\rangle\}$, here the coin can take all the possible states while in the classical implementation it can have only values equal to $\uparrow$ or $\downarrow$. Such fundamental difference between the dynamics produces a very distinct behavior in the output distribution as we will dettailed below. The total system then lives in the Hilbert space given by the tensor product $\mathcal{H}_w \otimes \mathcal{H}_c$.

The walker displacement on the lattice is governed by the *shift* operator, which increases or decreases the walker position depending on the coin state:

$$S = \sum_{k=-N}^{k=N} |k+1\rangle_w \langle k| \otimes |\uparrow\rangle_c \langle\uparrow| + |k-1\rangle_w \langle k| \otimes |\downarrow\rangle_c \langle\downarrow| \tag{1.37}$$

Hence, opportunely acting on the coin state at each step is possible to control the evolution of the walker and implement the desired protocol. At each step then also the state of the coin is changed, and a generic coin toss is represented by the following unitary operator acting in the bi-dimensional space [123]:

$$C(\xi, \zeta, \theta) = \begin{pmatrix} e^{i\xi}\cos\theta & e^{i\zeta}\sin\theta \\ -e^{-i\zeta}\sin\theta & e^{-i\xi}\cos\theta \end{pmatrix}, \tag{1.38}$$

where $\xi, \zeta \in [0, 2\pi]$ and $\theta \in [0, \pi]$. The total evolution after N steps is described as the unitary operator:

$$U_{QW} = \prod_i^N U_i = \prod_i^N S \cdot (C_i \otimes \mathbb{1}_w) \tag{1.39}$$

Therefore, given the initial state $|\psi(0)\rangle$ after N steps we have:

$$|\psi(N)\rangle = U_{QW}\,|\psi(0)\rangle = \sum_{k=-N}^{N}\sum_{s=\downarrow,\uparrow} u_{k,s}\,|k\rangle_w\,|s\rangle_c \tag{1.40}$$

The final state is a superposition of several walker positions, associated with one of the two possible coin states, and both the coin and walker states can be measured on a suitable basis. In particular, it is possible to act in two ways on the system to extract information upon the output of the quantum walk dynamics implemented: *i*) analyzing the walker distribution for a specific coin state, or *ii*) studying the walker position for any coin configuration. The first case consists of projecting the state in Eq. 1.40 over a specific coin state, for instance the basis element $|\uparrow\rangle$, and investigating the occupation probability of the lattice sites of the resulting walker state:

$$|\psi\rangle_\uparrow = \langle\uparrow|\psi(N)\rangle \tag{1.41}$$

$$p_k = \left|\langle k|\psi\rangle_\uparrow\right|^2 \tag{1.42}$$

The distribution of p_k depends upon the implemented DTQW evolution and on the coin projection, in fact both of them change the d-dimensional output walker state. Such property can not be reproduced in the classical random walk since it is due to the entanglement between the walker and coin states created by the controlled displacement operator of Eq. 1.37.

In the case *ii*) instead, the coin state is traced out and all the information about the walker, contained in the two different projections, is summed up. In particular, defined $\rho_{out} = |\psi(N)\rangle\langle\psi(N)|$ we perform a partial trace over the coin subspace:

$$\rho_w = Tr_c[\rho_{out}] = \sum_{s=\downarrow,\uparrow} \langle s|\,\rho_{out}\,|s\rangle = |\psi\rangle_\uparrow\,\langle\psi| + |\psi\rangle_\downarrow\,\langle\psi| \tag{1.43}$$

And we have that:

$$p_k = Tr_w[|k\rangle\langle k|\,\rho_w] = \left|\langle k|\psi\rangle_\uparrow\right|^2 + \left|\langle k|\psi\rangle_\downarrow\right|^2 \tag{1.44}$$

In this situation, we can make a comparison with the classical random walk distribution. The classical random walk is a stochastic process in which the walker moves to the right or the left upon the result of a coin toss, that is performed at the beginning of every step. Hence, each step can be modeled as a Bernoulli stochastic process and the output distribution of the walker positions follows the binomial distribution:

$$\mathcal{B}_k^{RW} = \begin{pmatrix} N \\ \frac{1}{2}(N+k) \end{pmatrix} p^{\frac{1}{2}(N+k)} q^{\frac{1}{2}(N-k)} \tag{1.45}$$

Where N is always the number of steps, k is the number of times in which head is obtained as the result of the coin toss and p is the coin bias, with therefore $q = 1 - p$. If we take a fair coin with $p = \frac{1}{2}$, the corresponding DTQW is represented by the Hadamard QW, i.e. the DTQW in which the coin operators are all Hadamard gates (see Eq. 1.29). Indeed, we saw that the Hadamard gates perform a basis transformation that creates an unbiased superposition of the basis elements $\{|\uparrow\rangle, |\downarrow\rangle\}$, emulating the coin toss with equal possibility of obtain head and tail.

In Fig. 1.2 the comparison between the distributions 1.44 and 1.45 is reported after 100 steps. The main difference between the two is the spreading in the walker position. In fact, for the binomial distribution the variance scales as $\sigma^2_{RW} \sim O(N)$, and the walker is centered around the initial position. Instead, we have that $\sigma^2_{QW} \sim O(N^2)$ for the QW, and the walker is localized at the lattice extremes. In particular, the walkers associated with the two possible coin states spread quickly to the limits of the lattice while interfering destructively in the central spots, creating the distribution reported in Fig. 1.2-b. The reason for this central disruptive interference is addressable to the minus sign comparing in the expression of the Hadamard coin (see Eq. 1.29).

This effect is called *ballistic behavior* and it is one of the main features characterizing the QW evolution for which it has several algorithmic applications.

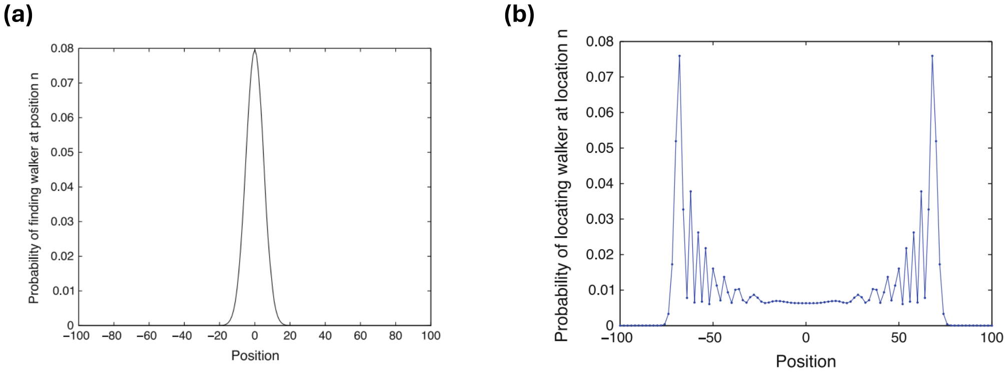

Figure 1.2. Walker distribution. Walker position output distribution for a classical random walk **a)** and a discrete-time quantum walk **b)** after 100 steps of evolution. It is possible to note the ballistic behavior of the quantum walk in the spreading of walker states over the lattice. Images taken from [63].

1.2.4 Fidelity of quantum states

The measurements of the output of a quantum computation process is one of the pivotal tasks in Quantum Information. In particular, using one of the procedures explained in Section 1.1.3, one of the main purposes is to compare an experimentally produced state to a theoretically expected one. The most used metric in this context is the *fidelity* between two quantum states [1, 124].

Classically, taken two random variables X, Y which can assume n values with probability $\{p_1, \dots, p_n\}$ and $\{q_1, \dots, q_n\}$, we define the fidelity between the two probability distribution as:

$$F(X,Y) = \left(\sum_{i=1}^{n} \sqrt{p_i q_i} \right)^2 \tag{1.46}$$

Similarly, given two quantum states described by density matrix ρ_1, ρ_2, the fidelity F can be defined as [124]:

$$F(\rho_1, \rho_2) = Tr\left[\sqrt{\sqrt{\rho_1}\rho_2\sqrt{\rho_1}}\right]^2 \tag{1.47}$$

For pure states $\{|\psi_1\rangle, |\psi_2\rangle\}$, Eq. 1.47 reduces to the overlap between quantum states:

$$F(|\psi_1\rangle, |\psi_2\rangle) = |\langle\psi_1|\psi_2\rangle|^2 \tag{1.48}$$

that is the probability of measure $|\psi_1\rangle$ when the system is in the state $|\psi_2\rangle$. A general definition of fidelity provides that it presents the following properties:

- Symmetry $\longrightarrow F(\rho_1, \rho_2) = F(\rho_2, \rho_1)$
- Bounded range values $\longrightarrow 0 \leq F(\rho_1, \rho_2) \leq 1, \ \forall \rho_1, \rho_2$
- Identity for indiscernible states $\longrightarrow \rho_1 = \rho_2 \ \ iff \ \ F(\rho_1, \rho_2) = 1$
- Invariance under unitary operators $\rightarrow F(\rho_1, \rho_2) = F(U\rho_1 U^\dagger, U\rho_2 U^\dagger) \ \ \forall \rho_1, \rho_2, U$

Thanks to these features, the fidelity results one of the most suitable choice for quantifying the distance between two quantum states and so to check if the quantum algorithm produced the wanted state as a result.

Chapter 2

Photonic Technologies

The beginning of the studies on light nature can be identified with the two seminal papers by Isaac Newton [125] and Christiaan Huygens [126]. These give different descriptions of light behaviour, Newton proposed a corpuscular interpretation in which light particles are spread in all directions from the source, while Huygens gave a wavelike explanation of the phenomenon in which each point of a wavefront is considered as a new source of wavelets that expand into space.

In the first theoretical and experimental studies, the second interpretation was the most followed one. The culmination of this approach can be seen in the important laws that James Clerk Maxwell collected in the XIX century [127]. This theory gives a complete explanation of the undulatory nature of light, proving that it can be described by time-position oscillating electric and magnetic fields that travel in vacuum at a speed equal to c and accounts for light typical phenomena, such as the interference [127]. However, this approach was challenged at the beginning of the XX century when it was not capable of explaining the radiative behaviour of a black body, resulting in the famous ultraviolet catastrophe. A solution to this problem was found by Max Plank, who proposed a quantization of the electromagnetic field [22]. In conclusion, a complete and consistent treatment of all optical phenomena is thus provided by the union of the classical Maxwell theory and the quantum theory. With the former describing the propagation of light and the latter describing instead the interaction with matter and the phenomena of emission and absorption. The combined theory is known as *Quantum Electrodynamics* [127].

From both the classical and quantum points of view, light possesses mechanical properties. The analysis of these properties started with the study of the influence of solar pressure on the comets tails made by Kepler, and gained new attention after Poynting showed that electromagnetic fields transport both energy and linear momentum [128]. Moreover, his other seminal paper [129] was the baseline for the analysis of another important property of light that has been a source of numerous studies: the *angular momentum.* In particular, the angular momentum is usually decomposed in the sum of a **Spin Angular Momentum** (SAM) and an **Orbital Angular Momentum** (OAM). The interest in SAM and its applications is based on its connection with circular polarization of the field, which was theorized by Poynting himself in [129] and then experimentally demonstrated by Beth [130] in 1936. In the same years, Darwin showed that the SAM is not the only angular momentum carried by light, formulating in this way the existence of an orbital angular momentum. However, only in the 1992 article by Allen *et al.* [24], the OAM was connected to the spatial structure of the field giving a new comprehension of the phenomenon. In particular, this work showed how all the helical beams that possess a phase term proportional to $e^{im\phi}$, with ϕ the azimuthal angle of cylindrical coordinates, transport an OAM equal to $\hbar m$ per photon. This property was directly observed in an experiment a short time later by He *et al.* [131]. Among the two components, the OAM has attracted a growing interest in recent times due to its several applications both in classical and quantum domains [26]. For instance, in the first one it has been employed for optical trapping [42], microscopy [43, 44] and classical communication [45–48]. While in the second one, various Quantum Information protocols have made use of it for quantum communication [31–34], computation [35–37], metrology [29, 38, 39] and cryptography [40, 41].

Moreover, especially Quantum Information field makes use of single photons as information carriers. Indeed respect to other platforms, such as trapped ions [132] or superconductive qubits [133], photons represent a suitable choice since they can be manipulated at room temperature, are easily transported through fibers or free air, and are systems with a low degree of decoherence [21]. Several degrees of freedom of the photons are exploited in different quantum protocols, one of the most used is the polarization, that living in a bi-dimensional Hilbert state is suitable to encode a qubit. High dimensional quantum states can instead be obtained using the orbital angular momentum, the path, and the time bin encoding. In particular, photons represent an essential resource and have been used in milestones experiments of Quantum Information, such as the first violation of EPR local causality [23] and the first quantum teleportation experiments [134, 135], and in a platform that achieved the *quantum advantage* [96].

In this chapter, we will start by illustrating classical and quantum descriptions of light in Section 2.1, giving their basic elements from the Maxwell equations to the quantization of the electromagnetic field. Then, we will focus on the description of the angular momentum of light, reporting its decomposition in the OAM and SAM parts in Section 2.2. Since the latter is performed in the paraxial approximation, we will continue by introducing the Helmholtz equation in Section 2.3, describing in detail its most interesting solutions. Finally, we will move to the Quantum Information experimental side by introducing the sources of single photons in Section 2.4 and how we can act on them to encode information in their degrees of freedom in Section 2.5.

2.1 Basis of classical and quantum description of light

The light undulatory nature is well described in classical electrodynamics by the four Maxwell's equations, that in vacuum and using the **SI** units take the form [136]:

$$\begin{cases} \nabla \cdot \mathbf{E} = \frac{\rho}{\epsilon_0} (\textit{Gauss' Law}) \\ \nabla \cdot \mathbf{B} = 0 \ (\textit{Gauss' Law}) \\ \nabla \times \mathbf{E} = -\frac{\partial \mathbf{B}}{\partial t} \ (\textit{Faraday's Law}) \\ \nabla \times \mathbf{B} = \mu_0 (\mathbf{J} + \epsilon_0 \frac{\partial \mathbf{E}}{\partial t}) \ \ (\textit{Ampère-Maxwell's Law}) \end{cases} \tag{2.1}$$

where $\mathbf{E}(\mathbf{r}, t)$ is the electric field, $\mathbf{B}(\mathbf{r}, t)$ is the magnetic field, $\rho(\mathbf{r}, t)$ is the density of free charges, $\mathbf{J}(\mathbf{r}, t)$ is the current density, ϵ_0 is the vacuum permittivity and μ_0 is the vacuum magnetic permeability.

Introducing the scalar potential ϕ and the vectorial potential $\mathbf{A}$, the electric and magnetic fields can be expressed as:

$$\mathbf{B} = \nabla \times \mathbf{A} \tag{2.2}$$

$$\mathbf{E} = -\nabla\phi - \frac{\partial \mathbf{A}}{\partial t} \tag{2.3}$$

These expressions have the property of being invariant under a particular kind of transformations called *gauge transformations.* Indeed, they have the same form if we change the potentials $\mathbf{A}, \phi$ with the potentials $\mathbf{A}', \phi'$ connected to the first in the following way:

$$\mathbf{A} = \mathbf{A}' - \nabla\Xi \tag{2.4}$$

$$\phi = \phi' + \frac{\partial \Xi}{\partial t} \tag{2.5}$$

where $\Xi(\mathbf{r}, t)$ is the *gauge function.* In particular, exploiting this invariance we can choose the *Coulomb or transverse gauge* for which $\nabla \cdot \mathbf{A} = 0$ and we can use a description based only on the transverse component of the vectorial potential $\mathbf{A}_T$, that is its divergence-free component. In particular, one can assume no free charges and currents, so in Eqs. (2.1) we use $\rho = 0$ and $\mathbf{J} = 0$. We then derive the following equations for the two potentials:

$$-\nabla^2\mathbf{A} + \frac{1}{c^2}\frac{\partial^2 \mathbf{A}}{\partial t^2} = 0 \tag{2.6}$$

$$\nabla^2\phi = 0 \tag{2.7}$$

where the first one has the form of the three-dimensional wave equation for the vectorial potential $\mathbf{A}$, with c the speed of light in vacuum, while the second one is known as *Laplace's equation.* Fixed the boundary conditions, solving the Eqs. 2.6 and 2.7 furnish us with a complete classical description of the electromagnetic field when it propagates in the vacuum. For instance, once retrieved the form of the electric and magnetic field from Eqs. 2.2-2.3, we can calculate the energy carried by the field as:

$$U_{em} = \frac{1}{2}\int_V \left(\epsilon_0 \mathbf{E}(\mathbf{r}, t) \cdot \mathbf{E}(\mathbf{r}, t) + \frac{1}{\mu_0}\mathbf{B}(\mathbf{r}, t) \cdot \mathbf{B}(\mathbf{r}, t)\right) d\mathbf{r} \tag{2.8}$$

For quantizing the electromagnetic field we can use the following argumentation. Equation 2.6 can be also solved by reducing the space to a cubic region of side L and imposing periodic conditions at the boundaries; this region is called the *quantization cavity.* In this case, it is then possible to expand the vector potential in the modes of the cavity [136]:

$$\mathbf{A}(\mathbf{r}, t) = \sum_{\mathbf{k}} \sum_{\lambda=1,2} \mathbf{e}_{\mathbf{k}\lambda} \mathbf{A}_{\mathbf{k}\lambda}(\mathbf{r}, t) \tag{2.9}$$

where $\mathbf{A}_{\mathbf{k}\lambda}(\mathbf{r}, t) = A_{\mathbf{k}\lambda}(t)\ e^{i\mathbf{k}\cdot\mathbf{r}} + A^*_{\mathbf{k}\lambda}(t)\ e^{-i\mathbf{k}\cdot\mathbf{r}}$ and $\mathbf{e}_{\mathbf{k}\lambda}$ is the polarization vector relative to λ. The components of the vector $\mathbf{k}$ have to respect the periodic conditions at the edges, so they can assume only the following values:

$$k_x = \frac{2\pi\nu_x}{L}, \quad k_y = \frac{2\pi\nu_y}{L}, \quad k_z = \frac{2\pi\nu_z}{L} \tag{2.10}$$

with $\nu_x, \nu_y, \nu_z = \{\pm 1, \pm 2, \pm 3, \dots\}$.

Each component of the vector potential expansion independently satisfies Eq.(2.6), which can be rewritten as:

$$\frac{\partial^2 A_{\mathbf{k}\lambda}(t)}{\partial t^2} + \omega_k^2 \, A_{\mathbf{k}\lambda}(t) = 0 \tag{2.11}$$

where $\omega_k = ck$ is the angular frequency of the mode, the solution of (2.11) associated with it is $A_{\mathbf{k}\lambda}(t) = A_{\mathbf{k}\lambda} \, e^{-i\omega_k t}$. In conclusion, the generic component of the potential vector $A_{\mathbf{k}\lambda}(\mathbf{r}, t)$ becomes:

$$A_{\mathbf{k}\lambda}(\mathbf{r}, t) = A_{\mathbf{k}\lambda} \, e^{i(\mathbf{k}\cdot\mathbf{r} - \omega_k t)} + A^*_{\mathbf{k}\lambda} \, e^{i(\omega_k t - \mathbf{k}\cdot\mathbf{r})} \tag{2.12}$$

Exploiting the relations (2.2) and (2.3), the components of the electric and magnetic fields in the chosen gauge can be derived:

$$E_{\mathbf{k}\lambda}(\mathbf{r}, t) = i\omega_k \left\{ A_{\mathbf{k}\lambda} \, e^{i(\mathbf{k}\cdot\mathbf{r} - \omega_k t)} - A^*_{\mathbf{k}\lambda} \, e^{i(\omega_k t - \mathbf{k}\cdot\mathbf{r})} \right\} \tag{2.13}$$

$$B_{\mathbf{k}\lambda}(\mathbf{r}, t) = ik \left\{ A_{\mathbf{k}\lambda} \, e^{i(\mathbf{k}\cdot\mathbf{r} - \omega_k t)} - A^*_{\mathbf{k}\lambda} \, e^{i(\omega_k t - \mathbf{k}\cdot\mathbf{r})} \right\} \tag{2.14}$$

In analogy to the classical case, we have that the energy assumes the following form:

$$U_{em} = \sum_k \sum_\lambda \epsilon_0 L^3 \omega_k^2 \left(A_{\mathbf{k}\lambda} A^*_{\mathbf{k}\lambda} + A^*_{\mathbf{k}\lambda} A_{\mathbf{k}\lambda} \right) \tag{2.15}$$

Finally, the electromagnetic field can be quantized by associating each mode of the cubic cavity with a quantum-mechanical harmonic oscillator. Therefore, we have the following Hamiltonian for the system [136]:

$$\mathcal{H} = \sum_{\mathbf{k}} \sum_\lambda \frac{1}{2} \hbar\omega_k \left(\hat{a}_{\mathbf{k},\lambda} \hat{a}^\dagger_{\mathbf{k},\lambda} + \hat{a}^\dagger_{\mathbf{k},\lambda} \hat{a}_{\mathbf{k},\lambda} \right) \tag{2.16}$$

where we have introduced the *creation* and *annhilation* operators:

$$\hat{a}_{\mathbf{k},\lambda} \left| n_{\mathbf{k},\lambda} \right\rangle = \sqrt{n_{\mathbf{k},\lambda}} \left| n_{\mathbf{k},\lambda} - 1 \right\rangle \tag{2.17}$$

$$\hat{a}^\dagger_{\mathbf{k},\lambda} \left| n_{\mathbf{k},\lambda} \right\rangle = \sqrt{n_{\mathbf{k},\lambda} + 1} \left| n_{\mathbf{k},\lambda} + 1 \right\rangle \tag{2.18}$$

where $\left| n_{\mathbf{k},\lambda} \right\rangle$ is the *Fock quantum state* associated with the mode identified by the indexes $\{\mathbf{k}, \lambda\}$, while $n_{\mathbf{k},\lambda}$ is the occupation number, which represents the number of photons excited in this cavity mode and it is the eigenvalue of the number operator $\hat{n}_{\mathbf{k},\lambda} = \hat{a}^\dagger_{\mathbf{k},\lambda} \hat{a}_{\mathbf{k},\lambda}$. A special state is the *vacuum* state, whose occupation number is equal to 0 and it is defined as $\hat{a}_{\mathbf{k},\lambda} \left| 0 \right\rangle = 0$ for all $\mathbf{k}, \lambda$. Different modes are independent and so their operators have to commute, then we have the following rules:

$$\left[\hat{a}_{\mathbf{k},\lambda}, \hat{a}_{\mathbf{k}',\lambda'} \right] = 0, \quad \left[\hat{a}^\dagger_{\mathbf{k},\lambda}, \hat{a}^\dagger_{\mathbf{k}',\lambda'} \right] = 0, \quad \left[\hat{a}_{\mathbf{k},\lambda}, \hat{a}^\dagger_{\mathbf{k}',\lambda'} \right] = \delta_{\mathbf{k},\mathbf{k}'} \delta_{\lambda,\lambda'} \tag{2.19}$$

and the total state of the system can be written as the tensor product of the individual modes Fock states:

$$\left| \{ \left| n_{\mathbf{k},\lambda} \right\rangle \} \right\rangle = \prod_i \left| n_{\mathbf{k_i},\lambda_i} \right\rangle = \left| n_{\mathbf{k_1},\lambda_1} \right\rangle \left| n_{\mathbf{k_2},\lambda_2} \right\rangle \left| n_{\mathbf{k_3},\lambda_3} \right\rangle \dots \tag{2.20}$$

In conclusion, by comparing the Hamiltonian of the field in Eq. 2.16 with the energy reported in Eq. 2.15, we obtain the following expression for the quantized vectorial potential:

$$A_{\mathbf{k},\lambda} \rightarrow \left(\frac{\hbar}{2\epsilon_0\omega_k L^3}\right)\hat{a}_{\mathbf{k},\lambda} \text{ and } A^*_{\mathbf{k},\lambda} \rightarrow \left(\frac{\hbar}{2\epsilon_0\omega_k L^3}\right)\hat{a}^\dagger_{\mathbf{k},\lambda} \tag{2.21}$$

Exploiting then the relation 2.3 and 2.2, we retrieve the expression for the quantized electromagnetic field.

2.2 Angular Momentum of Light

An electromagnetic wave transports energy (see Eqs. 2.8 and 2.15), linear momentum, identified as the *Poynting vector* $\mathbf{P} = \mathbf{E} \times \mathbf{B}$ [128], and an *intrinsic* angular momentum. The latter, instead of being linked to a fixed external point as it happens when we describe the angular momentum of a point particle in mechanics, is related to the spatial structure of the field and how the Poynting vector behaves during the wave propagation [24, 137, 138]. In particular, the angular momentum of light is composed of two components the *spin angular momentum* (SAM) and the *orbital angular momentum* (OAM). However, this decomposition is not straightforward if we are not under the *paraxial approximation.*

We start by giving the expression of the total angular momentum, which in analogy with the classical mechanics angular momentum is written as:

$$\mathbf{J} = \epsilon_0 \int \left[\mathbf{r} \times (\mathbf{E} \times \mathbf{B})\right] d\mathbf{r} \tag{2.22}$$

A canonical decomposition can be obtained by exploiting the relation in Eq. 2.2 to substitute the magnetic field with the vectorial potential [139]:

$$\mathbf{J} = \epsilon_0 \sum_{i=x,y,z} \int \left[E_i \left(\mathbf{r} \times \nabla\right) A_i\right] d\mathbf{r} + \epsilon_0 \int \left(\mathbf{E} \times \mathbf{A}\right) d\mathbf{r} \tag{2.23}$$

Where, recalling that the momentum operator in Quantum Mechanics is given by $\hat{\mathbf{p}} = -i\hbar\nabla$, by analogy we can associate the first integral with the OAM and the second one, which is independent of the space coordinates, with the SAM. However, this decomposition depends directly on the vectorial potential $\mathbf{A}$, so it is not gauge invariant and it doesn't give an unambiguous representation of the two components.

To have a decomposition that is gauge invariant we can exploit the **Helmholtz theorem** that states that we can divide each smooth and rapidly decaying vector field in a *transverse or solenoidal* part $\mathbf{E}_T$, for which $\nabla \cdot \mathbf{E}_T = 0$, and a *longitudinal or irrotational* component $\mathbf{E}_L$, for which $\nabla \times \mathbf{E}_L = 0$. Hence, by substituting $\mathbf{E} = \mathbf{E}_T + \mathbf{E}_L$ into Eq. 2.22 we obtain the standard decomposition [140]:

$$\mathbf{J}_L = \epsilon_0 \int \left[\mathbf{r} \times (\mathbf{E}_L \times \mathbf{B})\right] d\mathbf{r} \tag{2.24}$$

$$\mathbf{J}_T = \epsilon_0 \int \left[\mathbf{r} \times (\mathbf{E}_T \times \mathbf{B})\right] d\mathbf{r} \tag{2.25}$$

Exploiting Eq. 2.2 and 2.3 we can rewrite the longitudinal angular momentum $\mathbf{J}_L$ as:

$$\mathbf{J}_L = \int \left[\rho \left(\mathbf{r} \times \mathbf{A}_T\right)\right] d\mathbf{r} \tag{2.26}$$

This angular momentum is associated with the free charges, indeed if we substitute the density of charge $\rho = \sum_\beta q_\beta \delta(\mathbf{r} - \mathbf{r}_\beta(t))$ into Eq. 2.26 we have that:

$$\mathbf{J}_L = \sum_{\beta} q_{\beta} \left(\mathbf{r}_{\beta} \times \mathbf{A}_T(\mathbf{r}_{\beta})\right) \tag{2.27}$$

hence, when there are no free charges, this component can be neglected.

More interesting, it is the transverse component of the angular momentum, proceeding similarly to the longitudinal case and recalling that by definition $\nabla \cdot \mathbf{E}_T = 0$, we have that:

$$\mathbf{J}_T = \epsilon_0 \int \left[\sum_{\alpha=x,y,x} \mathbf{E}_{T,\alpha} \left(\mathbf{r} \times \nabla\right) A_{T,\alpha} + \mathbf{E}_T \times \mathbf{A}_T \right] d\mathbf{r} \tag{2.28}$$

$$\mathbf{L}_T = \epsilon_0 \int \left[\sum_{\alpha=x,y,x} \mathbf{E}_{T,\alpha} \left(\mathbf{r} \times \nabla\right) A_{T,\alpha} \right] d\mathbf{r} \tag{2.29}$$

$$\mathbf{S}_T = \epsilon_0 \int \left[\mathbf{E}_T \times \mathbf{A}_T\right] d\mathbf{r} \tag{2.30}$$

Since both of the terms depend only on the electric field $\mathbf{E}$ and on the transverse component of the vectorial potential $\mathbf{A}_T$ this decomposition is gauge invariant. Indeed, in the gauge transformation of Eq. 2.4 the term $\nabla\Xi$ is irrotational and so only the longitudinal component of $\mathbf{A}$ is modified under such transformation.

Another way to obtain a gauge invariant separation between OAM and SAM is the *Humblet decomposition* [141], where expressing the magnetic field as a function of the electric field curl, using Faraday law of Eqs. 2.1, we obtain:

$$L_i = \frac{i}{\mu_0} \sum_{j=x,y,z} \int \left[E_j^* \left(\mathbf{r} \times \nabla\right)_i E_j \right] d\mathbf{r} \tag{2.31}$$

$$S_i = \frac{i}{\mu_0} \int \left(E_j^* (-\epsilon_{i,j,k}) E_k \right) d\mathbf{r} \tag{2.32}$$

where $\epsilon_{i,j,k}$ is the Levi-Civita epsilon, that is the quantum mechanical spin 1 particle operator. Therefore, in this decomposition, we can see a similarity with the quantum mechanical calculation of an expectation value with a sandwich between the operators and the electric field.

Although both the previous separations solve the problem of invariance under a gauge transformation, in the most general configuration it is still not easy to distinguish between the two components of light angular momentum, uniquely attributing them to properties of the field. Moreover, they cannot be directly identified with the quantum mechanical generators of rotations [142–144].

Finally, to definitively solve the problem and make the two components separable, we consider a monochromatic beam that propagates along z in the paraxial approximation. In this case, the z-component of the electric field can be neglected compared to the transverse ones, since $E_z \approx \frac{i}{k} \nabla_T \cdot \mathbf{E}_T$. We obtain the following expression for the z component of the total angular momentum[145]:

$$\begin{aligned} J_z = \hbar\omega \frac{\epsilon_0 Re\left\{\int\int dxdy \left[\mathbf{r}_{xy} \times (\mathbf{E}^* \times \mathbf{B})\right]\right\}}{\frac{1}{2} Re\left\{\int\int dxdy \left(\mathbf{E}^* \cdot \mathbf{D} + \mathbf{B}^* \cdot \mathbf{H}\right)\right\}} \approx \\ \approx \frac{Re\left\{\hbar \int\int dxdy \left[\mathbf{E}_T^* \cdot \left(\mathbf{e}_z \cdot \left(\mathbf{r}_{xy} \times (-i\nabla)\right)\right) \mathbf{E}_T + \mathbf{e}_z \cdot \mathbf{E}_T^* \times \mathbf{E}_T\right]\right\}}{Re\left\{\int\int dxdy \mathbf{E}_T^* \cdot \mathbf{E}_T\right\}} \end{aligned} \tag{2.33}$$

where $\mathbf{r}_{xy} = (x, y)$ ed $\mathbf{e}_z$ is the unit vector of in the z-direction.

Using the circular basis $\{R, L\}$ for the polarization, and expressing the electric field $\mathbf{E}_T$ as the vector:

$$|\mathbf{E}_T\rangle = \begin{pmatrix} E_R \\ E_L \end{pmatrix} = \frac{1}{\sqrt{2}} \begin{pmatrix} E_x + iE_y \\ E_x - iE_y \end{pmatrix} \tag{2.34}$$

given a normalized field, i.e. having $\int\int dxdy(\mathbf{E}_T^* \cdot \mathbf{E}_T) = 1$, the equation (2.33) can be rewritten as:

$$J_z = \langle \mathbf{E}_T | \hat{L}_z |\mathbf{E}_T\rangle + \langle \mathbf{E}_T | \hat{S}_z |\mathbf{E}_T\rangle \tag{2.35}$$

where:

$$\hat{S}_z = \hbar \begin{pmatrix} 1 & 0 \\ 0 & -1 \end{pmatrix}, \qquad \hat{L}_z = -i\hbar \left(\mathbf{r}_{xy} \times \nabla\right) \tag{2.36}$$

where using the cylindrical coordinates (ρ, ϕ, z) we have that:

$$\hat{L}_z = -i\hbar \frac{\partial}{\partial \phi} \tag{2.37}$$

These are the well-known expressions for angular momentum in quantum theory, and hence OAM and SAM can be easily distinguished. This decomposition resembles the Humblet one in Eqs. 2.31-2.32. However, different from the general theory, here in the z-component of the paraxial approximation the separation in not space-dependent. Specifically it means that, since the longitudinal component of the angular momentum can be neglected, the average value of the z-component does not depend upon the position of the origin in the transverse plane.

Furthermore, using the notation introduced in Eq. 2.35, we have that

$$L_z = \hbar \int\int dxdy \left(E_R^* \partial_\phi E_R + E_L^* \partial_\phi E_L\right) \tag{2.38}$$

$$S_z = \hbar \int\int \; dxdy \left(|E_R|^2 - |E_L|^2\right) \tag{2.39}$$

Hence, we see how the orbital angular momentum depends on the spatial structure of the field, while the spin is related only to its polarization state. Therefore, we have that the eigenstates of the OAM are all the helicoidal beams for which the paraxial approximation is valid and that present a phase term of the form $e^{im\phi}$. In particular, the latter carry a quantized OAM equal to $\hbar m$ for each photon of the beam. We will give an explicit description of them in Section 2.3. Instead, for what concern the SAM component, since it depends only on the intensity of the electromagnetic field, we can express Eq. 2.39 in the basis of Fock number operators. Using the quantized expression for the electric field in Eq. 2.13 with the substitution reported in Eqs.2.21, we have:

$$\begin{aligned} \hat{\mathbf{S}} &= i\hbar \sum_{\mathbf{k}} \mathbf{e}_{\mathbf{k}} \left(\hat{a}^\dagger_{\mathbf{k}H} \hat{a}_{\mathbf{k}V} - \hat{a}^\dagger_{\mathbf{k}V} \hat{a}_{\mathbf{k}H}\right) = \\ &= \hbar \sum_{\mathbf{k}} \mathbf{e}_{\mathbf{k}} \left(\hat{a}^\dagger_{\mathbf{k}L} \hat{a}_{\mathbf{k}L} - \hat{a}^\dagger_{\mathbf{k}R} \hat{a}_{\mathbf{k}R}\right) = \hbar \sum_{\mathbf{k}} \mathbf{e}_{\mathbf{k}} \left(\hat{n}_{\mathbf{k}L} - \hat{n}_{\mathbf{k}R}\right) \end{aligned} \tag{2.40}$$

where H, V are respectively the horizontal and vertical polarization, and $\mathbf{e}_{\mathbf{k}}$ is the unit vector along the propagation direction.

In conclusion, we show how in the paraxial approximation it is possible to separate the two components of the angular momentum and give their description as quantum mechanical operators, introducing their eigenvalues and eigenvectors. Moreover, by quantizing the fields we obtained the relation between the spin angular momentum and the circular polarization of the field.

2.3 Paraxial Helmotz equation

As we saw in the previous Section, the paraxial approximation is the suitable working condition in which we can separate the two components of the light angular momentum and manipulate them separately. Therefore, it is interesting to analyze the class of optical beams that, with respect to this approximation, are all solution the solution of the **paraxial Helmholtz equation** [146]

We start by rewriting in two terms the solution of the wave equation that describes the electromagnetic field (see Section 2.1), of which one depends only on the space coordinates and the other on time. In particular, considering a monochromatic wave we can write the complex wavefunction of the field as:

$$U(\mathbf{r}, t) = U(\mathbf{r})\, e^{i\omega t} \tag{2.41}$$

where $U(\mathbf{r})$ is the complex amplitude of the field and ω is the angular frequency. To describe the electromagnetic field, $U(\mathbf{r})$ has to satisfy the wave equation:

$$\nabla^2 U - \frac{1}{c^2}\frac{\partial^2 U}{\partial t^2} = 0 \tag{2.42}$$

where ∇^2 is the Laplacian operator and c is the speed of light in vacuum. Using the formulation of Eq. 2.41 for the complex amplitude, we can set aside the time-dependent part of the field and obtain an equation for the space-dependent term. This is the Helmholtz equation:

$$\left(\nabla^2 + k^2\right) U(\mathbf{r}) = 0 \tag{2.43}$$

where we have introduced the *wavenumber* $k = \omega/c$, which can be also expressed as $k = 2\pi/\lambda$ whit λ equal to the *wavelength* of the field.

Considering then a wave that propagates along the z-axis, for which $U(\mathbf{r}) = A(\mathbf{r})\, e^{-ikz}$ where $A(\mathbf{r})$ is a complex function, we can introduce the concept of paraxial waves. In particular, we say that a wave is paraxial when the normal vectors to the *wavefronts*, i.e. the surface with constant phase, form a small angle with the optical axis of the system. To obtain this condition we ask that $A(\mathbf{r})$ is a slowly varying function of z, in this way the variation of $Arg\{A(\mathbf{r})\}$ is small over distances of the wavelength order and wavefronts are almost planar. This implies that for a variation $\Delta z = \lambda$, the change ΔA is much smaller than the value of A. Then, using $\Delta A = (\partial A/\partial z)\Delta z = (\partial A/\partial z)\lambda$, we have that:

$$\Delta A << A \Rightarrow \frac{\partial A}{\partial z} << \frac{A}{\lambda} = \frac{Ak}{2\pi} \Rightarrow \frac{\partial A}{\partial z} << kA \Rightarrow \frac{\partial^2 A}{\partial z^2} << k^2 A \tag{2.44}$$

Exploiting this condition for the field and substituting it inside the Eq. 2.43, we obtain the **paraxial Helmholtz equation**:

$$\nabla_T^2 A - 2ik\frac{\partial A}{\partial z} = 0 \tag{2.45}$$

where $\nabla_T^2 = \partial^2/\partial x^2 + \partial^2/\partial y^2$ is the transverse Laplacian operator.

The simplest solution of Eq. 2.45 is the parabolic wave, which is the paraxial approximation of the plane wave, but the most interesting solutions are the one based on a Gaussian envelope of the amplitude that we will describe in the following Sections.

2.3.1 Gaussian mode

Although the wavelike nature precludes its spatial confinement, light can assume the form of approximately localized and non-divergent beams. The plane and spherical waves represent the two extremes of respectively spatial and angular confinement. Besides these, there is the class of paraxial waves, introduced in the previous chapter, that concerns all beams for which the wavefront normals form a small angle with the direction of propagation. The latter are solutions of Eq. 2.45, among them an important one is the Gaussian beam:

$$U(\mathbf{r}) = A_0 \frac{W_0}{W(z)}\, exp\left[-\frac{\rho^2}{W(z)^2}\right]\, exp\left[-ikz - ik\frac{\rho^2}{2R(z)} + i\zeta(z)\right] \tag{2.46}$$

With:

$$W(z) = W_0\left[1+\left(\frac{z}{z_0}\right)^2\right]^{\frac{1}{2}} \tag{2.47}$$

$$R(z) = z\left[1+\left(\frac{z_0}{z}\right)^2\right] \tag{2.48}$$

$$\zeta(z) = tan^{-1}\left(\frac{z}{z_0}\right) \tag{2.49}$$

$$W_0 = \left(\frac{\lambda z_0}{\pi}\right)^{\frac{1}{2}} \tag{2.50}$$

where $\rho^2 = x^2 + y^2$, A_0 is the normalization factor that is calculated considering the boundary conditions, and all the other functions instead depend upon the beam parameter λ and z_0, where the first one is the wavelength and the second one is the *Rayleigh range*, i.e. the distance for which we can consider that the beam is collimated.

Another interesting parameter is the *beam waist* of Eq. 2.47, in fact, it represents the radius of the beam which increases during the propagation along z. This can be seen by analyzing the beam intensity:

$$I(\rho, z) = |U(\mathbf{r})|^2 = |A_0|^2\left[\frac{W_0}{W(z)}\right]^2 e^{-\frac{2\rho^2}{W(z)^2}} = I_0\left[\frac{W_0}{W(z)}\right]^2 e^{-\frac{2\rho^2}{W(z)^2}} \tag{2.51}$$

That has its maximum at $\rho = 0$ and then decreases with a Gaussian envelope, from here the name Gaussian beam, reaching the value $1/e$ at a radial distance equal to $W(z)$. Hence, the 86% of the beam is contained in a radial distance around the optical axis equal to the waist $W(z)$, which can be then considered as the radius of the beam.

Finally, the parameter $R(z)$ represents the wavefront radius of curvature. Indeed, analyzing the constant phase surfaces of the beam we obtain the equation:

$$z + \frac{\rho^2}{2R} = q\lambda + \zeta\frac{\lambda}{2\pi}, \quad q \in \mathbb{Z} \tag{2.52}$$

That is the equation of a paraboloid with a curvature radius equal to R. From Eq. 2.48 we can study the behavior of the radius during the propagation of the beam, we see that for $z = 0$ the radius is infinite and so the beam has a planar wavefront, while for $z >> z_0$ it increases linearly with the distance $R(z) \approx z$ and so the wavefront is spherical. More precisely, in both cases, the beam is delayed with respect to the planar or spherical wavefront of an amount equal to the *Guoy phase* $\zeta(z)$, that goes from $-\pi/2$ for $z = -\infty$ to $-\pi/2$ for $z = \infty$. Therefore, during the propagation the beam moves from having a planar wavefront to a spherical one, the two limits for spatial and angular confinement, reaching the maximum curvature for $z = z_0$.

A graphical representation of the intensity and the beam divergence during propagation is reported in Fig. 2.1.

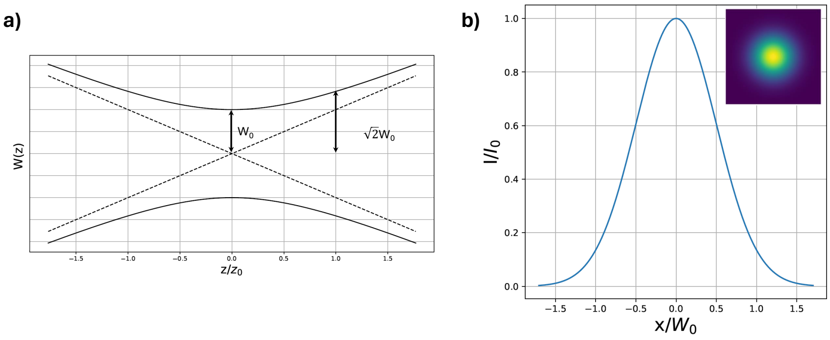

Figure 2.1. Gaussian Beam. a) Behaviour of the beam radius $W(z)$ in function of the propagation distance z. The Rayleigh range z_0 is the distance over which $W(z)$ changes from being the beam waist W_0 to being $\sqrt{2}W_0$. **b)** Normalized intensity I/I_0 of the Gaussian beam along the x-axis of the transverse plane, in the inset is reported the whole Gaussian intensity profile in the $x - y$ plane

2.3.2 Hermite-Gaussian mode

Another interesting class of solutions of Eq. 2.45 is represented by the **Hermite-Gaussian** (HG) modes, which present the same paraboloidal wavefront of the Gaussian beam but a different distribution for the intensity. The HG modes are a basis on which to decompose the transverse spatial structure of a field, and in particular, they can be considered as the modes emitted by a laser cavity.

We start considering a modulated version of a Gaussian beam [146]:

$$A(x, y, z) = \mathcal{X}\left[\sqrt{2}\frac{x}{W(z)}\right]\mathcal{Y}\left[\sqrt{2}\frac{y}{W(z)}\right] exp\left[i\mathcal{Z}(z)\right] A_G(x, y, z) \tag{2.53}$$

where $\mathcal{X}(.)$, $\mathcal{Y}(.)$, $\mathcal{Z}(.)$ are real functions and $A_G(x, y, z)$ is the Gaussian amplitude of Eq. 2.46. Hence, except for a phase term $\mathcal{Z}(z)$, which is a slowly varying function of z and independent from x and y, the phase of Hermite-Gaussian mode in Eq. 2.53 is the same as the Gaussian beam.

The beam in Eq. 2.53 has to satisfy the paraxial Helmholtz equation (2.45), so substituting its complex amplitude, exploiting the fact that A_G solves the equation and defining the variables $u = \sqrt{2}\,x/W(z)$ e $v = \sqrt{2}\,y/W(z)$, we obtain:

$$\frac{1}{\mathcal{X}}\left(\frac{\partial^2\mathcal{X}}{\partial u^2} - 2u\frac{\partial\mathcal{X}}{\partial u}\right) + \frac{1}{\mathcal{Y}}\left(\frac{\partial^2\mathcal{Y}}{\partial v^2} - 2v\frac{\partial\mathcal{Y}}{\partial v}\right) + kW^2(z)\frac{\partial\mathcal{Z}}{\partial z} = 0 \tag{2.54}$$

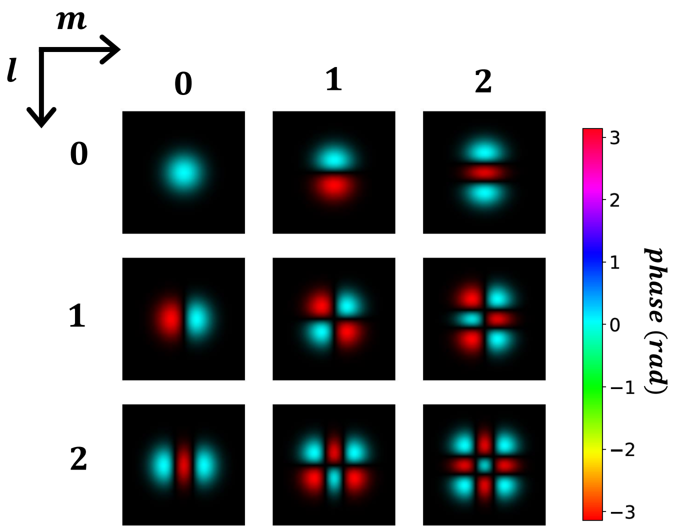

Figure 2.2. Hermite-Gaussian modes. Amplitude and phase distribution of Hermite-Gaussian modes as a function of the indexes l and m that appear in Eq. 2.59

Since the left-hand side of this equation is the sum of three terms that are functions of a single independent variable u, v or z, each of them must be constant. It is therefore possible to perform a separation of variables and obtain the following three differential equations:

$$-\frac{1}{2}\frac{d^2\mathcal{X}}{du^2}+u\frac{d\mathcal{X}}{du}=\mu_1\mathcal{X} \tag{2.55}$$

$$-\frac{1}{2}\frac{d^2\mathcal{Y}}{dv^2}+v\frac{d\mathcal{Y}}{dv}=\mu_2\mathcal{Y} \tag{2.56}$$

$$z_0\left[1+\left(\frac{z}{z_0}\right)^2\right]\frac{d\mathcal{Z}}{dz}=\mu_1+\mu_2 \tag{2.57}$$

The Eq. 2.55 represents an eigenvalue problem whose eigenvalues are $\mu_1 = l$ with $l = \{0, 1, 2, ...\}$ and the eigenstates are the *Hermite polynomials*, so $\mathcal{X} = H_l(u)$. Similarly, Eq.(2.56) has eigenvalue $\mu_2 = m$ and eigenfunction $\mathcal{Y} = H_m(v)$ with $m = \{0, 1, 2, ...\}$

Substituting $\mu_1 = l$ and $\mu_2 = m$ into Eq.(2.57) and integrating, we get:

$$\mathcal{Z}(z) = (l+m)\,\zeta(z) \tag{2.58}$$

and thus, the additional phase $\mathcal{Z}(z)$ varies slowly between $-(l+m)\pi/2$ for $z = -\infty$ and $(l+m)\pi/2$ for $z = \infty$.

Therefore, by substituting everything into the (2.53) and multiplying by $exp(-ikz)$, we obtain the complex amplitude of the Hermite-Gaussian mode:

$$HG_{l,m} = A_{l,m}\,\frac{W_0}{W(z)}G_l\left[\frac{\sqrt{2}x}{W(z)}\right]G_m\left[\frac{\sqrt{2}y}{W(z)}\right]\;exp\left[-ikz-ik\frac{\rho}{2R(z)}+i(l+m+1)\zeta(z)\right] \tag{2.59}$$

where $A_{l,m}$ is a constant and $G_l(u) = H_l(u)\, e^{-u^2/2}$ is called the *Hermite-Gaussian function* of order l. Since $H_0 = 1$, the Hermite-Gaussian function of order 0 is simply a Gaussian one. Thus the mode HG_{00} is the Gaussian mode described in the previous Section. For $l, m \neq 0$, the intensity distribution changes by presenting several peaks, the number of which depends on the order of the mode. In Fig. 2.2, there are reported the amplitude and phase profiles of the HG modes for different values of (m, l).

Finally, HG modes form a complete set of orthogonal solutions of the paraxial Helmholtz equation, so any other solution can be expressed as their superposition.

2.3.3 Laguerre-Gaussian mode

The **Laguerre-Gaussian modes**, similarly to Hermite-Gaussian ones, are a complete set of orthogonal solutions of the paraxial Helmholtz equation (2.45). These can be obtained by writing the differential equation in cylindrical coordinates (ρ, ϕ, θ) and making the separation of variables into ρ and ϕ instead of x and y. They are characterized by two indexes as well, the *radial index* p and the the *azimuthal index* m, and their expression is the following:

$$LG_{p,m}(\rho, \phi, \theta) = \sqrt{\frac{2\,p!}{\pi\,(p+|m|)!}}\frac{1}{W(z)}\left(\frac{\sqrt{2}\,\rho}{W(z)}\right)^{|m|} exp\left[-\frac{\rho^2}{W^2(z)}\right] L_p^{|m|}\left(\frac{2\rho^2}{W^2(z)}\right) \\ \times\, exp\left[im\phi - i\frac{k\rho z}{2\,(z^2+z_0^2)} + i\,(2p+|m|+1)\,\zeta(z)\right] \tag{2.60}$$

where $L_p^{|m|}$ is the *generalized Laguerre polynomial.* The mode order is defined as $N = 2p + |m|$, where p is a nonnegative integer that determines the number of nodes in the transverse plane, while m is an integer connected to the eigenvalues of the orbital angular momentum operator (see Section 2.2). A more formal derivation of it can be found in [24], where it is shown that the Poynting vector presents a component along the azimuthal direction $\mathbf{e}_\phi$, that makes it spiraling around the beam axis and results in an OAM along that direction. Moreover, it is demonstrated how single photons with energy $\hbar\omega$ carry an OAM equal to $\hbar m$.

Since Laguerre-Gaussian modes have a phase term $e^{im\phi}$, they present a helical wavefront that wraps around the propagation axis, in which the number of intertwined helices depends on the value of $|m|$. However, the phase term presents a singularity on the propagation axis and the intensity of the mode cancels out, so on the transverse plane the intensity takes the typical "doughnut" shaped pattern. For $p = 0$ we have a single ring with radius $\rho = \sqrt{|m|/2}W(z)$, if $p \neq 0$ instead we have several concentric rings, the number of which depends on the value of p. This is true apart from the mode with $m = p = 0$, for which the Laguerre-Gaussian mode is reduced to be the Gaussian beam. In the figure (2.3) the phase and amplitude distribution of the Laguerre-Gaussian mode for different values of p and m is shown.

From here, we can see that since only the phase of the mode depends upon the sign of the azimuthal index m, LG modes with the same $|m|$ present an identical intensity profile. This is a special case of a more general condition, for which the intensity of two arbitrary superpositions of LG modes is the same if it holds that [147]:

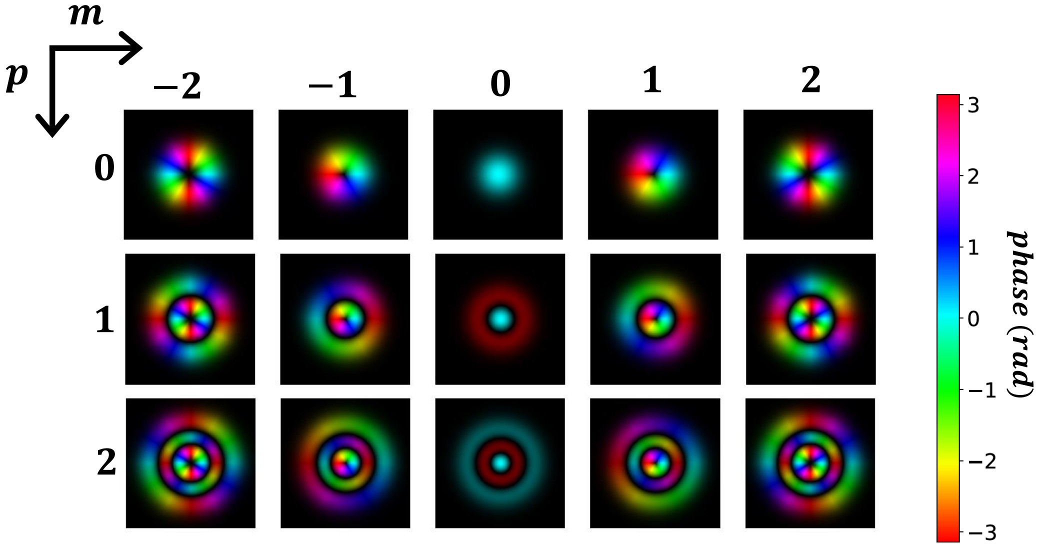

Figure 2.3. Laguerre-Gaussian modes. Amplitude and phase distribution of Laguerre-Gaussian modes as a function of the indexes p and m. The doughnut radius increases with m, while p is related to the number of nodes in the radial direction and therefore to the number of concentric circles. Moreover, the sign of m only modifies the phase distribution, represented here by the RGB colormap.

$$\left|\sum_{p,m} c_{p,m} LG_{p,m}\right|^2 = \left|\sum_{p,m} c^*_{p,m} LG_{p,-m}\right|^2 \tag{2.61}$$

where $c_{p,m}$ are the complex coefficients of the superposition for which $\sum_{pm} |c_{p,m}|^2 = 1$. This symmetry proves to be one of the greatest obstacles in OAM modes recognition when only the information on the intensity profile is accessible, so it often requires special procedures or optical elements to be successfully broken [71, 147, 148].

Finally, as mentioned at the end of the previous Section, Hermite-Gaussian modes represent a complete set of solutions, then it is possible to express the Laguerre-Gaussian modes as a superposition of Hermite-Gaussian ones of the same order in the following way [149]:

$$LG_{n,l}(x,y,z) = \sum_{k=0}^{n+l} i^k b(n,l,k) HG_{n+l-k,k}(x,y,z) \tag{2.62}$$

with coefficients $b(n,l,k)$ real and equal to:

$$b(n,l,k) = \sqrt{\frac{(n+l-k)!\; k!}{2^{n+l}\; n!\; l!}}\,\frac{1}{k!}\left[\frac{d^k}{dt^k}\left((1-t)^n\,(1+t)^l\right)|_{t=0}\right] \tag{2.63}$$

where the indices (n,l) are related to the indices appearing in Eq.(2.60) via the relations $p = min(n,l)$ and $m = n - l$.

In conclusion, LG modes are a complete basis for the paraxial optical states and carry OAM being eigenvalues of its quantum operator. For all these reasons they have found several applications in Quantum Information protocols that exploit high dimensional quantum encoding [21, 26, 48, 65, 66]

2.3.4 Hypergeometric-Gaussian mode

Hypergeometric-Gaussian modes are another family of paraxial beams that are solutions of the paraxial Helmholtz equation (Eq. 2.45), owing their name to the fact that in their expression appears the confluent hypergeometric function. In the dimensionless cylindrical coordinates ($\tilde{\rho} = \rho/W_0$, ϕ, $\xi = z/z_0$), their complex mode amplitude reads [150]:

$$\begin{aligned} HyGG_{p,m}(\tilde{\rho},\phi,\xi) = & \sqrt{\frac{2^{p+|m|+1}}{\pi\Gamma(p+|m|+1)}}\ \frac{\Gamma(1+|m|+\frac{p}{2})}{\Gamma(|m|+1)}\ i^{|m|+1}\ \xi^{\frac{p}{2}}\ (\xi+i)^{-\left(1+|m|+\frac{p}{2}\right)} \\ & \times\ \tilde{\rho}^{\,|m|}\ e^{-\frac{i\tilde{\rho}^{\,2}}{\xi+i}}\ e^{im\phi}\ {}_1F_1\left(-\frac{p}{2}, |m|+1; \frac{\tilde{\rho}^{\,2}}{\xi\,(\xi+i)}\right) \end{aligned} \tag{2.64}$$

where m is integer, $p \geq -|m|$ is real and ${}_1F_1(a,b;x)$ is the hypergeometric function.

The characteristic phase term $e^{im\phi}$, also present in Laguerre-Gaussian modes, identifies m as the eigenvalue of the OAM. Moreover, as expected for OAM eigenstates, the mode intensity cancels as $\tilde{\rho}^{\,|m|}$ at the center of the beam ($\rho \to 0$). Since the hypergeometric function ${}_1F_1(a,b;x)$ only cancels for x reals, the intensity of the beam in the transverse plane only cancels on the axis ($\tilde{\rho} = 0$) and at infinity. This gives the intensity pattern of the HyGG modes the typical 'doughnut' shape for each value of m and p, except for $m = 0$ and especially for $p = m = 0$ for which the Hypergeometric-Gaussian mode reduces to the Gaussian one (see Eq. 2.46). The amplitude and phase distributions of the HyGG modes are shown in the figure (2.4-a) for different combinations of p, m. Moreover, we will not go into details, but it is possible to divide the HyGG modes into subclasses depending on the values of the two indexes [150].

The set of modes HyGG is overcomplete and non-orthogonal; the inner product of two normalized modes is equal to:

$$\begin{aligned} \int_0^\infty d\tilde{\rho} \int_0^{2\pi} d\phi\ \tilde{\rho}\ HyGG^*_{p',m'}(\tilde{\rho},\phi,\xi) HyGG_{p,m}(\tilde{\rho},\phi,\xi) = \\ = \delta_{m,m'}\ \frac{\Gamma\left(\frac{p}{2}+\frac{p'}{2}+|m|+1\right)}{\sqrt{\Gamma(p'+|m|+1)\ \Gamma(p+|m|+1)}} \end{aligned} \tag{2.65}$$

where $\Gamma(z) = \int_0^\infty t^{z-1}e^{-t}\,dt$ is the gamma function.

Hypergeometric-Gaussian modes can be expressed in the complete basis of Laguerre-Gaussian modes. In general, the mode $HyGG_{p,m}$ can be written as the linear combination of infinitely many modes $LG_{q,m}$ having the same m index, since it still needs to be an eigenstate of the OAM, and any possible value of the radial index $q \geq 0$:

$$HyGG_{p,m} = \sum_{q=0}^{\infty} A_{pq}\ LG_{q,m} \tag{2.66}$$

Where:

$$A_{pq} = \sqrt{\frac{(q+|m|)!}{q!\ \Gamma(p+|m|+1)}}\ \frac{\Gamma\left(q-\frac{p}{2}\right)\ \Gamma\left(\frac{p}{2}+|m|+1\right)}{\Gamma\left(-\frac{p}{2}\right)\ \Gamma(q+|m|+1)}, \tag{2.67}$$

Unlike Laguerre-Gaussian modes, the profile of the Hypergeometric-Gaussian modes is not invariant during the propagation, where the invariance here is considered

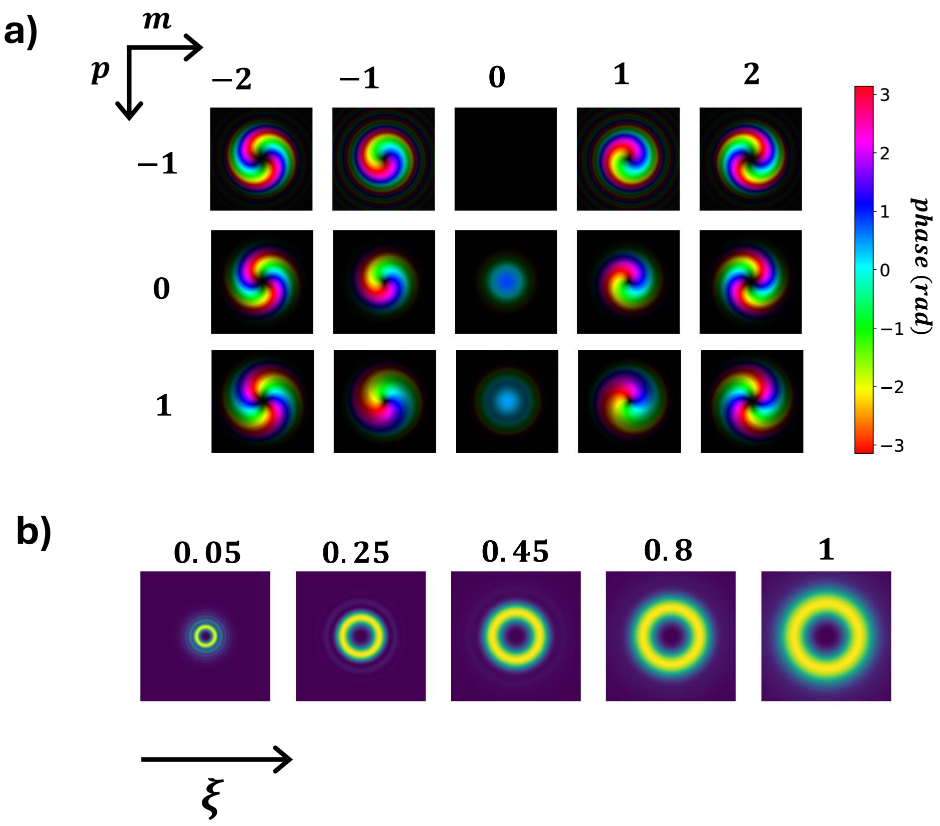

Figure 2.4. Hypergeometric-Gaussian modes. a) Amplitude and phase distribution of Hypergeometric-Gaussian modes in function of the indexes p and m for a propagation distance $\xi = 1$. **b)**Evolution of the intensity profile during the free propagation of a HyGG mode with $p = -2$ and $m = 2$. Over each image it is reported the value of ξ

except for the broadening of the profile happening due to the divergence of the beam. As shown by Eq. 2.66, a HyGG mode is obtained by the superposition of infinite modes LG each with a different phase term, dependent on the Gouy phase $\zeta(z)$, due to the different radial index q. So the relative phase between the various modes changes as z varies, this consequently changes the appearance of the intensity profile. Figure 2.4-b shows this behavior by reporting the evolution of the intensity in the transverse plane for a HyGG mode as ξ varies.

The HyGG modes have found several applications in practice since they represent a more accurate description of the modes produced by different OAM engineering platforms, such as pitch-fork holograms [151, 152] used in combination with SLM [153, 154] or the birefringent pattern of metasurfaces [53, 70, 155], situations where the LG modes furnish just a partial description.

2.4 Single photons sources

As we said, photons play a fundamental role in Quantum Information applications, since they represent an optimal physical system for several tasks, ranging from communication to test of quantum foundation, and have been used in milestone experiments. Therefore, sources capable of generating with high efficiency indistinguishable and entangled photons in a deterministic way are highly demanded.

Over the years, several platforms have been proposed to address these requests. The most used ones are the sources based on nonlinear effects. Among these, the second-order nonlinear Spontaneous Parametric Down Conversion (SPDC) process has been widely used to generate heralded single photons and entangled pairs using different degrees of freedom [156–161], this kind of sources are implemented both in bulk and integrated optics. Another process that is exploited is the spontaneous four-wave mixing [162] that takes place in integrated optics waveguides. However, both these processes are probabilistic, with a generally low probability of generating photons, which is detrimental for several Quantum Information protocols. Semiconductor Quantum Dots (QDs) have emerged as a platform to overcome these limitations. Acting as artificial atoms when pumped with pulsed lasers, QDs are capable of generating indistinguishable single photons with high brightness in a nearly-deterministic fashion [163–167].

In this thesis, we experimentally exploited both SPDC and QD sources to produce photonic OAM states, which we used to perform several Quantum Information protocols.

2.4.1 Nonlinear processes

Nonlinear optics is the branch that studies the phenomena that take place due to the modification of the optical properties of a material when light passes through it [168]. The nonlinearity here refers to the response of the material, which is proportional to a power of the strength of the applied electric field, and needs high intensities to be seen. The beginning of this research area is made to coincide with the observation of the second harmonic generation by Franken et *al.* [169].

To describe the response of a material to an applied electric field we make use of the dielectric polarization density ($\mathbf{P}$), which in this case can be decomposed in a linear part ($\mathbf{P_L}$) and in a nonlinear one ($\mathbf{P}_{NL}$):

$$\begin{aligned}\mathbf{P}(t) = \mathbf{P_L}(t) + \mathbf{P_{NL}}(t) = \epsilon_0\Big[\chi^{(1)}\mathbf{E}(t) + \chi^{(2)}\mathbf{E}^2(t) + \chi^{(3)}\mathbf{E}^3(t) + \dots\Big] = \\ = \mathbf{P}^{(1)}(t) + \mathbf{P}^{(2)}(t) + \mathbf{P}^{(3)}(t) + \dots\end{aligned} \tag{2.68}$$

where $\chi^{(1)}$ is the linear optical susceptibility, and $\chi^{(2)}, \chi^{(3)}$ are respectively the second- and third-order optical susceptibility. In particular, it can be shown that $\chi^{(2)}$ is different from zero only in noncentrosymmetric media, i.e. media that do not display inversion symmetry, and the second-order phenomena can occur only in these materials.

Focusing on the description of the types of second-order processes, we consider entering the material with an electric field having two distinct components $\mathbf{E}_1, \mathbf{E}_2$ with frequencies respectively ω_1, ω_2. The second-order nonlinear polarization of Eq. 2.68 can be written as:

$$\mathbf{P}_{NL}^{(2)} = \sum_n \mathbf{P}(\omega_n) e^{-i\omega_n t} \tag{2.69}$$

where the summation is performed over both positive and negative frequencies, and the term $\mathbf{P}(\omega)$ contains the dependence upon the field. These complex amplitudes describe several processes:

- **Second Harmonic Generation (SHG):** This process consists in the annihilation of two photons with frequency ω_i for the generation of one photon having frequency $2\omega_i$. We have $P(2\omega_i) = 2\epsilon_0\chi^{(2)}E_i^2$
- **Sum-Frequency Generation (SFG):** Here two photons with different frequencies annihilate to produce a photon with a frequency that is the sum of the original ones. We have thus $P(\omega_1 + \omega_2) = 2\epsilon_0\chi^{(2)}E_1E_2$.
- **Difference-Frequency Generation (DFG):** Here, entering the system with two fields having different frequencies, a photon with higher frequency ω_1 is converted into photons having lower frequencies ω_2 and $\omega_3 = \omega_1 - \omega_2$. Therefore this process produces an *optical parametric amplification* of the lower frequency field E_2. We have that $P(\omega_1 - \omega_2) = 2\epsilon_0\chi^{(2)}E_1E_2^*$.

The energy levels scheme for all these processes are reported in Fig. 2.5.

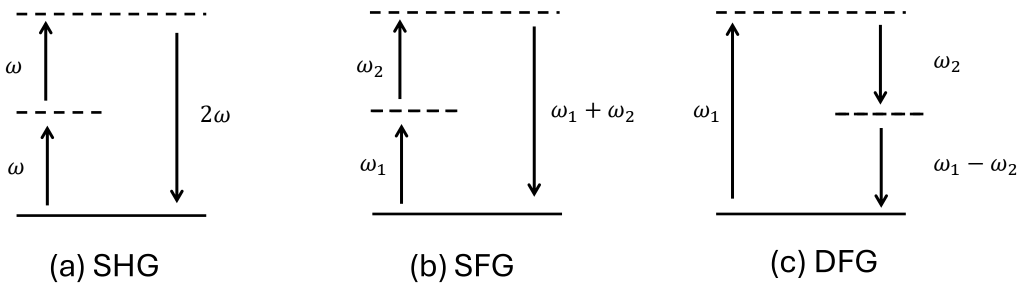

(a) SHG (b) SFG (c) DFG

Figure 2.5. Nonlinear processes energy levels. a) Second Harmonic Generation (SHG): two photons with frequency ω are converted to one photon having frequency 2ω. **b)** Sum Frequency Generation (SFG): two photons with frequency ω_1 and ω_2 are converted to one photon having frequency $\omega_1 + \omega_2$. **c)** Difference Frequency Generation (DFG): one photon with frequency ω_1 is converted into two photons having frequency ω_2 and $\omega_1 - \omega_2$.

To have a complete mathematical description of these nonlinear processes, we can proceed by solving the Maxwell equation (Eqs. 2.1) inside the medium. In particular, we can derive the following equation for the electric field inside the nonlinear material:

$$\nabla^2\mathbf{E} - \frac{\epsilon_1}{c^2}\frac{\partial^2}{\partial t^2}\mathbf{E} = \frac{1}{\epsilon_0 c^2}\frac{\partial^2}{\partial t^2}\mathbf{P}_{NL} \tag{2.70}$$

where c is the speed of light in vacuum and ϵ_1 is the relative permittivity, which is different for each material.

For instance, we can solve the Eq. 2.70 for the case of a SFG process. We consider entering a lossless material with monochromatic and collimated waves and we prove a solution of the form $E_3 = A_3e^{ik_3z-i\omega t} + c.c.$ for the output beam at frequency $\omega_3 = \omega_1 + \omega_2$, with $k_3 = n_3\omega_3/c$ and n_3 the refractive index experienced by the field for which stands that $n_3^2 = \epsilon_1(\omega_3)$. Making the slowly varying amplitude approximation for the field A_3 and using the Eq. 2.69 for the polarization density, by substituting everything inside Eq. 2.70, we obtain the following equation for the field amplitude:

$$\frac{dA_3}{dz} = \frac{2id_{eff}\omega_3^2}{k_3c^2}A_1A_2e^{i\Delta kz} \tag{2.71}$$

where $2d_{eff}(\omega_3, \omega_1, \omega_2) = \chi^{(2)}(\omega_3 = \omega_1 + \omega_2, \omega_1, \omega_2)$ and $\Delta k = k_1 + k_2 - k_3$ is the *momentum mismatch.* By integrating Eq. 2.71 over the crystal length L and considering the input field A_1, A_2 constant for a low probability conversion process, we obtain:

$$A_3(L) = \frac{2id_{eff}\omega_3^2A_1A_2}{k_3c^2}\left(\frac{e^{i\Delta kL}-1}{i\Delta k}\right) \tag{2.72}$$

$$I_3 = \frac{8d_{eff}^2\omega_3^2I_1I_2}{n_1n_2n_3\epsilon_0c^2}L^2sinc^2\left(\frac{\Delta k}{L}\right) \tag{2.73}$$

where I_i and n_i are respectively the intensity and refractive index for the field at frequency ω_i. From Eqs. 2.72-2.73, we see how the efficiency of the process strongly depends upon the *phase-matching condition*:

$$\Delta k = 0 \tag{2.74}$$

Indeed, the intensity is greatly dumped from the quadratically dependence on it. From a microscopic point of view, the phase-matching condition implies that the atomic dipoles of the material are properly phased and the fields generated from them coherently sum in the forward direction. The phase-matching condition of Eq. 2.74 is often difficult to reach since the refractive indices of lossless medium respect the normal dispersion condition, for which the refractive index is an increasing function of the frequency. Therefore the condition:

$$\frac{n_3\omega_3}{c} = \frac{n_1\omega_1}{c} + \frac{n_2\omega_2}{c} \tag{2.75}$$

cannot be fulfilled for $\omega_3 = \omega_1 + \omega_2$. In principle, the condition can be respected by exploiting the anomalous dispersion, for which the refractive index decreases with the frequency, but in practice, the most common procedure is to employ birefringent materials. The latter shows two refractive indices n_o (*ordinary*) and n_e (*extraordinary*) depending upon the polarization of the waves that propagate inside them. Therefore, to reach the phase-matching condition, the wave with the highest frequency ω_3 is polarized along the direction associated with the lower of the two indices. Considering a uniaxial birefringent crystal a wave polarized along its optical axis experiences a refractive index n_e, while a wave with an orthogonal polarization experiences n_o. In particular, if we assume a linearly polarized wave that propagates along a direction forming an angle θ with the optical axis, we have that:

$$\frac{1}{n_e^2(\theta)} = \frac{\sin^2\theta}{\overline{n}_e} + \frac{\cos^2\theta}{n_o} \tag{2.76}$$

where $\overline{n}_e$ is the *principal value* of the extraordinary index, and we have that $n_e(\theta) = \overline{n}_e$ for $\theta = \pi/2$ while $n_e(\theta) = n_o$ for $\theta = 0$. Therefore, we can tilt and rotate the crystal in order to obtain a value of $n_e(\theta)$ for which the phase-matching condition of Eq. 2.74 holds.

Furthermore, it is possible to define two phase-matching conditions depending on the polarization of the two lower-frequency fields:

- **Type I:** The two frequencies ω_1 and ω_2 have the same polarization. This is independent from the relative values of ω_1, ω_2 and it is the easiest achievable in practice.
- **Type II:** The two frequencies ω_1 and ω_2 have orthogonal polarizations. Here, the condition is easily reached if we associate the higher among ω_1, ω_2 to the bigger refractive index.

The consideration made for the phase-matching condition in the case of the SFG holds for all the other cases presented.

2.4.2 Spontaneous Parametric Down Conversion

In all the previously introduced nonlinear processes, the presence of two fields is necessary for the various phenomena to take place, so, in some sense, the conversion is stimulated by the presence of fields with the right frequencies. However, when entering the material with just one pump filed at a frequency ω_p, using a quantum mechanical framework, it is possible to describe a new type of phenomena. Among these, the most employed and studied one is the *Spontaneous Parametric Down Conversion* (SPDC) [170], that happens in materials showing a second-order nonlinear susceptibility $\chi^{(2)}$. The SPDC can be seen as the inverse of the SHG, here a pump photon is annihilated to generate two photons, called *idler* and *signal*, at frequencies ω_i and ω_s under the two conditions of:

- Energy conservation: $\omega_p = \omega_i + \omega_s$
- Momentum conservation (phase-matching condition): $\mathbf{k}_p = \mathbf{k}_i + \mathbf{k}_s$

Using the second quantization formalism, the Hamiltonian of the process can be written as a function of the creation and annihilation operators of each field as [170]:

$$H_{spdc} = K\left(a_i^\dagger a_s^\dagger a_p + c.c.\right) \tag{2.77}$$

where K, in the perfect phase-matching condition, is a constant depending upon the susceptibility $\chi^{(2)}$ and the material length L. From Eq. 2.77, we can derive the unitary time evolution operator:

$$U = \exp\left\{-i\tau\left(a_i^\dagger a_s^\dagger a_p + a_i a_s a_p^\dagger\right)\right\} \tag{2.78}$$

where $\tau = Kt$ with t the time of interaction.

Since the low efficiency of the phenomenon, we can make the approximation that the pump field E_p is undepleted during the process. Therefore describing it as a classical coherent state, the evolution is well described by the so-called two-modes squeezing operator [171]:

$$S = \exp\left\{-i\tau\left(\alpha_p a_i^\dagger a_s^\dagger + \alpha_p^* a_i a_s\right)\right\} \tag{2.79}$$

The SPDC process is obtained by applying this exponential operator to the input vacuum state $|0\rangle_{k_i}|0\rangle_{k_s}$, written in the Fock state notation for the modes k_i, k_s. From here, we obtain the output state of the SPDC:

$$\begin{aligned} S|0\rangle_{k_i}|0\rangle_{k_s} &= \frac{1}{cosh(\tau)}\sum_n \tau^n |n\rangle_{k_i}|n\rangle_{k_s} \approx \\ &\approx |0\rangle_{k_i}|0\rangle_{k_s} - i\tau|1\rangle_{k_i}|1\rangle_{k_s} + \tau^2|2\rangle_{k_i}|2\rangle_{k_s} + \dots \end{aligned} \tag{2.80}$$

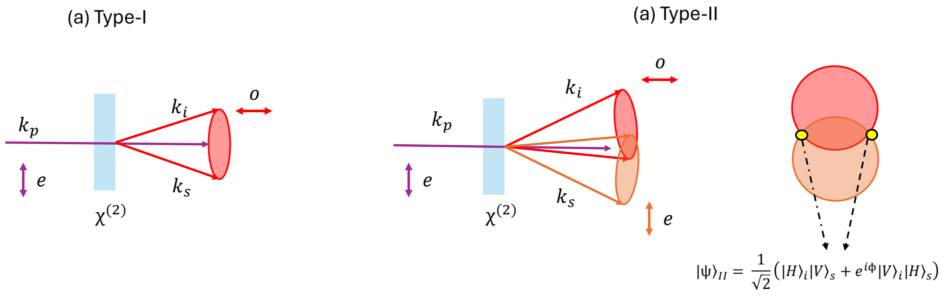

Figure 2.6. Spontaneous Parametric Down Conversion. a) Type-I: the photons share the same polarization and are emitted on the same cone satisfying the energy and momentum conservation. **b)** Type-II: The photons have orthogonal polarization states and, from the birefringence of the material, they are emitted along different cones. The intersection points of the latter can be exploited to generate an entangled state in the polarization degree of freedom (the $|\Psi^{\pm}\rangle$ Bell states of Eqs. 1.23).

Therefore the photons generation through SPDC is inherently probabilistic. In practice, we are always in the condition $\tau << 1$ since the efficiency of the process is low, and the generation of terms with $n > 1$ can be neglected. Therefore, when we experimentally detect a coincidence in the modes k_i, k_s, the state can be well approximated as a single photon pair. In particular, when only a pair of photons is generated in the process, we have that the joint photon state can be written as:

$$|\Psi\rangle_{spdc} \approx \mathcal{N} \sum_{\sigma_i,\sigma_j} \int d\omega_i d\omega_s \int d\mathbf{k}_i d\mathbf{k}_s \phi_{\sigma_i,\sigma_j}(\omega_i, \omega_s, \mathbf{k}_i, \mathbf{k}_s) \, |\sigma_i, \omega_i, \mathbf{k}_i\rangle \, |\sigma_i, \omega_i, \mathbf{k}_i\rangle \tag{2.81}$$

Where $\mathcal{N}$ is a normalization constant, σ_i, σ_s are the polarization states and $\phi_{\sigma_i,\sigma_j}(\omega_i, \omega_s, \mathbf{k}_i, \mathbf{k}_s)$ is the joint spectral function of idler and signal photons. The latter contains both the description of the frequency and spatial structures of the generated photons, depending explicitly on the phase-matching.

Considering the degenerate case, for which $\omega_i = \omega_s = \omega_p/2$, we can proceed as in the case of the SFG by defining the kinds of SPDC process depending on how the phase-matching condition of Eq. 2.74 is satisfied. From the condition that the wavevectors have to respect, the spatial distribution of the produced photons is described as k-vectors cones with the vertex centered in the active spot on the non-linear crystal, we have:

- **Type-I:** The signal and idler photons share the same polarization that is orthogonal to the pump one. They are emitted along opposite sides of the same k-vectors cone (see Fig. 2.6-a). For negative uniaxial crystal, having $n_e(\theta) < n_0$, we have the generation of two photons with ordinary polarization: $e \rightarrow o + o$. Otherwise, for positive uniaxial crystal, having $n_e(\theta) > n_0$, we have instead two extraordinary polarized photons: $o \rightarrow e + e$

- **Type-II:** The signal and idler photons possess orthogonal polarizations, and we have processes respectively for positive and negative uniaxial crystals: $o \rightarrow e + o$ and $e \rightarrow e + o$. Due to the birefringence of the material, the two photons are emitted along different cones (see Fig. 2.6-b).

The phase-matching condition and the energy conservation constraint generate correlations between the idler and signal photons. Such correlations can be exploited in suitable geometries to generate entangled states in different degrees of freedom. In the remaining of this Section, we will not consider the spatial structure of the generated photon, which will be treated in detail in Section 4.1, but we will focus only on sources of single and entangled photons in the polarization degree of freedom.

Quasi Phase-matching

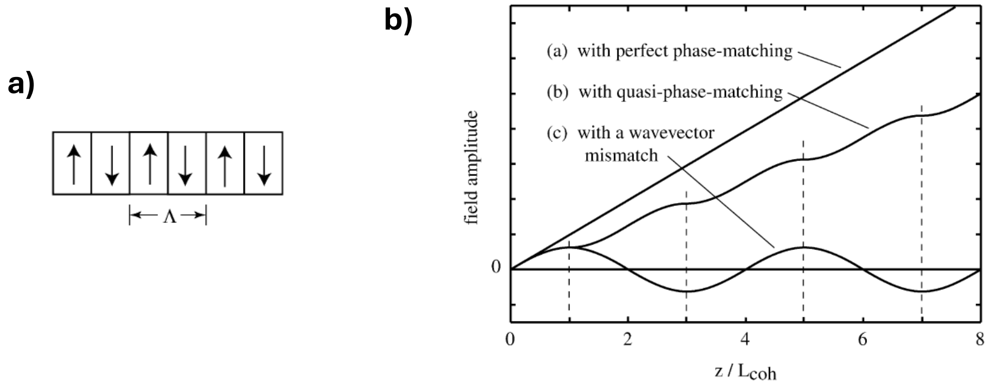

Figure 2.7. Quasi Phase-matching. a) Periodically Poled crystal with an inversion period Λ, the arrows indicate the orientation of the crystalline optical axis in each slice of the material. **b)** Amplitude of the generated field in a nonlinear interaction for three different phase-matching conditions. In a) a perfect phase-matching condition is considered, and therefore there is a linear growth of the amplitude. In c) instead, the phase mismatch Δk is different from zero, and then the amplitude oscillates with the propagation distance inside the crystal. In b) we consider a quasi phase-matching situation, in which the period of the poling is twice the coherent buildup length $L_{coh} = 2/\Delta k$. We see how the compensation enables a monotonic growth of the amplitude of the generated field, even if it is less rapid than the one observed for perfect phase-matching. Images taken from [168].

The phase-matching condition, being necessary to effectively generate single photon pairs, in practice strictly limits the geometries and classes of nonlinear crystal that can be used for this purpose. For instance, it prevents the employment of a material with high nonlinear second-order susceptibility, suitable to increase the efficiency of the process, but with a birefringence not sufficient to compensate for the refractive index dispersion. To overcome this limitation, a particular construction geometry of ferroelectric crystals can be exploited to produce a *quasi phase-matching* condition [168, 172]. In particular, it consists of a structure made of slices of nonlinear material positioned in such a way that the crystalline axes are inverted in two subsequent slices (see 2.7-a). These crystals are called *periodically poled*, and their configuration produces a periodical inversion, with period Λ, of the nonlinear coupling coefficient d_{eff} (see Eq. 2.71) sign that can compensate for a nonzero mismatch $\Delta\mathbf{k}$. This is explicitly shown in Fig. 2.7-b, where the amplitude of the generated wave is reported as a function of the propagation distance inside the crystal for a phase mismatch situation, the perfect phase-matching condition, and the quasi phase-matching configuration. For a wave propagating along the z direction on which the crystal slices are placed, we have then the quasi phase-matching condition:

$$\mathbf{k}_p(T) = \mathbf{k}_i(T) + \mathbf{k}_s(T) + \frac{2\pi}{\Lambda(T)}\mathbf{z} \tag{2.82}$$

Therefore, by properly choosing the period Λ and the working temperature T, one can fulfill the phase-matching condition and generate photon pairs at the desired wavelength and in the specific geometrical configuration [173]. In particular, periodically poled crystal permits the introduction of a new kind of SPDC process called *Type-0*, in which the emitted photons are generated with the same polarization as the input pump, also having the possibility of being collinear with its direction.

Type-I sources

To generate entangle photon pairs in the polarization degree of freedom with a Type-I SPDC source, we proceed by exciting simultaneously and coherently two crystals placed one after the other and to have orthogonal directions for the optical axis. Indeed, a single nonlinear crystal produces photons with the same polarization presenting therefore a correlation in this degree of freedom, but they are not in an entangled state. If instead, we consider two crystals with vertical and horizontal optical axis directions and we enter the system with a pump beam having a polarization vector at 45° respect to the vertical axis, we have that the two emitted photons propagate along the direction $\mathbf{k}_i, \mathbf{k}_s$ of the cone with a polarization that depends on when they have been generated. Indeed, the crystal with a vertical axis produces horizontally polarized photons, conversely, the idler and signal photons generated by the one with a horizontal direction of the optical axis have vertical polarization. Being unaware of when the generation occurred, the output state from the system is described as:

$$|\Psi\rangle_I = \frac{1}{\sqrt{2}}\Big(|H\rangle_i\,|H\rangle_s + e^{i\phi}\,|V\rangle_i\,|V\rangle_s\Big) \tag{2.83}$$

Where the phase term can be controlled by the input polarization in order to create the entangled Bell states $|\Phi^{\pm}\rangle$ reported in Eq. 1.23.

Type-II sources

Conversely to the previous case, Type-II crystals can be used to directly generate single photons entangled pairs. In particular, the photons generated by the crystal have orthogonal polarization and, due to the birefringence of the material, are emitted along two different k-vector cones. The directions of these cones depend upon the orientation of the crystal with respect to the propagation axis of the pump beam, and it is possible to select a configuration in which they intersect (see Fig. 2.6-b). The photons emitted in the intersection point results in being entangled [157]. Indeed, since each generated photon can belong to the horizontal or vertical emission cone, their state can be written as:

$$|\Psi\rangle_{II} = \frac{1}{\sqrt{2}}\Big(|H\rangle_i\,|V\rangle_s + e^{i\phi}\,|V\rangle_i\,|H\rangle_s\Big) \tag{2.84}$$

Therefore, by tuning their phase with a liquid crystal, it is possible to generate the $|\Psi^{\pm}\rangle$ states of the Bell basis.

Besides exploiting the two cones, it is possible also to use the Type-II SPDC process to generate entangled photons in a collinear fashion exploiting periodically pooled crystals. However, as in the Type-I case, in the collinear configuration, the two photons are correlated in having an orthogonal polarization state but they are not in an entangled state. In this case, it is therefore necessary to use additional interferometric schemes to produce the wanted entangled pairs. A suitable choice is to place the crystal inside a Sagnac interferometer as depicted in Fig. 2.8, this represents a valuable implementation since its geometry makes it intrinsically stable and can be used in the generation of entangled photons from visible to telecom wavelengths [156, 174, 175]. Here, the pump beam with a diagonal polarization is sent to a dual-wavelength polarizing beam splitter (DPBS), that works for both the wavelengths of the pump and generated photons. The vertically polarized component of the pump is then reflected by the DPBS and propagates clockwise inside the interferometer, before entering the crystal a dual-wavelength half-waveplate is used to rotate the polarization in order to satisfy the phase-matching condition. The generated photons are then split by the DPBS in two different spatial directions. Conversely, the horizontal component of the pump, being transmitted by the DPBS, follows the counterclockwise propagation direction generating a photon pair due to the SPDC process. The produced photons are thereafter split by the DPBS in the same two spatial directions as before, but they possess orthogonal polarization states with respect to the ones produced by the vertical component of the pump. Therefore, when observing the output photons, not knowing if the generation happened in the clockwise or counterclockwise direction, we have that the output state is the same as Eq. 2.84.

During my thesis, we exploited a Sagnac SPDC source to generate both entangled photon pairs and single photons in a heralded fashion, in which, by detecting a photon in one of the output modes, we ensure the presence of a photon in the other one, and we can therefore manipulate the state of the latter. In particular, we placed a 20 mm long Periodically Poled Potassium Titanyl Phosphate (PPKTP) crystal with $\Lambda = 9.825\ \mu m$, realized by Raicol company, inside a Sagnac interferometer (see Fig. 2.8-b). The crystal is pumped with a continuos-wave (CW) laser emitting at a wavelength of 404 nm with a power $P \approx 15\ mW$. To change the temperature and fulfill the quasi phase-matching condition (see Eq. 2.82), and consequently tune the generated wavelengths, the crystal is placed in a homemade oven. We found that the degenerate emission, for which the produced photons have a wavelength equal to 808 nm can be obtained by selecting $T = 40^{\circ} C$. In this configuration, we have a photon pairs rate or coincidence counting of $cc \sim 60kHz$. Moreover, to evaluate the quality of the generated entangled states, we performed a violation test of the CHSH inequality (see Appendix A), obtaining as a result a value for the parameter $S_{raw} = 2.69 \pm 0.01$

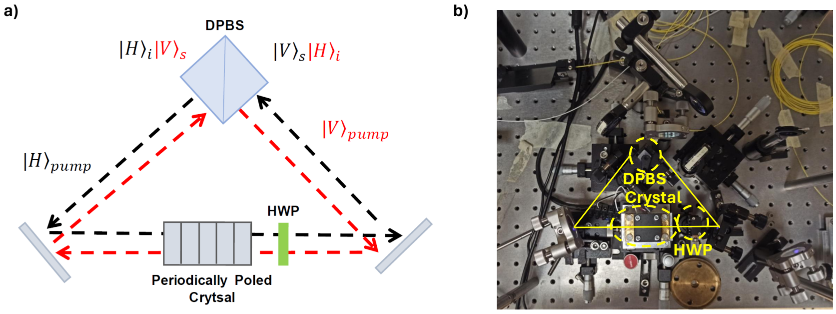

Figure 2.8. Sagnac configuration for Type-II SPDC. a) A periodically poled crystal designed to produce a collinear generation is placed inside a Sagnac interferometer. A diagonal-polarized pump is divided into its $|H\rangle_{pump}$ and $|V\rangle_{pump}$ components by a dual-wavelength polarizing beam splitter (DPBS), these run along the setup respectively in the counterclockwise and in the clockwise senses. A HWP is placed inside the interferometer to convert $|V\rangle_{pump}$ to $|H\rangle_{pump}$ before it enters the crystal, in order to match the polarization requirement for the generation process. The pair production could happen in both propagation directions, for this reason, by dividing the generated photons with the DPBS we have in the two output modes the entangled state of Eq. 2.84. b) Photo of the collinear Type-II entangle photons source used during the Ph.D. thesis, in yellow are evidenced the fundamental components. This setup works in a degenerate condition. Therefore, being pumped with a laser having a wavelength of 404 nm, it produces single photon pairs at 808 nm.

2.4.3 Quantum Dots

Despite their development and wide usage, SPDC sources suffer from a trade-off between the brightness and the purity of the produced single photons due to their intrinsic probabilistic nature. Indeed, to produce single and indistinguishable photons with high quantum purity, it is required to work with low emission probabilities, reducing in this way the scalability of the approach. Moreover, since in each process, it is always possible to generate more than one photon, these kinds of sources undermine the security of quantum cryptography schemes [60, 61]. To overcome these limitations, semiconductor Quantum Dots (QDs) have emerged as a suitable platform to produce high-purity, indistinguishable single photons in a nearly deterministic fashion [163, 165–167].

These QDs are made by spatially confining a semiconductor material inside another one having a higher band gap, i.e. the energy difference between the valence band and the conduction band of a semiconductor. This, acting as a quantum well, produces a discretization of the electrons energy levels, making the quantum emitters work as artificial atoms having excited $|e\rangle$ and ground $|g\rangle$ states. Indeed, considering systems with only one valence and conduction band and a potential well with dimensions $\{L_x, L_y, L_z\}$, we have that the Schrödinger equation describing the electronic state of the system is [176, 177]:

$$\left(\frac{\hbar^2}{2m^*_{e,h}}\nabla^2 + V(x,y,x)\right)\Psi(x,y,z) = E\Psi(x,y,z) \tag{2.85}$$

Where $m^*_{e,h}$ is the effective mass inside the material of the charge carrier (e^-

and h^+), $\Psi(x,y,z)$ is the electronic wavefunction and $V(x,y,z)$ is the infinite depth well external potential. Separating the analysis on the three spatial dimensions, the solution to Eq. 2.85 reads:

$$E_{e,h} = \frac{\pi\hbar^2}{2m^*_{e,h}}\left(\frac{n_x^2}{L_x^2} + \frac{n_y^2}{L_y^2} + \frac{n_z^2}{L_z^2}\right) \tag{2.86}$$

Where $n_x, n_y, n_z > 0$ and integers. Therefore, the electrons and holes energy levels in the QD configuration are discretized. In general, the growth of the various layers occurs through deposition, therefore the height of QDs is nanometric and there is only one confined state in the z-direction, while several levels are instead present in the x, y ones. Moreover, when considering the angular momentum of electrons and holes inside the Hamiltonian by adding a term that accounts for the exchange coulomb interaction [177], asymmetries in the x, y-plane are at the basis of an energy splitting in the excited energy level of the z-direction, the latter is called *fine-structure splitting* (FSS) [178]. Therefore, for a neutrally charged QD, i.e. having free electrons and holes in the same quantity, we have the three levels energy structure reported in Fig. 2.9. Where $|X\rangle$ and $|Y\rangle$ are the two exciton states, that by the selection rules of the angular momentum are optically coupled to the ground state $|g\rangle$ by the emission of photons in a superposition state of the two circular polarizations, respectively $(|R\rangle - |L\rangle)/\sqrt{2}$ and $(|R\rangle + |L\rangle)/\sqrt{2}$.

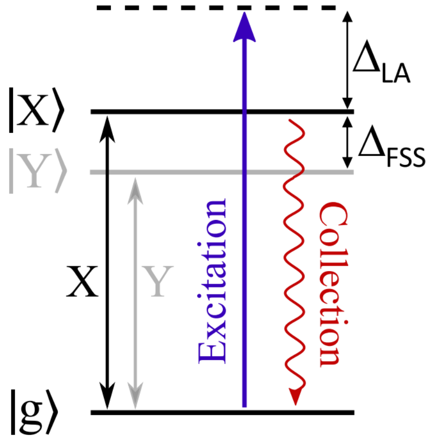

Figure 2.9. Quantum dot energy levels. Scheme of the energy levels for a neutrally charged Quantum dot (QD) emitter. We have a three-level structure characterized by two exciton states $|X\rangle$ and $|Y\rangle$ separated in energy by the fine-structure splitting factor Δ_{FSS}. The blue line indicates the excitation stimulated by the laser pump, while in red in reported the single photon emission. The Δ_{LA} represents the energy of the longitudinal phonon, produced when operating in a longitudinal acoustic (LA) phonon-assisted emission configuration. Image taken from [179].

This atom-like three levels energy structure can then be used to deterministically generate single photon states by exciting the QD with a laser pump and then collecting the photon produced by the de-excitation. However, this emission is isotropic in space, therefore to effectively collect the generated photons we need to exploit the method introduced by Purcell in [180] by enclosing the QD inside a cavity. Indeed, this additional confinement permits the control of the emission dynamics, producing an enhanced emission into the cavity modes that allows for a simplified extraction of the photons.

In particular, with the depicted experimental structure, we can operate in two modes to generate single photon states:

- **Resonance Fluorescence (RF).** In this configuration the QD is excited with a laser having a resonant frequency with the emitter energy levels, and the relaxation of the latter produces photons with the same frequency. Therefore, to separate the generated photon by the pump, we need to exploit a different degree of freedom, such as polarization. In this case, then, we are using a *cross-polarization* extraction strategy. In particular, we exploit the asymmetries, that arise from the fabrication process, of the cavity geometry in which the QD is contained. As a result of them, the cavity supports two linearly polarized modes, H and V, split by energy, that are coupled with the QD exciton states. Therefore, entering the system with a laser pump polarized along V, it is possible to show that is present an oscillation in the excited state populations which allows to generate also photons with a polarization directed along the H cavity mode [163, 177]. Since the latter is orthogonal to the laser one, we can separate the pump from single photons, and extract the latter, in polarization by using a PBS.
- **Longitudinal Acoustic (LA).** In this configuration, the laser frequency is off-resonant with the energy levels of the emitter, and the generation is phonon-assisted, i.e. a phonon is produced by relaxation during the emission. In this case, the produced photons frequency is red-shifted with respect to the laser one and we can separate the pump and the signal by using frequency filters. A schematic representation of the process can be seen in Fig. 2.9. Giving more details, the presence of a strong laser pulse produces an alteration, called *dressing*, in the QD levels. In particular, considering the presence of the pump, the total Hamiltonian presents as upper and lower eigenstates a superposition between the ground and excited bare QD states [181]. The gap between these new laser-dressed states produces, by relaxation from the upper to the lower one, a longitudinal acoustic phonon with a typical energy of a few meV [179]. At the end of the laser pulse, there is an adiabatic undressing and the lower dressed state can be transformed into the initial exciton level (for instance $|X\rangle$). Therefore, the final optical transition produces single photons shifted in frequency with respect to the pump laser. Contrary to the RF case, the LA emitted photons can be polarized along the direction of one of the exciton QD states, and therefore the LA can be used to efficiently generate linearly polarized single photons [179]. Finally, the delay of the exciton occupation generated by the adiabatic undressing allows a strong suppression of a re-excitation process and thus an improvement of the single photons purity [182].

Despite all the benefits of using QD sources, the major practical drawbacks are the need to accurately control the working environment, generally by placing the chip in a cryostat that maintains a temperature of around 4 K, and the fact that each QD works at a specific wavelength reducing in this way the control over the produced photons frequency. Moreover, while QDs represent a suitable choice for generating pure single photons state, compared to SPDC sources, greater caution and endeavor are needed for producing entangled photon pairs [183–187].

During the thesis work, we used a QD source that works in the longitudinal acoustic configuration. In particular, we employed the commercial *Quandela e-*

Delight-LA photonic chip [188] to generate on-demand single photons and, by acting on them, produce intra- and inter-particle OAM entangled states (see Section 4.2).

2.5 Manipulation of photons angular momentum

As highlighted in the previous chapter, light possesses two rotational degrees of freedom: SAM and OAM. The first is associated with the vector properties of the field and can take $\pm\hbar$ values in the direction of propagation, respectively, for beams with left and right circular polarization. The second, on the other hand, is related to the spatial structure of the field; for a beam with a helical front having phase factor $e^{im\phi}$, the value of the OAM in the propagation direction is $m\hbar$ for each photon.

These quantized degrees of freedom have found several applications in the field of Quantum Information to encode qubits and qudits. Therefore, it is interesting to describe how we can act on them to manipulate their state and perform the wanted protocol.

2.5.1 Polarization degree of freedom

The polarization is one of the most exploited light degrees of freedom both in classical and quantum implementations. This is in part because it interacts with birefringent crystals, being affected by their different refractive indices, and then can be trivially manipulated with devices that are easy to produce.

Classically, the polarization is associated with the direction of oscillation of the electric field, while in the quantum description it is associated with the two eigenvalues of the SAM degree of freedom of the photons. Therefore, it is naturally used for encoding qubits. Here, we associate the computational basis $\{|0\rangle, |1\rangle\}$ respectively with the horizontal and vertical polarization states $\{|H\rangle, |V\rangle\}$. In particular, by defining the diagonal and circular basis as:

$$\begin{aligned} |+/-\rangle &= \frac{1}{\sqrt{2}}(|H\rangle \pm |V\rangle) \\ |L/R\rangle &= \frac{1}{\sqrt{2}}(|H\rangle \pm i\,|V\rangle) \end{aligned} \tag{2.87}$$

These together with the computational one define a set of mutually unbiased bases (MUBs), which present the property of having an equal outcome probability $p = 1/2$ when a quantum system prepared in a basis is measured in one of the others. MUBs play an important role inside quantum cryptography and quantum key distribution protocols [21, 189]. Moreover, as we saw in the previous chapter, polarization is also interesting because it permits the easy engineering of entangled photon pairs using non-linear sources.

In this Section, we will describe the working principle of two fundamental optical elements, widely used for SAM manipulation in several photonic platforms: the *waveplates* and the *polarizing beam splitter*.

Waveplates

A waveplate is a linear optical element used for the manipulation of photon polarization. Typically, it consists of a layer of birefringent material that is cut in such a way that the optical axis of the crystal is parallel to the cutting plane. Since the material is birefringent, when light passes through it, the polarization parallel to the optical axis of the waveplate experiences the extraordinary refractive index

(n_e), while the orthogonal polarization experiences the ordinary one (n_o). The two polarizations, in this way, have different velocities within the waveplate: light with polarization parallel to the ordinary axis travels through the crystal with velocity c/n_o, while polarization parallel to the extraordinary axis has velocity c/n_e. This causes the following phase difference ϕ between the two orthogonal polarizations [190]:

$$\phi = \frac{2\pi d \Delta n}{\lambda} \tag{2.88}$$

where d is the thickness of the crystal, λ is the wavelength of the light beam in the vacuum, and the variation $\Delta n = n_o - n_e$ is the difference between the refractive indexes of the material.

Then using the horizontal polarization $|H\rangle = (1, 0)$ and the vertical polarization $|V\rangle = (0, 1)$, the matrix of a waveplate with an optical axis oriented along the horizontal direction is:

$$WP = \begin{pmatrix} 1 & 0 \\ 0 & e^{i\phi} \end{pmatrix} \tag{2.89}$$

Therefore, by opportunity tuning the parameter of Eq. 2.88 it is possible to perform several transformations of the polarization state of the beam. In particular, since it depends explicitly on the wavelength, different devices are designed to work with different wavelengths.

Interesting cases are represented by the *Half-Waveplate* (HWP) and the *Quarter-Waveplate* (QWP), which correspond respectively to a phase delay equal to $\phi = \pm\pi, \pm\pi/2$. In particular, relevant operations can be obtained when these waveplates are rotated, the general expression for their matrix is then given as:

$$HWP(\theta) = \begin{pmatrix} cos(2\theta) & sin(2\theta) \\ sin(2\theta) & -cos(2\theta) \end{pmatrix} \tag{2.90}$$

$$QWP(\theta) = \begin{pmatrix} cos^2(\theta) + isin^2(\theta) & cos(\theta)sin(\theta) - icos(\theta)sin(\theta) \\ cos(\theta)sin(\theta) - icos(\theta)sin(\theta) & sin^2(\theta) + icos^2(\theta) \end{pmatrix} \tag{2.91}$$

where θ is the angle between the waveplate fast axis and the horizontal direction. In particular, we can see that putting the HWP at angles $\theta = 0$ and $\theta = \pi/4$, it is possible to apply the Pauli operators σ_z and σ_x, while for $\theta = \pi/8$ we obtain the Hadamard matrix. Hence, it shows how it is possible to easily implement single-qubit gates in photonic implementations. Moreover, it can be shown that a set composed of two QWPs interspaced by a HWP rotated at proper angles can implement an arbitrary qubit transformation [191].

Polarizing beam Splitter

The Polarizing Beam Splitter (PBS) is an optical element for spatially splitting two orthogonal polarizations. A very common structure for the PBS is the Wollaston prism, which consists of two triangular calcite prisms with orthogonal optical axes, cemented together on their bases. Due to the geometry and birefringence of the material the condition of total internal refraction is obtained on the interface between the two prisms, an incident beam is then split into two beams polarized parallel and orthogonal to the PBS axes, respectively. A schematic representation of its action is shown in the figure (2.10).

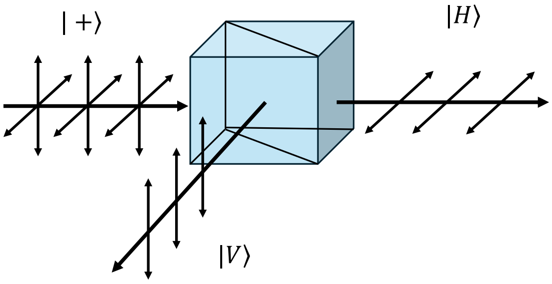

Figure 2.10. Polarizing Beam Splitter. Representation of the action of a Polarizing Beam Splitter (PBS). An impinging beam, in this case with polarization state $|+\rangle$, is divided by the device into its horizontal and vertical components. In particular, the first one is transmitted, while the second one is reflected.

Moreover, since it transmits only the horizontal polarization H, the PBS can be used to perform projective measurement in the polarization Hilbert space. In particular, a combination of QWP, HWP and PBS in a cascade configuration can perform a complete tomography of the polarization state of a qubit. Indeed, with this configuration it is possible to measure the Pauli matrices and locate the state in the Bloch sphere. To do so, we use the waveplates to convert one at a time the polarization of the MUBs set $\{H, V, +, -, R, L\}$ into the horizontal one, and through the PBS we project to measure only its intensity, or number of photons. Then, by combining the resulting intensities, we obtain the so-called *Stokes parameters* that are related to the coordinates (x, y, z) of the qubit on the Bloch sphere in the following way:

$$S_1 = x = \frac{I_H - I_V}{I_H + I_V} \tag{2.92}$$

$$S_2 = y = \frac{I_+ - I_-}{I_+ + I_-} \tag{2.93}$$

$$S_3 = z = \frac{I_R - I_L}{I_R + I_L} \tag{2.94}$$

where I_i is the measured intensity, or the number of collected photons, for the polarization state i.

In particular, the Stokes parameters have been extensively used from the beginning of the classical studies on light properties to describe its polarization states. Indeed, in 1892 Poincarè showed that the polarization state of a light beam can be mapped on a sphere known as *Poincarè sphere* [192]. The latter captures all the fundamental polarization descriptors and the coordinates on it are furnished by the Stokes parameters. Here, circularly polarized beams are placed at the poles of the sphere while the linear polarized ones reside on the equator, all the other points are instead associated with elliptical polarization states (see Fig. 2.11). Therefore, whenever the polarization degree of freedom is used for encoding information, the Poincarè sphere is directly connected to the Bloch sphere of the qubit.

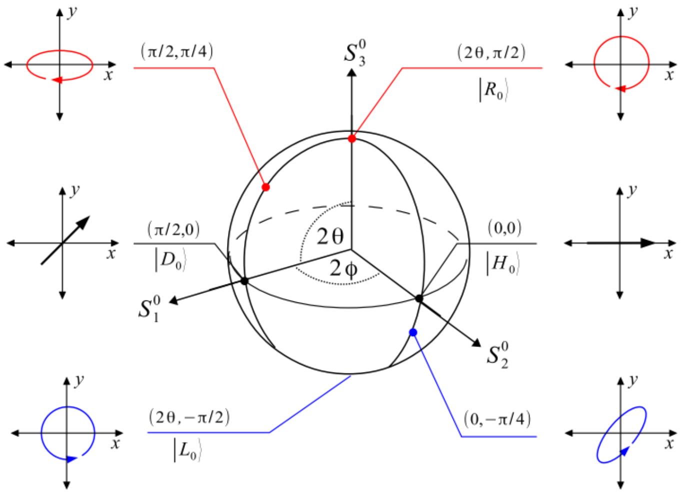

Figure 2.11. Poincarè Sphere. Representation of the polarization state of a field as a point over a sphere, called *Poincarè sphere*. The three Stokes parameters of Eqs. 2.92-2.94 are associated to the geometrical axes of the space. The right and left circularly polarized fields are placed at the two poles of the sphere, while the linear polarizations are along the equator. Image taken from [193].

2.5.2 Orbital angular momentum degree of freedom

Conversely to the polarization, the orbital angular momentum is an unbounded quantized degree of freedom of the photons. This intrinsic high dimensionality makes it a suitable candidate for the encoding of qudit in photonic Quantum Information implementations. As we said, the OAM is carried from all the fields that show a phase term proportional to $e^{im\phi}$, where ϕ is the azimuthal angle and m is an integer connected to the OAM value, which is equal to $\hbar m$ for each photon of the beam.

Being a spatial-related property of the beam, OAM is more affected by the spatial inhomogeneities of the media in which it is propagating and the tools designed to manipulate this degree of freedom exploit this characteristic. In this Section, we will introduce two devices that are widely used to act on the spatial structure of light state: the *q-plate* and the *spatial light modulator*.

Q-plate

After the paraxial decomposition of angular momentum, we obtain a description of the OAM and SAM in which they appear as distinct and noninteractive properties of the field. For this reason, after the seminal paper by Allen *et al.* [24], the first modulation devices designed for OAM states generation were polarization-independent [67, 68, 194]. In 2006 Marrucci *et al.* [51] proposed the idea that inhomogeneous and anisotropic media, such as liquid crystals, could give rise to an optical processes in which the variation in SAM, due to the birefringence of the material, results in OAM that depends on the inhomogeneity of the material. Indeed, such a process is called *Spin To Orbital Conversion* (STOC) of angular momentum and can be accomplished using an optical instrument that was called *q-plate*.

A q-plate is a plate of birefringent material having an uniform phase delay δ and a nonuniform transverse pattern of the optical axis [51, 52]. The pattern is defined by the number q of rotations, which is an integer or a half-integer, that the

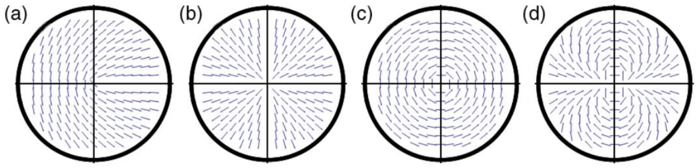

Figure 2.12. Q-plate patterns. In figure are reported the patterns of the optical axis $\alpha(\phi)$ for different values of the parameters α_0 and q. **a)** $(q,\alpha_0)=(\frac{1}{2},0)$, **b)** $(q,\ \alpha_0)=(1,0)$, **c)** $(q,\ \alpha_0)=(1,\frac{\pi}{2})$, **d)** $(q,\ \alpha_0)=(2,0)$. Image taken from [52].

optical axis performs in one revolution around the center of the device, where a topological defect is present. A second parameter on which the pattern depends is the initial orientation of the optical axis, specified by the angle α_0, with respect to the x direction of the transverse plane. In the discussion, it is possible to assume a dependence only on the azimuth angle ϕ, so the direction of the optical axis varies as follows [51]:

$$\alpha(\phi) = \alpha_0 + q\phi \tag{2.95}$$

Some examples of patterns are shown in Fig. 2.12.

The phase delay δ can be modified in such a way as to optimize STOC, this makes the q-plate a tunable device. Tuning can be achieved by mechanical pressure, thermal methods, and by using an external electromagnetic field. The latter allows for faster dynamic control of δ than the former, which are better suited for static conditions. The optimal tuning is for $\delta = \pi$, in that case the q-plate changes the m value of the angular momentum of a circularly polarized beam of light by a value $\Delta m = \pm 2q$, where the sign is positive for left circular polarization and negative for the right circular one. In the passage through the q-plate there is also a reversal of the spin angular momentum, this action is shown in the Fig. 2.13. Instead, in the case of suboptimal tuning, i.e. whenever $\delta \neq \pi$, there is a superposition between the transformed beam, as in the optimal case, and the original beam.

The action of the q-plate on a quantum single-photon state is essentially the same as for classical coherent light. We introduce the notation $|P,m\rangle = |P\rangle\,|m\rangle$ for the single-photon state, where P is the polarization state and m is the value of the OAM in units of $\hbar$. The action of the q-plate can be identified as the operator $\hat{QP}$:

$$\hat{QP}_\delta\,|L,m\rangle = \cos\frac{\delta}{2}\,|L,m\rangle + i\sin\frac{\delta}{2}\,e^{i2\alpha_0}\,|R,m+2q\rangle \tag{2.96}$$

$$\hat{QP}_\delta\,|R,m\rangle = \cos\frac{\delta}{2}\,|R,m\rangle + i\sin\frac{\delta}{2}\,e^{-i2\alpha_0}\,|L,m-2q\rangle \tag{2.97}$$

Using Jones' formalism, the q-plate action takes the following matrix form in the circular polarization basis $\{|R\rangle\,,|L\rangle\}$:

$$\hat{QP} = \cos\frac{\delta}{2}\begin{pmatrix}1 & 0\\ 0 & 1\end{pmatrix} + i\sin\frac{\delta}{2}\begin{pmatrix}0 & e^{-i2\alpha}\\ e^{i2\alpha} & 0\end{pmatrix} \tag{2.98}$$

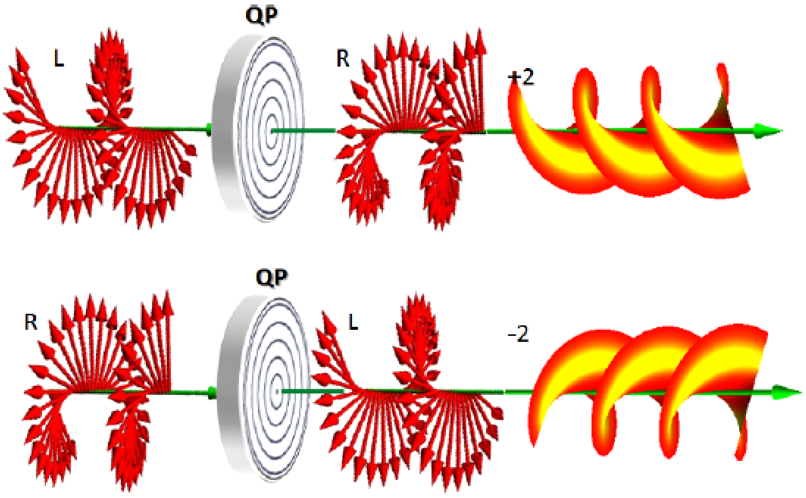

Figure 2.13. Q-plate action. Action of an optimally tuned q-plate ($\delta = \pi$) with a topological charge $q = 1$ on an input beam carrying a null OAM value ($m = 0$) and right (R) or left (L) circularly polarized. The output field has an OAM $m = \pm 2$, where the sign depends on its polarization. Image taken from [52].

The q-plate then originates a polarization-controlled change of orbital angular momentum, specifically for a q-plate with maximum conversion the change in total angular momentum of light in the direction of propagation is equal to [51, 52]:

$$\Delta j_z = \pm 2\,(q-1)\,\hbar \tag{2.99}$$

So in the case where $q = 1$ the total angular momentum of light is conserved since the change in OAM is balanced by the change in SAM, in this case we speak of pure STOC.

For the specific case of Quantum Information, the STOC property can be used to convert information stored in the polarization degree of freedom to the OAM and vice versa, implementing the operation [195]:

$$|\phi\rangle_\pi \, |0\rangle_o \rightleftharpoons |H\rangle_\pi \, |\phi\rangle_o \tag{2.100}$$

where $|\phi\rangle$ is the state relative to a generic qubit and we chose to use $|0\rangle_o$ and $|H\rangle_\pi$ as states, respectively in OAM and polarization, that do not possess information content.

In addition for generating states having OAM, the practical use of the q-plate lies in the coupling induced between spin angular and orbital angular momentum. This can be used to create *intraparticle entangled* states, in which entanglement is present between different degrees of freedom:

$$\hat{QP}\,|H,0\rangle = \frac{|R,2q\rangle + |L,-2q\rangle}{\sqrt{2}} \tag{2.101}$$

This kind of entangled state has been extensively used in several experimental platforms, for instance investigating fundamental properties of Quantum Information such as the optimal quantum cloning [196] or developing quantum communication protocols that do not depend upon the local reference frames of the sender and receiver [197]. Moreover, by encoding one qubit in each degree of freedom, namely one for the SAM and one for the OAM, in the Eq. 2.101 can be seen the mathematical expression of a *ququart* state [198].

Spatial Light Modulator

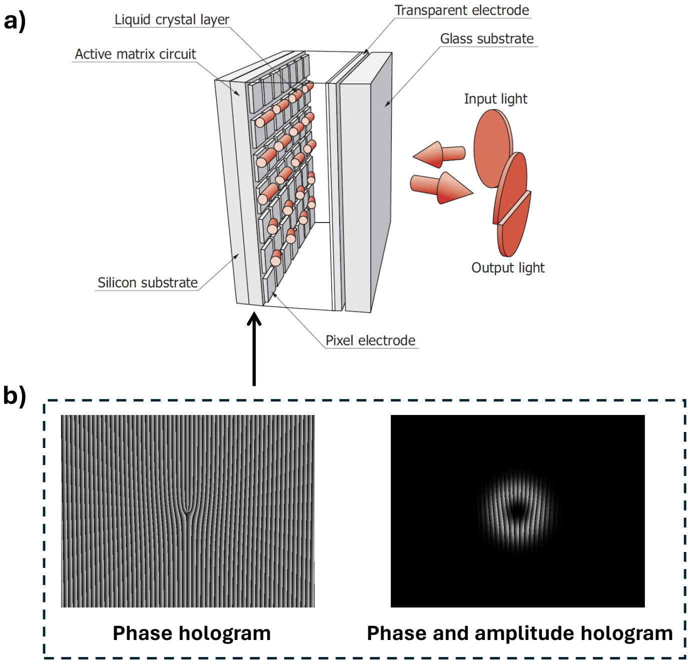

Figure 2.14. Spatial light modulator action. a) Schematic of the liquid crystal on silicon - spatial light modulator active window. This is made of a liquid crystal placed between a silicon and a glass substrate, on the first one are placed the electrically-controlled aluminum pixels, which by causing a tilt in the crystal molecules allow us to shape the spatial structure of an input beam. Image taken from [199]. **b)** Example of computer-generated holograms used to electrically control the active matrix of the device and designed for producing a helical beam carrying an OAM value $m = 3$. We report both the phase-only hologram (see Eq. 2.103), and the hologram in which is implemented the intensity masking introduced in Ref. [49] (see Eq. 2.104).

From the beginning of the investigations over the optical beams spatial properties, a widely employed approach to modulate their orbital angular momentum lied in the use of pitch fork *holograms* [49, 200, 201]. The latter are thin plates on which is registered a diffraction grating designed to produce the wanted field in an interference pattern at the output of the device.

Instead of using physical and not reprogrammable plates to encode the holograms, nowadays the holographic technique is mostly implemented by exploiting a commercial device called *Spatial Light Modulator* (SLM). One particular model is the Liquid Cristal On Silicon - Spatial Light Modulator (LCOS-SLM). This is an electronically controlled spatial phase modulator, based on the liquid crystal on silicon technology. The active part of the instrument consists of a liquid crystal layer placed between a glass substrate and a silicon substrate; aluminum pixels are placed between the latter and the liquid crystal layer. Each pixel can be manipulated autonomously through the application of an electric field, which allows the desired phase structure to be constructed. The phase modulation induced by the device is produced by the tilt, due to the presence of the electric field applied through the aluminum pixels, of the liquid crystal molecules. Indeed, depending on the tilt angle, there is a different refractive index and thus a different optical path length within the medium. To have optimal phase modulation, the entering field must be polarized in the same direction in which the molecules are tilted [199]. The phase pattern is programmable by sending a greyscale hologram to the SLM, in which the 255 grey levels are associated with a phase factor in the interval $[0, 2\pi]$. This allows one to analyze or generate with just one device different spatial characteristics of a beam, such for instance the decomposition over an OAM basis. Since the conversion of the holograms works through interference, the grating superimposed on the phase modulation is blazed, i.e. the grating has a step structure with a sawtooth-shaped cross-section. This is done to both increase the efficiency in a certain order and separate it from the others, usually the selected order is the first one, and the gating space Λ is chosen depending upon the input wavelength to maximize the conversion efficiency. A schematic representation of the SLM action is shown in the Fig. 2.14.

Although the LCOS-SLM is a phase-only modulator, by using appropriate hologram coding, the beam amplitude can also be modulated. This is achieved by an intensity masking procedure. For the construction of the mask, one can follow the protocol proposed in 2013 by Bolduc *et al* [49]. In the following, we will describe both the phase-only and the phase plus amplitude modulation.

Assuming that the device is etched with a plane wave, the outgoing beam in the first-order diffraction can be written in paraxial approximation as:

$$U(\mathbf{r}, z_0) = A(\mathbf{r}, z_0)\, e^{i\Phi(\mathbf{r}, z_0)} \tag{2.102}$$

where $\mathbf{r} = (x, y)$ is the coordinate in the transverse plane, $A(\mathbf{r}, z_0)$ and $\Phi(\mathbf{r}, z_0)$ are, respectively, the amplitude and phase of the optical field that we want to generate in a $z = z_0$ plane.

Phase-only holograms

A phase-only hologram can be used to modulate the entering plane wave to obtain a field with a specific phase. Considering the field of Eq. 2.102, we encode the following grating on the SLM:

$$\Psi(m, n) = \; Mod\left(\Phi(m, n) + \frac{2\pi m}{\Lambda}, 2\pi\right) \tag{2.103}$$

where $Mod(.)$ is the modulo operation and m, n are the pixels coordinates. Considering an infinite number of pixels, the field in the first diffraction order takes the form $U = FT\left[e^{i\Phi(m,n)}\right]$ where FT is the Fourier transform operation. In practice, to obtain the wanted field we insert a spatial filter to select only the first order of diffraction and look at the field in the Fourier plane of the spatial filter, for example using an optical lens. Therefore, the encoded phase is directly transferred to the field while the amplitude does not change. In particular, it can be shown that these holograms are not suitable to generate pure LG modes since they don't fix the radial index and the output beam results to be an HyGG mode [151, 153].

Phase and amplitude holograms

In the most general case in which we also want to obtain the correct amplitude, the diffraction grating codified in the hologram is the following:

$$\Psi(m,n) = \mathcal{M}(m,n)\ Mod\left(\mathcal{F}(m,n) + \frac{2\pi m}{\Lambda}, 2\pi\right) \tag{2.104}$$

where $0<\mathcal{M}<1$ is a function of the amplitude and $\mathcal{F}$ is an analytic function of the phase profile of the desired beam. Proceeding in the same manner as before, after filtering all the other orders, we have the following field at the output of the SLM:

$$T_1(m,n) = -sinc\left(\pi\mathcal{M} - \pi\right)\ e^{i(\mathcal{F}+\pi\mathcal{M})} \tag{2.105}$$

So choosing the modulation function to be $\mathcal{M} = 1+\frac{1}{\pi}sinc^{-1}(A)$ and $\mathcal{F} = \Phi-\pi\mathcal{M}$, we obtain within the experimental limits the desired field of Eq. 2.102.

In addition to generating an arbitrary light beam, SLM can be used together with the coupling in a single-mode fiber (SMF) to analyze the spatial profile of a beam incident on the device. This technique can then be used to measure the orbital angular momentum content of arbitrary paraxial beams. Therefore, in this case, we can consider entering the device with an OAM mode. The technique introduced by Mair *et al.* [159] consists of converting this field to the fundamental Gaussian mode through a hologram that presents the conjugate phase distribution. Since the Gaussian beam can be completely coupled into a SMF, the latter is used to analyze the "Gaussianity" of the output beam and accordingly quantify the similarity between the incoming mode and the one present in the hologram shown on the SLM. However, using the LG modes basis for the OAM eigenstates (see Section 2.3), it has been demonstrated how this technique presents a different efficiency depending on the OAM content and the radial structure of the beams written in the employed holograms [202]. Therefore, in practice, to perform a correct measurement the coupled signal has to be rescaled to account for the different efficiencies.

During the thesis work, q-plates and SLM have been widely used to address the generation and detection tasks, which represent the central topics of our work. In particular, q-plates represent the building blocks of our QW engineering platform (See Section 5.1), implementing the control shift operations, and therefore have been used in all the applications that leverage on its dynamics (See Sections 7.2-8.2). In all these cases, the SLM was instead principally used in the measurement stages to retrieve the OAM content of the setup output states (See also 6.1.1). Furthermore, in Section 8.2, it was also employed to opportunely shape the input state to be evolved via the QW.

Chapter 3

Machine Learning and Optimization Algorithms

Machine Learning (ML) is a wide branch of artificial intelligence that in the last years has received growing attention, with several applications in everyday life [203]. The main difference with respect to traditional computer science approaches is that a ML model is not fully programmed to solve a task but it is left free to learn from the data it is given. In this way, it tries to extract statistical structures from the furnished examples, adapting to them and creating a model capable of making reasonable predictions on previously unseen cases. This trainable structure makes ML paradigms versatile and capable of solving problems that cannot be stated easily as a set of mathematical rules such as image classification [204] or speech recognition [205], tasks emulating the capabilities of a human brain. Recently, machine learning has found several applications also in the field of Quantum Information [206–212]. In particular, combining the ML paradigm with Quantum Mechanics properties led to the birth of the new *quantum machine learning* research field [72–74]. Where it is present a fruitful exchange of expertise. On the one hand, ML implementations help in the optimization of Quantum Information protocols. On the other hand, quantum properties can be used to enhance the performance of ML paradigms. In this chapter, we will give an introduction to the basic concepts of ML describing the relevant model used during the thesis work.

Another approach frequently used in literature to solve specific tasks is represented by mathematical optimization algorithms. Being used both in combination or as an alternative to machine learning, optimization algorithms are based upon a mathematical model that has the aim to efficiently sample an *objective* or *cost* function to find its minimum. These find several applications even in the Quantum Information field. In the following, we will give a detailed description of the RBFopt algorithm [213, 214] that was used during the thesis work (see Section 5.2).

3.1 Optimization Algorithms

Mathematical optimization refers to the choice of the best element among a set of alternatives upon a fixed criterion. Usually, the problem is cast as the minimization of an objective function $f(.)$, and it proceeds by applying a sampling strategy to the function until the point x^* for which $f(.)$ assumes the minimal value is found.

Such an approach has several applications, ranging from computer science to economy [215, 216]. Also in the Quantum Information field, optimization algorithms have found implementations for solving various tasks inside quantum computation protocols [217, 218].

The mathematical optimization approaches can be described with 4 labels depending on the characteristics of the code that governs their strategy of operation:

- ***Gradient-based*****:** The function is analytically known and the algorithm exploits its gradient to reach the minimum value.
- ***Gradient-free*****:** The function is not known analytically, but we can only query it and obtain as a response its values. This class of algorithms proceeds by sampling the function using a strategy to find the minimum.
- ***Deterministic*****:** The algorithm ends always with the same final solution if we start from the same initial point.
- ***Stochastic*****:** The algorithms perform a random search of the solution, so it may give different results depending on the evolution even if we begin from the same initial state.

Usually, in experimental scenarios, the objective function is unknown or incomplete, since it doesn't account for uncontrolled noise that affects the implementation. Moreover, the furnished one could be obtained upon approximation and doesn't catch the full dynamics of the system under analysis. For all these reasons, gradient-free optimization algorithms could be beneficial. In the following Section, we will describe one of them, the RBFOpt [213, 214] that will be exploited in the following to optimize the engineering of high dimensional quantum states (see Section 5.2)

3.1.1 RBFOpt algorithm

The RBFOpt algorithm belongs to the previously introduced class of gradient-free optimization algorithms. Therefore, it works in a black-box fashion and specifically by building an approximated model of the unknown objective function, called *surrogate model*, via the exploitation of the Radial Basis Functions (RBFs) [213, 214, 219, 220]. These are real-valued functions that depend only on the radial distance from a fixed point $\mathbf{p}$, this means that they have the form $\phi_{\mathbf{p}}(\mathbf{x}) = \phi_{\mathbf{p}}(\|\mathbf{x}-\mathbf{p}\|)$. Frequently, this class of functions is used as a basis over which to decompose a given function through its approximation by an interpolant surrogate model. It has been observed that this approach is particularly efficient and suitable when the model presents few parameters, and when a limited number of queries to the function is allowed [219, 220]. The RBFOpt algorithm added to the standard RBFs methods refinements that increase the performance of the approach [213, 214].

The mathematical problem that we want to solve is the following:

$$\min_{\Theta} f(\Theta) \quad \text{for} \quad \Theta \in \Omega = [\Theta_L, \Theta_U] \tag{3.1}$$

where $f : \mathbb{R}^N \to \mathbb{R}$ and $\Theta_L, \Theta_U \in \mathbb{R}^N$ are the vectors defining the lower and upper bound of the compact domain Ω over which the function takes values. The surrogate model is constructed from the sampled values of the function. Given k distinct points $\Theta_1, \ldots, \Theta_k \in \Omega$ with corresponding cost function evaluation $f(\Theta_1), \ldots, f(\Theta_k)$, the associated surrogate model after k sampling is defined as:

$$s_k(\Theta) = \sum_{i=1}^{k} \lambda_i \phi(\|\Theta - \Theta_i\|) + p(\Theta) \tag{3.2}$$

where $\phi(.)$ is a radial basis function, $\lambda_1, ..., \lambda_k \in \mathbb{R}$ are real parameters and $p(.)$ is a polynomial of degree d. This degree is selected based on the type of RBF function used in the surrogate model. The possible RBF functions among which the algorithm can choose and the degree of the respective associated polynomial are reported in Table 3.1. The hyperparameter γ presents in the expression of the radial basis functions is set to 0.1 by default [221, 222]. Moreover, the RBFOpt algorithm automatically selects the radial basis function that appears to be the most accurate in the description of the problem. This selection is made using a cross-validation procedure, in which the performance of a surrogate model constructed with points $(\Theta_i, f(\Theta_i))$ for $i = 1, ..., k$ is tested at $\{(\Theta_j, f(\Theta_j))\}$ with $j \neq i$ [213, 214].

The value of the parameters λ_i with $i = 1, ..., k$ and the coefficients of the polynomial can be determined by solving the following linear system [213, 214, 219, 220]:

$$\begin{cases} s_k(\Theta_i) = C(\Theta_i), \quad i = 1, ..., k \\ \\ \sum_{i=1}^{k} \lambda_i \hat{p}_j(\Theta_i) = 0, \quad j = 1, ..., \tilde{d} \end{cases} \tag{3.3}$$

where, called Π_d the space of polynomials of degree less than or equal to d, $\tilde{d}$ is the dimension of Π_d and $\hat{p}_1, ..., \hat{p}_{\tilde{d}}$ is a basis of the space.

Radial Basis Function $\phi(x)$	Polynomial degree d
x	0
x^3	1
$\sqrt{x^2 + \gamma^2}$	0
$x^2 \log x$	1
$e^{-\gamma x^2}$	−1

Table 3.1. The RBFs exploited by the RBF algorithm and the degree of the polynomial used in the construction of the surrogate model [213, 214, 219, 220]. When $d = -1$ the polynomial is removed from the expression 3.2. The hyperparameter γ is set equal to 0.1 by default.

At the beginning of the optimization procedure, the surrogate model is constructed from a set of parameter points tunable in number and sampled using a *latin hypercube design* [221, 222], which distributes the initial sampled point in a manner to minimize the overlap between them while maximizing the explored hypervolume. In particular, 50 latin hypercubes are randomly generated and the one with the maximum relative distance between the points is taken for the initial sampling of the cost function. After that, the interpolant is used to choose the next point on which to compute the cost function. Hence, the evolution of the RBFOpt algorithm is composed of the repetition of the following steps (say k-th step) [213, 214]:

1. Compute the surrogate model $s_k(\Theta)$ from the data points $(\Theta_i, C(\Theta_i))$, with $i = 1, ..., k$, solving the linear system of Eq.(3.3)

2. Use the surrogate model to choose the next point Θ_{k+1}. In particular, the Metric Stochastic Response Surface Method (MSRSM)[220] is applied. Within this framework, the algorithm does a number of *global steps* controlled by the hyperparameter *num_global_searches* (default value 5 [221, 222]) and a *local step*. The latter gives as next point the one that minimizes the surrogate model.

3. Evaluate the cost function at Θ_{k+1} and add $(\Theta_{k+1}, C(\Theta_{k+1}))$ to the data points.
4. Decide if restart the model for lack of improvement. Specifically, if the algorithm does not find a new optimal solution after a number of evaluations defined by the hyperparameter *max_stalled_iterations* (default value 100 [221, 222]), the actual surrogate model is discarded and the optimization procedure is restarted from scratch.

In particular, the MSRSM used to select the next point to sample Θ_{k+1} works in the following way:

- Choose a parameter $\alpha \in [0,1]$
- Defined $dist(x) := \min_{i=1,...k} \|x - x_i\|$ and taken a set of reference point $P \subset \Omega \setminus \{\Theta_1, ..., \Theta_k\}$, the next point is obtained by solving:

$$\begin{aligned}\Theta^{k+1} = arg \min_{\Theta\in\Omega} \alpha \frac{max_{y\in P}\ dist(y) - dist(\Theta)}{max_{y\in P}\ dist(y) - min_{y\in P}\ dist(y)} + \\ + \frac{s_k(\Theta) - min_{y\in P}\ s_k(y)}{max_{y\in P}\ s_k(y) - min_{y\in P}\ s_k(y)}\end{aligned} \tag{3.4}$$

Hence, it tries to find a point that has both the maximum distance from $\{\Theta_1, ..., \Theta_k\}$ and the minimum value of the surrogate model.

As said before, the algorithm performs both global and local steps, the way to go from one to the other is governed by the value of α in Eq. 3.4. In particular, given h the value of the hyperparameter *num_global_searches*, the value of α is chosen cyclically in the following manner:

- Step $l \in \{0, \dots, h-1\}$ (*Global step*): $\alpha = \max\{1 - (l+1)/h, 0.05\}$. Balancing between exploration and exploitation.
- Step h (*Local step*): Choose $\alpha = 0$ and the solution of Eq. 3.4 is the point that minimizes the surrogate model $y^* = \arg\min_{y\in P} s_k(y)$. If $s_k(y^*) < f_{min} - 10^{-10}|f_{min}|$ with f_{min} the minimum value of the cost function found up to that point, we put $\Theta^{k+1} = y^*$. Otherwise, choose $\alpha = 0.05$, and an optimization phase called *AdjLocalStep* is performed to find a better minimum.

Finally, during the optimization, the algorithm executes also a *refinement step*. The purpose of this is to improve the optimal solution by doing a local search around it through a variation of a trust region method [213, 214]. The refinement step is triggered at the end of point (3) with a frequency controlled by the hyper-parameter *refinement_frequency*, with a default value equal to 3 [221, 222].

This algorithm will be exploited in Section 5.2 to optimize the engineering of qudit states encoded in the photons OAM degree of freedom.

3.2 Machine Learning

Machine learning is the study and development of algorithms capable of automatically improving themselves through experience. In particular, we say that a ML paradigm learns from experience E to solve a specific task T with performances measured by P, if its performance in solving T increases with the experience E [223].

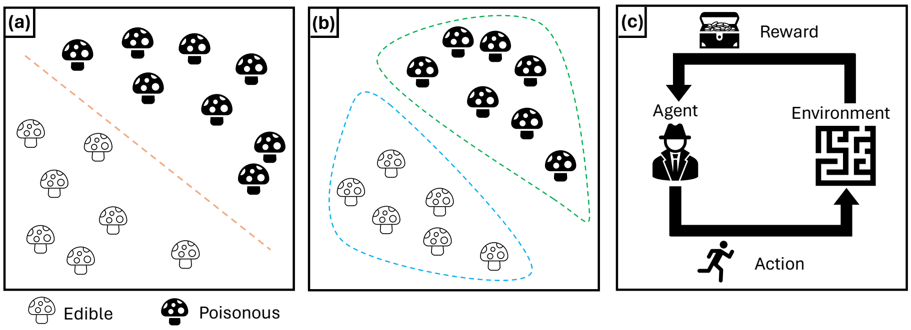

Figure 3.1. Machine Learning Paradigms. a) Supervised learning algorithms are trained to solve a task, such as classification, using a training dataset composed of labeled elements, that therefore contains the correct answers. **b)** Unsupervised learning algorithms learn by themselves how to cluster the data and retrieve significant features. **c)** Reinforcement learning algorithms provide an agent that tries to solve a task by interacting with an environment, based on the results of its actions the agent is either rewarded or punished.

Here, the ML algorithms develop a mathematical model with the aim of making predictions or taking action without being explicitly programmed to do so, the model is constructed upon a set of data, called the *training set*, that are exploited by the algorithm to gain experience and improve the model. This approach is very fruitful and enables the solving of complex tasks for which step-by-step programming coding is extremely challenging, such as speech recognition or self-autonomous driving, indeed in all these cases it is more efficient to help the computer to develop its own model than directly programming it. Moreover, in practice, we have to deal with large and complex datasets that are difficult to handle straightforwardly. ML instead is capable of finding meaningful structures in this complex conglomerate making it accessible. Finally, ML is also able to adapt itself to input that changes over time without the need to be reprogrammed.

Since the experience is gained from the interaction with the data environment, we can recognize 3 classes of ML paradigms based on it [224]:

- ***Supervised Learning:*** In this learning scenario, each element of the training set is associated with a *label* and the task of the ML algorithm is to find a map between the data features and the labels. The environment can be seen as a teacher that gives sufficient information to the learner. The performances of the model are then tested on a new set of labeled but unseen examples.

- ***Unsupervised Learning:*** In this framework instead, the examples of the training set are not labeled and the algorithm is asked to find significant structures in it. This approach is useful when facing clustering problems, in which we want to summarize and group a set of data through fewer relevant features.

- ***Reinforcement Learning:*** This is the most dynamical scheme and the one that reminds us most of our concept of learning. Here, an agent is given a set of tools and rules, with which it acts on the environment. The agent is asked to implement a strategy from what it possesses, and it is rewarded or punished depending on the success in solving the task. It aims to maximize the reward, and so it modifies its strategy consequently.

A pictorial representation of these machine learning protocols is reported in Fig. 3.1.

All the previous paradigms have been extensively used in different tasks of everyday life, ranging from spam detection to autonomous driving and smart chatbots [203]. Recently, the interaction between this research area and the field of Quantum Information brought to the birth of the *quantum machine learning* (QML) thread [72–74]. The union of these two fields falls within the scope of mutual benefit. The ML analysis strength can help in understanding complex quantum datasets and in controlling quantum devices, while the intrinsic power of quantum computation could be useful to increase the performances of the algorithms. In particular, ML can be useful to fully exploit the power of quantum computation, developing efficient ways of extracting the information encoded in the quantum states resulting from the computation and it is particularly interesting when dealing with high dimensional quantum states. Moreover, since quantum processes produce complex structured data, they can be used in combination with ML paradigms to analyze classical datasets that are difficult to analyze with a classical computer for their complexity.

During the thesis, working in this framework, we started by applying known supervised and unsupervised machine-learning algorithms for quantum data analysis (see Sections 6.2.1-6.2.2). Then we move to an implementation of a QML paradigm: the Quantum Extreme Learning Machine (QELM). That we used to solve the task of reconstructing quantum states from measurements of them (see Section 7.2). In the following, we will introduce all the classical ML models used throughout the thesis work.

3.2.1 Principal Component Analysis

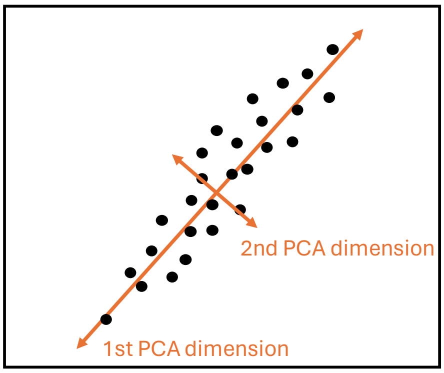

Figure 3.2. Principal Component Analysis. The principal component analysis works by building up a reduced representation of the input elements, called *latent space*. The dimensions of the latter capture the most important features and information about the samples in the dataset.

The Principal Component Analysis (PCA) is an unsupervised machine learning paradigm that is used to extract a meaningful and minimal representation of a dataset [225]. Its working principle consists of finding the *principal components*, a set of orthonormal vectors that span a linear vector space in which it is possible to have a reduced but nearly complete description of the data. For this reason, the PCA belongs to the class of linear *dimensional reduction* algorithms.

The PCA then can be described as a map between the sample space and the one spanned by principal components, called *latent space*. To capture most of the information about the statistical properties of the dataset, the principal components are built following the principle of maximizing the variance of the data when projected in their space. To easily understand the procedure we can adopt a graphical approach, the PCA then is represented as a fit of the samples with a k-dimensional ellipsoid, whose axes are the principal components (see Fig. 3.2 for the bidimensional case). These can have different dimensions and so different variances, the one with the maximum variance is then identified as the first principal component and the others follow sorted by their variance. The axes with a small variance can be discarded without losing significant information on the ensemble, since in these directions the elements of the dataset cannot be distinguished.

Let us now describe more formally the PCA technique. Taken a dataset composed of n elements each of whom is characterized by m features. We define the *dataset matrix* X as the $n \times m$ matrix containing all the information about the ensemble, for which each row is a different sample and the columns report its features. We also ask that each column has an average equal to zero, namely we have to shift the values in order to have zero mean. The PCA is an orthogonal transformation of the coordinates, given a set of k vectors $\mathbf{w}_j = \left(w_j^1, \ldots, w_j^m\right)$ with $j = 1, \ldots, k$ having dimension m, these are used to map each row $\mathbf{x}_i$ of X in a new target vector $\mathbf{t}_i = \left(t_i^1, \ldots, t_i^k\right)$ with a reduced dimension $k < m$:

$$\mathbf{t}_i^j = \mathbf{x}_i \cdot \mathbf{w}_j \quad with \;\; i = 1, \ldots, n \;\; and \;\; j = 1, \ldots, k \tag{3.5}$$

PCA then finds the weights for which the $\{\mathbf{t}_i\}$ have the maximum variance. Exploiting X, this problem can be stated as finding the eigenvalues of the covariance matrix $X^T X$. The first component is given as:

$$\begin{aligned} \mathbf{w}_1 &= \arg\max_{\|w\|=1} \sum_i (t_i^1)^2 = \arg\max_{\|w\|=1} \sum_i (\mathbf{x}_i \cdot \mathbf{w})^2 = \\ &= \arg\max_{\|w\|=1} \|X\mathbf{w}\|^2 = \arg\max_{\|w\|=1} \mathbf{w}^T X^T \cdot X\mathbf{w} = \\ &= \arg\max_{\mathbf{w}} \frac{\mathbf{w}^T X^T \cdot X\mathbf{w}}{\mathbf{w}^T \cdot \mathbf{w}} \end{aligned} \tag{3.6}$$

where in the last line we assumed a unitary principal component. It can be shown that Eq. 3.6 is maximized by the eigenvectors of the matrix $X^T X$, and so the principal components are the orthogonal eigenvectors of the covariance matrix associated with the greater eigenvalues.

The principal component gives an optimal representation of the data, reducing their dimension from m to k but maintaining the relevant statistical properties. This optimal representation can be used as a starting point in several ML implementations, being a way to reduce the sample size and increase the algorithm speed.

The PCA properties will be used in the following as a starting point for a linear regression approach to OAM reconstruction (see Section 6.2.2).

3.2.2 Neural Networks

Neural Networks (NNs) are computational paradigms whose modelization is inspired by the human brain working principle [224]. Being a simplification of the brain, NNs are composed of an ensemble of basic computational elements called

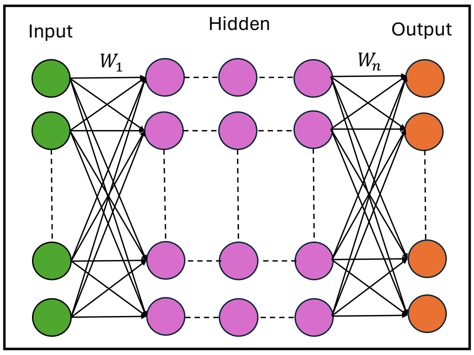

Figure 3.3. Neural Network. Schematic representation of a feed-forward Neural Network (NN). The NN is composed of n layers connected between them with weighted links $\{W_1, \dots, W_n\}$: the input layer that directly reads the samples, the hidden layers that elaborate them, and the output layer later that give us the results of the accomplished task. Each disk in the figure represents a neuron having an activation function of the form reported in Eq. 3.7

neurons interconnected by a complex structure of weighted links. Precisely this structure enables the network to solve complex tasks, a pictorial representation of it is reported in Fig. 3.3.

As in the human brain, each neuron propagates the electric signal only if it exceeds a certain threshold, the artificial neurons operate on the input signal with an *activation function* that emulates this behavior. In particular, given a neuron i and a set of inputs $\mathbf{x} = (x_1, \dots, x_n)$ coming from n neurons connected to the i-th through direct links weighted with values $\mathbf{w} = (w_1 \dots, w_n)$, we have that the response of i is described by:

$$AN_i(\mathbf{x}) = \phi_\theta(\mathbf{w} \cdot \mathbf{x}) \tag{3.7}$$

Where $\phi_\theta(.)$ is the activation function of the neuron and θ is the threshold that the inner product $\mathbf{w} \cdot \mathbf{x}$ has to surpass to activate the neuron response. Usually, nonlinear functions are used as activation functions, the most employed ones are the *sigmoid* and the $ReLu(x) = max(0, x)$ since they are capable of suppressing inputs that are too weak. Moreover, nonlinear functions are used because adding nonlinearity inside the networks increases the prediction power of the model, enabling for example the creation of complex decision boundaries. In particular, the activation function of a single neuron is capable of performing a linear classification task, indeed based on whether it exceeds the threshold or not the neuron recognizes if the input belongs to one of two target classes. While it is possible to show that a weighted arrangement of neurons, and thus a NN, is capable of reproducing any continuous real-valued function $f(\mathbf{x})$ of the inputs, being able to solve more complex tasks [224].

In the simplest architecture, the neurons of a NN are organized in multiple *layers*; starting with the input layer into which we load the sample features, then passing through a series of *hidden* layers that process the information and are not accessible by the user, and finally, the output layer on which we read the task results. In this simple formalization, the information flows from the input to the output, each neuron of a layer receives only the information from the neurons of the previous layer and sends its response to the ones of the following. This is called a *feed-forward* architecture.

A more complex version of the model can be obtained by adding layers that perform particular operations on the inputs. This is the case for example of the Convolutional Neural Network (CNN), a type of network that comprises a particular kind of layers called *convolutional* layers, whose action is invariant under translation making them ideal for image recognition tasks. A more detailed description of CNN will be given in a dedicated Section.

Moreover, we can think of changing how the information flows and is analyzed by the network. For instance, we can think of using a directed cyclic graph allowing each layer to both influence the following one and itself, so with a bi-directional flow of information. Then during the analysis of an element from a dataset, the state of a layer is influenced both by its response to the preceding input samples and by the current state of the previous layer. So this model enables the information to persist during the processing, and it is particularly suitable for analyzing temporal sequence, such as in speech recognition. This scheme emulates the typical intelligent process of a human brain, in which the information is processed gradually with an internal model that preserves the memory of previous input ad it is updated when new information is available.

The general training stage of a NN consists of optimizing the weights between the layers in order to solve a specific task creating the optimal solution between the input and the output. A metric called *loss function* is usually used to assess the performance of the model, and the objective of the network is to minimize its values for the training samples. The most used approach to find the weights is the *back-propagation*, in which the information about the network predictions flows back from the output to the input and it is used in the minimization of the loss, the most common strategy to do so is the *stochastic gradient descent* [226].

Finally, even if NN are architectures capable of solving efficiently several tasks, the connection between its parameter and the implemented function is not completely clear, appearing as a black box. This limits our capability to interpret the results of a deep network calculation. For this reason, recently a new branch called explainable artificial intelligence has been developed with the aim of investigating how NNs make their predictions [227].

Convolutional neural network

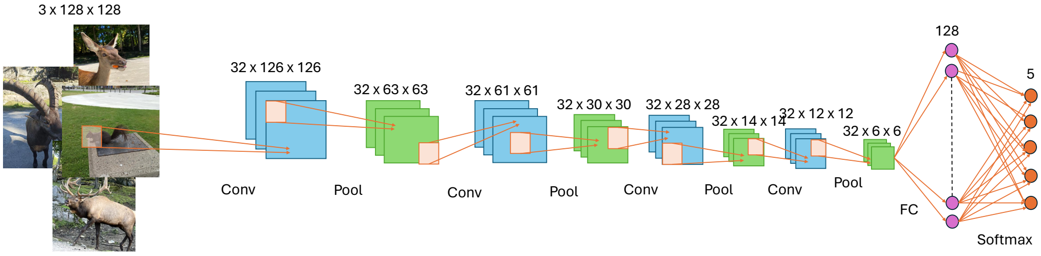

Figure 3.4. Convolutional Neural Network. Schematic representation of a Convolutional Neural network (CNN) used to solve a classification task. The CNN is made of a sequence of convolutional layers (Conv) and pooling layers (Pool), respectively blue and green colored in the image, followed by fully-connected (FC) layers, the latter of which is used to make the classification. Therefore the activation function of its neurons is the softmax reported in Eq. 3.10. Upon each layer is reported the correspondent dimension.

Convolutional Neural Networks (CNNs) are a special kind of feed-forward neural network whose work is inspired by the natural mechanism of visual perception of living creatures. They are frequently used for solving the image recognition task, in which they showed high performances even surpassing human capabilities [228, 229]. CNNs are characterized by the capability of learning translation-invariant features, optimal when considering image data, thanks to the 3 types of layers of which they are composed: *convolutional* layer, *pooling* layer, and *fully-connected* layer. A schematic of a CNN can be seen in Fig. 3.4.

The first one is used to extract features from an input image, so it represents the eyes of the network and works by applying a set of *filters* to the sample. Filters are $k \times k$ matrices and are applied by convolution on their input. This means that each filter of the set is applied to an element (x, y) of the image by performing the inner product between the filter matrix elements and the region neighboring the pixel (x, y). CNNs use many filters, each one extracting different features from the input, whose parameters are learned during the training stage. The filters size, their number, and the input entries on which they are applied are instead *hyperparameters* of the model and need to be fixed at hand. Finally, a nonlinear activation function is applied to the outputs of a filter introducing the nonlinearity needed to perform the task. Then, the output of the n-th filter of the m-th convolutional layer can be written as:

$$Y_{n,m} = \phi(W_{n,m} * X) \tag{3.8}$$

where $\phi(.)$ is the activation function, X in the input image data, $W_{n,m}$ is the filter matrix and $*$ indicates the convolution operation.

Pooling layers are instead used to eliminate redundant information. They perform a coarse grain of the image, mapping a window of size $p \times p$ of the input into a single value, where p is a hyperparameter of the model. Common choices to operate this reduction are the *average* pooling and the *max* pooling, which respectively substitute a selected window of the image with the average of its values or with the maximum one. The second one is nowadays the most used and is defined by the following mathematical operation:

$$Y_{i,j} = \max_{l,m \in \mathcal{R}_{i,j}} X_{l.m} \tag{3.9}$$

where $\mathcal{R}_{i,j}$ is the reception area obtained considering the window of size $p \times p$ centered on the input pixel (i, j). Pooling layers are important since they allow us to retrieve information about a greater part of an image, enabling the network to learn more complex features of it. Moreover, by decreasing the size of the image after their action, they reduce the number of trainable parameters greatly increasing the execution speed of the model.

Finally, the fully connected layers are the ones used in this context to classify the data and decide which of the output classes better describes the input. They are the basic layers of which a NN is made. In general, to solve a classification problem over a set N of classes the *softmax* activation function is used to calculate the probability that the sample belongs to the i-th class:

$$\phi_i(\mathbf{x}) = \frac{e^{x_i}}{\sum_{j=1}^{N} e^{x_j}} \tag{3.10}$$

where $i = 1, \dots, N$. In this case, the objective function minimized during the training stage is the *categorical cross-entropy*:

$$\mathcal{L} = -\sum_{i=1}^{N} x_i \log \phi_i(\mathbf{x}) \tag{3.11}$$

The performance of the network is quantified by the accuracy $\mathcal{A}$ of the CNN predictions.

In the following, we will describe the implementation of a CNN model to recognize high dimensional OAM states (see Section 6.2.1).

3.2.3 Extreme Learning Machine and Reservoir Computing

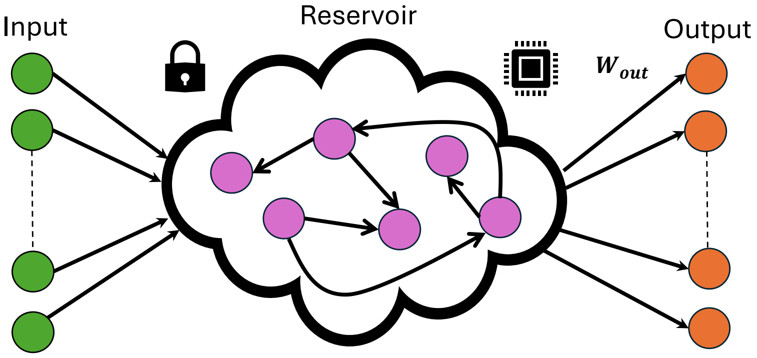

Figure 3.5. Extreme Learning Machine and Reservoir Computing. Schematic representation of the structure of extreme learning machine (ELM) and reservoir computing (RC) ML paradigms. Both of these models leverage upon the employing of a reservoir, that is a fixed and random system, such as a NN with randomly selected internal weights, that is used to connect the input data to the outputs. In particular, the reservoir is not modified during the training and the only parameters of the models are the weights of the output layer W_{out}. The difference between ELM and RC is that only in the second the reservoir has an internal memory, making it suitable for manipulating temporal data.

As we saw, neural network architectures are made of a series of neuron layers, the number of which is in principle arbitrary. This implies that the number of trainable parameters turns out to be incredibly large, especially when considering deep fully connected networks, and so the training cost became demanding in terms of time and energy [230]. To address these problems, the Extreme Learning Machine (ELM) [231, 232] and Reservoir Computing (RC) [233, 234] were formalized. These are computational paradigms that exploit fixed nonlinear dynamics to extract information about a dataset by acting only on the trainable output layer. In this context, the input samples are evolved through some nonlinear map with the objective of enlarging their dimensionality and easing the extraction of the properties of interest. Indeed, it has been shown how enlarging the working space helps simple models to solve tasks that are hard in a lower dimensional space [224].

The central nonlinear map is called in literature *reservoir*, and due to the general definition of the model it can be both a computational model, such as a fixed recurrent neural network, or a physical system [235], increasing in this way the possible implementations of the paradigms. Precisely the characteristics of the reservoir are what differentiate between ELMs and RCs, and in particular the fact that it has or does not have an internal memory. If this is the case the computational model is a RC, conversely it is an ELM. It follows then that only the RC is suitable for temporal data processing [234]. A representation of these models is reported in Fig. 3.5

In particular, an ELM is a supervised machine-learning protocol which, given a labeled training dataset $\{(\mathbf{x}_i, \mathbf{y}_i)\}_{i=1}^{N} \in \mathbb{R}^n \times \mathbb{R}^m$, is asked to find a map $f : \mathbb{R}^n \to \mathbb{R}^m$ connecting each input to the respective label. In particular, the ELM model is a function that for the i-th hidden reservoir neuron has the form:

$$\mathbf{x} \to \beta_i g_i(\mathbf{x}) \tag{3.12}$$

where $g_i(.)$ is the fixed nonlinear function implementing the reservoir dynamics and $\beta_i \in \mathbb{R}^m$ is the vector containing the weights that linearly connect the neuron response to the output layer. During the training, the algorithm optimizes the weights values through the minimization of a loss function, which usually is the Euclidean distance between the target values $\{\mathbf{y}_i\}$ and the predicted one. Taking into consideration a reservoir model with $\tilde{N}$ hidden neurons, we can state the problem in the following vectorial way:

$$\mathbf{H}\beta = \mathbf{Y} \tag{3.13}$$

where we have defined the matrices:

$$H = \begin{pmatrix} g_1(\mathbf{x}_1) & \dots & g_{\tilde{N}}(\mathbf{x}_1) \\ \vdots & \dots & \vdots \\ g_1(\mathbf{x}_N) & \dots & g_{\tilde{N}}(\mathbf{x}_N) \end{pmatrix}_{N\times\tilde{N}}, \quad \beta = \begin{pmatrix} \beta_1 \\ \vdots \\ \beta_{\tilde{N}} \end{pmatrix}_{\tilde{N}\times m} \quad \text{and} \quad \mathbf{Y} = \begin{pmatrix} y_1 \\ \vdots \\ y_N \end{pmatrix}_{N\times m} \tag{3.14}$$

If the number of training samples N is equal to the number of hidden neurons $\tilde{N}$, the $\mathbf{H}$ matrix is square and invertible. Hence, in this case, the problem can be directly solved.

However, in general, we are in a situation in which $\tilde{N} << N$ and so $\mathbf{H}$ is nonsquare and may not exist weights values that exactly resolve Eq. 3.13. In this case, we search for the optimal solution minimizing the Euclidean distance:

$$\min_{\beta} \|\mathbf{H}\beta - \mathbf{Y}\| \tag{3.15}$$

It can be shown that the solution with the minimal value of the squared errors is represented by [231, 232]:

$$\hat{\beta} = \mathbf{H}_{MP}^{-1}\mathbf{Y} \tag{3.16}$$

where $\mathbf{H}_{MP}^{-1}$ is the Moore-Penrose generalized inverse [236, 237]. Hence, the ELM training consists of finding this matrix for all the elements of the training set.

Since it is not interesting for the purpose of the thesis, we will not give a detailed description of the RC training that however can be found in [233, 234]. Instead, an instance of ELM in the quantum domain, namely a Quantum Extreme Learning Machine (QELM), will be described in Section 7.

Part II

Experimental engineering of orbital angular momentum states of light

Chapter 4

Generation of High Dimensional Orbital Angular Momentum Entangled States

In the last years, photonic qudits have emerged as an essential resource for environment-resilient quantum key distribution, quantum simulation, quantum imaging and metrology [21]. Therefore, at the same time, the demand for sources capable of producing single or entangled high dimensional quantum states has also grown. In particular, among the light degrees of freedom, the unbounded nature of the orbital angular momentum [24] has gained attention as a tool in which to encode information, in addition to its various applications both in classical and quantum domain [26].

In Section 2.4, we gave a description of the sources capable of generating single-photon states. In particular, among them, the SPDC process represents a natural candidate for producing entangled qudits. Indeed, when analyzing the spatial structure of the idler and signal photons generated by the spontaneous process in a nonlinear crystal, we observe strong spatial correlations [54]. In particular, when using the transverse basis of LG modes, the produced biphoton state can be described as a high dimensional entangle state in the OAM of the two photons [55–57], where the total angular momentum depends, due to the conservation law, upon the value carried by the input pump beam. Therefore, in our work [59], we studied the produced state from a $\beta-$Barium Borate (BBO) crystal when entering it with several LG modes as a pump. The reconstruction of the generated entangled state is nontrivial since a full quantum state tomography requires a number of measurements that scale quadratically with the dimensionality of the Hilbert space under consideration [1, 58]. Therefore, we proposed and demonstrated an approach inspired by classical digital holography [153, 238, 239]. The latter, exploiting a time-stamping camera (TPX3CAM) capable of detecting single photons, retrieves the biphoton state induced by an arbitrary pump field from an interference image between it and a reference beam. The adopted method allowed us to reach a 3-order of magnitude speed up in the measurement time needed to perform the state reconstruction [59], comparing it with projective measurement approaches. In particular, from a simple measurement, we retrieved information about two-photon states in arbitrary spatial mode bases, observing the conservation of the pump OAM and certifying the produced entangle state in this degree of freedom, which for instance can be used thereafter to perform the desired Quantum Information protocols.

Despite the SPDC sources automatically generating high dimensional OAM entangled states, the process is intrinsically probabilistic and it suffers from a trade-off between the brightness and the purity of the produced single photons. Moreover, we have also to account for multiphoton production which is detrimental to Quantum Information protocols [60, 61]. However, despite the large number of applications, sources that produce single photons carrying OAM deterministically and with high brightness are still under development [240]. In this context, Quantum Dots (QDs) have been recognized as platforms with which to overcome these limitations, and integrated sources based on microring resonators embedded with QDs have been implemented [240]. However, the latter lacks the capability of arbitrary manipulating the spatial structure of the generated photons, being then limited in the OAM modes that it is able to produce. Therefore, in our work [62] we proposed a platform in which by interfacing a commercial QD-based single-photon source [188] with the well-known OAM manipulation technologies, namely the q-plate devices [51, 52], we generated on-demand hybrid *intra*-particle entanglement between the OAM and polarization degree of freedom of a single photon. Additionally, we also used a bulk BS to implement a probabilistic quantum gate to create *inter*-particle entangled states in the OAM of two subsequently emitted single photons.

Some of the results reported in this chapter are included in the following works:

- Alessia Suprano, **Danilo Zia**, Mathias Pont, Taira Giordani, Giovanni Rodari, Mauro Valeri, Bruno Piccirillo, Gonzalo Carvacho, Nicolò Spagnolo, Pascale Senellart, Lorenzo Marrucci, and Fabio Sciarrino, “Orbital angular momentum based intra-and interparticle entangled states generated via a quantum dot source”, *Advanced Photonics*, vol. 5, p. 046008 (2023) [62].
- **Danilo Zia**, Nazanin Dehghan, Alessio D’Errico, Fabio Sciarrino, and Ebrahim Karimi, “Interferometric imaging of amplitude and phase of spatial biphoton states”, *Nature Photonics*, vol. 17, p. 1009 (2023) [59].

4.1 Spatial correlation in Spontaneous Parametric Down Conversion process

In Section 2.4.2 talking about nonlinear processes for photons generation, we introduce the SPDC, using the creation and annihilation operators quantum mechanical description. Specifically, we focused on its employment in the production of heralded single-photon states and entangled pairs in the polarization degree of freedom, describing several types of nonlinear sources. In all these cases, we ignored the description of the spatial profile of the generated photons since, via the coupling to SMF, we selected only the Gaussian component of the state. However, the complete description of the state presents correlations also in the spatial components, and then SPDC sources can be also employed to automatically generate high dimensional entangled states in the OAM degree of freedom. In particular, recalling the general expression reported in Eq. 2.80 for the output of the SPDC process in a nonlinear crystal. If we made the assumptions of short interaction time and thin crystal in the z direction, with transverse x, y dimension capable of containing the whole pump beam, we have that the joint spectral function of the signal (s) and idler (i) photons reads [54]:

$$\phi_{\sigma_i,\sigma_j} \approx C_{\sigma_i,\sigma_j} G_s(\omega_s) G_i(\omega_i) E_p(\mathbf{q}_s + \mathbf{q}_s) \delta(\omega_s + \omega_i - \omega_p) \mathrm{sinc}[(k_{sz} + k_{iz} - k_{pz}) L/2] \tag{4.1}$$

where σ_i, σ_s are the polarization state of the produced photons that depend upon the type of SPDC process implemented, C_{σ_i,σ_s} is a coupling constant which depends on the nonlinear susceptibility, $\{G(w_i), G(w_s)\}$ are the spectral function respectively for the idler and signal photons, $E_p(.)$ is the angular spectrum of the pump beam expressed in the transverse momenta space of $\mathbf{q}_j = (k_{jx}, k_{jy})$, $k_{sz} + k_{iz} - k_{pz}$ is the longitudinal wave vector mismatch and the $\delta(\omega_s + \omega_i - \omega_p)$ is a consequence of the energy conservation in the process. In general, the join spectrum ϕ_{σ_i,σ_j} is not a separable function in the transverse momentum degree of freedom. i.e $\phi_{\sigma_i,\sigma_j}(\mathbf{q}_i, \mathbf{q}_s) \neq F(\mathbf{q}_i)F(\mathbf{q}_s)$, therefore the two photons state present nonlocal and non-classical features.

Moreover, by considering the degenerate case $\omega_i = \omega_s = \omega_p/2$ and a quasi-collinear emission in a crystal thin enough to allow us to ignore the birefringence effect in the transverse momentum components, expressing the longitudinal wavevectors as a function of the transverse ones $k_z \approx k_z - |\mathbf{q}|^2/2k_z$, we have that the state produced by an SPDC process is [54, 241]:

$$|\Psi\rangle_{SPDC} \approx C_v\,|vac\rangle + \mathcal{N} \iint E_p(\mathbf{q}_i + \mathbf{q}_s)\,\mathrm{sinc}(\alpha|\mathbf{q}_i - \mathbf{q}_s|^2 - \zeta)\,|\mathbf{q}_i\rangle_{\sigma_i}\,|\mathbf{q_s}\rangle_{\sigma_s}\; d^2\mathbf{q}_i\, d^2\mathbf{q}_s \tag{4.2}$$

where $|vac\rangle$ is the vacuum state, $\alpha = Lc/4\omega_p$ with L the crystal length and c the speed of light in the medium, ζ is the longitudinal mismatch which depends on the crystal orientation and the sinc(.) contribution is indeed related to the phase-matching condition (see Eq. 2.74).

We recall that the transverse momentum coordinates are equivalent, apart from factors depending on the imaging system, to the far field coordinates with respect to the crystal image plane, where the signal and idler photons are generated. Thus, if $\mathbf{X}$ are the coordinates on the crystal Fourier plane, the SPDC, in the $\mathbf{X}$ coordinate basis, takes the form:

$$|\Psi\rangle = \mathcal{N} \iint E_p(\mathbf{X}_i + \mathbf{X}_s)\,\phi(|\mathbf{X}_i - \mathbf{X}_s|)\,|\mathbf{X}_i\rangle \otimes |\mathbf{X_s}\rangle\; d^2\mathbf{X}_i\, d^2\mathbf{X}_s. \tag{4.3}$$

where $\phi(.)$ is the phase-matching function. Therefore, we can retrieve the biphoton state at each distance by simply computing the spatial propagation of the field. This operation consists of a change of basis from the Fourier plane coordinates eigenstates to the coordinates of the plane of interest:

$$|\mathbf{X}'\rangle := \int F(\mathbf{X}', \mathbf{X}; z)\,|\mathbf{X}\rangle\, d^2\mathbf{X}, \tag{4.4}$$

where F is the free space propagator and z is the distance between the two planes. In the paraxial approximation, F is given by the Fresnel propagator:

$$F(\mathbf{X}', \mathbf{X}; z) \propto \exp(ikz)\exp\left(-i\frac{\pi}{\lambda z}(\mathbf{X}' - \mathbf{X})^2\right). \tag{4.5}$$

Hence, from the distribution in a generic plane, when postselecting the coincidences on correlations (anticorrelations), one can retrieve the propagated pump field (phase matching amplitude). See Appendix B for more details.

A particular case is the one in which we consider the propagation from the far field to the crystal image plane. The Fresnel transform is then replaced by a Fourier transform and the state on the crystal plane is thus:

$$|\Psi\rangle = \mathcal{N} \iint \mathcal{E}_p(\boldsymbol{\rho}_i + \boldsymbol{\rho}_s)\, \Phi(\boldsymbol{\rho}_i - \boldsymbol{\rho}_s)\, |\boldsymbol{\rho}_i\rangle \otimes |\boldsymbol{\rho}_s\rangle \; d^2\boldsymbol{\rho}_i\, d^2\boldsymbol{\rho}_s, \tag{4.6}$$

where $\mathcal{E}_p$ is the field describing the input pump beam on the crystal, and Φ is the 2D Fourier transform of ϕ.

Typically, we are in the so-called *thin crystal approximation* regime, in which $\Phi(.)$ is much narrower than $\mathcal{E}_p(.)$, and the phase-matching function can be then replaced by a delta function. This condition is also recovered when we consider the state of the emitted photons in the near-field of the crystal. This strong correlation can be intuitively understood as the fact that the two photons are born simultaneously from the same pump photon. Therefore, within this approximation, we have that the spatial structure of the biphoton field is described by:

$$|\Psi\rangle = \mathcal{N} \int \mathcal{E}_p(\boldsymbol{\rho})\, |\boldsymbol{\rho}\rangle \otimes |\boldsymbol{\rho}\rangle\, d^2\boldsymbol{\rho} \tag{4.7}$$

Hence, the spatial properties of the pump beam are transferred to the signal and idler photons. And, by opportunity shaping the pump field, it is possible to engineer arbitrary states for the generated photons. In particular, working in the paraxial approximation, we can decompose the produced state in the LG modes basis (see Eq. 2.60):

$$|\Psi\rangle = \sum_{p_i,\ell_i} \sum_{p_s,\ell_s} C^{p_s,\ell_s}_{p_i,\ell_i}\, |p_i, \ell_i\rangle \otimes |p_s, \ell_s\rangle \tag{4.8}$$

where:

$$C^{p_s,\ell_s}_{p_i,\ell_i} = \langle p_i, \ell_i, p_s, \ell_s | \Psi\rangle = \iint \mathcal{E}_p(r,\phi) LG_{p_i,\ell_i}(r,\phi)^* LG_{p_s,\ell_s}(r,\phi)^*\, r dr\, d\phi \tag{4.9}$$

The output state of the SPDC process is thus a high dimensional entangled state in the OAM degree of freedom and the source can be easily used to generate such states. However, in practice, to certify the produced state of Eqs. 4.6-4.8 and exploit its strong correlation in the transverse momentum and position, we have to fully reconstruct its spatial structure. In literature, the most used approach to do so is based on projective techniques [56, 154, 159, 242]. This method has drawbacks for what concerns measurement times since it needs successive measurements on non-orthogonal bases and scales quadratically with the dimension of the state under consideration. Furthermore, for spatial reconstruction, the most employed techniques suffer from signal losses due to diffraction. In our work [59], we proposed an imaging-based procedure capable of overcoming both issues mentioned above while giving us full state reconstruction of the biphoton state emitted by a nonlinear crystal, reaching up to a 3-order of magnitude faster reconstruction. This method will be described in the following Section.

4.1.1 Interferometric imaging for state reconstruction

In our work [59], we focused on the specific problem of reconstructing the quantum state, in the transverse coordinate basis, of two photons emerging from a degenerate SPDC process, that we described in the previous Section (see Eqs. 4.6-4.7). In particular, since it depends upon the input field structure, we demonstrate this technique for pump beams in different spatial modes, aiming to study and retrieve the physical properties of the biphoton state.

Our approach relies on extrapolating the state produced by an arbitrary pump from the interference pattern between the latter and a known reference beam. In particular, by assuming the SPDC state $|\psi_r\rangle$ induced by a Gaussian beam as known and superimposing this state with an unknown biphoton one $|\psi_u\rangle$, we want to reconstruct $|\psi_u\rangle$ from measurements performed on the superposition state $|\Psi_{\text{TOT}}\rangle = |\psi_r\rangle + |\psi_u\rangle$. In particular, studying the coincidence counts $\mathcal{C}(\mathbf{X}_1, \mathbf{X}_2)$ relative to the measurement of the idler photon in the transverse position $\mathbf{X}_1$ and a signal one in $\mathbf{X}_2$, we have that:

$$\begin{aligned}\mathcal{C}(\mathbf{X}_1, \mathbf{X}_2) :=& |\langle \mathbf{X}_1, \mathbf{X}_2 | \Psi_{\text{TOT}}\rangle|^2 = |\psi_r(\mathbf{X}_1, \mathbf{X}_2) + \psi_u(\mathbf{X}_1, \mathbf{X}_2)|^2 = \\ =& |\psi_r(\mathbf{X}_1, \mathbf{X}_2)|^2 + |\psi_u(\mathbf{X}_1, \mathbf{X}_2)|^2 + [\psi_r^*(\mathbf{X}_1, \mathbf{X}_2)\psi_u(\mathbf{X}_1, \mathbf{X}_2) + c.c].\end{aligned} \tag{4.10}$$

where the last term contains the interference between the two fields, and, by exploiting the knowledge on $|\psi\rangle_r$, it can be used to reconstruct the wanted state through a digital holography approach [153, 238, 239]. In particular, when visualizing the coincidence counts spatial distribution, the interference pattern can be retrieved by looking at Sections of the form $\mathcal{C}(\mathbf{X}_i, \mathbf{X}_s)\delta(\mathbf{X}_s \pm \mathbf{X}_i)$. This is showcased in Fig. 4.1 for the simplified case in which we consider only one coordinate per photon. By confronting this filtering with the marginal distribution, we see how the emergence of the interference pattern depends upon the strength of the correlations (parameter α in Fig. 4.1). In general, to have a good contrast, the amplitudes of ψ_r and ψ_u have to be of a similar order. For instance, the phase of an unknown state with strong position correlations would be well resolved if the reference has the same spread of the spatial correlations, while the information hidden in the interference term would be more difficult to retrieve if using a reference state that is spatially uncorrelated or anti-correlated. Interestingly, all these forms of correlations can be observed, in different propagation planes, in the state created in an SPDC source by a pump beam well approximated by a plane wave shining a thin crystal [54]. Indeed, such a state exhibits sharp correlations in the near field, i.e. the image plane of the crystal, and sharp anti-correlations in the far field, while in intermediate propagation planes, one observes a wider correlation pattern. We will use this as the reference beam in our analysis.

In particular, we restricted to consider the simplest case in which both $|\psi_r\rangle$ and $|\psi_u\rangle$ present sharp spatial correlation, as it happens in the degenerate SPDC pair emission by a thin crystal. Here, since the two photons are created in the same transverse position, from the thin crystal approximation the produced state is well described by Eq. 4.7. Therefore, by considering a pump beam in which we superimposed before entering the crystal a known reference state and the unknown one. Since Eq. 4.10 contains relevant contributions only for the case $\mathcal{C}(\mathbf{X}_1, \mathbf{X}_1)$ with $\mathbf{X}_1 = \boldsymbol{\rho}$, we have that:

$$\mathcal{C}(\boldsymbol{\rho}, \boldsymbol{\rho}) = |\mathcal{E}_u(\boldsymbol{\rho}) + \mathcal{E}_{\text{ref}}(\boldsymbol{\rho})|^2. \tag{4.11}$$

Hence, by controlling the reference beam, we can reconstruct the state produced by the other using interferometric techniques that are widely implemented in classical optics for amplitude and phase reconstruction. In particular, in the off-axis digital holography, where the reference beam is a Gaussian beam with a tilted wavefront, that is $\mathcal{E}_{\text{ref}}(x, y) = A\exp(-(x^2 + y^2)/w_r^2)\exp(i2\pi(x + y)/\Lambda)$, one has:

$$|\mathcal{E}_{\text{ref}} + \mathcal{E}_u|^2 = |\mathcal{E}_{\text{ref}}|^2 + |\mathcal{E}_u|^2 + 2Ae^{-\frac{r^2}{w_r^2}}(\mathcal{E}_u e^{-i2\pi\frac{(x+y)}{\Lambda}} + c.c.).$$

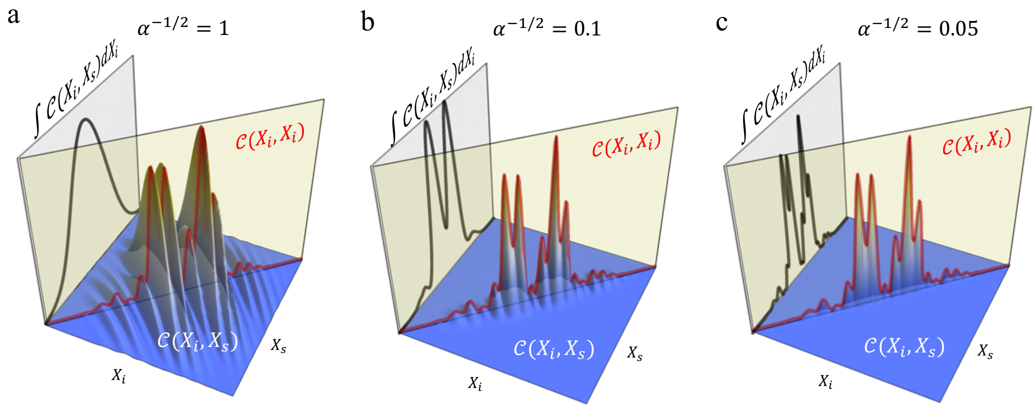

Figure 4.1. Biphoton state holographic reconstruction. Pictorial representations of Eq. (4.10) (in the simplified scenario of a two-dimensional space (X_i, X_s)) for different scenarios in which the biphoton wavefunctions have variable spatial correlations. To mimic typical SPDC states, we modeled the reference biphoton as a product $\psi_r = \exp\big(-\alpha(X_i - X_s)^2\big)\exp\big(-(X_i + X_s)^2/\sigma^2 + ik(X_i + X_s)\big)$ and the unknown wavefunction as $\psi_u = \exp\big(-\alpha(X_i - X_s)^2\big)\exp\big(-(X_i + X_s)^2/\sigma^2\big)h_2((X_i + X_s)/\sigma_2)$, where $h_n(x)$ are Hermite polynomials. The parameter α quantifies how narrow are the diagonal correlations. We show, together with the 3D plot of $\mathcal{C}(X_i, X_s)$, the marginal correlation $\int \mathcal{C}(X_i, X_s)dX_i$ (which corresponds to the coincidence image obtained when no spatial post-selection is performed) and the section $\mathcal{C}(X_i, X_i)$ which can be obtained post-selecting on diagonal correlations. We chose $\sigma = 1$, $\sigma_2 = 0.6$, $k = 2\pi/(0.2\sigma)$, and $\alpha = 1$ (panel a), $\alpha = 100$ (panel b), and $\alpha = 400$ (panel c). In each panel the correlation width $1/\sqrt{\alpha}$ is reported. We see that, in the strong correlation limit (panel c), interference is also retrieved in the marginal distribution.

Therefore, from a spatial Fourier transform one can isolate the contribution of $\mathcal{E}_u$ and retrieve it. Indeed, thanks to the phase term of the tilted Gaussian beam which brings an additional momentum component, the interference term will be displaced from the center of the Fourier space, and thus we can identify it and reconstruct the amplitude and phase of the unknown field knowing the reference one.

4.1.2 Experimental Setup and Results

We experimentally implemented the described approach in the reconstruction of the pairs emitted via SPDC by a Type I crystal of $\beta-$barium borate. Here, employing a Michelson interferometer and placing a SLM in one of its arms, we can easily superimpose a reference tilted Gaussian beam and an arbitrarily shaped pump beam $\mathcal{E}_p$. In particular, The mean transverse momentum $2\pi/\Lambda$ of the Gaussian beam is chosen to maximize the spatial resolution of the reconstructed field and, modulating the amplitude of $\mathcal{E}_p$ (see Section 2.5.2), we choose its waist ω_p to be smaller than the Gaussian one, in this way, we can consider the latter approximately as a plane wave. The produced idler and signal photons are then separated by a beam splitter and sent into different regions of a camera sensor, allowing one to check for coincidences between different pixels. Specifically, we used a time-stamping camera (TPX3CAM) composed of a matrix of 256×256 square pixels, each one with a size of 55 μm per side and temporal resolution of ≈ 1 ns. The experimental setup is schematically reported in Fig. 4.2, where the two regions of the camera are pictorially represented as two different sensors.

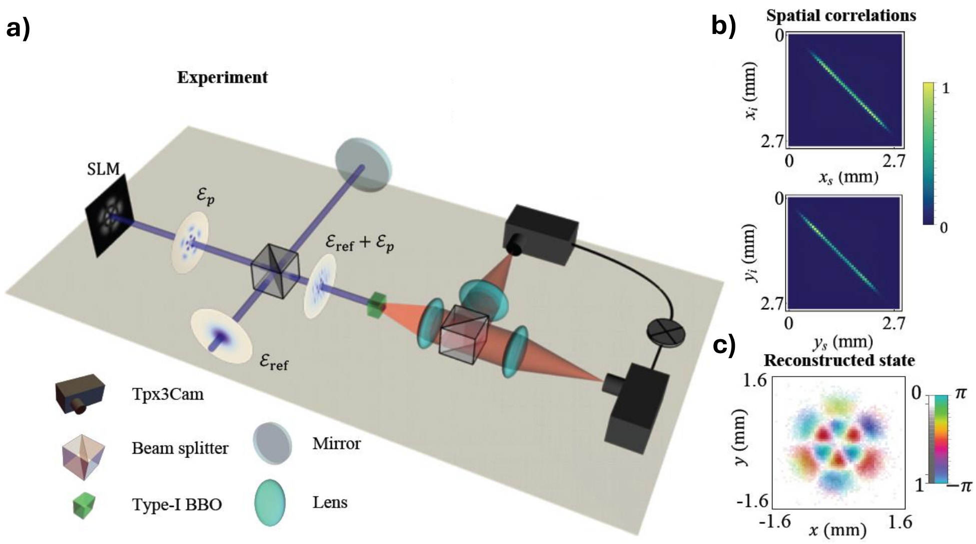

Figure 4.2. Experimental setup and state reconstruction: a) Sketch of the experimental setup: a 405 nm laser in a Gaussian mode ($\mathcal{E}_{\text{ref}}$) enters a Michelson interferometer, where a Spatial Light Modulator (SLM) in one arm is used to shape and generate the unknown pump field ($\mathcal{E}_p$). The interferometer output is the superposition of the reference and unknown pump field, which is then shined on a 0.5-mm-thick Type-I BBO crystal. Photon pairs are consequently generated and, after being separated through the beam splitter, sent on single photon sensor arrays. The experiment was conducted with one camera and the figure is just for illustration. **b)** Experimental correlations in the x and y coordinates obtained by placing the sensors in the image plane of the crystal. **c)** Example of reconstructed phase and amplitude of a biphoton state when pumping the crystal with a superposition of LG modes: $\text{LG}_{1,3} + \text{LG}_{1,-3}$.

In our study, we performed the state measurement on the crystal image plane by imaging it on the TPX3MAC through a system of lenses. In this configuration, the biphoton states respect the thin crystal approximation. Indeed, we verified the correctness of this framework by observing sharp, ≈1-pixel wide, spatial correlations in all the cases under analysis (an example of which is reported in Fig. 4.2-b).

Finally, for each state used as a pump ($\mathcal{E}_p$), we collected data for about 1 minute of exposure of both its interference pattern with the reference beam and the down-converted state produced by it alone. The first one is used to retrieve the phase of $\mathcal{E}_p$, while the second one already gives its amplitude. In particular, the acquired data files report the timestamp at which counts were detected (for more information see Refs. [243–246]). Therefore, using a time window of 5 ns, the coincidence images are obtained by plotting the positions of the counts selected as coincidence in the two regions of the camera. Furthermore, the accidental noise in the acquired data is reduced by removing the counts outside the correlation region. An example of a state reconstructed with our method is reported in Fig. 4.2-c.

In the following, we will describe the implementation of the described method restricting on considering input LG modes in the thin crystal framework. Instead, more details on the results for other spatial modes, a discussion on how to apply the approach in a general case beyond approximations, and a possible implementation for quantum imaging protocols can be found in Appendix B.

Spatial Modes Reconstruction

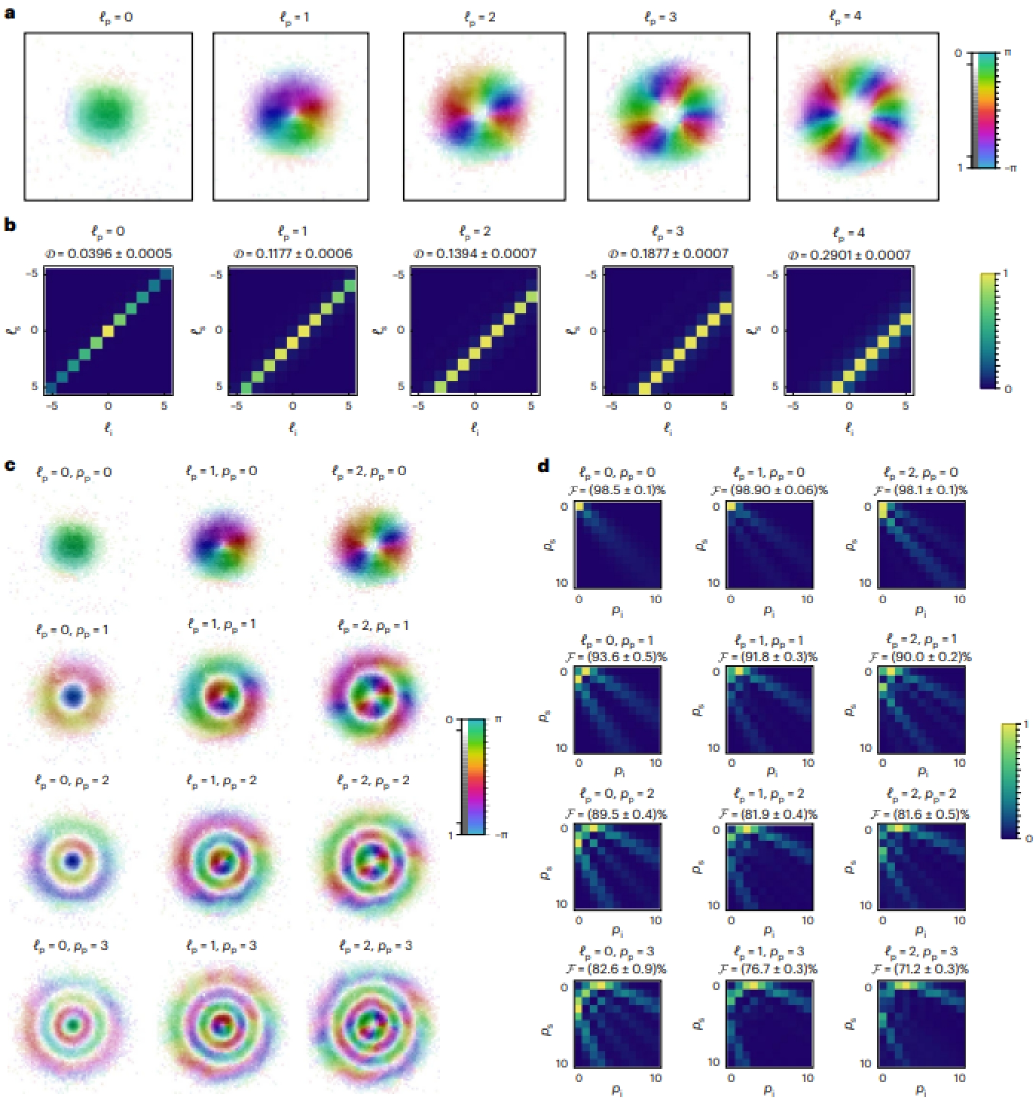

Figure 4.3. OAM and radial correlations in SPDC biphotons. Reconstructed field of the biphoton state for different OAM-carrying pump beams in LG modes. **a)** Shows the amplitude and phase of the state for different values of the pump OAM ℓ_p. **b)** Shows the OAM correlations density plots of generated SPDC photons. It can be seen how increasing the pump OAM, the sum of the OAM values for the idler and signal photons shift in agreement with the conservation law of Eq. (4.12). **c)** Reconstructed biphoton fields obtained by pumping the crystal with LG modes changing the ℓ and p indexes. **d)** Shows the correlations in the radial number p. In all the plots, the OAM of signal and idler has been fixed to $\ell_i = 0, \ell_s = \ell_p$. The fidelities are obtained assuming the theoretical state calculated in the thin crystal approximation. The errors are calculated by considering a Poissonian statistic on the measured counts.

To verify the capability of the SPDC source in producing high dimensional entangled states, we investigated the produced state when the input beam $\mathcal{E}_p$ is an OAM eigenstate. In particular, we enter the crystal with the LG eigenmodes and, exploiting the decomposition in this basis (see Eqs. 4.8-4.9), we started by assessing the OAM conservation law [159]:

$$\ell_p = \ell_i + \ell_s, \tag{4.12}$$

where $\ell_{p,i,s}$ are respectively the OAM values of the pump, idler and signal photons.

In particular, we used the SLM to generate states having azimuthal index $\ell \in \{0, 1, 2, 3, 4\}$ and we studied the probabilities of detection for the azimuthal component given by:

$$P_{\ell_i,\ell_s} = \sum_{p_i,p_s} P^{p_i,p_s}_{\ell_i,\ell_s} = \sum_{p_i,p_s} \left| C^{p_s,\ell_s}_{p_i,\ell_i} \right|^2 \tag{4.13}$$

where we restricted the sums over the radial indexes for $p_{i,s} = 0, \ldots, 10$. The results for the experimentally reconstructed biphoton states and the OAM matrices values of the idler and signal photons are reported in Fig. 4.3-a,b. Where, it can be seen how increasing the OAM carried by the pump causes the OAM correlation to shift according to Eq. 4.12. Moreover, the accuracy in the reconstruction is showcased by the low values of the trace distances between the theoretical and experimental distributions $\mathcal{D} = \sum_{\ell_i,\ell_s} \left| P_{\ell_i,\ell_s} - P^{th}_{\ell_i,\ell_s} \right| /2$, reported over each matrix in the figure.

Then we focus also on the correlation of the generated fields in the radial indexes $p_{i,s}$, related to the number of nodes of the LG modes spatial profile and that can be treated as a quantum number as well [247, 248]. We enter the crystal with several combinations of (ℓ_p, p_p), and we retrieved with our approach the amplitude and phase of the biphoton states, these are reported in Fig. 4.3-c. Using then the decomposition of Eq. 4.8, we proceed by calculating the fidelities and the correlations in the radial indexes. In particular, from the OAM conservation law, we fixed $\ell_i = 0, \ell_s = \ell_p$, and by choosing the waist parameter of the decomposition to be equal to the pump one [249], the correlations are maximized for $p_{i,s} = p_p$, $p_{s,i} = 0$. This is clearly shown in Fig. 4.3-d and can be understood from the integral expression of $C^{p_s,\ell_s}_{p_i,\ell_i}$ and the orthogonality relationship of LG modes. For the fidelities estimation, we reduced always in the space where indices $p_{i,s}$ are bounded from 0 to 10. Here, assuming a pure state production from the nonlinear process, we evaluate $\mathcal{F} = |\sum_{p_i}^{p_s} C^{*p_s,\ell_p}_{p_i,0} C^{th\,p_s,\ell_p}_{p_i,0}|^2$, following Eq. 1.48. Where $C^{*p_s,\ell_p}_{p_i,0}$ are the measured coefficients and $C^{th\,p_s,\ell_p}_{p_i,0}$ are the ones expected from the thin crystal approximation, both of them are obtained after normalizing the state in the reduced subspace. The fidelities of each state are reported upon the corresponding radial indexes correlation matrix in Fig. 4.3. In particular, we observed an average value equal to 87%, with a decrease of the fidelities when the radial and azimuthal indexes of the pump are increased. This is mainly due to imperfect preparation and detection stages, which are limited by the discrete number of pixels of the SLM and of the time-stamping camera, and not to intrinsic limitations of the technique. Moreover, it is worth noticing that even if the fidelities are calculated under the assumption of a pure state, our method retrieves the full biphoton state description enabling the decomposition in arbitrary spatial modes. In particular, this is obtained in a few minutes, outperforming the most commonly used approach in the literature based on projective measurement [56, 154, 159, 242].

In conclusion, we showcase how an SPDC source can be used to directly generate high dimensional entangled OAM states, which for instance can be used to violate high dimensional Bell inequalities as demonstrated in Refs. [56, 57].

4.2 Entangled OAM states generate via a quantum dot source

As mentioned before, despite the SPDC sources automatically producing high-dimension OAM entangled states, their applications are restricted by their probabilistic nature, which affects their brightness and the purity of the emitted photons. To solve both these issues, we decide to investigate the application of a QD source in combination with q-plates devices inside a versatile setup, aiming to produce OAM entangled states in a nearly deterministic fashion. Therefore, in Section 4.2.1 we will describe the employed source, while in Section 4.2.2 we will report the results obtained when studying the production of intra- and inter-particle entangles state in our experimental apparatus.

4.2.1 Characteristics of the quantum dot source

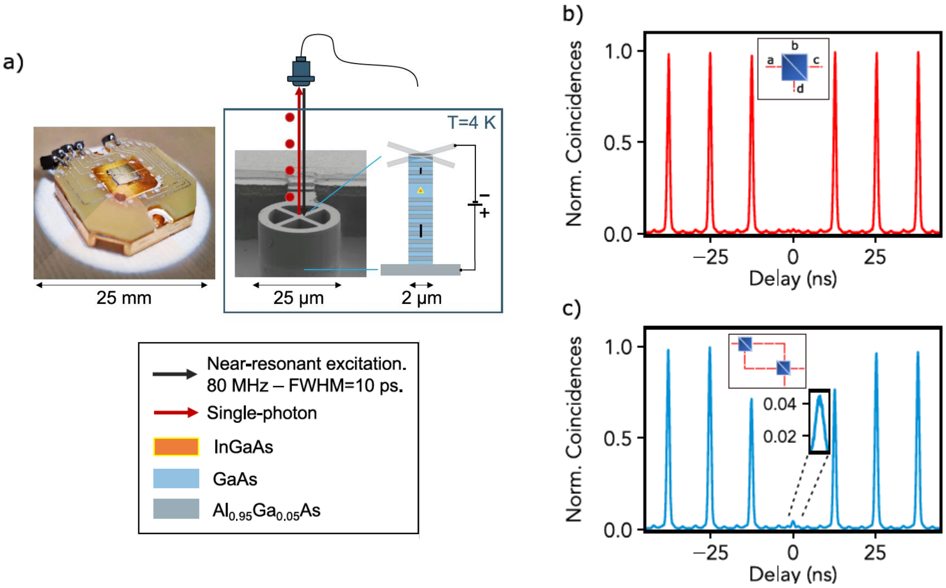

Figure 4.4. Source Hong-Ou-Mandel interference and second-order correlation function. a) The single-photon source (left) is a commercial device (Quandela): InGaAs quantum-dot based bright emitters are embedded in electrically-contacted micropillars (right). The source is pumped with a near-resonant ($\Delta\lambda$=-0.6 nm) pulsed laser, having a full width at half maximum of 10 ps and a repetition rate of 79 MHz. The single photons (red dots) are emitted at a wavelength of 927.8 nm and are directly coupled to a SMF. **b)** Through a standard Hanbury Brown and Twiss setup, we measure the second-order autocorrelation histogram of our QD-based source as a function of the delay. We obtain a single-photon purity of $g^{(2)}(0) = (1.26 \pm 0.05)\%$. **c)** Normalized correlation histogram, obtained via a HOM interference experiment, through which we measure a 2-photon interference fringe visibility between subsequent single photons emitted by the QD source of $V_{HOM} = (93.05 \pm 0.06)\%$. Moreover, following Ref. [250], we obtain an indistinguishability value of $M_s = (95.5 \pm 0.1)\%$.

The single-photon source is a quantum dot based emitter embedded in an electrically controlled cavity on a commercially available *Quandela e-Delight-LA* photonic chip. A single self-assembled InGaAs QD is surrounded by two Braggs reflectors made of GaAs/$Al_{0.95}Ga_{0.05}As$ $\lambda/4$ layers with 36 (16) pairs for the bottom (top) and positioned in the center of a micropillar [163, 188]. The micropillar is connected to a larger circular structure that is electrically contacted enabling the tuning of the emission frequency of the QD via Stark effect. The sample is kept at 4 K in a low-vibration closed-cycle He cryostat *Attocube - Attodry800.* The QD source is pumped with a 79 MHz-pulsed laser shaped with a QShaper (Quandela) 4f pulse shaper to select a specific wavelength and achieve a bandwidth of ∼ 100 pm. The photon generation is obtained using the Longitudinal Acoustic (LA) configuration described in Section 2.4.3. Here, the QD is pumped with a laser having a wavelength of 927.2 nm, that is blue-detuned from the transition energy levels [251], and it enables a single-photon generation by exciton emission at (927.8 ± 0.2)nm (see Figs. 2.9-4.4-a). The emitted photons are directly coupled in SMF, then spectrally separated by the residual pumping laser with a sequence of three bandpass filters (< 0.8nm) in free space and coupled again to a SMF. The effectiveness of the source in producing single photons is estimated through the *first lens brightness*, which gives an indication about the produced signal and is calculated as:

$$\mathcal{B} = \frac{R_{\mathbf{det}}}{R_{\mathbf{exc}}\eta_{\mathbf{det}}\eta_{\mathbf{setup}}} \tag{4.14}$$

where $R_{\mathbf{exc}}$ is the pump frequency, $R_{\mathbf{det}}$ is the single-photon count rate collected at the exit of the chip, $\eta_{\mathbf{det}}$ is the detector efficiency and $\eta_{\mathbf{setup}}$ is the extraction setup efficiency. The latter depends mainly on the coupling efficiency into the SMFs and the spectral separation transmission of the single-photon stream from the pump laser, we estimated it to be $\eta_{\mathbf{setup}} \sim 52\%$. Moreover, the employed APD presents for the working wavelength a detection efficiency $\eta_{\mathbf{det}} \sim 38\%$. Finally, we experimentally measured $R_{\mathbf{det}} = 4$ MHz, resulting therefore in an overall efficiency $\mathcal{B} \sim 26\%$.

To assess the quality of the produced signal, we perform tests on the multi-photon emission of the source and the indistinguishability of the generated single-photon states. In particular, we started by studying the second-order auto-correlation $g^{(2)}(0)$ function, which considering the quantum nature of light is defined as [136]:

$$g^{(2)}(0) = \frac{\langle \hat{n}^2 \rangle - \langle \hat{n} \rangle}{\langle \hat{n} \rangle} \tag{4.15}$$

where $\hat{n}$ is the number operator introduced in Section 2.1. Therefore, for pure single-photon Fock states we theoretically expect to observe a $g^{(2)}(0)$ value equal to 0. We can experimentally measure this value by implementing a Hanbury Brown and Twiss setup, sketched in the inset of Fig. 4.4-b. In particular, it consists of entering one port of a 50 : 50 beam splitter (BS) and observing the coincidences between the signals at the two output ports to retrieve the second-order auto-correlation. Indeed, only in the case in which more than one photon enters the BS it is possible to observe a coincidence from its output. We measured a $g^{(2)}(0) = (1.26 \pm 0.05)\%$, that showcases the quality of the employed source in producing single photons. In particular, this value of the $g^{(2)}(0)$ is computed by normalizing the zero-time delay coincidences to the side peaks coincidences which correspond to the correlations between two consecutive near-resonant excitations (see Fig. 4.4-b).

Therefore, we proceed by studying the indistinguishability of the produced single photon state through an Hong-Ou-Mandel (HOM) interference experiment [252]. The scheme of the experimental setup is reported in the inset of Fig. 4.4-c. Here, the stream of emitted photons is equally split by a BS into two arms and coupled in SMFs, the length of the latter is chosen to delay one of them by ≈12.5 ns, ensuring in this way a temporal overlap between the photons on a second BS. Calling $\{a, b\}$ input modes and $\{c, d\}$ the output ones of the latter, the quantum description of the BS action on the creation and annihilation operators of a field is the following [136]:

$$\begin{pmatrix}\hat{a}\\ \hat{b}\end{pmatrix} = \frac{1}{\sqrt{2}}\begin{pmatrix}1 & 1\\ 1 & -1\end{pmatrix}\begin{pmatrix}\hat{c}\\ \hat{d}\end{pmatrix} \tag{4.16}$$

Therefore, by considering two photons at the two inputs of the BS, the initial state is $\hat{a}^\dagger \hat{b}^\dagger |0,0\rangle$ and the output state results to be:

$$\frac{1}{2}\left(\hat{c}_a^\dagger \hat{c}_b^\dagger + \hat{c}_a^\dagger \hat{d}_b^\dagger - \hat{c}_b^\dagger \hat{d}_a^\dagger - \hat{d}_a^\dagger \hat{d}_b^\dagger\right)|0,0\rangle\,, \tag{4.17}$$

where $|0,0\rangle$ refers to the vacuum in the two output ports of the BS and the subscripts a and b to the field modes at the inputs, thus making explicit from which input mode each output one originates. We say that two photons are indistinguishable if their state, associated with each degree of freedom, is the same from the point of view of the observer. In this case, when the two initial modes a and b are identical, it is not possible for the observer to discriminate which one of the two photons comes out from the two inputs. In other words, the term $\hat{c}_a^\dagger \hat{d}_b^\dagger - \hat{c}_b^\dagger \hat{d}_a^\dagger$ vanishes.

Therefore, when the two generated photons are indistinguishable, we have a bunching effect and no coincidences are revealed between the BS output ports. By collecting the photons with Avalanche Photodiode Detectors (APDs), we evaluate 2-photon interference visibility from the correlation histogram, reported in Fig. 4.4-c, as:

$$V_{HOM} = 1 - 2\frac{C_0}{\langle C\rangle_{t\to\infty}} \tag{4.18}$$

where C_0 are the counts when the two photons are synchronized and $\langle C\rangle_{t\to\infty}$ are the average peak counts for relative temporal delays larger than one repetition rate of the laser. We measure an interference visibility $V_{HOM} = (93.05 \pm 0.06)\%$.

The latter can be further corrected to account for unwanted multi-photon components following the indication reported in Ref. [250], resulting in a final photon indistinguishability equal to $M_s = (95.5 \pm 0.1)\%$.

4.2.2 Experimental platform for generating intra- and interparticle entangled OAM states

After assessing the quality of the photons produced with our source, we implemented a scalable platform in which, by interfacing well-known OAM manipulation devices with the QD source, we can generate entangled *intra*- and *inter*-particle states in the hybrid Hilbert space composed of OAM and polarization. A schematic representation of the experimental setup is reported in Fig. 4.5.

The key element of this system is the exploitation of the q-plate action described in Section 2.5.2, which is capable of coupling the SAM and OAM degrees of freedom of single photons. In particular, the stream of single photons generated by the QD source is preliminary split through a fiber-BS and OAM manipulation is performed separately on the two BS outputs. After entering the setup with a null OAM value due to the coupling into a SMF, we use in each arm a set composed of a PBS, waveplates and a q-plate to independently generate the wanted OAM-encoded single-photon states. Specifically, using a q-plate with topological charge $q = 1$ and recalling is polarization driven action of Eqs. 2.96-2.97, from the input state $|H, 0\rangle$, we are able to engineer arbitrary superpositions of $|L, -2\rangle$ and $|R, 2\rangle$ as given by:

$$|\Phi\rangle = \cos(\theta/2)\,|L, -2\rangle + e^{i\psi}\sin(\theta/2)\,|R, 2\rangle \tag{4.19}$$

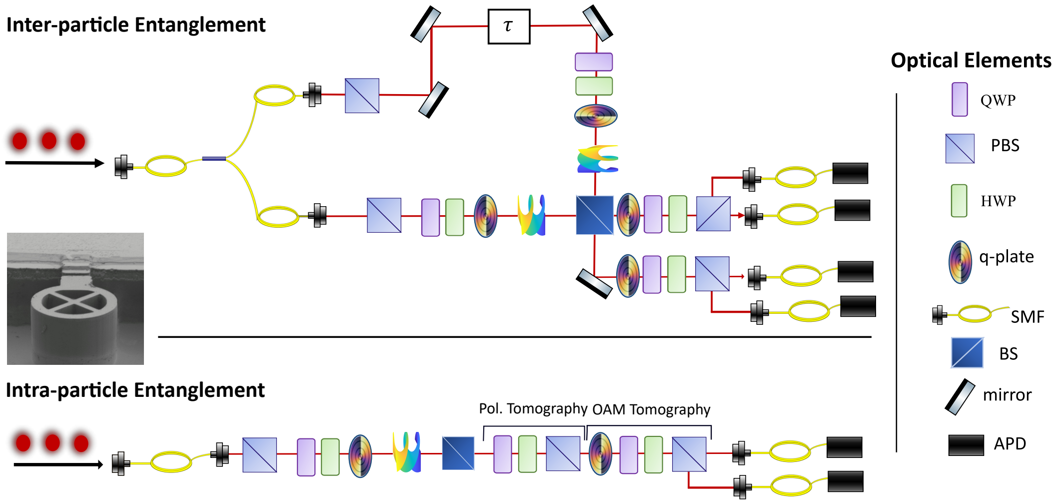

Figure 4.5. Experimental Setup. Single-photon states at a wavelength of 927.8 ± 0.2 nm are generated using a QD source pumped with a shaped 79 MHz-pulsed laser at 927.2 nm. Then a fiber-BS splits the photons between the two arms of the setup, and after passing through a PBS the input states have horizontal polarization and OAM eigenvalue $m = 0$. In both paths, series of QWP, HWP and q-plate are used to produce OAM modes of the form reported in Eq. (4.19), while in one of the arms, a delay line (τ) is inserted in order to synchronize on the BS the photons emitted in different pulses of the pump beam. The *intra*-particle regime is investigated by removing the fiber-BS and performing all the experiment on a single line, involving the first input and output of the BS, as shown in the below panel. On the other hand, in the *inter*-particle experiment, the photons are sent to the fiber-BS and the gate is implemented interfering on the second BS. After passing through the BS the state of the photons is analyzed, coupled to SMFs and detected by APDs. The measurement setup consists of two different stages, a series of q-plate, QWP, HWP and PBS is used to study the OAM states of the photons coupled with the polarization, while a QWP, HWP and a PBS compose the polarization analysis setup. In the *inter*-particle regime only OAM analysis is performed on the photon pairs. While, in the *intra*-particle regime both analysis setups are used to separately investigate the polarization and OAM content of single photons, as shown in the below panel.

where, $\theta \in [0, \pi]$ and $\psi \in [0, 2\pi]$ can be set by properly orienting the optic axes of QWP and HWP.

Therefore, we can easily obtain the intraparticle entangled state between the OAM and polarization degrees of freedom of a single photon on each arm of the setup. Instead, for generating the interparticle entangled one, we synchronized the time of arrival of the two subsequently generated photons on a bulk BS. This is done by inserting in on one arm of the setup both a fixed delay in fiber and a tunable one in air. Then, from the BS action on OAM-carrying photons, we can implement a probabilistic quantum gate that, by postselecting on the measured events, produces the wanted output state.

For both the one and two photons entangled states produced by our platform, we evaluated their entanglement content through a Bell inequality violation (see Appendix A) and assessed their quality by performing a quantum state tomography and estimating their fidelity. In particular, the state reconstruction is performed in each arm by using q-plates and polarization tomography setups comprising a QWP and a HWP followed by a PBS. Indeed, the OAM tomography setup can be simply implemented by adding a q-plate in front of the polarization tomography one to convert the correlations present in the OAM degree of freedom on the polarization space [195].

Intraparticle entanglement

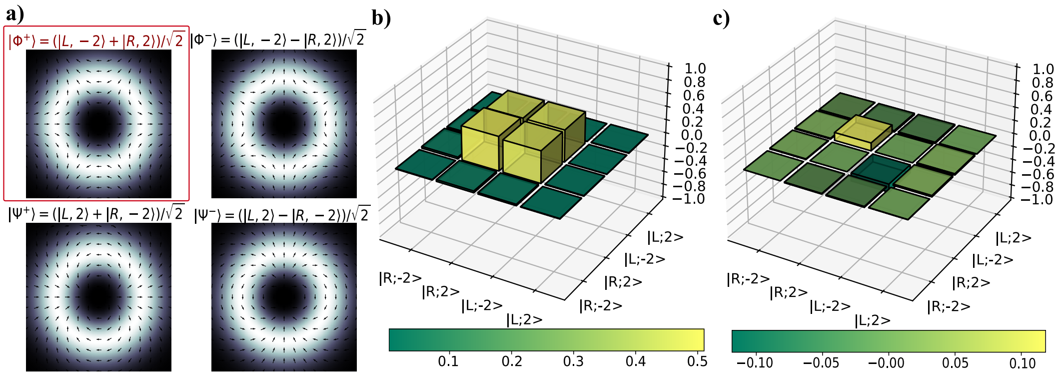

Figure 4.6. ***Intra*-particle entangled state:** a) Intensity and polarization patterns of the Bell states basis in the combined OAM and polarization space. As highlighted by the red box, we focused our attention on the $|\Phi^+\rangle$ state. b) Real and c) imaginary parts of the measured density matrix for the $|\Phi^+\rangle$ state reconstructed via quantum state tomography. The fidelity between the reconstructed state and the theoretical one is equal to $\mathcal{F} = 0.9714 \pm 0.0007$, where the standard deviations are estimated through a Monte Carlo approach assuming Poissonian statistics.

For the intraparticle generation scenario, to increase the production rate, we just consider one arm of the interferometer reported in Fig. 4.5. In particular, the initial fiber-BS is removed and the entangled state is generated along the lower one. By opportunely selecting the waveplates angles and accounting for an additional phase term due to the α_0 of the q-plate with a further HWP (not shown in Fig. 4.5), we generated the state:

$$\left|\Phi^+\right\rangle = \frac{1}{\sqrt{2}}\left[|L,-2\rangle + |R,2\rangle\right] \tag{4.20}$$

In which we can recognize one of the maximally entangled Bell states of Eqs. 1.23, for the OAM-polarization encoding considered here. Although such entanglement structure is not associated with non-local properties since it is encoded in a single carrier, these correlations can be detected using Bell-like inequalities. We refer to such type of quantum correlations as intraparticle entanglement. In particular, the state of Eq. 4.20 belongs to the class of Vector Vortex Beams (VVBs). These are modes presenting a coupling between the polarization degree of freedom and the helical wavefront, which produce the characteristic nonuniform distribution of their polarization state in the transverse plane (see Fig. 4.6-a). A more detailed description of VVBs properties is reported in the following Section 6.2.1.

The quality of the intraparticle entangled state has been certified by performing a quantum state tomography through the measurement stages shown in the below panel of Fig. 4.5. In particular, we analyzed both the OAM and polarization contents of the state independently via a cascaded configuration of setups designed to perform a complete tomography of each degree of freedom. The resulting density matrix is reported in Fig. 4.6 and the relative fidelity, computed by subtracting for dark counts and using the expression reported in Eq. 1.47, is $\mathcal{F} = 0.9714 \pm 0.0007$. Moreover, we also study the entanglement content of the state by evaluating the violation of a CHSH inequality. Collecting data for 20 s with a signal rate of 268 kHz, we obtained raw and dark counts filtered violation of respectively $S^{(raw)} = 2.736 \pm 0.008$

and $S = 2.792 \pm 0.008$, that exceed the separable bound by 92 and 99 standard deviations, respectively.

Interparticle entanglement

In the interparticle scenario, we exploit the interference of two photons on a bulk BS to implement a probabilistic quantum gate capable of generating the wanted entangled state. We have already described how a similar setup can be used to assess the indistinguishability of two emitted single photons through the HOM effect. However, when the photons are characterized by OAM values different from zero and superposed polarizations, it is necessary to take into account the effect of reflections. Indeed, in a physical beam-splitter, the semi-reflective mirror flips the elicity of both OAM and polarization. In other words, after one reflection we have $\{|R\rangle, |L\rangle\} \to \{|L\rangle, |R\rangle\}$ and $|\pm 2\rangle \to |\mp 2\rangle$, while horizontal and vertical polarizations are eigenstates of this operation with eigenvalues of opposite signs. Then, considering the quantum description of the BS action, we have that the creation operators are changed as follows:

$$\begin{aligned}\hat{a}_R^\dagger, \hat{b}_R^\dagger &\longmapsto \tfrac{1}{\sqrt{2}}\left(\hat{c}_R^\dagger - \hat{d}_L^\dagger\right), \ \ \tfrac{1}{\sqrt{2}}\left(\hat{c}_L^\dagger + \hat{d}_R^\dagger\right)\\ \hat{a}_L^\dagger, \hat{b}_L^\dagger &\longmapsto \tfrac{1}{\sqrt{2}}\left(\hat{c}_L^\dagger - \hat{d}_R^\dagger\right), \ \ \tfrac{1}{\sqrt{2}}\left(\hat{c}_R^\dagger + \hat{d}_L^\dagger\right)\\ \hat{a}_m^\dagger, \hat{b}_m^\dagger &\longmapsto \tfrac{1}{\sqrt{2}}\left(\hat{c}_m^\dagger - \hat{d}_{-m}^\dagger\right), \ \ \tfrac{1}{\sqrt{2}}\left(\hat{c}_{-m}^\dagger + \hat{d}_m^\dagger\right). \end{aligned} \tag{4.21}$$

Therefore, we expect no interference when the two photons are prepared as $|R,2\rangle_a |R,2\rangle_b$, since the reflected beam and the transmitted one in the outputs c and d will display orthogonal states. Conversely, the HOM effect will occur when the BS input state is $|R,2\rangle_a |L,-2\rangle_b$. Since the two single photons are emitted by the QD at different times, to observe it we need to use a delay line to synchronize the photons in the temporal domain. The correlation histograms, obtained via a HOM interference experiment, for both input states $|R,2\rangle_a |R,2\rangle_b$ and $|R,2\rangle_a |L,-2\rangle_b$, are reported in Fig. 4.7. The respective estimated visibilities, which gives information about the probability of finding photons on the output ports of the BS, are $V_{|R,2\rangle,|R,2\rangle} = -4 \pm 1\%$ and $V_{|R,2\rangle,|L,-2\rangle} = 90.1 \pm 0.3\%$.

Therefore, after setting the waveplates angles in both the two arms to enter the BS with the input state $|R,2\rangle_a |R,2\rangle_b$, by post-selecting on the two-photon coincidence events we have the following output state:

$$\begin{aligned}|\Phi\rangle &= \frac{|L,-2\rangle_c |R,2\rangle_d + |R,2\rangle_c |L,-2\rangle_d}{\sqrt{2}} = \\ &= \frac{|10\rangle|01\rangle + |01\rangle|10\rangle}{\sqrt{2}},\end{aligned} \tag{4.22}$$

Where we took off the direction subscript $\{c, d\}$ and we identified $|L,-2\rangle = |10\rangle$ and $|R,2\rangle = |01\rangle$. Hence, since we consider only the coincidence events, we generated with probability $p = 1/2$ an entangled state between the four-dimensional qudits defined by the tensor product of the states encoded exploiting the OAM and polarization degrees of freedom. However, in the hybrid OAM-SAM space, this state can be also considered equivalent to a two-dimensional maximally entangled state. Indeed, relabelling the state $|L,-2\rangle$ as qubit $|0\rangle$ and the state $|R,2\rangle$ as qubit $|1\rangle$, the state in Eq. (4.22) results to be equivalent to a triplet Bell state:

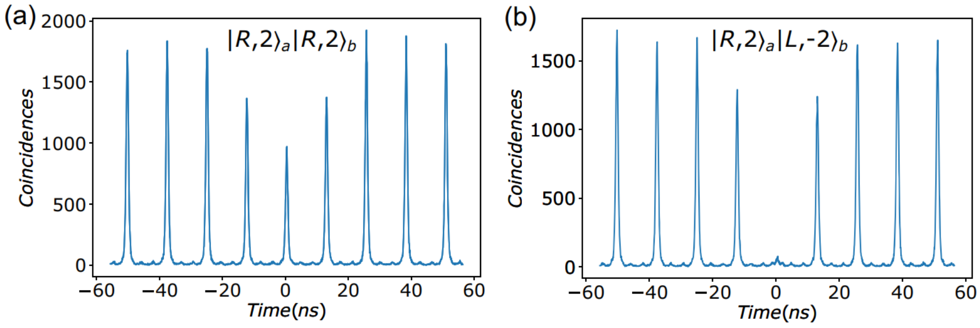

Figure 4.7. Hong-Ou-Mandel interference for OAM states. Measured coincidences at the output of the final BS, see Fig. 4.5, for different input states in the hybrid space of OAM and polarization: **a)**$|R,2\rangle_a\,|R,2\rangle_b$ and **b)** $|R,2\rangle_a\,|L,-2\rangle_b$. A perfect HOM interference can be obtained only when the photon states are indistinguishable from the point of view of the observer. By knowing the BS action on circular polarization and OAM reported in Eqs. 4.21, we observe near-unitary visibility when the photons have opposite circular polarization and OAM values.

$$
\begin{aligned}
|\Phi\rangle &= \frac{|L,-2\rangle_c\,|R,2\rangle_d + |R,2\rangle_c\,|L,-2\rangle_d}{\sqrt{2}} = \\
&= \frac{|0\rangle\,|1\rangle + |1\rangle\,|0\rangle}{\sqrt{2}}
\end{aligned}
\tag{4.23}
$$

Consequently, we can perform a Bell test on it by violating a CHSH-like inequality. In particular, by collecting data for 400 s and with a coincidence rate of 146 Hz, we obtained a raw violation of $S^{(raw)} = 2.516 \pm 0.006$ which exceeds the classical bound by 86 standard deviations. Moreover, we can subtract accidental coincidences due to background noise, obtaining in this way a value of the parameter $S = 2.779 \pm 0.006$, which exceeds the separable bound by 130 standard deviations. Finally, we also performed a quantum state tomography of the state. Specifically, the measurement apparatus selects only the 4-dimensional sub-space $\{|R,2\rangle_1, |L,-2\rangle_1\}\otimes\{|R,2\rangle_2, |L,-2\rangle_2\}$ in which the inter-particle entangled state lives. Indeed, density matrix elements outside this subspace are due to an imperfect conversion from the q-plate, and then their contribution can be kept low and in practice neglected by tuning the δ parameters of the devices towards the π value. Hence, by performing a complete quantum state tomography in this space employing only the OAM tomography setup, after subtracting for accidental coincidences and using the expression of Eq. 1.47, we obtain a fidelity $\mathcal{F} = 0.935 \pm 0.002$. The retrieved density matrix is shown in Fig. 4.8

It is worth noting that the reduction in the coincidence rate for the interparticle with respect to the intraparticle, it is mainly due to the probabilistic nature of the gate and to the experimental losses that has to be consider for both the photons, producing in this way a quadratic decrease. For instance, the coupling efficiency into SMFs in the detection stage, which is of about 45%. This lower value depends on both the limited conversion efficiency of the QPs and on the higher divergence to which beams endowed with orbital angular momentum are subjected. Moreover, at

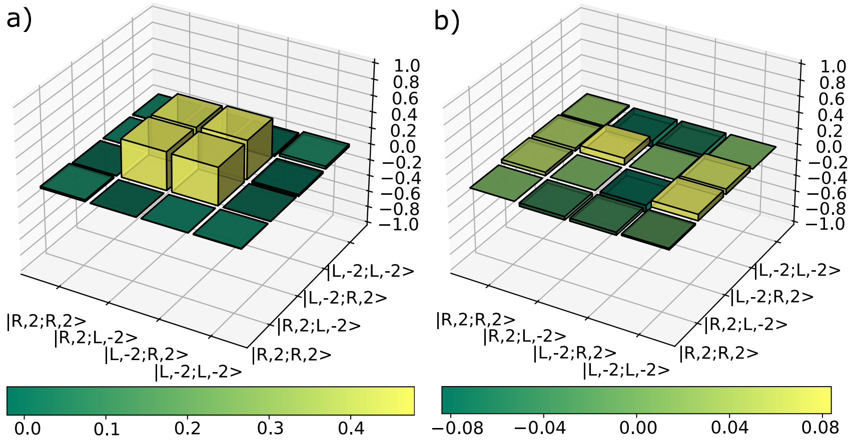

Figure 4.8. ***Inter*-particle entangled state:** Real **a)** and imaginary **b)** parts of the measured density matrix for the two photons state in the hybrid OAM-polarization space reported in Eq. (4.23), these are reconstructed via quantum state tomography. The fidelity between the reconstructed state and the theoretical one is equal to $\mathcal{F} = 0.935 \pm 0.002$, where the standard deviation is estimated through a Monte Carlo approach assuming Poissonian statistics.

the working wavelength the q-plates present transmission of about 75%, introducing in this way additional losses. Therefore, looking toward gates with more than two photons, where the weight of the losses increases exponentially in their number, the rate could be improved by compensating for the beams divergence and adopting experimental devices with higher efficiency. Finally, note that there are some previous examples of HOM experiments with single-photon states carrying OAM [196, 253], but our tests are among the first to be applied to vector beams generated by a deterministic single-photon source.

4.3 Conclusions

In this chapter, we analyzed the generation of high dimensional entangled states in the OAM of single photons. We started our discussion focusing our attention on the SPDC process exploited by nonlinear sources, in which the idler and signal photons present strong correlations in their spatial degrees of freedom. In particular, we investigate the emission of a Type I BBO crystal, verifying its capability of automatically creating OAM entangled states. For this purpose, we proposed a novel reconstruction approach that exploits the coherent superposition of two SPDC states and the possibility of imaging the amplitude of this superposition with a time-stamping camera. Specifically, by forming a coincidence image of the interference between a reference and an arbitrary pump beam, it is possible to retrieve, in postprocessing, a large amount of information about a two-photon spatial state, e.g. correlations in different degrees of freedom, entanglement, and spatial mode decomposition in arbitrary bases. Our method presents several advantages with respect to the projective approaches in terms of measurement times and signal losses that characterize the techniques and devices typically used to implement the projections. Hence, we observed the generated state when entering the crystal with several LG modes, assessing the OAM conservation and performing the reconstruction of high dimensional entangled states with an average fidelity of 87%, showcasing the quality of the produced states.

Since the SPDC process is probabilistic and presents limitations on the efficiency and purity of the emitted single photons, we decided also to investigate the employment of a QD source to produce OAM entangled states in a nearly deterministic fashion. In particular, by combining a bright QD source with q-plates placed in an interferometric configuration, we focused on the generation and analysis of entangled states in the hybrid space composed of orbital angular momentum and polarization. The setup allows us to study both the *intra-* and *inter*-particle entanglement. In particular, for the former, we generated on demand entangled state between the OAM and SAM of the same photon by opportunely modulating its polarization before entering the q-plates. Instead, for the latter, we exploited the interference between modulated single photons generated by the QD in two consecutive excitations to implement a probabilistic quantum gate capable of producing entangled two-photon states. The quality of both the *intra-* and *inter*-entangled states were assessed by performing a full quantum state tomography and through the violation of Bell inequalities in the CHSH fashion. The employed simple and effective scheme could be extended to the multi-photon regime, opening the way to high dimensional multi-photon experiments, whose scalability is extremely demanding for platforms based on probabilistic sources.

Chapter 5

Photonic Orbital Angular Momentum States Engineering Platform

The engineering of high dimensional quantum states is a pivotal task in the Quantum Information field. Indeed, the capability to encode a larger amount of information on a single carrier is beneficial for several applications, for instance enhancing the security of quantum cryptography and communication schemes [8–11] or enabling better-performing quantum error correction [16–18], fault-tolerant quantum computation [19, 20, 35, 36] and quantum machine learning [73–76] schemes. Therefore, this has resulted in an increasing demand over the years for platforms to generate such states. To this aim, several implementations have been proposed and successfully realized using different quantum systems [254–257]. However, in general, such schemes propose *ad-hoc* solutions that are strongly platform-dependent. To overcome this limitation, Innocenti *et al.* in [64] proposed a general scheme based on Discrete-Time Quantum Walks (DTQWs), the quantum counterpart of the classical random walk that we introduced in Sec. 1.2.3. In particular, the proposed protocol exploits the interdependence between the walker and coin states to engineer arbitrary high dimensional quantum states. Indeed, by appropriately selecting the coin parameters at each step, it is possible to completely control the walker evolution and obtain arbitrary states in the coin-walker space. Then, after projecting over the coin state to remove the correlation between the two, it is possible to obtain the desired high dimensional quantum state in the walker Hilbert space. This engineering approach has been proven capable of generating with high fidelity and probability the wanted state both theoretically [64] and experimentally [65].

From the experimental point of view, several platforms have been successfully used to implement the QW dynamics, such as trapped ion [258, 259] and atoms [260] or optical lattices [261]. In this chapter, instead, we will focus on photonic platforms [262–270] and especially the ones based on the OAM of light [37, 65, 70, 271–273]. In the latter, working in the paraxial approximation in which the orbital and spin components of the angular momentum can be controlled independently, we codify the coin and walker states respectively in the bidimensional SAM space and in the OAM degree of freedom. The advantage of this kind of implementation is that the QW evolution proceeds on a line, the one on which the photons propagate, and there is a linear scaling between the reachable dimension of the walker Hilbert space and the number of optical elements used to realize the dynamics. In particular, to couple these two degrees of freedom and perform the shift operation, we will make use of the q-plate introduced in Section 2.5.2.

Although optimal results can be obtained within these engineering platforms, their performance is damped by the presence of experimental imperfections, when they are not correctly characterized. To solve the problem, recently, optimization algorithms and machine learning have found several applications for tasks such as detection and reconstruction of quantum states [274–277], quantum state and gate engineering [207, 209, 278–280], automated engineering of experimental platforms [211, 281] and the study of Bell nonlocality [210, 282]. In particular, we decide to apply a gradient-free algorithm to the OAM-based QW platform with the aim of optimizing the engineering of arbitrary quantum states. We used the *black-box* algorithm RBFopt introduced in Section 3.1.1, that, without being endowed with a description of the experimental setup, acts on the parameters Θ that control the evolution and try to minimize a cost function $C(\Theta)$ that provides an estimation of the produced state quality. Since it has no information on the setup, the algorithm automatically constructs a model that accounts for experimental noises. In conclusion, we showcase how this approach is capable of enhancing the engineering performances of the setup, being robust also under external perturbations on the control parameters [66].

The chapter is divided as follows. We start by introducing the theoretical model of the engineering protocol proposed in [64] and reporting an OAM-based experimental implementation of it (Section 5.1). Then we describe the black-box approach showing the results obtained for the engineering of different target states both in classical and quantum regimes (Section 5.2).

Some of the results reported in this chapter are included in the following works:

- Alessia Suprano, **Danilo Zia**, Emanuele Polino, Taira Giordani, Luca Innocenti, Alessandro Ferraro, Mauro Paternostro, Nicoló Spagnolo, and Fabio Sciarrino,"Dynamical learning of a photonics quantum-state engineering process", *Advanced Photonics*, vol. 3, p. 066002 (2021) [66].

5.1 Engineering protocol and Experimental setup

The theoretical protocol proposed in [64] showed how, with a suitable choice for the coin operators of each step of a DTQW, it is possible to generate an arbitrary state in the total Hilbert space $\mathcal{H}_t = \mathcal{H}_c \otimes \mathcal{H}_w$, where $\mathcal{H}_c$ and $\mathcal{H}_w$ are respectively the coin and walker Hilbert spaces. Let us introduce this method and consider a QW evolution described by the shift operator of the form introduced in Eq. 1.37, where in this case we consider that instead of going to the right or the left, the walker can move only to the right or remain stationary in the same position. The operator then modifies as follows:

$$S = \sum_{k=0}^{N} |k\rangle_w \langle k| \otimes |\uparrow\rangle_c \langle\uparrow| + |k+1\rangle_w \langle k| \otimes |\downarrow\rangle_c \langle\downarrow| \tag{5.1}$$

Given a target state after N steps:

$$|\psi\rangle_N = \sum_{k=0}^{N} \sum_{s=\downarrow,\uparrow} u_{k,s} |k\rangle_w |s\rangle_c = \begin{bmatrix} \sum_k u_{k,\uparrow} |k\rangle_w \\ \sum_k u_{k,\downarrow} |k\rangle_w \end{bmatrix} \tag{5.2}$$

It is useful to define the vector that collects the evolution at the n-th step of the amplitudes characterizing the i-th position of the walker at the previous $(n-1)$-th step:

$$\mathbf{v}_i^{(n)} = \begin{bmatrix} u_{i,\uparrow}^{(n)} \\ u_{i+1,\downarrow}^{(n)} \end{bmatrix} = \mathcal{C}_n \begin{bmatrix} u_{i,\uparrow}^{(n-1)} \\ u_{i,\downarrow}^{(n-1)} \end{bmatrix} \tag{5.3}$$

where $\mathcal{C}_n$ is the coin operator of the step. Using this vector, it is possible to define the condition that each quantum walk state has to respect at the end of the evolution, regardless of the initial state:

$$\begin{aligned} & u_{0,\downarrow}^{(N)} = u_{N,\uparrow}^{(N)} = 0 \\ & \sum_{i=0}^{s} \mathbf{v}_i^{(N)\dagger} \mathbf{v}_{(N-1)-s+i}^{(N)} = 0 \end{aligned} \tag{5.4}$$

for each $s = 0, \ldots, N-2$. These conditions completely characterize the output states of the QW, the first one can be easily derived from the definition of the shift operator, for which the walker moves only when it possesses a specific coin state, while the second one can be obtained by studying step-by-step the evolution of the system. Furthermore, the implication goes both ways, not only does each quantum walk output state have to respect Eqs. 5.4, but also each quantum state $|\Phi\rangle$ that respects these conditions can be written as the results of a QW dynamics. Therefore, there exists a set of coin operators $\{\mathcal{C}_i\}_{i=1}^N$ and an initial state $|\psi\rangle_0$ for which $|\Phi\rangle = |\psi\rangle_N = \prod_{i=1}^N U_i |\psi\rangle_0 = \prod_i^N S \cdot (\mathcal{C}_i \otimes \mathbb{1}_w) |\psi\rangle_0$. For retrieving this evolution, we start by noting that the condition $\mathbf{v}_0^{(N)\dagger}\mathbf{v}_{N-1}^{(N)} = 0$ of Eqs. 5.4 implies the existence of unitary matrix $\mathcal{C}_N$ and complex numbers a, b for which the following applies:

$$\mathbf{v}_0 = \mathcal{C}_N \begin{bmatrix} a \\ 0 \end{bmatrix}, \quad \mathbf{v}_{N-1} = \mathcal{C}_N \begin{bmatrix} 0 \\ b \end{bmatrix} \tag{5.5}$$

The first of the above equations implies that the second row of $\mathcal{C}_N^{-1}$ is orthogonal to $\mathbf{v}_0$, along with the normalization constrain for a unitary matrix, this allows us to retrieve the second column of the matrix $\mathcal{C}_N$ up to a phase. The condition of orthonormality for a unitary matrix allows us to derive also the first column up to a phase. Therefore, neglecting a global phase, we have that:

$$\mathcal{C}_N = \mathcal{N} \begin{bmatrix} u_{0,\uparrow} & -e^{i\alpha} u_{1,\downarrow}^* \\ u_{1,\downarrow} & -e^{i\alpha} u_{0,\uparrow}^* \end{bmatrix} \tag{5.6}$$

where α is the remaining arbitrary phase between the columns and $\mathcal{N}$ in the normalization constant. This coin operator can thus be expressed in the generic representation reported in Eq. 1.38:

$$C(\xi, \zeta, \theta) = \begin{pmatrix} e^{i\xi} \cos\theta & e^{i\zeta} \sin\theta \\ -e^{-i\zeta} \sin\theta & e^{-i\xi} \cos\theta \end{pmatrix}, \tag{5.7}$$

whit $\theta \in [0, \pi/2]$ and $\{\xi, \zeta, \theta\}$ respecting the relations $\tan\theta = |u_{1,\downarrow}|/|u_{0,\uparrow}|$ and $\xi + \zeta \pm \pi = \arg(u_{0,\uparrow}/u_{1,\downarrow})$. Where the freedom in α has been converted in the phase difference $\zeta - \xi$ not being completely determined.

To obtain the operators of the previous steps we move backwardly, using $\mathcal{C}_N$ we can compute the inverse U_N^{-1} and obtain the amplitudes of the vector at the step $N-1$. The latter respect the orthogonality relation as well, then using $\mathbf{v}_0^{(N-1)\dagger}\mathbf{v}_{N-2}^{(N-1)} = 0$

and following the same procedure of before, we retrieve the expression of $\mathcal{C}_{N-1}$. We can proceed with this approach to obtain all the coin operators except for the first one, since it does not respect the orthogonality condition but only the vanishing of the extremal amplitude. However, it can be easily obtained as the operator that maps the initial amplitude $\left\{u_{0,\downarrow}^{(0)}, u_{0,\uparrow}^{(0)}\right\}$ to the two $\left\{u_{1,\downarrow}^{(1)}, u_{0,\uparrow}^{(1)}\right\}$ obtained as the output of the first step.

Rather than considering the full coin+walker space, one could be interested in generating a target qudit state only in the walker degree of freedom. In particular, fixing the number of steps n and a wanted superposition over the sites $|\phi\rangle_w = \sum_{i=0}^{n} u_i\,|i\rangle_w$, we want to find a set of coins operator $\{\mathcal{C}_i\}_{i=1}^{n}$ and a coin state $|\eta\rangle$ such that $|\Phi\rangle_w = \langle\eta|\, U_n \ldots U_1\, |\psi\rangle_0$, up to a normalization factor. For illustrative purposes, we can think of choosing to project over the coin state $|+\rangle = (|\uparrow\rangle + |\downarrow\rangle)/\sqrt{2}$ and exploiting the previous procedure we search for a quantum state $|\Phi\rangle$ in the total space such as $|+\rangle_c \langle +|\Phi\rangle \propto |\phi\rangle_w\, |+\rangle_c$. It is therefore useful to reparametrize the quantum walk output state $|\Phi\rangle$ using the target qudit amplitudes $\{u_i\}$, so, in this specific case $|\Phi\rangle$ has to respect the conditions of Eq. 5.4 and that $N(u_{i,\uparrow} + u_{i,\downarrow}) = u_i$, then we have that:

$$|\Phi\rangle = N\left(u_0\,|0,\uparrow\rangle + u_n\,|n,\downarrow\rangle + \sum_{i=1}^{n-1}\left[(u_i - d_i)\,|i,\uparrow\rangle + u_i\,|i,\downarrow\rangle\right]\right) \tag{5.8}$$

Where $\{d_i\}$ are arbitrary parameters, and it is trivial to see how projection over the $|+\rangle$ state gives the target $|\phi\rangle_w$ independently from the values of these parameters. Therefore, by imposing the constraints 5.4 to the expression of Eq. 5.8, we obtain the following system of $2(n-1)$ equations in $2(n-1)$ variables:

$$\sum_{i=0}^{s}(u_i - d_i)^*(u_{(N-1)-s+i} - d_{(N-1)-s+i}) + d_{i+1}^* d_{(N-1)-s+i+1} = 0 \tag{5.9}$$

For $s = 0, \ldots, n-2$, where $d_1 = 0$ and $d_n = u_n$. Therefore, by solving the system of Eqs. 5.9, we can find the parameters $\{d_i\}$ of the total state $|\Phi\rangle$ and by using the previous approach we can obtain the coin operators $\{\mathcal{C}_i\}$ of the QW evolution.

It is worth noticing that, due to the coin projection over the state $|+\rangle$, even if the target state can be produced with unitary fidelity, the qudit engineering process is intrinsically probabilistic. Therefore, it is important to ensure that the generation probabilities are not vanishing small. Indeed, the system of Eqs. 5.9 admits a different number of distinct solutions for different target states and number of steps, therefore, after solving the system, we can choose the ones with higher projection probability. As pointed out in [64], the system can be easily solved for a few steps of the quantum walk, while numerical approaches are used when this number increases. Anyway, it has been theoretically [64] and experimentally [65] proven how it is possible to find coin parameters able to generate arbitrary target states with both high probabilities and fidelities.

Regarding the experimental platforms, the QW dynamics can be reproduced using several architectures [258–261]. We will focus on the photonic ones [37, 65, 70, 262–271, 283], these have the benefits that permit to work at room temperature with simple optical elements and, since the photons hardly interact with the environment, the system is nearly decoherence-free. Our engineering implementation exploits the two components of the angular momentum of light to encode both coin and walker states. In particular, living in a bidimensional Hilbert space the SAM, i.e. the polarization, is used to codify the coin state, while the unbounded nature of the OAM makes it suitable to encode the walker position state. As shown, the QW dynamics is completely controlled by the coin operators, which in our platform are equivalent to arbitrary polarization transformations, so they are implemented using two QWP interspaced with a HWP [191]. On the other hand, the q-plate action in the SAM-OAM space, reported in Eqs. 2.96-2.97, makes it a natural candidate for implementing the shift operator. Indeed, for a tuned q-plate ($\delta = \pi$) with topological charge $q = 1/2$ we have that :

$$\hat{QP}_\pi = \sum_m e^{2i\alpha_0} \left|R, m+1\right\rangle\!\left\langle L, m\right| + e^{-2i\alpha_0} \left|L, m-1\right\rangle\!\left\langle R, m\right| \tag{5.10}$$

where m is the eigenvalue of the OAM. The expression is equivalent to the shift action of Eq. 1.37 except for the phase factors $e^{\pm 2i\alpha_0}$ and an additional reversal of the polarization state, both of which can be compensated for by the waveplates present in the coin operators.

We performed the engineering protocol both in classical and quantum regimes. In the first case, we use a laser source (CNI laser PSU-III-FDA) to generate classical coherent states at a wavelength of 808 nm, while single photons at the same wavelength are produced by a Type II collinear SPDC process through a PPKTP nonlinear crystal placed in a Sagnac interferometer (see Section 2.4.1 for more details). The latter produces a pair of photons of which one is used as a trigger, while the second is coupled to a SMF and sent to the QW setup. Finally, we consider as success events only the two-fold coincidences between these photons.

Before entering the setup, a PBS selects only the horizontal polarization, thus the initial state of the engineering protocol is $\left|\psi\right\rangle_0 = \left|0\right\rangle_w \otimes \left|+\right\rangle_c$, since the SMF transports only the Gaussian fundamental mode ($m = 0$) and in the circular basis $\left|H\right\rangle = (1/\sqrt{2})[\left|R\right\rangle + \left|L\right\rangle] = \left|+\right\rangle$. Following the theoretical procedure for obtaining the desired qudit, at the end of the platform, a set composed of a QWP, a HWP, and a PBS performs a further projection over the polarization state $\left|\eta\right\rangle_c$. The output walker state is finally analyzed by a SLM followed by the coupling to a SMF. These estimate the quality of the produced state by computing the fidelity with the desired state. Indeed, since the SLM modulates the beam shape through computer-generated holograms, the operation of this measurement station is equivalent to a projective measurement on the state encoded in the employed hologram (see Section 2.5.2). Thus, displaying on the SLM the hologram corresponding to each element of an orthonormal basis, we can characterize the state of the photons that pass through the device. A scheme of the experimental setup is reported in Fig. 5.1-a. As can be seen, the implementation of the QW dynamics using the angular momentum of light has the advantage of allowing us to perform the whole evolution on a line without the need for interferometric schemes, used in other architectures. Thus, avoiding a nonlinear growth of the optical path and elements and resulting in a scalable and stable platform

5.2 Black box approach to OAM engineering

As demonstrated in the previous Sections, the QW dynamics has proven to be a suitable tool for the engineering of arbitrary quantum states independently from the specific platform used to implement it. However, in practical scenarios, such an approach still requires a full knowledge of the inner workings of the underlying experimental apparatus. This feature makes it harder to flexibly adapt this protocol to the perturbations arising in realistic conditions, due to the presence of both uncontrolled experimental noises and temporal changes in the setup. To solve this

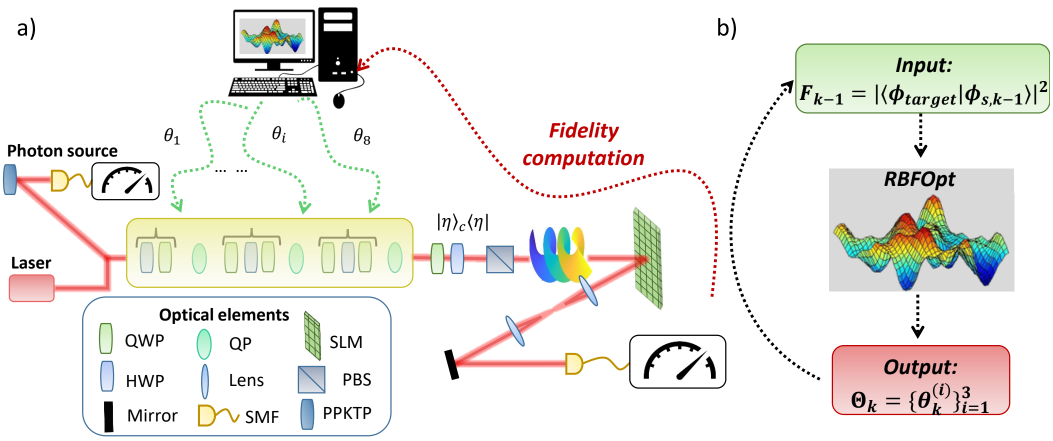

Figure 5.1. Black box engineering experimental apparatus. a) The engineering protocol has been tested experimentally in a three-step discrete-time QW encoded in angular momentum of light with both single-photon inputs and classical continuous wave laser light (CNI laser PSU-III-FDA) with a wavelength of 808 nm. The single photon states are generated through a Type-II spontaneous parametric down-conversion process in a PPKTP crystal (see Section 2.4.1). The input state is characterized by a horizontal polarization and OAM eigenvalue $m = 0$. Each step of the QW is made by a coin operator, implemented through a set of waveplates (QWP-HWP-QWP), and the shift operator, realized by a q-plate (QP). To obtain the desired state in the OAM space a suitable projection in the polarization space is performed through a quarter-waveplate, a half-waveplate and a polarizing beam-splitter. The measurement station of the OAM state is composed of a SLM followed by a single-mode fiber and the coupled signal is measured through a power meter, in the classical regime, or an APD, in the quantum one. In particular, in quantum optimizations pairs of photons are generated and heralded detection is performed by computing the two-fold coincidences between the detectors clicks from the QW-evolved photon and the trigger one. The RBFOpt ignores the features of the experimental implementation that it is seen as a black box. The algorithm has access only to the Θ parameters of the coin operators and to the computed fidelity. **b)** During the iterations of the algorithm, the RBFOpt samples the black-box function to construct a surrogate model that is employed in the optimization. In the k-th iteration, the algorithm receives as input the fidelity computed in the previous iteration and uses it to improve the surrogate modeling. Moreover, the new parameters Θ_k are computed based on the optimization process (see Section 3.1.1). This procedure is repeated for each iteration of the algorithm.

common problem, optimization algorithms have been increasingly used for tasks such as the detection of qudits states [274] and quantum state engineering [275, 278]. In particular, *black box* approaches are especially suited to accomplish the task, since they don't need to be imbued with a detailed description of the experimental setup. In this context, we decide to apply an open-source gradient-free optimization algorithm called RBFOpt [213, 214] (see Section 3.1.1) to improve the engineering performance of the setup and automatically account for experimental imperfections. Indeed, RBFOpt is a black box optimization algorithm based on the radial basis functions method [284–286], that is designed to approximate and find the minimum of unknown and arbitrary *cost function* $C(\Theta)$ by controlling the real parameters $\{\Theta\}$ and having access only to the values that the function assumes, after choosing a set of them. As shown in [213, 214], RBFOpt is particularly suited to optimize problems with few parameters, with a focus on operating regimes where only a small number of function evaluations is allowed. This is fully apt to our scenario, where function evaluations involve the generation and measurement of photonic states and are thus relatively costly.

Considering the general quantum state engineering scenario that can be modeled with a parametrized unitary operation $U(\Theta)$, for some set of real parameters $\Theta \in \mathbb{R}^N$. Given a pair of initial and target states $|\phi_{\text{in}}\rangle$ and $|\phi_{\text{target}}\rangle$, the state engineering task consists of finding values $\Theta^\star \in \mathbb{R}^N$ such that $U(\Theta^\star)\,|\phi_{in}\rangle = |\phi_{target}\rangle$. In our implementation, the evolution $U(\Theta)$ is represented by a 3-step discrete-time quantum walk (see Fig. 5.1) and the cost function that the RBFOpt algorithm has to minimize is the infidelity $C(\Theta) \equiv 1 - F(\Theta)$, where $F(\Theta) \equiv |\,\langle\phi_{\text{target}}|\,U(\Theta)|\phi_{\text{in}}\rangle|^2$ is the fidelity between the theoretical target states and the experimental state produced by the setup. To solve the task, the parameters on which the algorithm acts are the orientation angles of the waveplates that govern the evolution, while the q-plate action is kept fixed with a tuning value $\delta = \pi$. Therefore, the coin and shift operators are defined as follows:

$$
\begin{aligned}
\hat{C}(\boldsymbol{\theta}) &= \begin{pmatrix} e^{-i\beta}\cos\eta & (\cos\mu + i\sin\mu)\sin\eta \\ (-\cos\mu + i\sin\mu)\sin\eta & e^{i\beta}\cos\eta \end{pmatrix}, \\
\hat{S} &= \sum_k |k-1\rangle\langle k|_w \otimes |{\downarrow}\rangle\langle{\uparrow}|_c + |k+1\rangle\langle k|_w \otimes |{\uparrow}\rangle\langle{\downarrow}|_c
\end{aligned}
\tag{5.11}
$$

where $\beta \equiv \theta_1 - \theta_3$, $\eta \equiv \theta_1 - 2\theta_2 + \theta_3$, $\mu \equiv \theta_1 + \theta_3$, and $\boldsymbol{\theta} \equiv (\theta_1, \theta_2, \theta_3)$ are the control parameters tuned by the algorithm, i.e the waveplates angles. This parametrization arises from the sequence of three polarization waveplates used to implement each coin operation. The case in which there are only two waveplates, as in the first step (see Fig. 5.1-a), it is simply obtained from this putting $\theta_1 = 0$, and optimizing the values of θ_2 and θ_3. Denoting with $\boldsymbol{\theta}^{(i)} \equiv (\theta_1^{(i)}, \theta_2^{(i)}, \theta_3^{(i)})$ the free parameters characterising the coin operation at the i-th step, the full set of parameters characterising an n-step QW dynamics is then $\Theta = (\boldsymbol{\theta}^{(1)}, ..., \boldsymbol{\theta}^{(n)}) \in \mathbb{R}^{3n}$. In our specific case, since in the first iteration only two free parameters are used, we have a total of 8 control parameters: $\Theta = (\boldsymbol{\theta}^{(i)})_{i=1}^3$ with $\boldsymbol{\theta}^{(1)} \equiv (0, \theta_2^{(1)}, \theta_3^{(1)})$.

Therefore, at each step of the optimization, the algorithm selects the parameters following the strategy depicted in Section 3.1.1 and rotates the angles of the waveplates, without knowing how this is modifying the evolution. Then, in the measurement stage, an estimation of the fidelity is made and its value is given as feedback to the algorithm, which uses it to update the surrogate model that approximates the engineering protocol function $U(\Theta)$. This procedure is repeated at each step of the optimization (see Fig. 5.1-b).

The experimental demonstration of the black-box optimized engineering is performed in both classical and quantum regimes, and the equivalence is verified. Moreover, to check the adaptability of the optimization protocol, we analyzed the performances of the approach also when sudden changes, due to possible external perturbations, are applied on the controlled parameters Θ. We started by studying the performances in a simulated environment, introducing errors that reproduce the ones most likely observed in the experimental implementations (Section 5.2.1). Then we moved to the experimental realization of the protocol, the results are reported in Section 5.2.2.

5.2.1 Theoretical Simulations

In order to study the effects of noise on the RBFOpt algorithm and its feasibility in engineering target quantum states, we apply it to numerically simulated data reproducing the most likely sources of noise in our experimental apparatus. We study, in particular, the effects of Binomial and Poissonian fluctuations on the cost function used by the algorithm, reproducing in this way respectively the effects of finite statistics and laser oscillation.

Hence, we simulated the experimental calculation of the fidelity for a given target state by constructing an orthonormal basis $\{|\psi_j\rangle\}_{j=1}^{d}$, where d is the dimension of the target state and $|\psi_1\rangle = |\phi_{\text{target}}\rangle$, through the Gram-Schmidt algorithm. This approach of estimating the cost function is used to simulate the experimental statistics collection process. In particular, the number of counts associated with each basis element is extracted from a Binomial distribution $(\mathcal{B}(N,p))$, where N is extracted from a Poissonian distribution $(\mathcal{P}(\lambda))$ with a parameter $\lambda = 10^4$, while the probability p is equal to the fidelity between the state proposed by the algorithm, in the k-th iteration, and the specific element of the basis. Therefore, Poissonian fluctuations are introduced to take into account laser oscillations, while Binomial fluctuations reflect the probabilistic nature of the measurement setup. The noisy fidelity between the proposed state and the target state is then calculated as the ratio between the counts for the element $|\psi_1\rangle$ and the total number of counts, and then by calculating the probability distribution and using the fidelity formulation of Eq. 1.46. This value is given as feedback to the algorithm for its action on the parameters of the setup.

Before applying the algorithm, we made a preliminary comparative study. In particular, to validate the choice of the RBFOpt algorithm, we compared it with two basic gradient-free methods suitable for multi-parameters black-box optimization. We consider both non-adaptive and adaptive approaches. Regarding the first class, among the simplest, there is the Random Search method. As suggested by the name, in each iteration of the optimization process the parameters are randomly extracted with a uniform distribution in the parameter space and independently from values assumed in previous steps. The second comparative algorithm is among the simplest gradient-free adaptive methods, it is known as the Powell method [287]. It attempts to find the local minimum nearest to the starting point. Initially, a set of directions is defined and the algorithm moves along one of them until a minimum is reached. This minimum becomes the uploaded starting point for the following minimization performed in the second direction. After repeating this procedure for each direction, a new direction is defined and the algorithm proceeds to upload the set of directions. We apply all these optimization protocols to 10 random four-dimensional target states, repeating the optimization 10 times for each state. The trends corresponding to each compared algorithm obtained averaging over the 10 distinct states are reported in 5.2-a. As expected, both adaptive approaches are advantageous compared to the random one for a considerable number of function evaluations. Moreover, since the RBFOpt spans the whole parameter space through the global steps, its performances are substantially better. In particular, in Fig. 5.2-b it is reported in detail the behavior of the RBFOpt algorithm, in which after 1000 iterations the maximum value, that is the minimum for the cost function, for the fidelity $F = 0.994 \pm 0.002$ is reached. This in combination with the obtained trend demonstrates that, also in noisy conditions, the algorithm manages to minimize the function, and promising results are obtained.

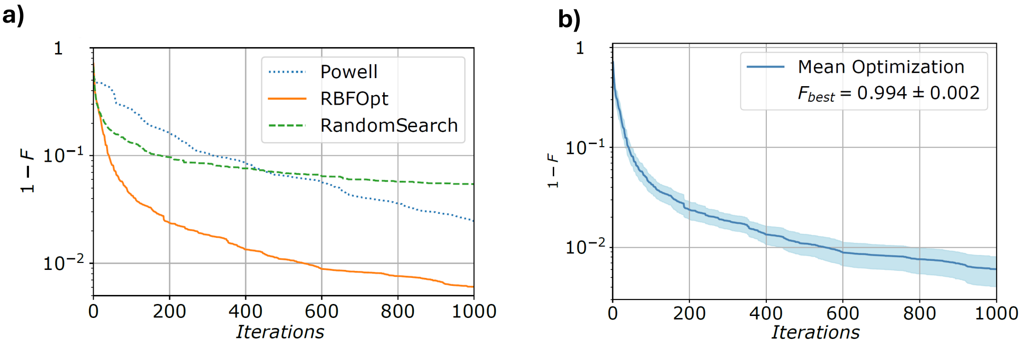

Figure 5.2. Simulated Results. **a)** Comparison between different optimization algorithms: The plot reports the simulated performances of the three different algorithms averaged over the optimization of 10 different states each of which is repeated 10 times. Dotted blue, dashed green, and continuous orange lines report the trends corresponding to Powell, Random Search, and RBFOpt, respectively. RBFOpt is found to perform significantly better than the alternatives in most cases. b) Details of the RBFOpt performance on simulated data. The infidelity $1 - F$ obtained at each iteration of the optimization is reported. The highest average fidelity obtained is 0.994 ± 0.002. The shaded area represents the standard deviation of the mean. All curves are generated by simulating experimental noise with both Poissonian ($\lambda = 10^4$) and Binomial fluctuations.

Moreover, we also investigate the scalability of the proposed approach when the number of parameters increases. In particular, we simulated different experimental configurations with quantum walk steps ranging from 3 to 17 and thus considered up to 50 parameters. Indeed, being N_{steps} the number of steps and considering only two waveplates in the first coin, the number of parameters N_{par} follows the relation:

$$N_{par} = 3\ N_{steps} - 1 \tag{5.12}$$

For each case, we generated at random 50 target states and investigated the optimization procedure stopping the process when a fidelity of at least 98% was reached. In all the evolutions, we added the same Poissonian and Binomial noises described before.

The computational cost of performing a black-box optimization in high dimensional spaces can be extracted by analyzing how the mean number of iterations changes with the number of parameters. The values obtained averaging over the 50 states considered in our study are reported in Fig. 5.3 for each simulated configuration. As can be seen from the plot, the RBFOpt algorithm appears to have a linear scaling over the number of parameters when applied to our implementation. This theoretically showcases the effectiveness of the proposed approach for the engineering of higher dimensional OAM states and similar behaviors are expected experimentally taking into account the device response time and adapting properly to the related implementation.

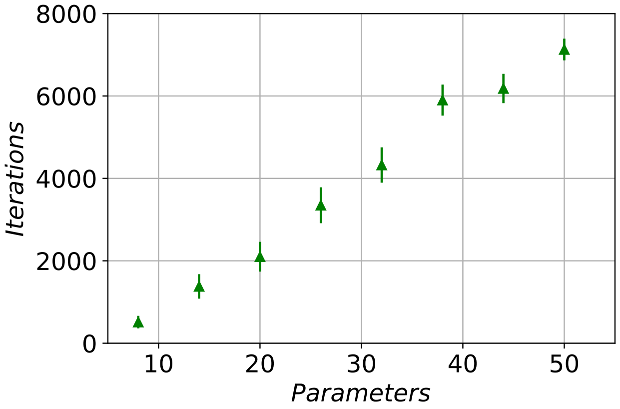

Figure 5.3. Scalability: The plot shows the mean number of RBFOpt algorithm iterations as a function of the black-box problem parameters. Here, the optimization process is interrupted when a value of the fidelity between the target state and the one proposed by the algorithm of at least 98% is reached. For each configuration, the iteration values are obtained averaging over 50 random target states and simulating experimental noise using Binomial and Poissonian distributions. The uncertainty associated with each point is provided by the standard deviation of the mean.

5.2.2 Experimental results

We experimentally applied the optimization protocol to the 3-step discrete-time quantum walk platform described in Section 5.1 and reported in Fig. 5.1. The computed fidelities are then fed to the RBFOpt algorithm to tune the waveplate parameters Θ. To achieve this, the algorithm does not require knowledge on the final target state or the generation and measurement functioning, as shown in Fig. 5.1-b. However, since the algorithm has no control over the measurement station, the parameters of the latter have been fine-tuned a priori and we are confident of the correctness of this step, thus we consider this stage a trusted device. Therefore, through dynamic control of the waveplates orientation, the algorithm is able to optimize the fidelity value in real-time.

To showcase the efficiency of the protocol on our experimental platform, we applied it to engineer different kinds of target states in both classical and quantum regimes. In particular, we start by focusing our analysis on the elements of the computational basis $|m\rangle$ with $m \in \{-1, 1, -3, 3\}$ and on the balanced superposition of two OAM values. We considered both real $SR_{m_1}^{m_2} = [|m_1\rangle - |m_2\rangle]/\sqrt{2}$ and complex superpositions $SC_{m_1}^{m_2} = [|m_1\rangle - i|m_2\rangle]/\sqrt{2}$, where $m_1, m_2 \in \{-1, 1, -3, 3\}$ with $|m_1| = |m_2|$. Moreover, to verify the efficiency of the protocol we optimize the engineering of a randomly extracted state (R) in the four-dimensional Hilbert space with no zero coefficients corresponding to each basis element.

The average trend of the infidelity $1 - F$ for these states is reported in Fig. 5.4-a. As can be seen, optimal average values are obtained in 600 algorithm iterations and the minimization values are in accordance with the simulated results reported in Section 5.2.1, reaching as maximum value for the fidelity $F = 0.983 \pm 0.004$. Moreover, in Fig. 5.4-b we report, for each engineered state, the ratio between the fidelities found by the RBFOpt algorithm, and those obtained using the theoretical method presented in [64] (see Section 5.1) to find the optimal values of the coins operators parameters. As can be seen, the ratio is always higher than one, and thus the fidelities reached by the RBFOpt algorithm are always higher than the ones computed using the direct method of Ref. [64]. This is due to the dynamical learning algorithm we employ, which working in a black-box fashion automatically compensates for experimental imperfections, such as errors in the calibration of the waveplates angles. Thus showcasing the benefits brought by the implementation of gradient-free optimization algorithms for quantum state engineering in realistic scenarios.

Notably, we extended the experimental demonstration of the protocol also in the quantum regime of single photon states. We performed 5 times the optimized engineering of the superposition state SR_1^{-1}, considering only 100 iterations. In Fig. 5.4-c we reported the average behavior for both the raw data and the one obtained after subtracting for the accidental counting of the detectors, and we compare them with the results acquired in the classical scenario. As evident, the two curves are between the worst and the best results of the classical case, the yellow area in Fig. 5.4-c, and thus are compatible with the optimization performed in this regime. The corresponding mean fidelities in the quantum regime are $F = 0.972 \pm 0.003$ and $F = 0.989 \pm 0.003$, respectively. In conclusion, since very high fidelities are reached in only 100 steps, the proposed approach can be efficiently applied to quantum situations.

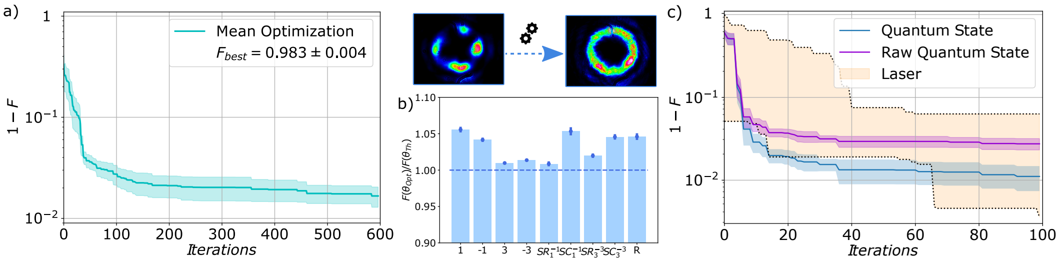

Figure 5.4. Experimental Results. a) Minimization of the quantity $1 - F$ averaged over the algorithm performances for different experimental states. The mean maximum value reached is 0.983 ± 0.004. **b)** Ratio between the maximum experimental values of the fidelities resulted after the optimization $F(\Theta_{Opt})$ and the fidelities measured with the theoretical parameters $F(\Theta_{Th})$. For each engineered state, the ratio is higher or compatible with the value 1 highlighted by the dashed line. This confirms that the adopted algorithm can reach performances compatible or even superior with respect to the one obtained with the direct method presented in Ref. [64] that consider ideal experimental platforms. In this sense, the algorithm can take into account and compensate for the experimental imperfections. All the error bars reported are due to laser fluctuations affecting each measurement and are estimated through a Monte Carlo approach. **c)** Comparison between the performances reached in 100 iterations using classical or single photon input states. In yellow is reported the area between the best and worst optimization performed in the classical case. The blue and violet curves are associated with the minimization of the quantity $1 - F$ averaged over 5 different optimizations for the state SR_1^{-1} engineered in the quantum domain. In particular, the raw data are shown in violet, while in blue we report the data after accidental counts subtraction.

Uncontrolled perturbations are always present in realistic conditions, which make the capability of an algorithm to adapt to real-world perturbations pivotal. To test the robustness of RBFOpt, we have thus added external perturbations to the experimental setup, by considering a scenario where a sudden perturbation on the parameters is introduced. The algorithm is then asked to find again the optimal parameters required to engineer the target state in the new experimental condition. The considered perturbations act probabilistically on the HWP of the second step and on the first QWP of the third step, this disturbance consists of a permanent offset δ in the angle at which the waveplates are rotated. In particular, at each iteration and with probability q the orientation of the waveplates optical axis is changed by the addition of an angle sampled from a normal distribution with mean $\mu = -30^{\circ}$ and standard deviation $\sigma = 5^{\circ}$. Here, we worked in the classical domain and investigated the algorithm response when engineering some of the previously generated states. In these cases, several values for the parameter q are used for different states, the engineered states and the probability q used for them are reported in Table 5.1.

Target State	Perturbation Probability	Restart Threshold
$\|1\rangle$	0.0015	0.02
$\|3\rangle$	0.0015	0.02
$\frac{1}{\sqrt{2}}(\|-1\rangle + \|1\rangle)$	0.008	0.02
$\frac{1}{\sqrt{2}}(\|-1\rangle + i\|1\rangle)$	0.004	0.02
$\frac{1}{\sqrt{2}}(\|-3\rangle + \|3\rangle)$	0.0015	0.05
Random	0.0015	0.02

Table 5.1. The table shows the parameters used in the study of the optimization under perturbations for the engineered states. In the second column we report the values of the perturbation occurrence probability q, while in the third column we report the threshold values t used for deciding the algorithm restart.

To determine whether a perturbation occurred, and thus if the control parameters need to be re-optimized, we added the following checking step to the algorithm working flow:

1. Every 10 iterations, we used the optimal parameters found by the algorithm up to that time Θ_{best} to obtain a new estimate of the cost function $C_{\text{new}}(\Theta_{\text{best}})$.
2. To spot if a perturbation occurred, we compared the new value with the one obtained during the algorithm evolution $C_{\text{sampled}}(\Theta_{\text{best}})$. Hence, chosen a threshold t, we proceed as follows:
    (a) If $C_{\text{new}}(\Theta_{\text{best}}) \leq C_{\text{sampled}}(\Theta_{\text{best}}) + t$, the optimization is continued.
    (b) If $C_{\text{new}}(\Theta_{\text{best}}) > C_{\text{sampled}}(\Theta_{\text{best}}) + t$, the algorithm is restarted.

Therefore, the surrogate model is discarded and rebuilt from scratch every time the quantity of interest deteriorates over a certain limit. The control is made every 10 algorithm iterations to have a quick response to perturbations without excessively increasing the optimization time. Indeed, each function evaluation consists of a time-consuming projective measurement with the SLM, and we want to keep low their number. For each engineered state the value of the threshold was fixed analyzing the fluctuations in the value of the measured fidelity F, these values are reported in Table 5.1 as well.

An example of the dynamics under perturbations is reported in 5.5-a, where the engineering of the state $|1\rangle$ is considered. Here the iteration in which a perturbation is introduced is highlighted by a vertical red or green line respectively for shift on

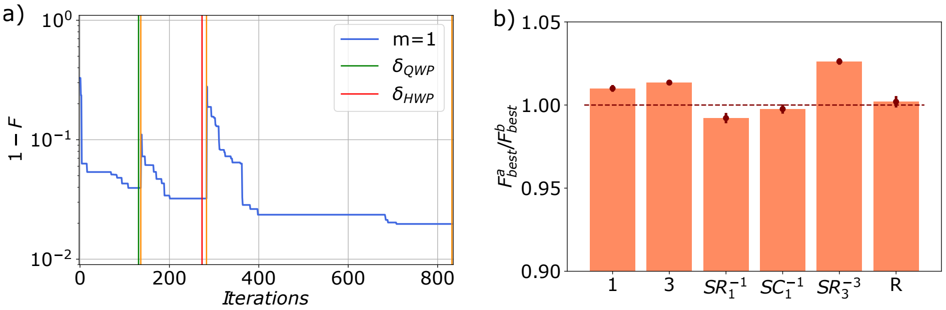

Figure 5.5. Experimental Perturbation Results. **a)** Optimization under external perturbation of the quantity $1-F$ for the state $|1\rangle$. The iterations in which a perturbation δ occurs are highlighted by a vertical red line (second step HWP) or by a vertical green line (third step QWP), a vertical orange line highlights the iteration in which the algorithm is restarted. b) Mean ratio between the best value obtained for the fidelity after (F^a_{best}) and before (F^b_{best}) the perturbation for the different engineered states. The ratio is close to or higher than 1 for all of them, this showcases that the algorithm is able to re-obtain and eventually improve the best value sampled before the perturbation. All the error bars reported are due to laser fluctuations affecting each measurement and are estimated through a Monte Carlo approach.

the HWP or on the QWP. Instead, the restart of the algorithm is indicated with a vertical orange line. As shown, after the perturbation, the minimum found by the algorithm is no longer the optimal solution, thus the algorithm is forced to restart. The latter allows the algorithm to reach a new optimal solution in a different environmental condition. In particular, we analyzed the quality of this adjustment by comparing the fidelities obtained before and after the perturbation. The ratio between the two is reported in Fig. 5.5-b, and since for each state more than one perturbation could be performed, the mean ratio is computed averaging over all of them. The presence of mean ratios with values equal or greater than 1 showcases how the algorithm is indeed able to re-adapt its optimal solution, and eventually improve the previously obtained fidelity.

5.3 Conclusions

In conclusion, we presented a universal quantum state engineering protocol based on the QW dynamics. This has been proven capable of generating arbitrary high dimensional quantum states, with both high fidelity and probability. Although, this QW-based approach is proposed to work without being *ad hoc* designed for a specific platform, in experimental implementation its performances could be dumped due to unwanted and uncharacterized imperfections and noises. For this reason, we decided to employ a gradient-free optimization algorithm called RBFOpt to enhance the quality of the generated states. In particular, we analyzed a platform that implements a 3-step fashion DTQW exploiting the two components of light angular momentum, allowing the algorithm to act on the parameters that control the evolution and studying several states in both quantum and classical regimes. We saw how the RBFOpt results in higher fidelities than those computed using the direct method of Ref. [64]. Therefore, showcasing that the real-time optimization algorithm allows us to take into account and compensate for experimental imperfections automatically. Moreover, to carry out a complete analysis, and as the adaptation capability of an algorithm is pivotal in realistic conditions, we simulated the effect of sudden external perturbations studying whether and how the algorithm readapts itself to new environment conditions. The results presented indicate that the algorithm indeed manages to adjust itself reaching fidelities comparable with those obtained before the perturbation. Our results prove the advantages of adopting real-time optimization algorithms for experimental quantum state engineering protocols. Moreover, working in a black box fashion, the algorithm does not require information on the function to be optimized and on the employed experimental platform. Therefore, our scheme can find applications in different engineering protocols and Quantum Information tasks , leveraging on electronically controllable devices. For instance, in principle, it could be used to optimize the number of quantum gates needed to solve a specific problem, in the calibration of complex optical circuits that find applications in tasks like Boson Sampling [96, 288–290] and in the engineering of multiphoton quantum states [291]. With extension of the approach also to different degrees of freedom, such as time [265, 267, 269], frequency [270] or path [264, 266, 268]. In all this cases, it would be crucial to tailor a suitable cost function. Finally, the proposed DTQW platform can be extended to higher dimensions by increasing the number of steps, using system of lenses or a loop configuration to address the beam divergence [283], and by entering the system with multiphoton states, enabling the study of phenomena such the entanglement transfer [292].

Chapter 6

Detection of Orbital Angular Momentum States

One of the main steps of every Quantum Information protocol is the retrieval of the information encoded in a quantum state, this is in general obtained by observing the state through the measurement of its physical properties. Therefore, after describing the generation and manipulation of high dimensional quantum states, we will focus in this chapter on their detection, both enhancing the performance of already known techniques and describing machine learning-based approaches.

In practice, a quantum state is completely characterized through a quantum state tomography procedure (see Section 1.1.3), which allows us to retrieve its density matrix. However, the feasibility of this approach decreases when increasing the dimension of the state under analysis. Indeed, the number of observables to measure grows quadratically with its dimension [1, 58], and the procedure could be impractical in several scenarios. In particular, for the purpose of the thesis, we are interested in qudits encoded in the OAM of light states. Indeed, despite their potential in Quantum Information applications, the capability to accurately generate and detect OAM states remains a challenging task. Detection techniques that have been proposed in the literature include interferometric schemes [67, 68, 293, 294], the use of diffractive elements [295–299], tilted convex lens [300], interference patterns with reference beams [153, 301–304], methods exploiting Doppler frequency shift [305–307], weak measurements [69], metamaterials [151, 308–314] and holographic techniques [65, 159, 202, 315–321].

In particular, we described the latter of them in Section 2.5.2, describing how it can be used to perform projective measurements in the OAM Hilbert space. Therefore, we analyzed the measurement station composed by a SLM followed by the coupling to a SMF, in which the projections are made by showing on the active part of the first the holograms corresponding to the basis elements and the similarity between them and the state under analysis is estimated from the amount of the detected signal. Thus, the performances of the protocol strongly depend upon the model that describes the state that is used to create the holograms. When working with OAM eigenstates, most of the proposed and employed protocols use the LG modes (see Eq. 2.60) to describe their spatial structure. However, this description may not fully capture the structure of the optical modes generated by any given experimental implementation, therefore damping the accuracy of the detection schemes. For example, concerning q-plate action, the modulated output beam can be properly modeled using the LG basis only in the pupil plane, i.e. when the propagation distance goes to zero, under the assumption of a thin device. Indeed, in the general case, the diffraction effects due to the phase singularity of the device have to be taken into account and the output beam can be described more accurately by a model based on Hypergeometric-Gaussian functions [150, 155] (see Eq. 2.64). Similar considerations work also when analyzing the SLM action with pitchfork holograms [151]. In our work [70], starting from this discussion, we developed a refined model to describe the OAM state generated by a 5-step QW platform. Here, the states produced by the q-plates placed in a cascaded configuration result more efficiently described by a superposition of HyGG modes. To assess it, we studied the measurement performances obtained by adopting the HyGG-based model to create computer-generated holograms exploited in the SLM-based measurement. We observe higher state fidelities when coupling the resulting output modes into a single-mode fiber, as well as increased coupling efficiency. These results highlight the importance of using an accurate model of the incoming beams to optimize the detection process and could be adopted for different techniques that need an accurate model of the generated state.

Despite the results achieved in improving the performances of the hologram-based detection techniques, these methods are still affected by noise and loss due mainly to the efficiency of the SLM and the coupling of the converted beam to the SMF [202]. Recently, artificial intelligence has been widely employed in Quantum Information protocols, and particularly machine learning techniques resulted to be a valuable tool to overcome the experimental and theoretical limitations related to the reconstruction of OAM states. In particular, ML models have been used to recognize and classify structured light states such as superposition of OAM [322–327] and vector vortex beams (VVBs) [70, 277], structured light beams whose helical wavefront is associated to a nonuniform distribution of the polarization on the transverse plane [25, 193, 328]. Moreover, ML has been also employed considering the propagation in turbulent environments [47, 48, 329–339]. In our works [70, 71], we applied ML algorithms to both solve classification and regression tasks of OAM modes. We first employed a CNN (see Section 3.2.2) to study the polarization distribution of VVBs experimentally generated with our platform and approached the detection as a classification task, in which, starting form an RGB image of the states, we retrieve their OAM content from the class to which they belong. In particular, to have a model less conditioned by the experimental noises, we trained the network only with simulated images while we tested it on the experimental ones. This enabled us also to validate the refined beam propagation model aforementioned. Indeed, by using images generated considering the HyGG-based description of the output beam, we observed an enhancement in the classification performances of the CNN. Therefore, we have proven the importance of appropriately modeling the engineered states for improving both hologram-based and ML-based techniques.

After that, we moved to consider not just the detection and recognition of an OAM component in a state, but instead the retrieving of the phase and amplitude of the coefficients describing an arbitrary OAM superposition. For this purpose, we solved a regression task intending to reconstruct the Bloch vectors associated with high dimensional light states [340]. In particular, we worked in a combined unsupervised and supervised fashion, using firstly the PCA (see Section 3.2.1) to find a dimensional reduced representation of the dataset, that allows us to speed up the protocol while filtering the noise, and then employing a linear regressor [341] to find the map between the PCA latent space and the Bloch vector, which is used as label during the training. Moreover, since the inputs are images of the OAM superpositions intensity profile, in our approach we have to deal with the symmetry of Eq. 2.61, an issue that greatly affects the capabilities of the regressor in reconstructing the states. Therefore, to break it, we decide to generate a second image of the states with an increased value of the OAM for each mode appearing in the superposition. Indeed, the two new states are distinguishable, and by giving both images to the regressor is performances are greatly enhanced. In particular, the high values for fidelity showcase the effectiveness of our approach.

Some of the results reported in this chapter are included in the following works:

- Alessia Suprano, **Danilo Zia**, Emanuele Polino, Taira Giordani, Luca Innocenti, Mauro Paternostro, Alessandro Ferraro, Nicolò Spagnolo, and Fabio Sciarrino,“Enhanced detection techniques of orbital angular momentum states in the classical and quantum regimes”, *New Journal of Physics*, vol. 23, p. 073014 (2021). [70]
- **Danilo Zia**, Riccardo Checchinato, Alessia Suprano, Taira Giordani, Emanuele Polino, Luca Innocenti, Alessandro Ferraro, Mauro Paternostro, Nicolò Spagnolo, and Fabio Sciarrino, “Regression of high dimensional angular momentum states of light”, *Physical Review Research*, vol. 5, p. 013142 (2023). [71]

6.1 Refined theoretical model for an enhanced holographic technique: q-plate action

In Section 2.5.2 we have preliminary introduced the q-plate action on OAM eigenstates just as a modification in the OAM value by a factor $2q$, where q is the topological charge written on the device during its fabrication. Moreover, we saw how modes that carry a defined amount of OAM can be expressed using the Helmotz paraxial equation solutions (see Section 2.3). In particular, the most commonly used are the Laguerre-Gaussian modes (LG) that form a complete and orthogonal basis and are defined by two indexes the radial one (p), which is associated with the number of nodes in the radial direction over the transverse plane, and the azimuthal one (m), which instead is associate with the OAM eigenvalue. Therefore, the q-plate action is commonly described as a modification of the azimuthal index of an incoming beam $LG_{p,m}$, while the radial one is kept fixed. However, this is an approximate action that is valid in the pupil plane of the device, where the diffraction effects can be neglected. Conversely, in the most general propagation case, the diffraction produced by the topological defect of the device has to be considered, and as we will see this produces a modification also in the radial structure [151, 155]. This effect can then be described by solving the propagation integral for the beam exiting the device. In the Fresnel diffraction region, posed $z = 0$ the position of the q-plate, this integral has the form:

$$\begin{aligned}\mathbf{E}_{out}(x,y,z) = -\frac{e^{-ikz}}{i\lambda z}\int_{-\infty}^{\infty}\int_{-\infty}^{\infty} & d\tilde{x}d\tilde{y}\;\mathbf{E}_{in}(\tilde{x},\tilde{y},0)\times \\ & \times\, exp\left\{-i\frac{k}{2z}\left[(x-\tilde{x})^2+(y-\tilde{y})^2\right]\right\}\end{aligned} \tag{6.1}$$

where $\tilde{x}, \tilde{y}$ are the coordinate on the device plane, z is the propagation distance, λ and k are respectively the wavelength and the wavenumber of the input beam.

We explicitly solve the integral for the case in which we are entering it with a Gaussian beam ($E_{in}(\tilde{x},\tilde{y}) = \exp\{-(\tilde{x}^2+\tilde{y}^2)/W_0\}$) in an arbitrary polarization state $|P\rangle = c_-\,|R\rangle + c_+\,|L\rangle$, where $\{|R\rangle\,, |L\rangle\}$ are respectively the right and left circularly polarized states. Therefore, considering separately the two integrals related to the two circular polarizations, in cylindrical coordinates ($\tilde{x} = \tilde{r}\cos\phi,\ \ \tilde{y} = \tilde{r}\sin\phi,\ \ x = r\cos\theta,\ \ y = r\sin\theta$) we have:

$$\begin{aligned} E^{\pm}_{out}(r,\theta,z) = -c_{\pm}\frac{\exp\left\{-ik\left(z+\frac{r^2}{2z}\right)\right\}}{i\lambda z}\int_0^{\infty}\int_0^{2\pi} d\tilde{r}d\phi\ \tilde{r}E_0(\tilde{r})\times \\ \times\exp\left\{-ik\frac{\tilde{r}^2}{2z}+i\frac{kr\tilde{r}}{z}\cos\left(\phi-\theta\right)\pm i2\tilde{\alpha}\right\} \end{aligned} \tag{6.2}$$

where the q-plate contribution is represented by the phase factor $\tilde{\alpha} = \alpha_0 + 2q\phi$, whit α_0 is the initial angle between the optical axis of the device and the x direction which depends on its construction. The integral over ϕ can be performed by exploiting the Jacobi-Anger expansion for which $exp(iu\cos\varphi) = \sum_{m=-\infty}^{\infty} i^m J_m(u)exp(-im\varphi)$, where J_m is the Bessel function of first order for which $J_m(-u) = J_{-m}(u) = (-1)^m J_m(u)$. Then, exploiting the well-known integral for the Bessel function reported in Ref. [342] for solving the integral in $\tilde{r}$, we obtain as output field:

$$E^{\pm}_{out}(\rho,\theta,\xi) = c_{\pm}e^{-ikz\pm i2\alpha_0}HyGG_{-2|q|,\,\pm 2q}\left(\rho,\theta,\xi\right) \tag{6.3}$$

where $\rho = r/W_0$ e $\xi = z/z_0$ are the adimensional cylindrical coordinates and the expression of $HyGG(.)$ is reported in (2.64). So. we have that the q-plate also modifies the radial profile of the beam, indeed we can express the HyGG mode in equation 6.3 as an infinite superposition of LG modes where the sum is performed over the radial index while the azimuthal one is kept fixed (see Eqs. 2.66-2.67). Furthermore, when entering the device with an arbitrary mode $LG_{k,m}$ having a circular polarization, the output results in a superposition of $k+1$ HyGG modes, where the number $k+1$ is related to the number of terms appearing in the Laguerre Polynomial expression. More details about the integrals and their solutions for input Laguerre-Gaussian modes can be found in Appendix C.

In our work [70], we moved from considering the action of a single device and instead we studied the propagation along a cascade of several q-plates, that reproduce our 5-steps QW-based engineering platform (see Fig. 6.1-a), more details are reported in Section 5.1 for a 3-step implementation. In particular, entering the setup with a Gaussian beam, the action of the first q-plate is completely described by the result reported in Eq. 6.3. Since we have a method to compute the integrals for the LG modes, as mentioned before, we express the HyGG mode in a superposition of LG ones. Here, at variance with previous approaches that reduce to consider only the radial index $p = 0$, and hence non considering a variation from the input in the radial profile, we include all terms up to $p = 3$. This allowed us to reach a higher overlap between the theoretical and the experimental produced states without substantially increasing the computational cost. After solving the integral in 6.2 for each considered LG mode, the output beam from the second q-plate is described by a finite superposition of HyGG modes. Exploiting again 2.66, the procedure is repeated for all the q-plates of the setup to obtain the final description of the output beam. Consequently, the output state engineered via the platform is expressed as a superposition of HyGG modes with different radial indices but with the same azimuthal indexes of the simplified model. We refer to the approximated model that cuts the superposition at $p = 0$, and thus it is valid only when the distance of propagation $z \to 0$, as the **LG model**, while the one developed in [70] as the **HyGG model**. The latter goes indeed beyond the LG assumption and provides a more accurate description of the beam propagation inside the quantum walk platform. An example is shown in Fig. 6.1-b, where the intensity distribution obtained using the

LG and the HyGG models are compared with the experimental collected ones. In the following Sections, we exploit this refined model to reach enhanced performances in OAM detection techniques using both holographic projection (Section 6.1.1) and machine learning-based approaches (Section 6.2.1).

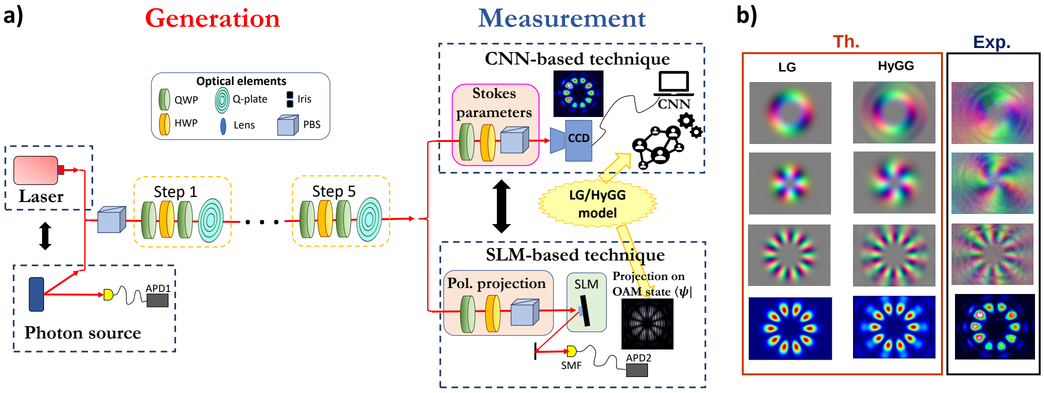

Figure 6.1. Experimental generation and detection of OAM-based states. a) The employed experimental platform is based on a five-step quantum walk to generate OAM and VVB states with both single-photon inputs and classical laser light. Each step is composed of a set of two quarter waveplates (QWP) interspersed by a half waveplate (HWP) and a q-plate. The states resulting from these arrangements are measured using two different detection apparatuses. In the classical domain, the detection system is composed of a polarization analyzer and a Charge-Coupled Device camera (CCD). This arrangement measures the spatial distribution of the input beam and sends the acquired images to a computer that classifies the states using a suitably trained Convolutional Neural Network (CNN). In the single-photon domain, the OAM measurement stage consists of a polarization analyzer and an SLM followed by the spatial filter provided by a single-mode fiber (SMF) and connected to a single-photon detector (APD). **b)** Example of experimentally measured patterns generated by the quantum walk platform (right), and the corresponding theoretical predictions obtained via the LG and HyGG models. The first three rows represent the colored maps of three different VVBs corresponding to $\{m_1, m_2\} = [\{3, 5\}, \{-1, 3\}, \{5, -5\}]$. Each color in the map is associated with a different direction of the polarization and the distribution of the colors depends on the value of m_1 and m_2. Instead, in the last row is reported the pattern distribution associated with OAM state obtained as the balanced superposition of $m_1 = 5$ and $m_2 = -5$.

6.1.1 Experimental results of the enhanced holographic technique

In Section 2.5.2 we have introduced a standard technique to detect OAM states. This consists of using diffraction gratings, encoded in the so-called holograms, that allow us to modulate the phase and amplitude of a field passing through them. In particular, we described how it is possible to perform projective measurement employing the combination of a SLM and the coupling to a SMF. The first one is used to show the holograms and manipulate the field spatial structure, while the second one, by selecting the Gaussian component, estimates the mutual overlap between the field and the hologram. Therefore, we can compute the fidelity between the experimental produced state and the theoretical target one by using a set of holograms in which is encoded an orthonormal basis that contains the state under analysis. From the measurements, we can retrieve the probability distribution over the basis and confront it with the target one using the fidelity expression reported in Eq. 1.46.

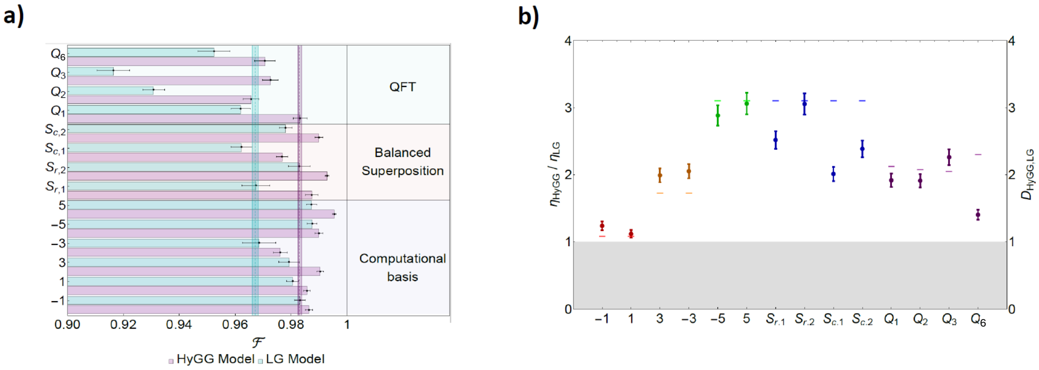

Figure 6.2. Experimental results of the enhanced holographic technique. a) Summary of the fidelities obtained by performing the measurements of the 14 engineered states with the holograms based on the HyGG model (purple bars) or the LG one (cyan bar). We reported the comparison for different classes of state: elements of the computational basis, superposition of large OAM states (Balanced Superposition) and elements of the Fourier basis (QFT). The purple and cyan lines that represent the mean values are 0.9831 ± 0.0005 and 0.9671 ± 0.0010, respectively. **b)** Coupling Efficiency of single photon states. The points represent the ratio between the coupling efficiency associated with the holograms programmed using the HyGG model and the ones obtained with the LG model. The ratio is always greater than 1, confirming the coupling improvement. Moreover, the experimental values are compared with the quantity $D = \frac{|\langle\Phi_{\text{HyGG}}|\Phi_{\text{exp}}\rangle|^2}{|\langle\Phi_{\text{LG}}|\Phi_{\text{exp}}\rangle|^2}$, where $\Phi_{exp} = \Phi_{\text{HyGG}}(w_0^{\text{exp}})$, w_0^{exp} is the experimental beam waist that has been considered equal to $w_0^{\text{HyGG}} + \delta$, with $\delta = 0.062$ mm, and w_0^{HyGG} is the beam waist chosen for the computer-generated holograms. Such a quantity δ has been added to take into account experimental imperfections. The different colors are associated with the previous three classes of states, which are characterized by similar theoretical predictions.

Usually, the analysis of the OAM content of an input state is made by assuming that its eigenstates $|m\rangle$ can be represented by the Laguerre-Gaussian modes, based on which the holograms of the basis are constructed. However, this approach might not fully capture the structure of the optical modes generated by any given experimental apparatus, which would limit the accuracy of the detection scheme. Indeed, as described in the previous Section for our platform, to correctly account for the diffraction effects of the cascaded q-plates a more rigorous description based on the HyGG modes is needed. Therefore, when analyzing the state produced by our QW-based platform, their detection is enhanced if we use this refined description.

To validate this assertion, we first set the platform parameters so as to generate OAM eigenstates $|m\rangle = \{|\pm1\rangle, |\pm3\rangle, |\pm5\rangle\}$ which correspond to the computational basis in Quantum Information language, comparing then the fidelities obtained performing the measurement with the holograms generated with the LG and HyGG models. To further assess the generation and measurement capabilities of our apparatus, we also showcase the generation of more complex OAM states. In particular, we have considered coherent superpositions of the extreme sites of the walker, both with real and complex coefficients, $S_{r,c} = \frac{|5\rangle + e^{i\beta}|-5\rangle}{\sqrt{2}}$ where $\beta \in [0, \pi/2, \pi, 3\pi/2]$, and four states of the Fourier basis associated to the Hilbert space of the walker, $QFT_k = \frac{1}{\sqrt{6}}\sum_{j=1}^{6} e^{\frac{i\pi jk}{3}}|j\rangle$ where $\{|j\rangle\}$ are the elements of the computational basis previously introduced and $k = 1, 2, 3, 6$. In Fig. 6.1.1-a the cyan and purple bars report the values of fidelities $\mathcal{F}$ obtained with the two models, as can be seen, these are higher when the HyGG one is used. In particular, we obtained an average fidelity over the engineered states equal to $\mathcal{F}_{HyGG} = 0.9831 \pm 0.0005$ and $\mathcal{F}_{LG} = 0.9671 \pm 0.0010$, for the corresponding models. Moreover, in Appendix Table D.1, we also report the explicit values of the fidelities obtained for each considered state.

Importantly, we observe also higher coupling efficiencies in the SMF for each hologram associated with an engineered target state. In particular, encoding a field $|m\rangle$ in the hologram which projects the incoming beam onto the Gaussian one, an increase in the coupling efficiency corresponds to a higher mutual overlap between the two fields. To support this conclusion, in Fig. 6.1.1-b we report the agreement between the measured coupling efficiency ratio ($\eta_{\mathrm{HyGG}}/\eta_{\mathrm{LG}}$) and the theoretical expectation D calculated from the employed holograms and the actual experimental states. Such theoretical value is computed as $D = \frac{|\langle \Phi_{\mathrm{HyGG}}|\Phi_{\mathrm{exp}}\rangle|^2}{|\langle \Phi_{\mathrm{LG}}|\Phi_{\mathrm{exp}}\rangle|^2}$, where $|\Phi_{\mathrm{LG}}\rangle$ and $|\Phi_{\mathrm{HyGG}}\rangle$ are the states encoded in the measurement hologram exploiting respectively the LG and HyGG models, while $|\Phi_{\mathrm{exp}}\rangle$ is defined as $\Phi_{exp} = \Phi_{\mathrm{HyGG}}(w_0^{\mathrm{exp}})$, where w_0^{exp} is the experimental beam waist that has been considered equal to $w_0^{\mathrm{HyGG}} + \delta$, with $\delta = 0.062$ mm, and w_0^{HyGG} is the beam waist chosen for the computer-generated holograms. Such a quantity δ has been added to take into account experimental imperfections and the comparison showcases a good agreement [70]. Furthermore, in Appendix Table D.2 we report these values for the coupling efficiency associated with each hologram. These results showcase the enhancement achieved in the measurement of the experimental states engineered through our QW platform.

This capability of significantly improving the detection efficiency represents a fundamental aspect, especially at the single photon level. Indeed, in this scenario, photon losses undermine the security and feasibility of quantum communication and cryptography protocols. Furthermore, when moving to multi-photon protocols, losses affect the amount of detected signal as η^n, being n the number of involved photons, and thus an improvement in η will result in a magnified overall efficiency.

6.2 Machine learning-based approach to OAM measurement

Machine learning algorithms have been proven to be useful tools in everyday life, and recently they have attracted an increasing interest for application also inside the Quantum Information field, leveraging on the ability of ML protocols to manipulate complex structured data. Following this trend, we decide to exploit ML techniques in the detection of OAM-encoded high dimensional states. In particular, we used a CNN for the detection of the OAM content of VVBs, classifying them into 15 different categories (Section 6.2.1). Then, we go further in this direction by addressing the problem of exactly retrieving the coefficients of arbitrary OAM superposition. In particular, we use a combination of PCA and linear regressor to solve the task, proposing also a method to break the symmetry of Eq. 2.61 and obtaining high values of the fidelities for the retrieved states (Section 6.2.2).

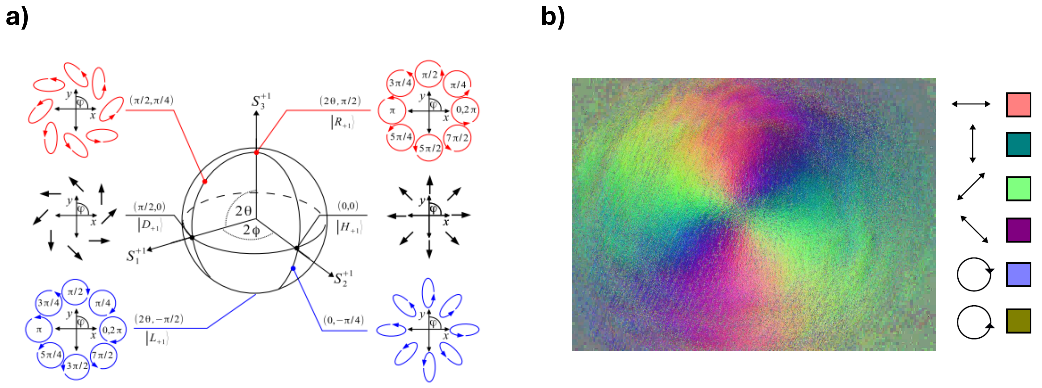

Figure 6.3. Vector Vortex Beams. a) High order Poincarè sphere representation of a VVB. On the poles are reported the two orthogonal states $|-1, R\rangle$ and $|1, L\rangle$, having definite values of OAM and polarization and characterizing the VVB under analysis (see Eq. 6.4). On the equator are placed the states having a linear but nonuniform polarization, such as the TM_{01} and TE_{01} fiber modes. Finally, all the other points are associated with elliptical polarization states. Image taken from [193]. **b)** RGB encoding of the VVB $|\psi\rangle_{1,-1}$ .Each primary color is associated with a Stokes parameter $\{S_i\}_{i=1}^3$ (see Eqs. 2.92-2.94), the legends show explicitly the polarization-color encoding.

6.2.1 Classification of vector vortex beams via convolutional neural networks

In Section 2.2 we have shown how in paraxial approximation it is possible to decompose the total angular momentum of light in its spin and orbital component, reporting also solutions of the paraxial Helmholtz equation that are eigenstates of the OAM. However, in all these cases we considered beams with a homogeneous polarization, reducing then our analysis to the scalar expression of Eq. 2.45. Conversely, if we take into account the vectorial nature of the field and we solve the vectorial Helmholtz equation, it is possible to obtain solutions for which the SAM and OAM degrees of freedom are found to be coupled [343]. In particular, when a nontrivial phase structure, such as the one present in helical beams, is coupled to a nonuniform transverse polarization pattern, we have a Vector Vortex Beam (VVB) [25, 193, 328]. This kind of state has found several applications both in classical and quantum regimes, ranging from optical trapping [26, 344] to metrology [30, 39, 345–348] and communication [27, 197, 345, 349, 350]. In particular, such implementations mostly exploit the OAM content of VBBs and the hyperentaglement of the latter with the polarization degree of freedom. For example, exploiting the rotational invariance of the polarization pattern, due to this coupling, for creating quantum communication protocols that are insensitive to the orientation of the sender and receiver local frames [197].

In general, a VVB state is given by the superposition of two OAM states, each of whom is associated with an orthogonal polarization:

$$|\psi\rangle_{m_1,m_2} = \cos\frac{\theta}{2}\,|m_1, L\rangle + e^{i\phi}\cos\frac{\theta}{2}\,|m_2, R\rangle \tag{6.4}$$

where $\theta \in [0, \pi]$, $\phi \in [0, 2\pi]$ and $m_1 \neq m_2$. Even if these states are intrinsically high dimensional having an encoding that exploits the OAM degree of freedom, for how they are defined, single VVBs are restricted to span bidimensional Hilbert spaces. Therefore, as in the case of qubits, VBBs can be mapped on a sphere: the *higher-order Poincarè sphere* [193]. In Section 2.5.1, we have already introduced the Poincarè sphere as a tool for completely describing the polarization state of a light beam. The higher-order one applies the same concept to the nonuniform polarization state of VBBs. In particular, given the set of parameters describing a generic VVB (m_1, m_2, θ, ϕ) it is possible to locate it on a sphere, in which the poles are represented by the eigenstates of the total angular momentum $|m_1, R\rangle$ and $|m_2, L\rangle$, that therefore show a uniform polarization pattern. Instead, as for the Poincarè sphere, the states on the equator of the higher-order ones present a linear polarization, however, this is not directed in the same way over all the transverse plane. An example of a higher-order Poincarè sphere describing the polarization pattern of a VBB having $m_1 = 1$ and $m_2 = -1$ is reported in Fig. 6.3-a. The interest in this geometrical representation is because it allows us to easily describe several kinds of state, ranging from the simpler states transmitted by an optical fiber, such as the TM_{01} and TE_{01} fiber mode [351] appearing on the equator in Fig 6.3-a, to more exotic ones, such as the full Poincarè beams [352].

Furthermore, a manner to reconstruct the polarization profile of a VVB is to measure point by point the Stokes parameter of Eqs. 2.92-2.94, obtaining with this procedure the degree of polarization in each of the 3 MUBs $\{H, V\}$, $\{+, -\}$ and $\{R, L\}$ over all the transverse plane. From that, a pictorial way to represent this polarization distribution is to associate each one of the Stokes parameters $\{S_i\}_{i=1}^{3}$ to the intensity of one of the primary colors red, green, and blue of an RGB image [277], examples are showed in Fig. 6.3-b and Fig. 6.1-b. In particular, this encoding will be used in the following to collect the information stored in the VBBs and reformulate the detection problem of OAM states in an image recognition task.

Experimental platform

Several architectures and devices have been proposed to experimentally couple the OAM and SAM degrees of freedom, and generate then VVBs. For instance, interferometric schemes relying on spatial modulation through holograms [39, 328], integrate photonic platforms [353–355] and metasurfaces [151, 276, 356] have been effectively employed. Among them, a device that can be naturally used to generate VVBs is the q-plate introduced in Section 2.5.2. Indeed, by comparing its action reported in Eqs. 2.96-2.97 with the general expression for a VVB of Eq. 6.4, we see how it automatically generates a VVB. In particular, by properly acting on the tuning parameter δ it is possible to regulate the efficiency of the device, and then it can be used to generate a VVB between the original beam $|m\rangle$ and the converted one having OAM $|m \pm 2q\rangle$. Instead, when using a switched-on q-plate ($\delta = \pi$), by suitably manipulating the polarization of a beam before it enters the device, it is possible to engineer a VBB between the $|m + 2q\rangle$ and $|m - 2q\rangle$ OAM modes.

Despite the number of accessible VVBs with a single device being quite reduced, q-plates appear to be one of the most suitable solutions due to their efficiency and ease of handling. Indeed, as shown in Ref. [65, 277] an OAM-based QW platform implemented employing q-plates in a cascaded configuration can be used to engineer arbitrary VVBs, whose number depends only upon the number of steps of the dynamics and then can be in principle arbitrary enlarged. In our implementation, we use a 5-step QW-based platform schematically depicted in Fig. 6.1-a, the function of which has been described in detail in Section 5.1. By controlling the coin parameters, i.e. the angle of the waveplates, this implementation allowed us to engineer arbitrary VBB having $m_1, m_2 \in \{\pm 1, \pm 3, \pm 5\}$, therefore reaching 15 different kind of states.

VVBs detection as an image recognition task

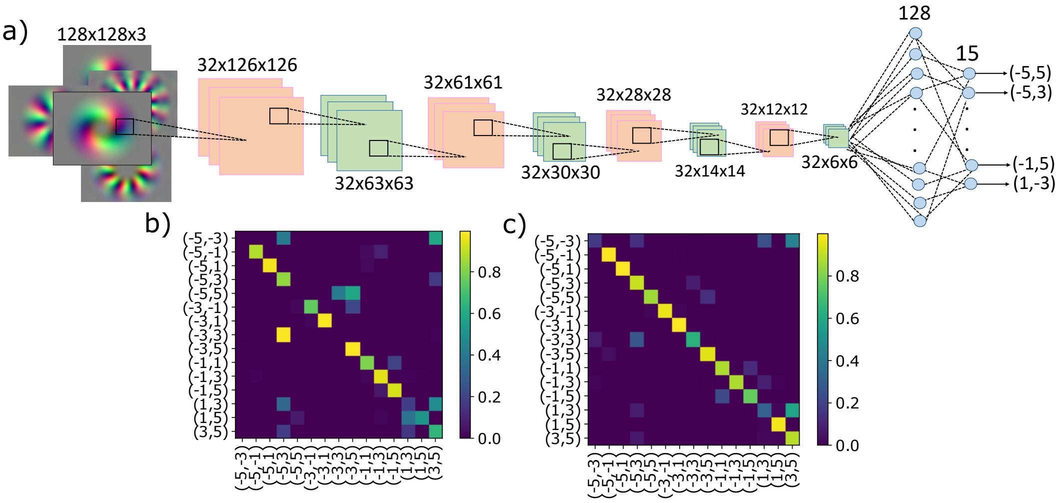

Figure 6.4. Convolutional Neural Network. a) Schematic representation of the CNN architecture. For each layer the correspondent dimension is shown in the figure. The Convolutional layers are represented in orange, while the max pooling ones are shown in green. The last two layers are two fully connected ones. The specific classification task is performed by the last layer, i.e. the softmax one (see Eq. 3.10). **b-c)** Truth-tables for the two models: **b)** LG model and **c)** HyGG model. The matrix elements have been averaged over 100 experimental images per class, and the percentage of images belonging to the i-th class (row) classified by the CNN in the j-th class (column) are represented by the different colors. The numbers in parentheses are the two OAM values m_1, m_2 that appear in the VVB expression (see Eq.6.4).

Following the approach proposed by Giordani *et al.* in [277], we decided to address the problem in the detection of VVBs as an image recognition task [70], exploiting the RGB encoding previously introduced and acquiring the experimental intensity images via a Charged-Coupled Device (CCD) camera. In particular, we used a CNN since it belongs to a class of neural-network architectures especially suited to process images for classification and regression tasks. Moreover, their specific structure allows them to recognize translation-invariant features, making CNNs effective in recognizing images produced in realistic experimental conditions. The detailed description of the CNNs working principle is reported in Section 3.2.2.

In particular, we exploited the QW platform for engineering VVBs having $\theta = \pi/2$ and arbitrary phase ϕ, and we divided them into 15 different classes depending on the different combinations of $m_1, m_2 \in \{\pm 1, \pm 3, \pm 5\}$. Therefore, the CNN is used to correctly classify between them an input image showing the nonuniform polarization pattern of a VVB. In particular, we apply the CNN to classify experimental images of VVBs using only *simulated* ones in the training set. Comparing the performances when the model is trained with images generated using either the LG or the HyGG model described in Section 6.1. Notice however that, for the sake of the training, in both cases, a validation set comprising only experimentally generated images is used. We have observed that the inclusion of the latter is necessary in order to achieve satisfactory performances in both cases over the experimental test set, indeed this enables us to choose the paradigm weights that better perform in the recognition of the experimental data without direct access to them.

To build and train the CNN we used the Python library Keras [357], with TensorFlow [358] as the backend. Specifically, we use a CNN composed of four convolutional layers each of which is followed by a max-pooling layer, a pictorial representation of the network is reported in Fig. 6.4-a. In each convolutional layer, we use 32 filters of size 3×3 with ReLU activation function. For the pooling layers, we apply the max operation to blocks of size 2×2. The final classification is performed by a fully connected layer with 128 nodes followed by a softmax layer. As already introduced, for the training we used 400 simulated images (either via the LG or the HyGG model) for each of the 15 involved classes. While, at each training step we use a mini-batch of 30 simulated images to update the parameters, and a fixed validation set of 1500 experimental images to assess the CNN performance. We then tested the classification accuracy of the network with 1500 new experimental images.

We repeated the protocol 22 times, in Fig. 6.4-b,c we report the best performances, where each VVB state has been labeled according to the OAM numbers of the two beams in the state superposition (see Eq. 6.4). These networks give average accuracies of 0.632 ± 0.097 and 0.815 ± 0.065 respectively for the LG and HyGG models. Instead, when considering the whole repetitions of the approach, we find mean accuracies equal to 0.553 ± 0.013 (LG) and 0.662 ± 0.019 (HyGG). In Fig. 6.5-b is reported the performance trend of the 22 CNN trainings for the two models with their averaged values. Despite the HyGG model allowing us to reach higher values for the accuracies, its performances are still sub-optimal due to the presence of relevant differences between the simulated images and the experimental collected ones (see Fig. 6.1-b). Therefore, trying to compensate for them, we consider experimental issues related to the possibility of making errors when calibrating or rotating the waveplates. In order to account for this kind of error we generated a new set of theoretical images, both for the LG and the HyGG model, with a random error in the experimentally used angles up to a maximum value equal to $3°$ for each waveplate. These images were added to the training set and we repeated the same analysis illustrated before. The accuracy increased for both models achieving a mean of 0.605 ± 0.018 (LG) and 0.765 ± 0.015 (HyGG), with the best performances of the second case that surpass the 90% value, these results are shown in Fig. 6.5-a,c.

In general, these results showcase how training a CCN with images generated using the HyGG model allows us to achieve significantly higher classification accuracy than those resulting from the LG-trained case, assessing its refined description of the dynamics.

6.2.2 Regression of high dimensional light states

As we already have introduced previously and explicitly shown in the previous chapter, ML techniques represent a valuable tool to overcome the many experimental and theoretical limitations related to reconstructing OAM states [70, 277, 322–327], also considering the propagation in turbulent environments [47, 48, 329–339]. However, most of the efforts have been focused on detecting the probability of finding OAM states on a fixed basis, such as the classification task described in the previous Section 6.2.1, as opposed to being able to resolve coherence terms between different modes. Nevertheless, the latter is of fundamental importance when we want to completely reconstruct the state under analysis. In this context, ML approaches have been mostly used to reduce the number of measurements needed to retrieve the coefficients of a quantum state, making therefore feasible the

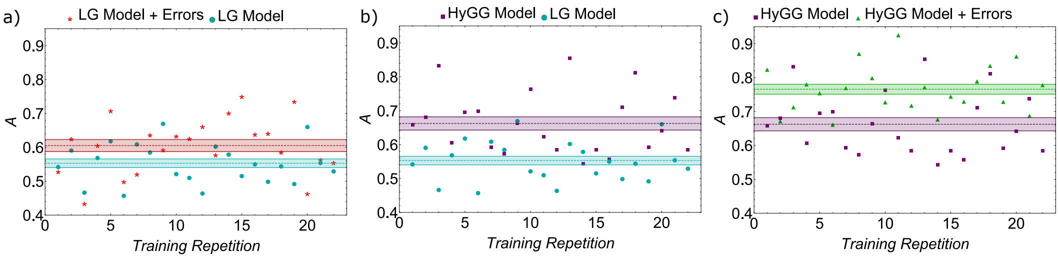

Figure 6.5. Training Accuracy. In the image, we show the distinct values of accuracy reached for different and independent training. **a)** We compare the CNN performances trained with simulated images obtained through the LG model (sky-blue) and theoretical images computed with the LG model taking into account experiment errors regarding the orientation of the waveplates (red). **b)** CNN accuracies obtained with a theoretical training set based on the LG model (sky-blue) and on the HyGG model (purple). **c)** We compare the CNN performances trained with simulated images obtained through the HyGG model (purple) and theoretical images computed with the HyGG model taking into account experiment errors regarding the orientation of the waveplates (green). The sky-blue, red, purple, and green areas are the respective average values with their standard deviations: 0.553 ± 0.013, 0.605 ± 0.018, 0.662 ± 0.019, 0.765 ± 0.015.

execution of quantum state tomography [208, 359–364], a procedure that requires a number of measurements scaling quadratically with the state dimension [1, 58], unless we have some prior information about it [365]. Moreover, CNN models have been successfully used to solve the task of directly recovering the coefficients of an arbitrary quantum state [147, 277]. However, the training of these CNN-based approaches involves in general a high computational cost. For this reason, in our work [71], we presented an approach to overcome these limitations thanks to the combined use of dimensionality reduction [366] and regression techniques [341] in a mixed unsupervised and supervised fashion ML approach.

Dimensional reduction for the regression task

Our goal is to retrieve the complex amplitudes of given LG states with respect to the LG basis $|\ell\rangle$, while we will consider that the radial index $p = 0$ (see Eq. 2.60), from measurements of their intensity profiles. To solve this task, we decided to use the PCA as a dimensional reduction algorithm (see Section 3.2.1). The latter takes as input data in a high dimensional space $\mathbb{R}^d$, such as datasets of images with dimensions equal to the number of pixels in the image, and maps them into a new space $\mathbb{R}^n$ whit dimensionality $n << d$, while preserving the relevant features of the dataset. This preprocessing approach presents two benefits, first of all, reducing the dimension of the inputs enables for a consistent speedup in the learning process performed by the regressor. Secondly, this provides a method more resilient to noise. Indeed it furnishes a representation of the data that best reflects the relevant features of the given data while the noise is mapped into the less representative dimensions, that are therefore cut during the reduction. We applied this protocol both on simulated images of LG modes and on experimentally generated states, the conceptual scheme describing the procedure followed in our work is reported in Fig. 6.6.

Furthermore, being a *linear* dimensionality reduction algorithm, the PCA is particularly suited for reconstructing quantum states from measurement outcomes, due to the linearity intrinsic to this problem [277]. To clarify this feature and the correlated advantages, consider states of the form:

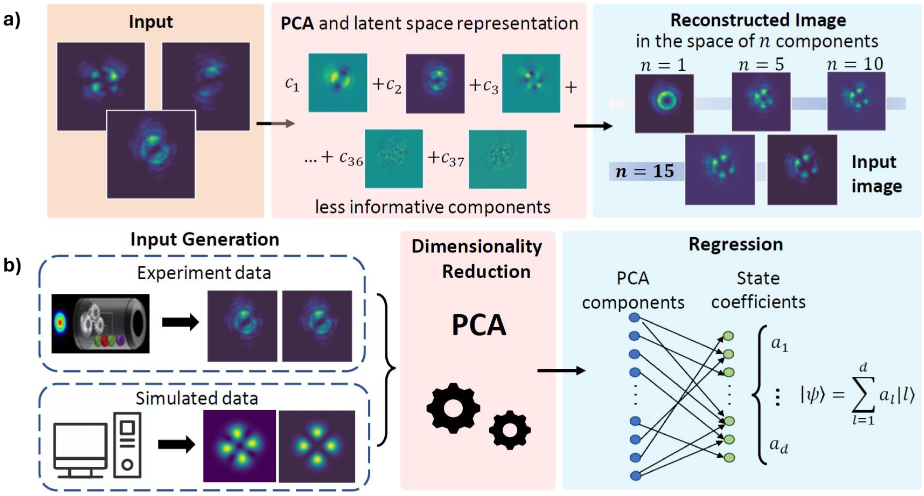

Figure 6.6. Summary of the protocol. a) PCA is used to find a lower-dimensional representation of the 64x64 pixel input images. Working in an unsupervised fashion it derives the axes of the reduced space that best represent the input, in this specific case they are identified as images in which we can decompose the data. By tuning the number of reduced dimensions obtained via PCA, we have different reconstruction accuracies. **b)** The proposed method works through the following 3 steps. Firstly, the dataset is generated theoretically with a computer simulation or experimentally exploiting a setup suited for the engineering of OAM states. Secondly, the data are given to the PCA algorithm that, reducing their dimensions, decreases the noise present in them and speeds up the training phase of the regressor. The latter is finally used to obtain the coefficients of arbitrary superpositions of OAM modes.

$$|\Psi\rangle = \cos\frac{\theta}{2}|1\rangle + e^{i\phi}\sin\frac{\theta}{2}|-1\rangle\,, \tag{6.5}$$

where $\theta \in [0,\pi]$ and $\phi \in [0,2\pi]$. Applying PCA on the training dataset, three dimensions of the latent space are sufficient to capture almost all of the relevant information. We expect to retrieve in the latent space the Bloch sphere representation of the Hilbert space associated with one qubit. Indeed, focusing only on four distinct classes characterized by $\theta = \{\pi, 7\pi/8, 3\pi/4, \pi/2\}$ and arbitrary ϕ, the distribution of the dataset in the latent space is characterized by four circular structures with a growing radius that corresponds to the different θ values, while each of such circumferences is given by the parameter $\phi \in [0,2\pi]$ (see Fig. 6.7-a). Furthermore, we also reported the reduced dimension for the experimentally collected images in Fig. 6.7-b, where we see the same behavior observed for the theoretical ones. Therefore, PCA preserves the geometrical feature of the space directly correlating the original parameters θ and ϕ with the position in the latent space.

Therefore, we employed linear regression to solve the task of connecting the latent space representation to a physical description of the states under analysis. More precisely, we performed a supervised training of the regressor using as objective the vector that collects the coefficients that appear when we decompose the density matrix of the states in the Generalized Gellmann Matrices basis (GMM) [340]. These are a basis of orthogonal traceless operators, which can be used to define a Bloch representation for high dimensional states, and that in the bidimensional case reduces to the Pauli matrices basis (see Eq. 1.26). Then, we assessed the performances of our protocol by computing the fidelity between the Bloch representation predicted by the algorithm and the corresponding ground truth target state by using the expression in Eq. 1.47.

It is worth noticing that in our approach, to avoid the possibility of non-physical states that might result from the algorithm, each state gets projected to the nearest pure physical state before calculating the fidelity. In particular, in this projection procedure, the predicted state is considered as the eigenvector associated with the higher eigenvalue of the density matrix recovered from the Bloch representation outputted by the regressor. This constitutes our best guess for an input pure state.

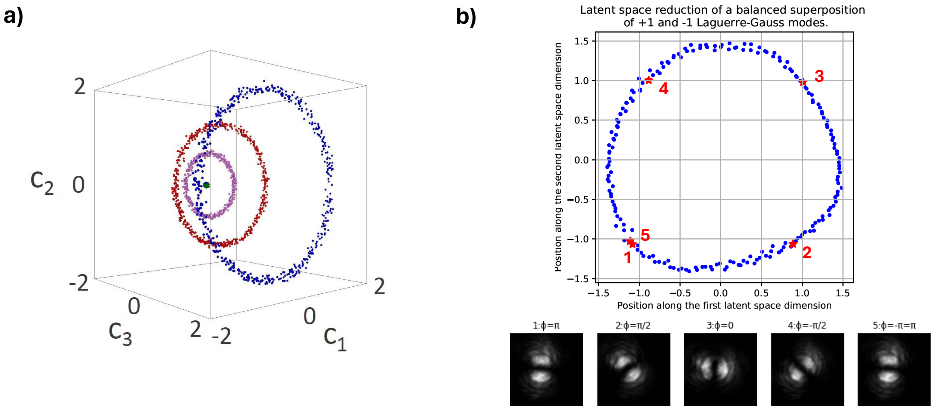

Figure 6.7. Principal Component Analysis Latent Space. a) Representation of the simulated data reduced via PCA in the space composed by the first three components $\{c_1, c_2, c_3\}$ of the latent space. Here, we consider states of the form described by equation 6.5. Each color corresponds to a set of states corresponding to a fixed value of θ. More specifically, $\theta = \pi$ (green), $\theta = 7\pi/8$ (purple) $\theta = 3\pi/4$ (red) and $\theta = \pi/2$ (blue). It can be noted that the circular structure given by the phase ϕ is preserved in latent space. This statement is also supported by the fact that the states with $\theta = \pi$, in green, are invariant with respect to the parameter ϕ and are mapped in the same region and not on a circle. **b)** Application of the PCA to experimentally collect images. In particular, we report the position along the latent space principal components of the intensity profiles for simple experimental superposition of LG modes corresponding to the case $\theta = \pi/2$. The five images at the bottom correspond to the red star symbols in the main graph at the top. Also in this case, we note that the change in the phase angle ϕ generates a rotation in the respective images and that is connected to the circular structure of the latent space.

Simmetry Breaking

One of the main problems, arising when we address the task of retrieving the coefficients of an arbitrary OAM state from an image of its intensity, is related to the inherent symmetry of LG modes introduced in Eq. 2.61. This comes from the fact that in the Laguerre-Gaussian modes the only term that depends on the sign of the azimuthal index m, and therefore on the OAM eigenstate, is the helical phase term $e^{im\phi}$. Consequently, when observing the intensity of a single mode, it is impossible to discern from it if the profile is associated with $LG_{p.m}$ or $LG_{p,-m} = LG^*_{p.m}$. This is simply extended to arbitrary superposition states, and Eq. 2.61 is easily obtained.

To address this fundamental problem for the reconstruction, we decided to act on the modes in a way that breaks this symmetry. In particular, our approach consists of a transformation of the reference state through the modification of the azimuthal index for all the modes that appear in the superposition. This produces two different superpositions and, hence, two distinct images that can be employed to reconstruct the state encoded in the initial image. For instance, let us consider the following arbitrary superposition in the Hilbert space spanned by the computational basis $\{|m\rangle\}$ with $m \in \{-2,-1,0,1,2\}$:

$$|\Psi\rangle = a\,|-2\rangle + b\,|-1\rangle + c\,|0\rangle + d\,|+1\rangle + e\,|+2\rangle\,. \tag{6.6}$$

From the symmetry rule of Eq. 2.61 we have that the state $|\Phi\rangle$ which is indistinguishable from $|\Psi\rangle$ using only an intensity profile measurements is:

$$|\Phi\rangle = e^*\,|-2\rangle + d^*\,|-1\rangle + c^*\,|0\rangle + b^*\,|+1\rangle + a^*\,|+2\rangle\,. \tag{6.7}$$

However, if we increase by one unit the OAM value of each mode in the superposition we obtain the following two states:

$$\begin{cases} |\Psi'\rangle = a\,|-1\rangle + b\,|0\rangle + c\,|+1\rangle + d\,|+2\rangle + e\,|+3\rangle \\ |\Phi'\rangle = e^*\,|-1\rangle + d^*\,|0\rangle + c^*\,|+1\rangle + b^*\,|+2\rangle + a^*\,|+3\rangle\,. \end{cases} \tag{6.8}$$

They are thus always distinguishable, except when $|\Psi\rangle$ and $|\Phi\rangle$ are identical from the beginning. In other words, even though directly measuring the intensity profile of a given $|\Psi\rangle$ we cannot univocally determine that the input was $|\Psi\rangle$ rather than $|\Phi\rangle$, such degeneracy is lifted if for each state we measure both the intensity profile of $|\Psi\rangle$ and of the state obtained from $|\Psi\rangle$ after applying a transformation that increases each OAM values by one unit, namely $|\Psi'\rangle$.

To see how symmetry breaking is a requirement for enhancing the regressor performance and obtaining the correct description of the state under analysis, we can start by analyzing the qubit case, which can be easily visualized using the Bloch sphere representation. Here, when we use just one image for each state, the algorithm is not capable of discerning whether the state belongs to the left or the right hemisphere of the sphere. This usually results in the model placing the states in the middle of the two hemispheres, along the equator, as a strategy to minimize the errors. Indeed, it can be seen that the effect on the Bloch sphere of the transformation described by Eq. 2.61 is the reflection symmetry along the x-y plane. As a consequence, the points on the equator are invariant under this transformation, and, for the same reason, it is not surprising that these points are correctly identified. Therefore, when the algorithm fails to break the symmetry, it tends to put the states near the equator to limit the errors in the state reconstruction. If instead we furnished the second image per state, in which we augmented the OAM values of the superpositions, the algorithm is capable of mapping the states to the right position on the spherical surface. This behavior is explicitly shown in Fig. 6.8, in which the positions of the states in the Bloch space are reported for both approaches.

Moreover, a similar trend is also pointed out when we observe the fidelity distribution of the predicted states. Here, when we use only one image to train the algorithm and then we applied it to two test sets, one with the correct labels and one with the labels obtained using the symmetry property, the distributions are almost identical since the regressor is not able to distinguish between the two descriptions (see Fig. 6.9-a,b). Instead, if we use also the additional augmented image the symmetry in lift and the distributions look different, with results for the mean fidelity that are not compatible with each other (see Fig. 6.9-c,d).

This showcases how the preprocessing proposed to lift the symmetry effectively helps in solving the task at hand. Moreover, if compared to other methods proposed to break such degeneracy [147], our approach is fully generalizable and independent of the structure of the state.

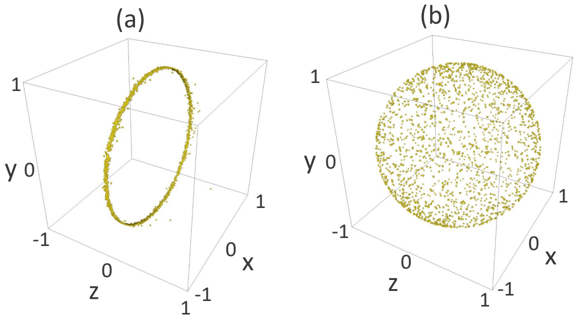

Figure 6.8. Two-dimensional symmetry breaking. Representation of the output of the regression algorithm on theoretical superpositions with $l \in \{-1, +1\}$, after the projection on the nearest pure state. We compare the position of each state on the Bloch sphere obtained from the regressor using one image **a)** and two images **b)** per state. In panel **a)** the higher values of the fidelities are obtained on the equator, this is the strategy adopted by the regressor to minimize the errors. In fact, not being able to distinguish states placed on the two hemispheres, this approach enables the regressor to obtain a higher mean fidelity. Instead in panel **b)** the effects of symmetry breaking are evident, here the regressed states are placed in their real position.

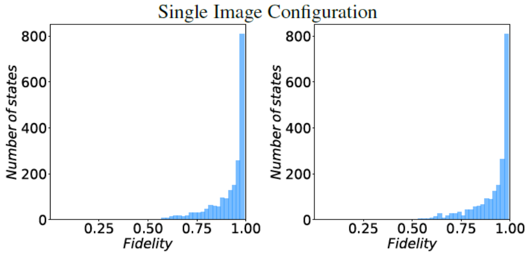
Single Image Configuration

(a) Correct coefficients (b) Inverted coefficients

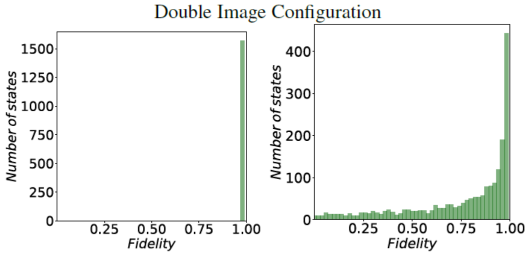
Double Image Configuration

(c) Correct coefficients (d) Inverted coefficients

Figure 6.9. Two-dimensional fidelities distribution. Fidelity calculated on superpositions with $l \in \{-1, +1\}$. Using only one image per state, the values of fidelity were calculated between the output of the regression with both the expected theoretical state **a)** and the theoretical state after the inversion of the coefficients described by Eq. 2.61 **b)**. The mean value of the fidelity in both graphs is $\bar{F}_a = 0.923 \pm 0.002$ and $\bar{F}_b = 0.923 \pm 0.002$, respectively. They are compatible within the statistical error and thus the process can not distinguish the two cases. Computing the same fidelity in the double image configuration, the mean value of the graph in panel **c)** is $\bar{F}_c = 1$, while the mean value of the graph in panel **d)** is $\bar{F}_d = 0.764 \pm 0.006$. They are incompatible and thus the process has broken the symmetry.

Simulated results and experimental results

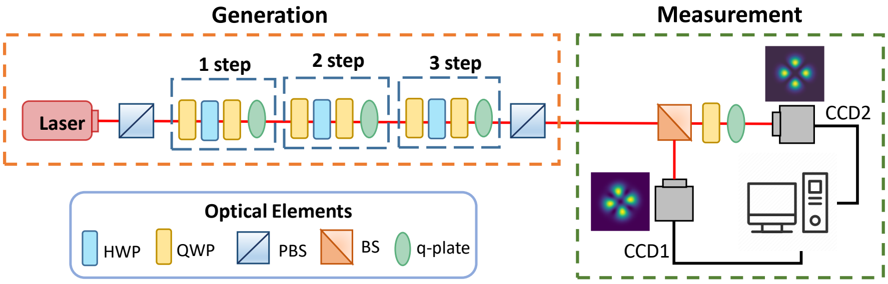

Figure 6.10. Experimental Setup. Diagram of the experimental apparatus used in the generation and measurement of spatially modulated photonic beams. The setup is composed of three blocks containing a cascade of waveplates, half-waveplate (HWP) and quarter-waveplates (QWP), followed by a q-plate. Each block implements a step of the quantum walks dynamics. The input state is a Gaussian mode obtained through the coupling of an 808 nm laser to single mode fiber. After projection on the polarization degree of freedom, the intensity profile corresponding to the resulting OAM state is recorded with a CCD camera. To uniquely retrieve input states from intensity profiles, the measurement stage uses two CCD cameras, one of which is placed after a QWP and a q-plate.

We applied our approach both on simulated and experimentally collected data. In particular, our experimental setup is similar to the one described in Section 5.1. It consists of a 3-step QW implemented exploiting the angular momentum of light, and then realized by three blocks containing waveplates and q-plates in a cascaded configuration (see Fig. 6.10). Therefore, by tuning the angle of the waveplate that governs the dynamics, we are able to generate arbitrary superposition in a 4-dimensional Hilbert space: $|\psi\rangle = a\,|-3\rangle + b\,|-1\rangle + c\,|1\rangle + d\,|3\rangle$ with $a, b, c, d \in \mathbb{C}$. At the end of the QW, after a projection on the polarization space, the intensity distribution of the state is collected with CCD cameras. With respect to the previous setup, here we use an additional beam-splitter, which is used to divide the beam into two arms and perform the augmentation needed to lift the symmetry of Eq. 2.61. In particular, we directly measure the beam with the CCD1 on one arm, while on the other one, the measurement is performed after the evolution through an HWP and a q-plate (CCD2). Here, after transforming the polarization from horizontal to circular, the q-plate is used to perform the OAM value-increasing step for each element of the superposition under analysis.

The images collected by the CCDs are 1280x1024 pixels, but we scale them down to 64x64 pixels before feeding them to the algorithm to further speed up the whole protocol. Moreover, we employ two different PCAs separately on the dataset. In particular, the first one is used to reduce the dimensions of the image of the states, while the second one is applied in the same manner to the superposition state with the augmented OAM values. This two PCAs approach was chosen since we observed an increase in the performances of the method. The latent space representation of the data is thereafter passed to the regressor during the supervised training stage. Finally, the accuracy of the protocol is evaluated on a test dataset composed of images that the algorithm has never seen before. The latter are firstly mapped to the latent space that best describes the training set, and then the trained linear regressor is applied to them.

To show the effectiveness of the procedure, we compared the results of the

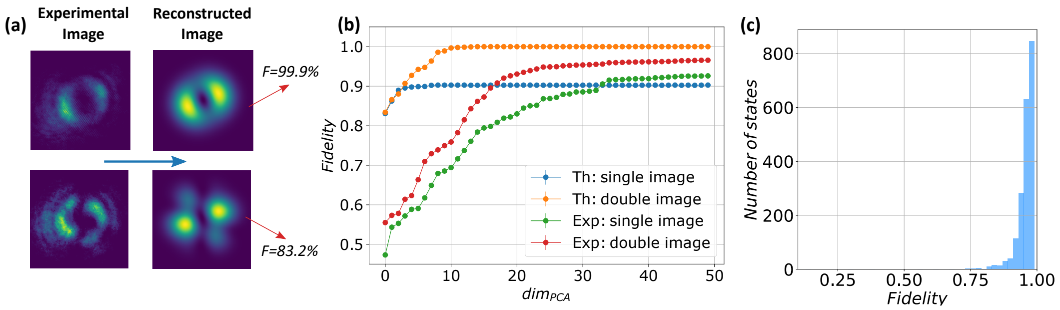

Figure 6.11. Experimental and Simulated Results. a) Comparison between the intensity distributions of collected experimental states and of reconstructed states whose coefficients of the LG superposition are retrieved through the regression analysis. To showcase the performances of the method, results for values of the fidelity equal to $F = 99.9\%$ and $F = 83.2\%$ are reported. **b)** Trend of average fidelity obtained by increasing the number of PCA dimensions passed to the regression algorithm by state in the space spanned by $l \in \{-3, -1, +1, +3\}$. Theoretically, the regression algorithm approaches its maximum fidelity with PCA dimensions close to 15. Using single images does not allow to reach fidelity higher than $F = 90\%$ (blue line), while employing double images the fidelity value approaches the 100% (orange line). Although experimental imperfections appear to break the symmetry feature also in the single image configuration (green line), the exploitation of double images increases the performances (red line). The points constituting all lines are obtained averaging over 2000 random states, while the correspondent error is not appreciable with respect to the size of the marker.**c)** Experimental fidelity distributions calculated over 2000 random states in the double image configuration for state experimentally engineered in the space spanned by $l \in \{-3, -1, +1, +3\}$. The mean value of the fidelity is $F = 0.9661 \pm 0.0009$, where the error is given by the standard deviation on the average.

regression obtained using only the intensity profile of the state with those reached by processing the augmented dataset, containing also the profile of the superposition with increased azimuthal index. We collected a dataset of 10^4 images for both the experimental and simulated cases and we divided them randomly into training and test sets, respectively composed of 8000 and 2000 images. In Fig. 6.11-b we report the behavior of the fidelity as a function of the PCA dimensions given to the regressor for both the simulated and experimental datasets. The results showcase how, by using the additional information, the algorithm is capable of lifting the degeneracy and obtaining better performance in solving the task. In particular, in the simulated case it succeeds in overcoming the plateau resulting from using just one image. Instead, for the experimental scenario, the symmetry appears to be broken also in the one-image configuration (green line in Fig. 6.1.1-b), this is due to experimental imperfection that makes distinguishable intensity profiles that theoretically are predicted to be equal. However, also in this case, the two-images approach enhances the performance of the method enabling us to reach a higher value of fidelity with fewer dimensions of the PCA. Finally, the experimental fidelity histogram is reported in Fig. 6.1.1-c, we obtained an average fidelity over the test set states of $F = 0.9661 \pm 0.0009$.

Furthermore, for the simulated case, we also expanded the analysis by considering Hilbert spaces $\mathcal{H}_d$ of dimension $d \in [2, 8]$. In particular, by studying the fidelity behavior in function of the dimension of the PCA latent space, we found out the that the linear regressor obtains a value for the mean fidelities nearly equal to 1 when the number of PCA components is close to $(d^2 - 1)$. This is an interesting result since the latter is exactly the dimension of the Bloch vector that describes

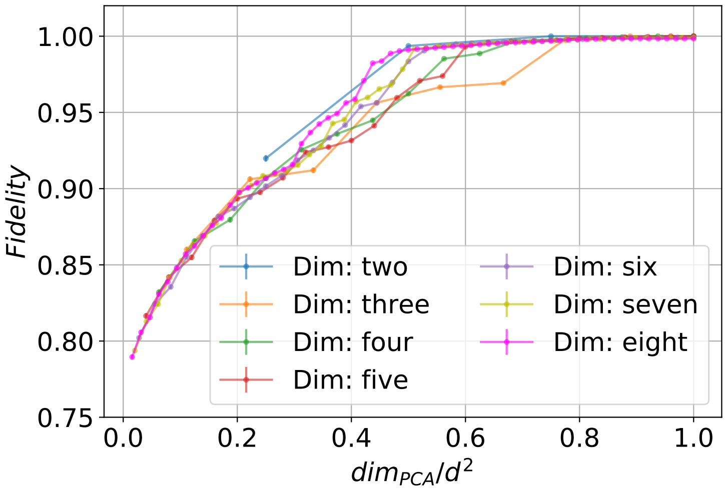

Figure 6.12. Result for higher dimensional simulated images. The plots show the results of the linear regressor when applied to theoretically simulated states with Hilbert space dimension up to 8. The number of PCA components given to the regressors is reported on the x-axis, in order to consider various dimensions in a single plot we normalize it to the factor d^2. From the computed fidelities it can be seen that the linear regressor reaches a value of fidelity nearly equal to 1 for all the dimensions when we approach the value of $(d^2 - 1)$ PCA components, which is the dimension of the Bloch vector. All the fidelity values are obtained averaging over 2000 random states.

the states, and then this number of components should indeed give a fairly physical representation of the dataset, sufficient enough to properly describe the states in it. The results of this study are reported in Fig. 6.12 for all the considered dimensions.

6.3 Conclusions

In this chapter, we focused on one of the main issues in Quantum Information implementations, namely the efficient retrieval of the information stored in a quantum state. In particular, we analyzed the detection of high dimensional quantum states encoded employing the angular momentum of light. We start by experimentally demonstrating the enhancement of a widely used measurement protocol, the holographic technique. In particular, we developed a refined model for describing the output states from a series of q-plates in a cascaded configuration. Conversely to what is often done, instead of using the LG modes, which might not fully capture the spatial structure of the state, it describes the state through the HyGG ones. The use of HyGG to create the holograms allowed us to reach higher fidelities in quantum state discrimination, with also an increase in the coupling efficiency of each hologram. The latter represents a substantial improvement at the single-photon level, where the overall detection efficiency and accuracy represent a fundamental requirement for robust and secure quantum communication and quantum cryptography protocols.

Moreover, we applied two machine learning protocols to address the detection problem in the form of both classification and regression tasks. In particular, we first studied the problem of finding the OAM values describing a VVB with an RGB image of its polarization distribution. We used simulated images in the training using both the LG and HyGG models, and we asked the network to classify the experimental ones into 15 different classes. We observed enhanced learning performances when the HyGG was used for simulating the distribution, then we can assert that this captures more successfully the features of the experimental images. Furthermore, we also consider the complete retrieval of the coefficients that describe an arbitrary OAM superposition starting from its intensity profile. In particular, here we have to deal with the symmetry property of Eq. 2.61 that greatly affects the recognition capabilities of the algorithm. However, we saw how the latter can be lifted by using for each data during the training an additional image, that contains the profile of the state under analysis but with each value of the OAM increased by one unity. Therefore, by exploiting this method and using the combination of a PCA and a linear regressor to learn from intensity images the Bloch vectors of the superpositions in the dataset, we obtained high values of the fidelities. This showcases the effectiveness of our approach. Furthermore, it is worth noting that, even if they have been applied in the classical domain, the introduced ML approaches can be extended in the quantum regime by substituting the laser source with a single photon source and using a CCD sensitive to single-photon signal, like the one used in Chapter 4.

Part III

Orbital Angular Momentum for Quantum Information Protocols

Chapter 7

Quantum Machine Learning

In the previous chapters, we saw how optimization algorithms and machine learning techniques can be effectively employed for solving specific tasks in the experimental implementation of Quantum Information protocols. For instance, in engineering quantum states and in their measurement and detection. All these approaches can be seen as belonging to the broader field of Quantum Machine Learning (QML), where Quantum Mechanics meets information theory with the aim to create powerful tools that help in the study of physical systems. Indeed, inside QML we can recognize two kinds of procedure, having an increasing difficulty. The first step consists of applying the known machine-learning paradigms to the quantum realm in order to enhance our comprehension of it, this is the one with the largest number of contributions and to which our previously introduced experimental realizations appertain. In particular, ML algorithms have been also used to analyze quantum datasets with the aim of finding signature characteristics such as the bosonic statistics produced by a chip [206, 367, 368] or the entanglement and non-locality [369, 370], acting as entanglement witnesses. Moreover, they were exploited either to increase the performance of known approaches in quantum metrology [207, 290, 371], quantum state tomography [208, 360, 363, 372], or to find new ways of performing quantum experiments discovering better implementations and interesting routes to follow [211, 281].

The second step is instead trying to implement existing ML paradigms on quantum computer hardware or develop a quantum version of the knowing paradigm, hoping for a quantum speed-up. Here, the problem starts from the base of the task, and it is not completely understood and stated. Indeed, regarding the classical counterpart, the best possible performance of a typical ML algorithm is not well-known and it is not clear how it scales with the size of the input, making it difficult to compare accurately its performance with a quantum implementation. However, several of the most used machine learning models have been reformulated in a quantum version, for instance principal component analysis [373], support vector machine [374], extreme learning machine [375–377] and neural networks [378–380].

By exploiting our QW platform, we used OAM states to perform an experimental implementation of a QELM, with the aim of estimating quantum observables on a state encoded in the polarization degree of freedom [377]. We identified the QW evolution as the unknown reservoir quantum channel that is used to enlarge the Hilbert space from the polarization to the OAM one, the outputs of which are used to train the model. We found out that the QELM is a resource-efficient and effective approach to solving the task at hand. Some of the results reported in this chapter are included in the following works:

- Alessia Suprano, **Danilo Zia**, Luca Innocenti, Salvatore Lorenzo, Valeria Cimini, Taira Giordani, Ivan Palmisano, Emanuele Polino, Nicolò Spagnolo, Fabio Sciarrino, G Massimo Palma, Alessandro Ferraro, and Mauro Paternostro,"Experimental property-reconstruction in a photonic quantum extreme learning machine", *Physical Review Letters*, vol 132, p. 160802 (2024). [77]

7.1 Quantum extreme learning machine

The quantum extreme learning machine is the quantum version of the ELM paradigm introduced in Section 3.2.3, and has recently attracted significant attention thanks to its potential in Quantum Information processing [375–377]. A standard way to quantize an ELM is to substitute the reservoir dynamics represented by the nonlinear and fixed beforehand function $g(.)$ (see Section 3.2.3) with a quantum dynamics, i.e. using a quantum system as a reservoir, followed by a measurement [377]. In a general scenario, we consider a completely positive and trace-preserving quantum channel Φ, that will represent our *reservoir dynamics* hereafter, followed by a setup performing a POVM (see Section 1.1.3). Defining $\{\mu_b\}$ the set of measurement operators with possible outcomes $b \in \Sigma$, and taking as training inputs the density matrices ρ_k with associate label $\mathbf{y}_k \in \mathbb{R}^m$, the aim of the QELM is to find a linear map W such that:

$$\sum_{b\in\Sigma} W_{a,b} Tr[\mu_b \Phi(\rho_k)] = (\mathbf{y}_k)_a \tag{7.1}$$

where $a = 1, \dots, m$ and $k = 1, \dots, N_{tr}$, with N_{tr} the size of the training set. Therefore, we have that the classical nonlinear function here becomes:

$$g_{\Phi,\mu} : \ \rho \to (Tr[\mu_b \Phi(\rho)])_{b=1}^{|\Sigma|} \in \mathbb{R}^{\Sigma} \tag{7.2}$$

that depends upon the implemented quantum evolution and the kind of performed measurements. Moreover, we can reframe the function $g_{\Phi,\mu}$ as a direct measurement on the state ρ in the following way:

$$p_b(\rho) = (g_{\Phi,\mu}(\rho))_b = \mathrm{Tr}[\mu_b \Phi(\rho)] = \mathrm{Tr}[\Phi^\dagger(\mu_b)\rho] = \mathrm{Tr}[\tilde{\mu}_b \rho] \tag{7.3}$$

where p_b is the probability to obtain the outcome $b \in \Sigma$ from the performed measurement, $\Phi^\dagger$ is the adjoint of Φ and we have introduced the *effective* POVM $\tilde{\mu}_b = \Phi^\dagger(\mu_b)$, which defines our direct measurement on ρ. In particular, the input state can be recovered from the output probabilities if and only if $\tilde{\boldsymbol{\mu}}$ is *informationally complete*, meaning that the span of the operators $\tilde{\mu}_b$ is the full space of Hermitian linear operators.

In general, in the described configuration, performing a supervised learning of the QELM, it is possible to retrieve the expectation values of a target observable $\mathcal{O}$. Therefore, the training dataset has the form $\{(\rho_k, o_k)\}_{k=1}^{N_{tr}}$, with ρ_k input states and $o_k = \mathrm{Tr}(\mathcal{O}\rho_k)$ the associated expectation values. More generally, the target can be a set of expectation values, such as the Pauli matrices (see Eq. 1.26) and we can write the training dataset as $\{(\rho_k, \mathbf{o}_k)\}_{k=1}^{N_{tr}}$, with $\mathbf{o}_k \in \mathbb{R}^\ell$ a vector with elements $(\mathbf{o}_k)_j = \mathrm{Tr}(\mathcal{O}_j \rho_k)$, and with $(\mathcal{O}_j)_{j=1}^{\ell}$ the target observables we mean to learn how to compute.

During the training of the model, each input state ρ_k is measured N times in the effective POVM framework and the collected statistics is used to estimate the frequency $\mathbf{f}_k$. Then, we search for the linear map W, reformulating the Eq. 7.1, as:

$$(WP)_{jk} = \mathrm{Tr}(\mathcal{O}_j \rho_k), \qquad j = 1, ..., \ell, \quad k = 1, ..., N_{\mathrm{tr}} \tag{7.4}$$

where P is the matrix whose k-th column is $\mathbf{f}_k$. Note that P depends on the statistics N used to estimate the outcome probabilities for each state. In the limit $N \to \infty$, its elements thus tend to the true output probabilities: $P_{bk} \to \mathrm{Tr}(\tilde{\mu}_b \rho_k)$.

Following the same approach of the classical ELM (see Section 3.2.3), we can solve the linear system through the pseudoinverse method, and the solution reads:

$$W_{jb} = \sum_{k=1}^{N_{\mathrm{tr}}} \mathrm{Tr}(\mathcal{O}_j \rho_k)(P^+)_{kb}, \qquad P^+ \equiv P^T (PP^T)^{-1} \tag{7.5}$$

where P^+ is the pseudoinverse of P, which can always be written in the above form, as long as P is surjective, which is always the case for sufficiently many training states.

Having a trained model, we can proceed by performing a test on the QELM over states ρ that it has never seen before. After retrieving the measurement frequencies for the new inputs, we apply the W on them and assess the accuracy of the resulting estimates by computing the Mean Squared Errors (MSEs) for the target observable:

$$\mathrm{MSE}(\rho, \mathcal{O}_j) \equiv \left(\sum_{b \in \Sigma} W_{jb} f_b - \mathrm{Tr}(\mathcal{O}_j \rho) \right)^2 \tag{7.6}$$

and we average this quantity over all the states present in the test set (N_{test}) to quantify the overall accuracy.

A final remark on the theoretical protocol is that its expressivity, that is the space of observables that can be accurately retrieved for a given choice of Φ and $\boldsymbol{\mu}$, was proven to depend exclusively on the properties of the effective POVM. In particular, a necessary condition for enabling the reconstruction of arbitrary observables is that the reservoir dynamic Φ must enlarge the dimension of the input space in order to guarantee a sufficiently large number of measurement outcomes [377, 381].

Here, we described only the reconstruction of linear operations on the input states. However, it can be shown how performing multiple injections it is possible to reconstruct nonlinear functionals of the input state [377]. Considering for instance a polynomial target of the form $\mathrm{Tr}\left(\mathcal{O}\rho^k\right)$, this can be reconstructed only if the number of injections is greater than or equal to the degree of the target function.

7.2 Experimental Photonic QELM

We experimentally implemented the QELM described in the previous Section in an OAM-based QW photonic platform [77]. The reservoir dynamics Φ is here represented by the coined QW evolution. Our goal is to extract expectation values of observables on the input polarization states, using the reservoir dynamics to transfer this information into the larger OAM space that is then measured (see Fig. 7.1-a).

Our setup (reported in Fig 7.1-b) consists of an initial stage used to generate input states in the polarization degree of freedom. Indeed, the photons coming out from the SMF possess a null OAM value, and their polarization is modified through a series of PBS, HWP and QWP, that enable us to create the input state:

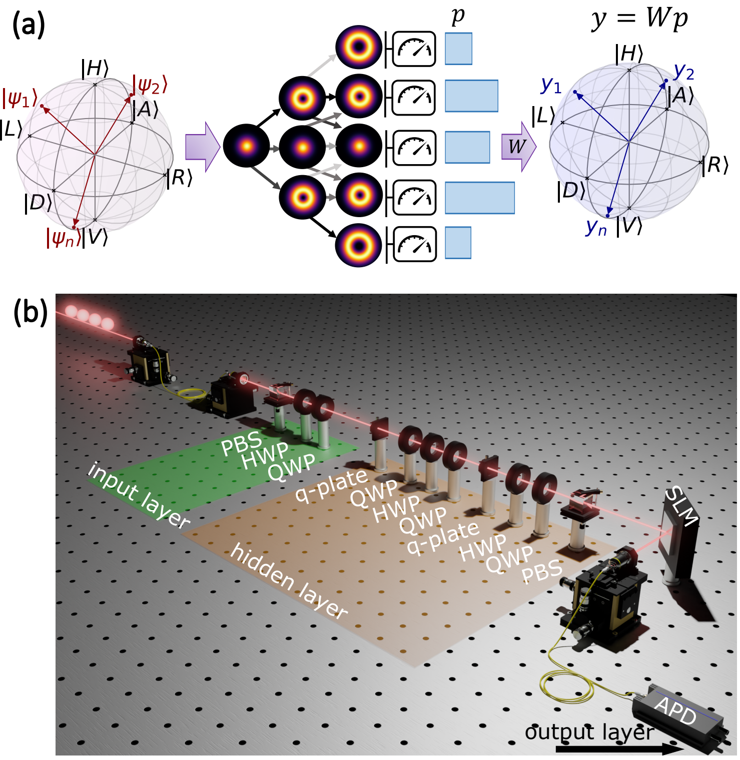

Figure 7.1. Experimental QELM. a) Schematic overview of the experimental QELM. Initial quantum states $|\psi_1\rangle, |\psi_2\rangle, \cdots, |\psi_n\rangle$ encoded in the polarization degree of freedom of single photons evolve through a reservoir dynamic, in which the information encoded in the initial two-dimensional space is transferred into the larger Hilbert space of the OAM. By performing only projective measurements on the OAM computational basis, the QELM is trained to reconstruct a set of target values $y_1, y_2, \cdots, y_n$. **b)** Experimental implementation. Single photons, generated at 808 nm via spontaneous parametric down-conversion, are sent through the state-preparation stage (*input layer*) made by a Polarizing-Beam Splitter (PBS), a Half-Wave Plate (HWP) and a Quarter-Wave Plate (QWP) to encode the initial state in the polarization degree of freedom. Subsequently, the input states evolve through the *hidden layer* following the quantum walk dynamics implemented by HWPs, QWPs, and q-plates. After projecting onto the polarization state $|\psi_{\text{pol}}\rangle$ with a sequence of HWP, QWP, and PBS, projective measurements in the OAM computational basis, $\mathcal{B} = \{|n\rangle\}$ with $n = \{-2, .., 2\}$, are performed through a Spatial Light Modulator (SLM) followed by the coupling into a single-mode fiber. From the counts measured by an Avalanche Photodiode (APD), the output layer of the QELM is trained to retrieve the expectation values of the Pauli observables $\{\sigma_x, \sigma_y, \sigma_z\}$.

$$
\begin{aligned}
|\psi\rangle = \frac{1}{\sqrt{2}}[&e^{i\theta_1}(\cos(2\zeta_1 - \theta_1) - \sin(2\zeta_1 - \theta_1))\,|L\rangle \\
&+e^{-i\theta_1}(\cos(2\zeta_1 - \theta_1) + \sin(2\zeta_1 - \theta_1))\,|R\rangle]
\end{aligned}
\tag{7.7}
$$

where θ_1 and ζ_1 are the rotation angles of the waveplates optical axis. This input state then evolves through a series of waveplates and q-plates, implementing the coin and shift operators of the QW dynamics, that in the machine learning formalism represent the fixed hidden layers of the reservoir dynamics. In particular, for the sake of completeness we report again that the coin operation is implemented as $C(\zeta, \theta, \phi) = \text{QWP}(\zeta)\text{HWP}(\theta)\text{QWP}(\phi)$, with ζ, θ, ϕ tunable angles, while each q-plate implements a controlled-shift operation $S(\alpha, \delta)$ with characteristic parameters

α, δ. More explicitly, these operations take the form:

$$C(\zeta,\theta,\phi)=\begin{pmatrix} e^{-i(\zeta-\phi)}\cos\eta & e^{i(\zeta+\phi)}\sin\eta \\ -e^{-i(\zeta+\phi)}\sin\eta & e^{i(\zeta-\phi)}\cos\eta \end{pmatrix}, \tag{7.8}$$

$$\begin{aligned} S(\alpha,\delta)=&\sum_{n=-N+1}^{N-1}\cos\frac{\delta}{2}\left(|L,n\rangle\langle L,n|+|R,n\rangle\langle R,n|\right) \\ &+i\sin\frac{\delta}{2}(e^{2i\alpha}|L,n\rangle\langle R,n{+}1|+e^{-2i\alpha}|R,n\rangle\langle L,n{-}1|) \end{aligned} \tag{7.9}$$

with $\eta=\zeta+\phi-2\theta$ and $|L,n\rangle$ ($|R,n\rangle$) denote left- (right-) circular polarization, and OAM with azimuthal quantum number n.

In particular, we implemented the evolution:

$$U=S(\alpha_2,\pi)C(\zeta,\theta,\phi)S(\alpha_1,\pi/2) \tag{7.10}$$

where $\alpha_1=105°,\alpha_2=336°$ are fixed by the fabrication process. Moreover, we decide to tune the efficiency parameter δ for the two q-plates respectively at $\pi/2$ and π to enlarge the space without increasing the number of steps. Indeed, thanks to the not-converted part that accounts for a stationary walker, the number of possible final positions is larger than what is obtained for a walker who is always moving.

After the evolution, a combination of waveplates and a polarizing beam splitter are used to project the polarization, while a SLM and a SMF are employed to measure the final OAM states, obtaining the occupation probabilities for the basis states $|n\rangle$, $n=\{-2,-1,0,1,2\}$. These represent the reservoir outputs, therefore the obtained counts are given to the computer, where the training of the QELM takes place, and the target expectation values are estimated.

Using the notation of Section 7.1, we have that the overall quantum channel can be written as:

$$\Phi(\rho)=\mathrm{Tr}_{\mathrm{pol}}[(|\psi\rangle\langle\psi|\otimes I_{\mathrm{OAM}})U\rho U^\dagger], \tag{7.11}$$

where U is the QW dynamics of Eq. 7.10, $|\psi\rangle$ is the polarization state onto which we project, and $\mathrm{Tr}_{\mathrm{pol}}$ denotes the partial trace with respect to the polarization degree of freedom. The final projective measurement can be written in this notation simply as $\mu_b=|b\rangle\langle b|$. However, it is worth noting that, because of the polarization projection, Φ is technically not a quantum channel, since it can be seen that it doesn't preserve the trace (Supplementary Information of Ref. [77]). Nonetheless, this does not affect the QELM reconstruction procedure and only affects the observed statistics. Therefore, in the following, we can neglect this detail and consider Φ a proper quantum channel.

Experimental Results

For the experimental realization of QELM, we consider two different configurations of the QW dynamics. In the first, we exploit the theoretical knowledge of the dynamics to tune the waveplates angles of the coin $\{\zeta,\theta,\phi\}$ and of the projection to obtain an almost uniform coverage of the OAM space. Conversely, in the second, the angles are randomly chosen and we act only on the training of the accessible output layer to optimize the performance of the characterization protocol.

Giving more details, the optimization of the experimental setup in the first configuration proceeds by exploiting the formalism of the *measurements frames* [381], in order to analyze estimation errors for arbitrary target observables and POVMs.

From the effective POVM measurements $\tilde{\mu}_b$ previously introduced, we can define the canonical *dual measurement frame* $\tilde{\mu}_b^{can}$ that are used as estimator, in the following way:

$$\tilde{\mu}_b^{\text{can}} = \frac{F^{-1}(\tilde{\mu}_b)}{\text{Tr}(\tilde{\mu}_b)/d} \ , \qquad F(X) \equiv \sum_{b\in\Sigma} \frac{\text{Tr}(\tilde{\mu}_b X)\tilde{\mu}_b}{\text{Tr}(\tilde{\mu}_b)/d}, \tag{7.12}$$

where d is the dimension of the underlying state space and F in this context is called *superoperator*. As discussed in detail in [381], this estimator is "optimal" in the sense of being the unbiased estimator for $\text{Tr}(\mathcal{O}\rho)$ with the lowest possible variance when no prior knowledge on ρ is assumed. We have that the variance defining estimation accuracy of the canonical estimator for an observable $\mathcal{O}$ is given by:

$$\overline{\text{Var}[\hat{o}]} = \langle \mathcal{O}, F^{-1}(\mathcal{O})\rangle - \beta, \qquad \beta \equiv \frac{\text{Tr}(\mathcal{O})^2}{d^2} + \frac{dP-1}{d^2-1}V, \qquad V \equiv \frac{\text{Tr}(\mathcal{O}^2)}{d} - \frac{\text{Tr}(\mathcal{O})^2}{d^2}, \tag{7.13}$$

where the constant β, crucially, does not depend on the choice of measurement and $\overline{\text{Var}[\hat{o}]}$ is the variance of $\hat{o}$, averaged over all possible input states. Therefore, by substituting the measurement and evolution of our experimental implementation and minimizing the variance, we obtain the following optimal parameters:

$$\zeta = 0.82223, \quad \theta = 1.14266, \quad \phi = 2.26421, \quad \theta_p = 0.78539, \quad \phi_p = 0.75016 \tag{7.14}$$

where θ_p, ϕ_p are the angle defining the polarization state on which we project at the end of the evolution, that is $|\psi\rangle = \cos(\theta_p)\,|H\rangle + \sin(\theta_p)e^{i\phi_p}\,|V\rangle$. More details on the optimization and the study on how the variance changes when we move from the optimal parameters can be found in Appendix E.

Our experimental implementation aims to exploit the QELM properties to reconstruct the three Pauli operators $\{\sigma_x, \sigma_y, \sigma_z\}$, and therefore characterize the coefficients of the qubit encoded in the input photons polarization. As a figure of merit for the quantification of the protocol performances, we used the MSE introduced in Eq. 7.6. In particular, we collected 300 experimental states and split them into training and test sets, each one composed of 150 elements. The experimental results for the MSE of the retrieved expectation values over the test set are studied against the number N_{train} of states used for the training, the behavior of the MSE for both the configurations is reported in Fig. 7.2.

These results highlight how a large enough training set clearly results in a decrease of the MSE, and thus in significantly enhanced reconstruction accuracies for all considered target observables. Moreover, we see from Fig. 7.2-a that the optimized configuration only results in a slight improvement in the MSE, therefore showcasing how a detailed characterization and a fine-tuning of the setup are not mandatory to obtain high estimation accuracy. Finally, the protocol results to be resource efficient since roughly 20 states are already sufficient to train the QELM and obtain a good estimate of the expectation values. To give a visual representation of the results of the reconstruction protocol, in Fig. 7.3 we reported the Bloch sphere for the first 100 states of the test set, showing in red their true position and in blue the retrieved one by the QELM.

In conclusion, we point out that these results are obtained from a collected statistics for each input state of ~ 3000 counts. As discussed in Ref [377], the amount of statistics collected for each state crucially affects the reconstruction accuracies.

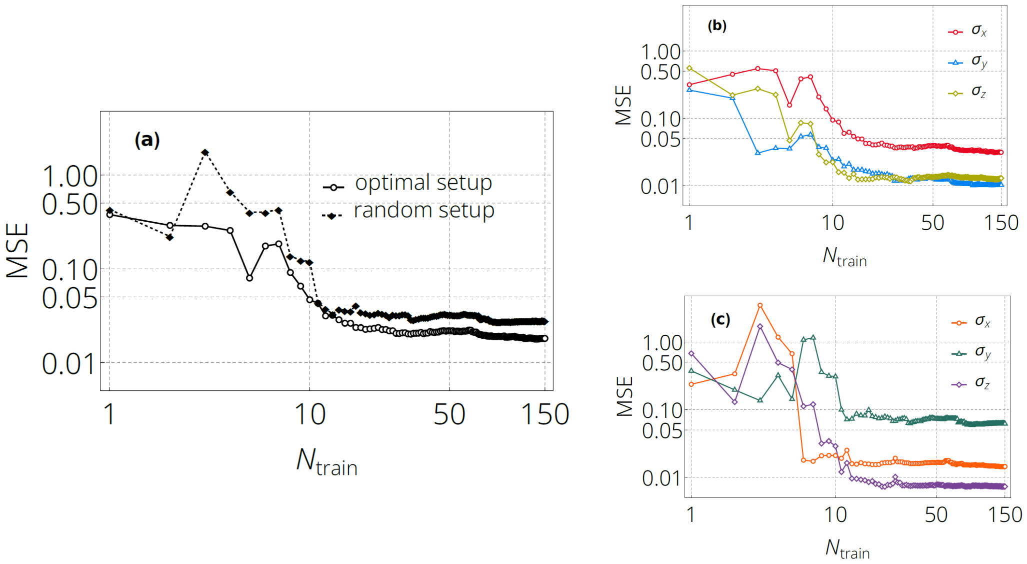

Figure 7.2. Experimental results. Estimation of MSE obtained by training and testing the QELM with experimental data. The target is estimating the expectation values of the Pauli matrices, $\sigma_x, \sigma_y, \sigma_z$ on the input polarization state. We study the MSE as a function of the number of training states N_{train}. To test the protocol, we generated 300 random input states and tested the estimation when the first $1 \leq N_{\text{train}} \leq 150$ are used to train the QELM. The set of 300 states remains unchanged throughout all experiments. The last 150 of these 300 states are always used for testing, to compute the MSE. **a)** Average of the MSE estimated for all three target observables: $\{\sigma_x, \sigma_y, \sigma_z\}$. We show the results for both optimized and random setups. **b)** MSE for each individual target observable for the optimized setup. **c)** MSE for each individual target observable for the random setup. The reported results are obtained with average experimental statistics of ~ 3000 counts.

Therefore, we studied the dependence of the estimate quality on it.

Dependence on the statistics

To explicitly study how estimation accuracies vary with the statistics, we repeated the whole acquisition procedure 12 times, we will refer to these repetitions as *batches* in the following. Specifically, to measure each state in each batch, we projected, via an SLM, and collected data for an acquisition time of $\sim$ 4s. Note that due to the polarization projection probability depending on the input state, the constant acquisition time results in different numbers of observed events for different states.

Each batch contains 300 measured states that are then split in half between training and test sets. We started by repeating the whole training procedure separately for all the 12 batches. This allowed us to assess the stability of the apparatus, the results obtained using the full 150 elements of the training set are reported in Fig. 7.4-a. The observed fluctuations in the MSE are attributed to natural statistical fluctuation, and thermal fluctuations causing perturbations in the experimental apparatus between different batches.

Instead, in Fig. 7.4-b we consider the acquired data cumulatively for each state. In this way, we can study how the estimation accuracy changes with the amount of statistics used to measure it. In particular, we studied the trend of the accuracy as a function of the number of considered batches, where the last point is obtained when the training is performed using the sum of all the collected counts for each

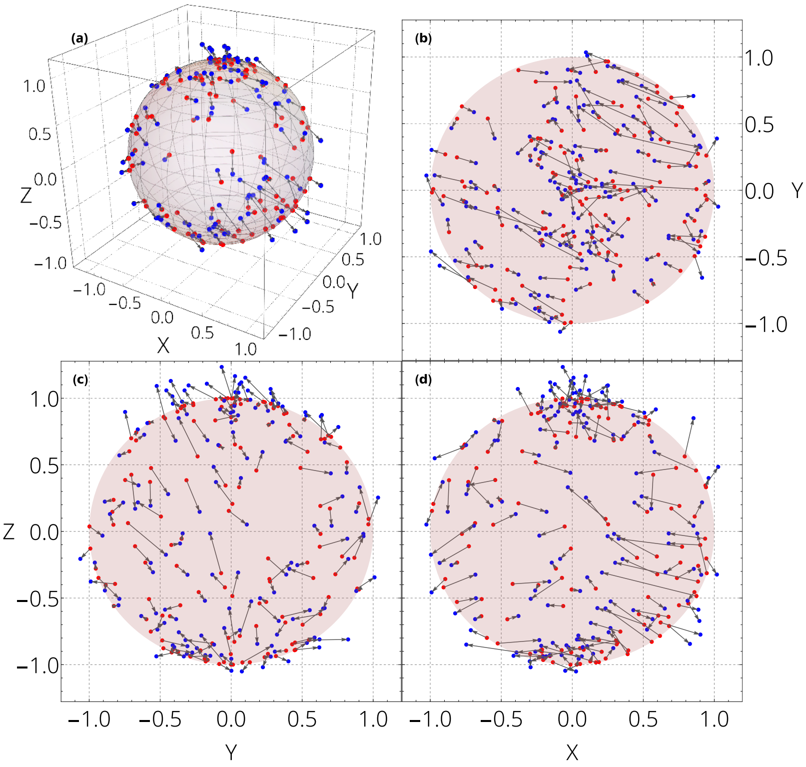

Figure 7.3. Estimated vs true expectation values. Direct comparison between true and estimated expectation values for the three Pauli observables. For each input state ρ, we show in red the point $(\mathrm{Tr}(\sigma_x\rho), \mathrm{Tr}(\sigma_y\rho), \mathrm{Tr}(\sigma_z\rho)) \in \mathbb{R}^3$, while the connected blue point at the end of each arrow shows the reconstruction with the trained QELM. The data shown here corresponds to the first 100 test states, using all training states to train the QELM, with the experimental data obtained with the optimal configuration and using all the available statistics of $\sim$ 3000 counts.

state. As expected, the plot clearly shows how the value of the MSE decreases with the increase of the average number of counts, computed over the whole dataset of 300 elements and reported on the x-axis. Moreover, these results showcase that even in the presence of instabilities in the experimental apparatus (Fig. 7.4-a), which would undermine the reconstruction performances of standard techniques due to systematic errors, the QELM-based approach can automatically account for such imperfections and still provide accurate results.

Comparison with alternative reconstruction methods

To assess the quality of the proposed estimation model applied in our specific experimental implementation, we decided to compare its performances with the one obtained using a standard non ML-based approach. Since we want to estimate the expectation values of target observables, the natural protocol to follow is the framework for the linear reconstruction of target observables for arbitrary POVMs [382–385]. In particular, we use the same approach followed to find the optimal parameters of the setup. Therefore, from the canonical dual frame description, we compute and minimize the estimate variance reported in Eq. 7.13 to obtain the optimal effective POVM operators:

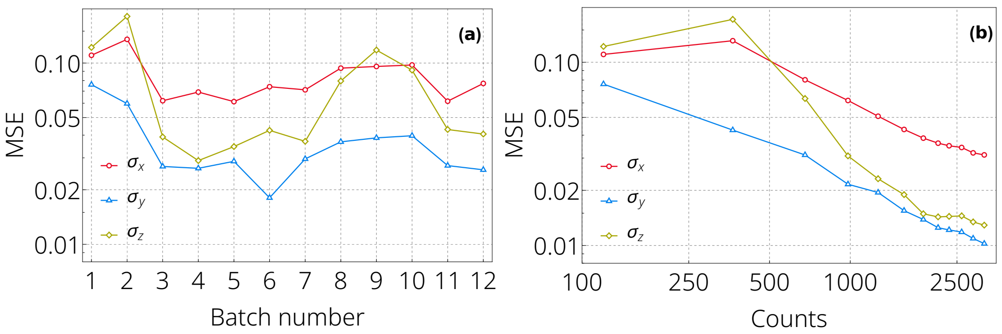

Figure 7.4. MSE vs statistics. Reconstruction MSE for the observables $\sigma_x, \sigma_y, \sigma_z$ averaged over the training states, measuring states with the optimal experimental configuration described in 7.2. **a)** MSE for each of the three target observables, for each batch of collected data. Each batch contains 300 states, half of which are used to train the QELM, and the remaining half is used to compute the reported MSE. Each batch contains the experimental counts obtained measuring the same set of 300 states, and they therefore only differ due to statistical fluctuations and thermal fluctuations potentially affecting the alignment of the apparatus. Training and testing are performed independently in each batch. **b)** MSE for each of the three target observables, where we merge the data in the 12 batches to study how the MSE changes with the amount of collected statistics. We cumulatively merge the statistical data for each of the 300 states used in all 12 batches, thus simulating an experiment where each of the states has been measured with longer and longer acquisition times. The training and testing is then performed on the resulting data.

$$\tilde{\mu}_b = U^\dagger(|\psi\rangle\langle\psi| \otimes \mu_b)U \tag{7.15}$$

where, as before, U is the QW evolution operator, $|\psi\rangle$ is the polarization state on which we are projecting at the end of the QW, and $\mu_b = |b\rangle\langle b|$ with $b \in [-2, -1, 0, 1, 2]$ is the projective measurement on the OAM space. The explicit form of the $\tilde{\mu}_b$ minimizing the variance is reported in Appendix E. Therefore, having the effective POVM operators at hand and leveraging on 7.12, we compute the unbiased estimator for $\mathcal{O}$ as $\mathrm{Tr}(\mathcal{O}\tilde{\mu}_b^{can})$. Then, considering a previously unseen test state ρ that evolves through the setup and measuring it N times, we have that the estimate for $\mathrm{Tr}(\mathcal{O}\rho)$ is given by:

$$\hat{o}_N = \sum_{b\in\Sigma} \mathrm{Tr}(\mathcal{O}\tilde{\mu}_b^{can})\frac{N_b}{N} \tag{7.16}$$

where N_b is the number of times we get b as the outcome from our measurement. Compared with the QELM method, the optimality of the estimator reported in Eq. 7.16 needs that $\tilde{\boldsymbol{\mu}}$ perfectly models the actual experimental setup, so any error in doing that will produce errors into the associated estimation. Instead, QELM does not need an accurate description of the evolution, but only to access a pre-characterized training dataset, which in many scenarios is easier to achieve.

To obtain the best possible performance in the introduced approach, we simulate the evolution and measurement of the same experimental collected states optimizing the estimate of the Pauli operators also on the parameter N, that is the number of times the states enter the setup and it can be seen how the average statistic collected for each of them. The results obtained in this best-case scenario are reported in Fig. 7.5

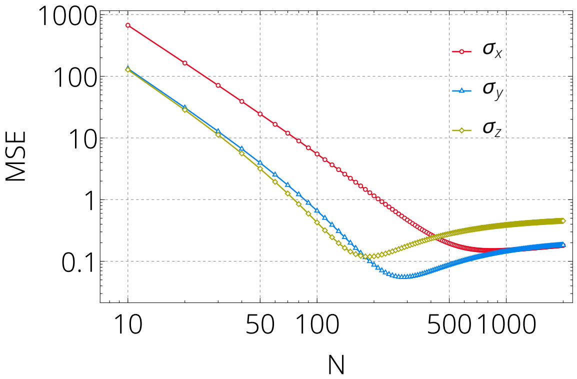

Figure 7.5. Measurement frames reconstruction. We report the MSE for the Pauli observables, using the measurement frames approach, as a function of the prior total statistics N used to compute the estimator with 7.16. This approach relies on the knowledge of the effective POVM $\tilde{\boldsymbol{\mu}}$ and the total number of input states N. The MSE for all observables remains higher than 0.05 in all cases. In particular, for σ_y the minimum is 0.055 at $N = 290$, for σ_x the minimum is 0.15 at $N = 850$, and for σ_z the minimum is 0.12 at $N = 190$.

If we compare the obtained MSEs for the three Pauli operators with the ones obtained exploiting the QELM and reported in Fig. 7.2, we see how the latter presents significantly better performance. In particular, the MSE achieved within the canonical dual frame framework remains higher than 0.05 in all the considered cases. While, with the trained QELM, we reach values always lower with respect to this threshold. In particular, for σ_y and σ_z the MSE is lower than 0.015. It is worth noticing, that in the non ML-based approach, even worse performances are achieved when we move from the best-case and choose for the three operators the same value N, as it happens in practice. Therefore, it follows that the QELM method represents a suitable choice for solving the task of estimating the expectation values of quantum observable.

7.3 Conclusions

In this chapter, we described and analyzed the experimental realization in a photonic platform of a quantum machine learning paradigm. Here, instead of applying ML techniques to our experimental setup, such as done in the previous chapters, we exploit it to implement a QELM. The latter is the quantum version of the ELM introduced in Section 3.2.3, and it has been employed to solve the task of reconstructing the properties of a quantum state.

In particular, entering the setup with a state encoded using the polarization degree of freedom of single photons, we recognize in the QW evolution implemented by our setup (see Section 5.1) the quantum channel that reproduces the reservoir action, which is as the basis of the classical protocol. In our case, the quantum reservoir is used to enlarge the Hilbert space by intertwining the polarization and OAM degrees of freedom, and the reconstruction of the input state features is performed through projective measurement on the output state living in this enlarged space.

Interestingly, the QELM paradigm does not require exactly knowing the reservoir action to solve the task, therefore our protocol can be applied without the need for the accurate and careful characterization of the experimental platform.

The results obtained exploiting the QELM demonstrate the algorithm excellent performance of property reconstruction of a qubit state, through the estimation of the three Pauli operators. This approach is resource efficient since only training sets with moderate size are needed to achieve low values of the MSE of the reconstruction. Moreover, we also saw that the effects of finite statistics of the dataset, that significantly affect the performance of the protocol, can be fully accounted for. Finally, by comparing the QELM performances with a non ML-based method, it was pointed out how QELM represents a suitable choice for solving the task. Indeed, the non-ML-based methods rely on accurate modeling of the experimental apparatus, which can be quite costly to achieve in practice, whereas QELM can easily adapt to experimental fluctuations without significantly impacting the reconstruction accuracies.

In conclusion, our experimental QELM-based reconstruction demonstrates the viability of photonic platforms for non-standard approaches to quantum property retrieval, with the expectation of significantly reducing the burden, in terms of resources, of resource characterization in a computational register. Therefore, presenting promising applications to the reconstruction of high dimensional or multiphoton entangled states, for which direct quantum state tomography methods become impractical.

Chapter 8

Quantum Simulation via Quantum Cellular Automaton

Following the path of the OAM applications in Quantum Information protocols, here we move from studying the properties of a quantum state encoded in this degree of freedom and, instead, we investigate its employment for Quantum Simulation, one of the three Quantum Algorithms classes. For this purpose, we experimentally implemented a one-dimensional Quantum Cellular Automaton (QCA) [82–86]. The latter is a model for universal quantum computation, and it is a natural candidate as a digital quantum simulator of relativistic quantum fields. The notion of a cellular automaton was introduced in classical information theory by von Neumann [386]. This is a discrete model of computation that describes the evolution of a grid of cells through a local update rule, for which the state of a cell changes depending only on the state of the neighbour cells and on itself, and can produce complex behaviours on a macroscopic scale. Moreover, the paradigm has been demonstrated to be Turing-complete [387], i.e. it can implement any classical algorithm.

The quantum version of cellular automata, namely the QCA, was first envisaged by Feynman in his seminal paper [388], where he immediately proposes their use as quantum simulators. A QCA consists of a lattice of finite-dimensional quantum systems, along with an evolution occurring in discrete steps, which can be summarized in a local update rule. In the last years, quantum cellular automata have attracted great interest due to their potential in quantum computation [87–89] and because they are *universal* digital quantum simulators [389–397].

In this context, we focused on the DTQWs which are identified as a special case of a QCA, whose action is linear in the field operators. In particular, we realized a Dirac Quantum Cellular Automaton (DQCA) [78–81], a special case of a fermionic cellular automaton which reproduces the dynamics of a free Dirac field in the limit of small wave-vectors. We experimentally simulated this relativist system through the photonic OAM-based QW, which is an improved version of the platform described in Section 5.1, in which we reach 8 steps of the QW dynamics obtaining a controllable initial state and an arbitrary projective measurement by placing the setup between two SLMs. Encoding the particle position in the OAM of single photons, with this platform we studied the step-by-step evolution of a QW presenting the same dispersion relation of the DQCA and observed the *Zitterbewegung*, a quivering motion of a relativistic particle that, despite being practically impossible to observe in relativistic systems, is considered as one of their benchmark signatures. Indeed, it was also investigated in the pioneering, and to date one of the very few, quantum simulation of the Dirac equation by Gerritsma *et al.* in Ref. [81]. In our work [398], to the best of our knowledge, we achieved the first photonic quantum simulation of Zitterbewegung, demonstrating the capability of photonic platforms to simulate relativistic behaviors, that are difficult to observe in real-case scenarios.

Some of the results reported in this chapter are included in the following works:

- Alessia Suprano, **Danilo Zia**, Emanuele Polino, Davide Poderini, Gonzalo Carvacho, Matteo Lugli, Alessandro Bisio, Paolo Perinotti, and Fabio Sciarrino, "Photonic cellular automaton simulation of relativistic quantum fields: observation of Zitterbewegung", arXiv preprint arXiv:2402.07672v1

8.1 Linear Quantum cellular automaton

A quantum cellular automaton is a computational paradigm that, as its classical analogue, describes the evolution of a grid of cells, but each one is represented by a quantum system. The unitary evolution of the whole system occurs in discrete steps and it is *local.* Specifically, given the state of a cell at time t, this evolves according to a fixed rule U, and at time $t+1$ it depends only on the state at step t of finitely many neighboring cells, including the cell itself.

The QCA shows different behaviors depending upon the dimension of the space in which the grid is embedded, here we will focus on a one-dimensional lattice, more details for the other cases can be found in Ref. [85]. We consider a one-dimensional nearest-neighbor lattice $\mathbb{Z}$ and a local Bosonic (Fermionic) mode per cell. At each site $x \in \mathbb{Z}$ is associated with a field operator $\psi_{x,a}$, where the index $a \in S$ belongs to a finite set S and denotes some internal degree of freedom of the quantum system, that is for instance the spin. Using the Fock representation of the quantum states (see Section 2.1), we have that the N-excitations (particles) states $|(x_1,a_1),\dots,(x_N,a_N)\rangle = \psi^\dagger_{x_1,a_1}\cdots\psi^\dagger_{x_N,a_N}|\Omega\rangle$ where $|\Omega\rangle$ is the vacuum state, i.e the state with no excitations which obeys $\psi_{x_i,a_i}|\Omega\rangle = 0$ for all i. If we consider the particular case of a free, i.e. non-interacting, evolution, the QCA action is linear in the field operators, namely

$$U(\psi_{x,a}) = \sum_{y\in\mathbb{Z}}\sum_{b\in S} U^*_{y,b;x,a}\psi_{y,b}, \tag{8.1}$$

where the coefficients $U_{y,b;x,a}$ turn out to be matrix elements of a unitary operator on the subspace spanned by single-particle states. Thus, this particular one-dimensional dynamics of the QCA, is completely identifiable with a one-dimensional DTQW (see Section 1.2.3). In particular, we have that:

$$\begin{aligned} |\psi(t+1)\rangle =& U|\psi(t)\rangle, \\ U|a\rangle|x\rangle =& \sum_{y\in\mathbb{Z}}\sum_{b\in S} U_{y,b;x,a}|b\rangle|y\rangle \end{aligned} \tag{8.2}$$

Since the considered evolution is translationally invariant, it is convenient to represent the unitary operator U through the momentum representation:

$$U = \int_{-\pi}^{\pi} \mathrm{d}k\ U(k)\otimes|k\rangle\langle k|,\ \ U(k)|\pm\rangle_k = e^{\mp i\omega(k)}|\pm\rangle_k \tag{8.3}$$

where we introduced the plane waves $|k\rangle := \sum_x \frac{e^{ikx}}{\sqrt{2\pi}}|x\rangle$, and, when considering a bidimensional internal degree of freedom, $U(k) \in SU(2)$ is a unitary matrix with eigenvectors $|+\rangle_k$ and $|-\rangle_k$. In our specific case, the one particle sector of the Quantum Cellular Automaton [90, 91, 399] reads as follows:

$$U(k) = \begin{pmatrix} ne^{-ik} & -im \\ -im & ne^{ik} \end{pmatrix}, \quad \omega(k) = \arccos(n\cos(k)) \tag{8.4}$$

for some real numbers n, m such that $n^2 + m^2 = 1$. From here, we can introduce an *effective Hamiltonian* of the evolution H by defining $U := \exp(-iH)$, the latter gives a continuous evolution that interpolates the DTQW one and we have:

$$\begin{aligned} H &= \int_{-\pi}^{\pi} \mathrm{d}k \; H(k) \otimes |k\rangle \langle k| , \\ H(k) &= \frac{\omega(k)}{\sin\omega(k)} \begin{pmatrix} n\sin(k) & m \\ m & -n\sin(k) \end{pmatrix}, \end{aligned} \tag{8.5}$$

Therefore using this formulation, we can describe a linear one-dimensional QCA evolution as a QW and implement it in our setup (see Section 5.1).

8.2 Dirac cellular automaton: simulation of relativistic particles

The description of the previous Section is particularly interesting when we consider the limit of Eqs. 8.5 for small values of m and k. Indeed, in this case, we recover the one-dimensional Dirac equation:

$$i\partial_t \psi(k,t) = (k\sigma_z + m\sigma_x)\psi(k,t) \tag{8.6}$$

Therefore, the linear QCA provides a framework in which to perform quantum simulation of the one-dimensional Dirac free field. In this context, we introduce the concept of *Dirac Quantum Cellular Automaton* (DQCA).

A DQCA can be used to observe relativistic quantum effects pertaining to regimes that are difficult to access experimentally. For instance, the interference of a Dirac particle with its antiparticle that is responsible for the so-called *Zitterbewegung* effect [92, 400, 401], namely the oscillation of the expected value of the position operator X. Direct observation of this phenomenon in particle physics would be prohibitive since it requires preparing a coherent superposition of particle and antiparticle and the oscillation amplitude is of the order of the Compton wavelength (10^{-12} m for an electron).

In our description, introducing the support $\mathcal{H}_+$ (resp. $\mathcal{H}_-$) of the projector $P_\pm := \int \mathrm{d}k \; |\pm_k\rangle\langle\pm_k| \otimes |k\rangle\langle k|$ as the subspace of *positive* (resp. *negative*) *energy* states we can easily simulate this behavior. Indeed, given the position operator $X := \sum_{x\in\mathbb{Z}} x\, I \otimes |x\rangle\langle x|$ and its time evolution $X(t) = U^{-t} X U^t$, we have the differential equation:

$$\frac{\mathrm{d}^2}{\mathrm{d}t^2} X(t) = -[H,[H,X]] \tag{8.7}$$

and for the effective Hamiltonian of Eq. 8.5, the solution reads:

$$\begin{aligned} X(t) &= X(0) + Vt + \frac{1}{2iH}\left(e^{2iHt} - I\right) F, \\ V &:= \int_{-\pi}^{\pi} \mathrm{d}k \; \frac{\omega'(k)}{\omega(k)} H(k) \otimes |k\rangle \langle k| , \quad F := [H,X] - V. \end{aligned} \tag{8.8}$$

where V is the velocity operator and F is responsible for the oscillating motion. Since $FP_\pm = P_\mp F$, we have that the Zitterbewegung occurs only for states which are a superposition of positive energy (particle) and negative energy (antiparticle) states. Indeed, by taking the expectation value of $X(t)$ with respect to a state $|\psi\rangle = |\psi\rangle_+ + |\psi\rangle_-$, where $|\psi\rangle_\pm \in \mathcal{H}_\pm$, we have:

$$\langle X(t)\rangle = x_+(t) + x_-(t) + x_0 + z(t) \tag{8.9}$$

where:

$$\begin{aligned} x_\pm(t) &:= \langle\psi_\pm|\, X(0) + Vt\, |\psi_\pm\rangle \\ x_0 &:= 2\,\mathrm{Re}[\langle\psi_+|\, X(0) - (2iH)^{-1}F\, |\psi_-\rangle] \\ z(t) &:= 2\,\mathrm{Re}[\langle\psi_+|\, (2iH)^{-1}e^{2iHt}F\, |\psi_-\rangle], \end{aligned} \tag{8.10}$$

Therefore we see how the interference between positive and negative energy states causes a shift x_0 of the mean value of the position and an oscillating term $z(t)$. In particular, considering particle and antiparticle states peaked around some momentum eigenstate:

$$|\psi\rangle_{in} = c_+\,|\psi_+\rangle + c_-\,|\psi_-\rangle\,, \quad |\psi_\pm\rangle = \int \frac{\mathrm{d}k}{\sqrt{2\pi}} g(k)\, |\pm\rangle_k\, |k\rangle \tag{8.11}$$

where $|c_+|^2 + |c_-|^2 = 1$ and $|g(k)|^2$ is an envelope peaked around k_0. For small value of t, the oscillating terms can be approximated as follows:

$$z(t) = |c_+||c_-||f(k_0)|\cos(2\omega(k_0)t + \phi_0) \tag{8.12}$$

where we defined $f(k) = \langle +_k|\, F\, |-_k\rangle / (2i\omega(k))$ and ϕ_0 is a suitable phase.

8.2.1 Experimental Simulation of the *Zitterbewegung* effect

Exploiting its connection with a one-dimensional DTQW, we can experimentally reproduce the dynamics of a Dirac particle living in a one-dimensional space by using a setup similar to the one introduced in Section 5.1 (See Fig. 8.1-a). In our work [398], we proposed a photonic simulation platform, in which we employed the two components of the light angular momentum, the SAM and OAM. In particular, being bidimensional, the former was used to reproduce the two states associated with positive and negative energies $\left\{|\psi\rangle_+, |\psi\rangle_-\right\}$ in the circular polarization basis $\{|R\rangle, |L\rangle\}$. Instead, the eigenstates of the OAM were used to codify the particle position $\{|x\rangle, x \in \mathbb{Z}\}$, making thus the relation $|x\rangle = |m\rangle$. This encoding is explicitly reported in Fig. 8.1-b, while a conceptual representation of the simulation approach implemented in our work is shown in Fig. 8.1-c.

With respect to the previously introduced one, the setup proposed in this work goes beyond the present status of experimental OAM-based quantum walk platforms, increasing the depth of the dynamics to 8 steps while having at the same time a controllable initial state and an arbitrary projective measurement stage at the output. In particular, each step is made by a set composed of a QWP and a HWP followed by a q-plate, and the evolution in the simulation framework is given as:

$$U(k) = Q(k)C(\alpha, \beta) \tag{8.13}$$

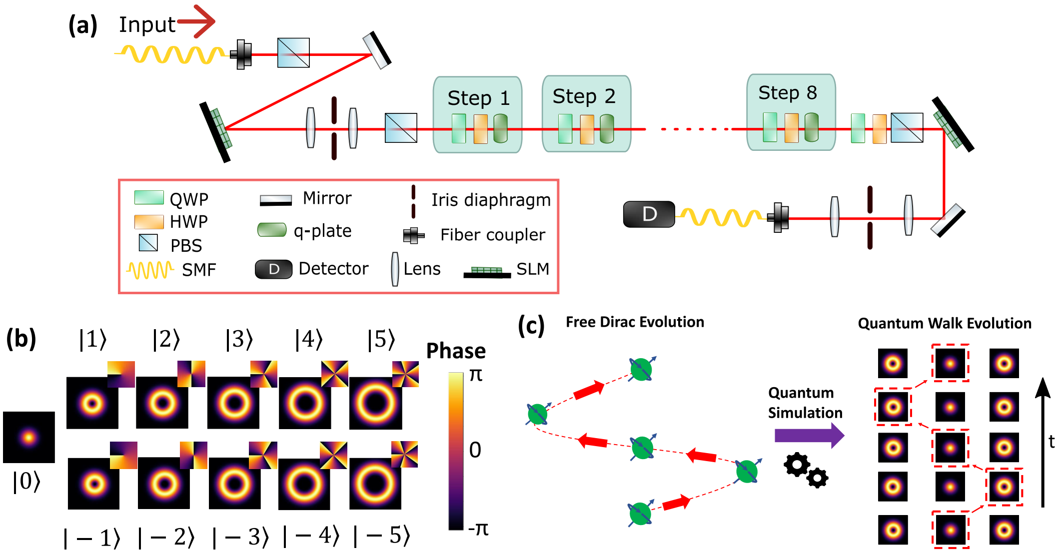

Figure 8.1. Experimental setup: a) The quantum cellular automaton evolution is implemented through an eight-step discrete-time quantum walk in the OAM of light. First of all, single photon states are generated through spontaneous parametric down-conversion in a Periodically Poled Potassium Titanyl Phosphate (PPKTP) non-linear crystal. After projecting the polarization of single photons on the horizontal one through a Polarizing Beam Splitter (PBS), the desired input state is produced via a spatial light modulator (SLM) and, after a spatial filtering performed with an iris diaphragm, is sent to the DTQW. Each step of the latter consists of a coin operator, implemented by a quarter-waveplate (QWP) and a half-waveplate (HWP), and a shift operator performed using a q-plate. Then, the polarization is traced out using a series of QWP, HWP and PBS. The output state probability distribution is measured with a projective measurement executed via a further SLM followed by a single-mode fiber (SMF), the resulting coupled signal is detected by an avalanche photodiode detector. **b)** Mapping between the OAM space and the position space. In particular, each position of the Dirac particle is identified with a different OAM eigenstate. For the latter, we report both the intensity and the phase of the wave function as expressed in the Laguerre-Gaussian modes basis. **c)** The time evolution of a free Dirac particle is simulated through the DTQW platform using the orbital angular momentum of single photons. Here, a modification in the particle position is identified with a variation of the OAM value.

where $Q(k)$ is the q-plate action:

$$Q(k) = \begin{pmatrix} \cos\frac{\delta}{2} & ie^{i2\alpha_0}\sin\frac{\delta}{2}\,e^{ik} \\ ie^{-i2\alpha_0}\sin\frac{\delta}{2}\,e^{-ik} & \cos\frac{\delta}{2} \end{pmatrix}, \tag{8.14}$$

where $k = 2q\phi$ with ϕ the azimuthal angle, and $\delta \in [0, \pi]$ is the q-plate tuning, which controls its conversion efficiency. Instead, $C(\alpha, \beta)$ is the coin operator that in our implementation represents a modification of the polarization state expressed as:

$$C(\alpha, \beta) = \frac{1}{\sqrt{2}} \begin{pmatrix} e^{2i(\alpha-\beta)} & ie^{2i\alpha} \\ ie^{-2i\alpha} & e^{-2i(\alpha-\beta)} \end{pmatrix} \tag{8.15}$$

where α, β are the angles of the fast-axes of the two waveplates with respect to the horizontal one.

The entire setup is enclosed between two spatial light modulators as shown in figure 8.1-a, in a configuration that has been already proven suitable for the implementation of the DTQW dynamics [37, 65]. The inputs of the setup are triggered single-photon states produced via SPDC in a PPKTP nonlinear crystal (for more details see Section 2.4.2). These are coupled into a SMF and then sent to the first SLM, which is used to modulate the spatial profile of photons to obtain the desired initial state of the evolution. In particular, following the description of Eq. 8.11, the input state has the following factorised form:

$$|\psi\rangle_{\text{in}} = \frac{1}{\sqrt{2}}\Big(\,|R\rangle + |L\rangle\,\Big) \otimes \sum_{x\in\mathbb{Z}} g(x)\,|x\rangle\,, \tag{8.16}$$

where $g(x) \in \mathbb{R}$ and $\sum_x |g(x)|^2 = 1$.

The second SLM instead is employed in the measurement stage along with a single mode fiber to project the output state onto the computational basis and extract the occupation probability of each OAM mode [49, 159, 202, 315, 316], enabling thus for the reconstruction of the particle position at each step of the dynamics. Before doing that, the polarization degree of freedom is traced out using a series composed of a QWP, a HWP and a PBS to project on both the $|H\rangle$ and $|V\rangle$ polarization states. In this way, we are able to both measure only the OAM components of the state at the end of the DTQW and to see the interference between its positive and negative energy components.

In our simulation approach, we choose the parameters of the setup to be $\delta = \pi$, $\alpha_0 = \pi/4$, $\alpha = -\pi/4$ and $\beta = \pi/4$ and, therefore, the implemented QW evolution reads:

$$U(k) = \frac{1}{\sqrt{2}}\begin{pmatrix} e^{ik} & e^{ik} \\ -e^{-ik} & e^{-ik} \end{pmatrix}, \tag{8.17}$$

One can show that the dispersion relation $\omega(k)$ of this $U(k)$ is equivalent to that characterizing Eq. 8.4 for $m = n = \sqrt{2}/2$. In particular, we are then interested in those states that are superposition of positive and negative energy eigenstates, and at the peak angular wavenumber k_0 feature the following properties (see Eq. 8.12):

(i) Zero group velocity $\omega'(k_0) = \partial_k\omega(k_0) = 0$, in order to keep the oscillation centered around the initial position ($x_0 = 0$).

(ii) Angular frequency equal to $\omega_0 = \pi/4$, in order to observe two complete oscillations. This is because the Zitterbewegung period is given by $T = 2\pi/2\omega_0$

(iii) Appreciable *Zitterbewegung* amplitude given by $|c_+| = |c_-| = 1/\sqrt{2}$ and $|f(k_0)| = 1$

Therefore, we use the initial SLM to shape the photon field creating a Gaussian superposition of the OAM eigenvalues between $|-5\rangle$ and $|5\rangle$, centered in $x_0 = |0\rangle$, and with standard deviation $\sigma = 3.0$, that is $g(X) = \mathcal{G}_{x_0,\sigma}(x)$. For such a spatial distribution, the wavefunction in momentum representation resembles a normal distribution peaked at $k_0 = 0$ and with standard deviation $1/\sigma = 1/3$. Moreover, the initial $|H\rangle$ polarization, needed to work with our SLM (see Section 2.5.2), automatically respects the requirement of point (iii).

Within our setup, we studied the step-by-step dynamics of the evolution by simply switching on the right number of q-plates. In particular, for each step, we turned on the relative q-plate setting $\delta = \pi$, traced out the information stored in

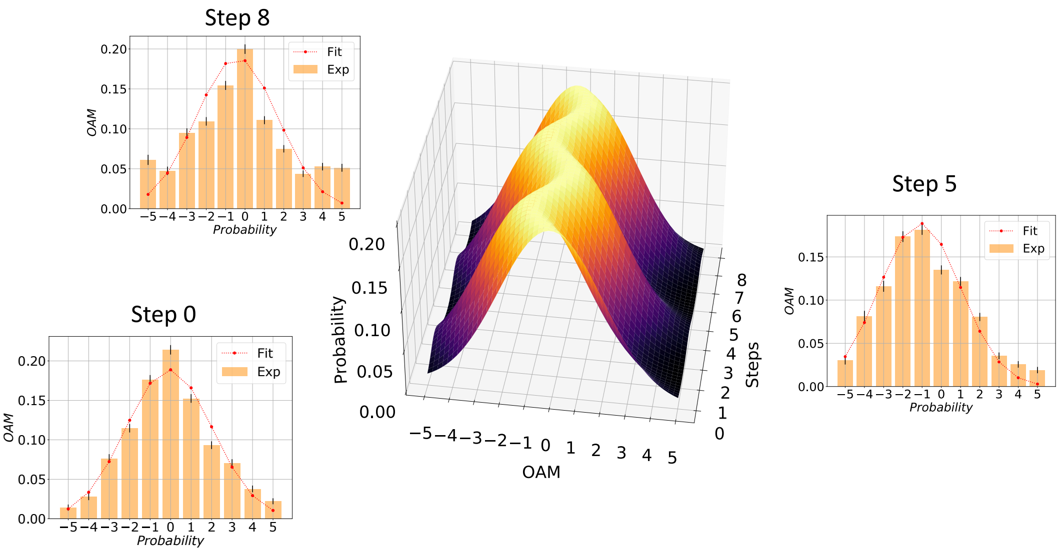

Figure 8.2. Data analysis: Representation of the Gaussian fit performed on experimental data. The 3D function shown is obtained by fitting the experimental data with the function in Eq. 8.18, where the assumed theoretical model is characterized by a Gaussian distribution that oscillates around the initial position during the evolution. In side panels, the comparison between the experimental distribution and the fitted function is reported for three different steps of the evolution (here 0 represents the input state). Although satisfactory similarities can be observed, the difference between histograms and plotted curves increases with the step evolution and this is mainly due to experimental imperfections. The reported errors in experimental data are due to the Poissonian statistics of the measured counts.

the polarization, and measured via the second SLM and the SMF the walker state distribution over the computational basis $\{|i\rangle\}_{i=-5}^{5}$, opportunely taking into account for the efficiencies of the measurement holograms [49, 202]. From the measurements, we extracted the occupation probabilities of each site and derived the evolution of the mean position.

From a theoretical perspective, we expect a Gaussian distribution that oscillates around the position $x = 0$ during the evolution. The oscillation of the Gaussian peak follows the sinusoidal expression in Eq. 8.12 with frequency $\omega = 2\omega(k_0) = \pi/2$ and amplitude $A = |c_+||c_-||f(k_0)| = 0.5$. Since, in the experiment, we focused only on the portion of the distribution between $x = -5$ and $x = 5$, the reference values for ω and A are different. Therefore, at each step, we performed a fit over the distributions in a truncated interval of the position space spanned by $x \in [-5, 5]$ with Gaussian functions whose mean values oscillate along the evolution direction:

$$f(t, y) = \frac{e^{-(y-\mu_0-A\cos(\omega t+\phi))^2/(2\sigma^2)}}{\sigma\sqrt{2\pi}} \tag{8.18}$$

where t represents the step of the DTQW, y the values of probability distributions over the OAM basis, μ_0 the mean of the Gaussian distribution and σ its standard deviation. This fitting procedure is used to derive the oscillation parameters for both theoretical and experimental distributions. The results in the experimental case are shown in Fig. 8.2, where the 3D plot reports the time evolution of the fitted Gaussian envelopes. From both the fit on the theoretical noiseless model for the evolution and the experimental implemented one, we derived the value of the two parameters characterizing the Zitterbewegung oscillations, the amplitude A and the frequency ω_0. In the theoretical case, we retrieve values equal to $\omega = 1.714 \pm 0.017$ and $A = 0.695 \pm 0.032$, and experimentally we observed an oscillation very similar to this with $\omega = 1.655 \pm 0.009$ and $A = 0.615 \pm 0.017$. The two behaviors are reported in Fig. 8.3, where the yellow dashed lines represent the oscillations of the mean values of the fitted Gaussian functions. From both numerical results and plots shown in Fig. 8.3 it can be seen how the implemented platform is capable of simulating the dynamics of a free relativistic particle, reproducing its typical Zitterbewegung trembling motion.

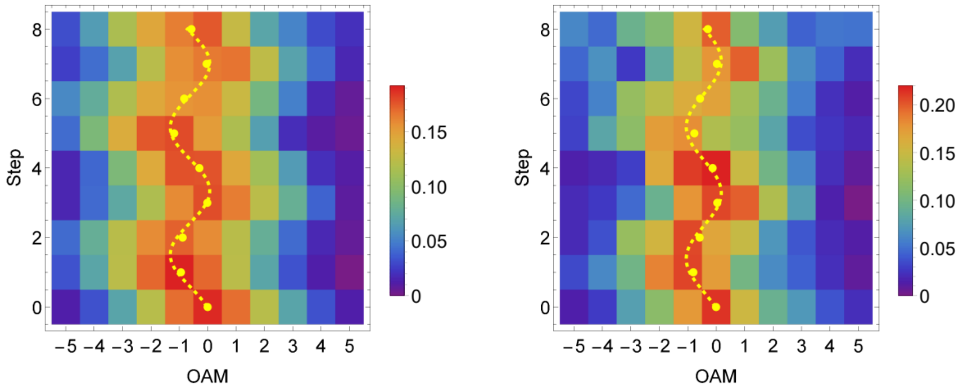

(a) Ideal distribution

(b) Experimental distribution

Figure 8.3. Zitterbewegung dynamics: The plots show the output state distribution over the OAM computational basis for each time step considered, we indicate with 0 the initial input state. In **a)** it is reported the evolution obtained following the ideal noiseless model of the quantum walk, instead in **b)** experimental data are shown. Yellow points represent the behavior of the mean position during the steps of the evolution while the dashed line is obtained as the step-dependent mean values of the fitted Gaussian functions.

8.3 Conclusion

In this chapter, we showcased the employment of our photonic QW platform for a quantum simulation protocol, by reproducing the well-known QCA computational paradigm. In particular, we focused on its one-particle sector, describing the state evolution of a one-dimensional grid of cells and connecting it to the one-dimensional Dirac equation. Thus, we experimentally realized a DQCA and studied the evolution of a Dirac free particle. We reproduce a typical behavior that appears during the free space propagation of a Dirac particle, namely the *Zitterbewegung*. This is a trembling motion that emerges in the expected value of the particle position and it is the result of the interference with its antiparticle (see Eqs. 8.9-8.10).

Exploiting the angular momentum components of light, we codified the particle and antiparticle states with the polarization degree of freedom, while the position was identified with the eigenvalues of the OAM carried by the photons. Specifically, we extended the previously introduced platform (see Section 5.1), by using a cascade of 8 q-plates interspaced with waveplates, and we placed the whole setup between 2 SLMs. This, advancing the state-of-the-art of OAM-based DTQW platforms, allowed us to have high control over the input state and the capability to perform 8 steps of the automaton evolution. We studied the dynamics step-by-step by switching on the q-plates, and, from the reported results, we see the capabilities of the simulation platform in reproducing the Zitterbewegung effect. Indeed, we observed an oscillatory behavior in the OAM space with an amplitude and a frequency in agreement with the theoretical predictions (see Fig. 8.3), simulating an effect that for its characteristics is prohibitive to observe in particle physics both for its amplitude and since it needs to have a coherent superposition of particle and antiparticle states.

In conclusion, the proposed experimental protocol constitutes a first step towards the simulation of more complex dynamics where position-dependent evolutions are necessary, such as the Dirac particle evolution subject to external potential [394, 402] and curved spacetime [393, 403, 404], and paves the way for photonic implementations of QCAs.

Conclusions

From the beginning of its formulation, photonic technologies and platforms have been extensively used as testbeds for the implementation of Quantum Information protocols, such as the milestone violation of Bell's inequality and the quantum teleportation experiments. In practice, several degrees of freedom of the photons are exploited to codify information in the computational elements, namely the *qubit* and *qudit* states. In particular, the latter represent pivotal resources, since they allow one to encode a great amount of information on a single carrier, with benefits for the computation, and enable more secure communication schemes. In this thesis, we focused on the two components of light angular momentum as information encoders, developing protocols relying on OAM states and concerning: (i) their generation, (ii) their manipulation and measurement, and (iii) their application in different Quantum Information tasks. For each of these subjects, we proposed innovative and state-of-the-art methods that showcased high performances and present a broad range of applications, being propitious for the further development of OAM-based technologies.

In the first chapters, we gave an introduction to the basic concepts which represent the theoretical background of the thesis. In particular, we started by reporting fundamental notions of Quantum Mechanics and Information, useful for the comprehension of the underlying framework and formalism. Then, we furnished an overview of photonic technologies, from the classical and quantum description of light to the single photons sources and the manipulation of the angular momentum. Finally, we concluded the beginning part by outlining the relevant machine learning paradigms that have been experimentally applied in our work. After these opening parts, we proceed by delineating the main results achieved during the Ph.D. program.

In our work, we began by developing protocols for the generation of OAM states, employing both probabilistic SPDC and nearly deterministic QD sources. In the former case, we analyzed the spatial structure of the idler and signal photons emitted by a BBO nonlinear crystal. In particular, we focused on the simple case of the SPDC process for a thin crystal and investigated the produced biphoton state for several input pump beams. In this approximation, the spatial structure of the pump is transferred to the state of the emitted photons, and we studied OAM and parity conservation, radial mode correlations, and the production of high dimensional entangled states in the OAM. Indeed, they are automatically created by SPDC sources and we proposed an approach for a fast and reliable characterization of such states, to certify their generation before employing them in Quantum Information protocols. In particular, our method is based on the off-axis digital holography techniques, well-known in classical optics, and exploits a time stamping single photons sensitive camera. The latter was used to collect an image of the biphoton state produced by the superposition among a reference beam and an arbitrary pump. From this, making use of the knowledge of the reference beam properties, it was possible to extract in post-processing the state induced only by the arbitrary input beam. The proposed approach showed enhanced performance to projective measurement ones, reaching high values of the fidelities on a 10x10 dimensional subspace while improving the state reconstruction time of 3 orders of magnitude. However, since the probabilistic nature of the SPDC sources limits their employment, being detrimental to the protocols security, and their brightness, we decided to investigate a nearly deterministic source, namely a semiconductor QD. We combined it with q-plate devices in an interferometric setup, which enabled us to generate intra- and inter-particle entangled states. For the former, using just one arm of the interferometer, we produced on-demand entangled state between the OAM and polarization of a single carrier, namely a VVB. While, for the second one, we exploited a bulk BS to implement a probabilistic gate able to entangle the OAM of two subsequently emitted photons by the QD source. The quality of the produced states was estimated in both cases by performing quantum state tomography and violating Bell's inequalities. This simple and effective scheme could be extended to the multi-photon regime, opening the way to high dimensional multi-photon experiments, whose scalability is extremely demanding for platforms based on probabilistic sources.

After studying the sources of OAM states, we moved to implementing an engineering platform for efficiently creating arbitrary qudits in the OAM space, having thus more control over the produced states while increasing their dimension. We relied on a protocol based on the QW dynamics, which is therefore platform independent and has been proven capable of engineering high dimensional quantum states both theoretically and experimentally. Since the walker evolution is conditioned by its internal coin state, the approach opportunely selects the operators acting on the latter to produce the desired superposition in the walker space. We investigated its experimental realization using the two angular momentum of light components, encoding the coin and walker states respectively in the polarization and OAM degrees of freedom. Therefore, the experimental setup consists of a set of waveplates, implementing the coin operators, and q-plates, reallizing the conditional shift of the walker, placed in a cascaded configuration. This design presents advantages for what concern the scalability of the approach. Indeed, since the dynamics lies in the same beam, the number of optical elements required to generate a given state increases linearly with the Hilbert space dimension. Despite being proven effective in solving the task, the engineering protocol relies on the assumption of an ideal experimental setup, not accounting for detrimental imperfection and noises. To address this problem and improve the quality of the produced states, we proposed the employment of a black-box optimization algorithm. Indeed, since it doesn't need to be imbued with any description of the setup, it automatically accounts for experimental errors in the procedure. We tested this feature by using the RBFOpt algorithm to tune the waveplate angles while furnishing to it as input only the measured fidelity of the produced states. We demonstrated an enhancement in the fidelity values for several states with respect to the direct theoretical protocol, assessing therefore the capability of the approach to compensate for incomplete characterization in experimental scenarios. We also studied the algorithm response to external perturbation, showcasing its capability to adapt to sudden changes. Since the algorithm does not require information on the function to be optimized and on the employed experimental setup, our scheme can find applications in different engineering protocols. By making use of the platform-independent nature of the DTQW, its dynamics can be straightforwardly implemented by employing several degrees of freedom such as time, frequency or path. Furthermore, the proposed approach can be applied to various Quantum Information implementations, that make use of controllable device parameters. Indeed, through an appropriate tailoring of the cost function, it could be used to deal with tasks outside the quantum state engineering. The scaling of the OAM-based DTQW to larger dimensions can be feasible by opportunely addressing for the divergence of the beam, for example through the adoption of collimation systems of lenses or implementing a platform that make use of a loop configuration. Moreover, moving to the multiphoton regime, the QW dynamics can be used to study several phenomena, such as the entanglement transfer.

Another issue that has been tackled during the thesis is the problem of accurate detection of OAM states, which is mandatory to retrieve the encoded information. We addressed the problem in our engineering platform both improving a widely used measurement approach, namely the holographic technique, and proposing ML-based methods, solving classification and regression tasks on OAM states. Therefore, analyzing the photon propagation inside the setup, we started by retrieving a refined model (HyGG model) that accounts for the diffractive effects of the cascade of q-plates. This has been used to give a better description of the platform output states and to construct more faithful holograms, that, when shown to the SLM, increased the coupling efficiency to the SMF producing an improvement in the reconstruction fidelities of the quantum states, thus enhancing the performances of the holographic technique. This refined model was also applied in a ML-based method to generate simulated images of the VBBs engineered with our setup. Here, casting the measurement as an image recognition task, thanks to an RGB encoding of the VVBs polarization state, we employed a CNN and observed an increase in the prediction accuracy over 15 classes, corresponding to as many different states, when using the HyGG improved model. However, this approach just recognizes the OAM content of VBBs without retrieving a complete description of the superposition. To achieve also this goal, we adopted a different ML paradigm, namely a combination of PCA and linear regression, working thus in a mixed unsupervised and supervised fashion to obtain the coefficients from images of arbitrary OAM states. By solving the inherent problem related to the symmetry of OAM modes, that dumps the recognition performance, and obtaining thus high values for the fidelities for the reconstructed states, we demonstrated how ML can be effectively employed in OAM detection protocols.

Finally, after studying and addressing the principal problems arising when working with the OAM, we employed it and our QW platform for Quantum Information protocols. We first investigated its application in the field of QML by identifying the QW dynamics as the quantum channel of a QELM. In the latter, the OAM states represent the hidden layers of the reservoir, and the paradigm has been applied to reconstruct the quantum state of polarization-encoded qubits. Since we reached low values for the errors in the estimation of the three Pauli operators while considering limited statistics for the data and without accurately characterizing the setup, we demonstrated a robust and resource-efficient QELM-based property reconstruction protocol. Moreover, individual target observables of interest can be accurately reconstructed with statistics that do not scale with the state dimension but rather depend on specific symmetries of the overall dynamic and measurement. The approach can therefore be adapted to work with high dimensional or multi-photon input states with promising reconstruction performances. Thereafter, we also demonstrated the simulation capabilities of the QW setup. In particular, it can be shown that the evolution of a one-dimensional Dirac free particle can be reproduced by the one-dimensional QW dynamics, in the limit of small wavevectors. Therefore, we showcased the photonic implementation of a QCA computation paradigm, that is able to simulate features typical of the Dirac free particle evolution, namely we experimentally realized a DQCA. In this context, we built a state-of-the-art

OAM-based QW platform, that allowed us to have high control over the input state and the capability to perform 8 steps of the automaton evolution. The simulation power of the DQCA was used to reproduce the Zitterbewegung oscillatory behavior when encoding the particle position in the OAM of single photons. These results represent a proof of principle for the photonic realization of a QCA, but they pave the way for further implementations that consider more complex dynamics.

The reported findings represent an important step in the development of high dimensional Quantum Information protocols in photonic platforms. Addressing the central topics of generation, engineering and detection, we proposed methods that can be useful tools for future developments of OAM-based implementations. In particular, the interferometric approach to state reconstruction can be applied to study the photons transmitted or reflected by an object in quantum imaging experiments. Moreover, the detection techniques, especially the ML-based one, could be useful for implementations outside the controlled laboratory environment, namely in fiber and free air quantum communication and key distribution schemes. Finally, QELM and DQCA, being seminal realizations promise to be powerful instruments to employ in the framework for both observables estimation and dynamical simulations.

Appendices

Appendix A

EPR Paradox and Bell's inequality

In Section 1.1 we introduced the concept of separable and entangled states. In this Appendix, we give further details about them, describing in detail the EPR paradox and deriving the violation of Bell's inequality, also dwelling on its possible loopholes.

A.1 EPR Paradox: Quantum Mechanics incompleteness

The intriguing non-classical aspect of entanglement was first highlighted by the seminal paper of Einstein, Podolsky and Rosen (EPR) in 1935 [107], in which the authors attempted to demonstrate through a paradox the *incompleteness* of Quantum Mechanics in describing the physical reality.

In particular, a theory is successful if it is capable of accurately predicting the experimental results and it is complete. The EPR discussion moves upon the following 3 definitions:

Completeness of a theory: *A theory is said to be completed if every element of the physical reality has a counterpart in the theory.*

Physical reality: *A physical quantity is an element of reality if, without disturbing the system in any way, we can predict its value with certainty (i.e. with unitary probability).*

Locality principle: *Given two non-interacting systems, the evolution of the single system is not affected by the operations performed on the other system.*

Assuming the completeness of the quantum theory together with the concept of reality and locality, EPR showed a paradox that questions the completeness of the theory. For simplicity, we decide to follow the discussion of the EPR paradox made by Bohm and Aharonov in 1957 [405].

Suppose we have a bipartite system of total spin zero, divided into 1/2 spin particles produced by the same source and then sent to two distant parties. The total system is described by the singlet state:

$$|\psi\rangle = \frac{1}{\sqrt{2}}(|\uparrow\rangle_1 |\downarrow\rangle_2 - |\downarrow\rangle_1 |\uparrow\rangle_2) \tag{A.1}$$

where $\{|\uparrow\rangle, |\downarrow\rangle\}$ are the eigenstates of the operator σ_z, that is the spin operator along the z-axis. The singlet state is maximally entangled.

A property of this state is its invariance under rotations, thus it can be rewritten in the same form using both the eigenvalues of σ_x and σ_y, respectively the projection of the spin over x, y.

Then, if two observers decide to perform a spin measurement on each subsystem, their results will be perfectly anti-correlated whenever they choose the same axis of observation. Assuming the local realism, and so the fact that a measurement over one subsystem doesn't affect the state of the other, we can gain access to the value of the spin of system 1 along a specific direction in two ways. Both directly measuring the spin of subsystem 1 or making use the correlation present in Eq. A.1 and measuring the spin of subsystem 2. In this way, one can simultaneously know the values of the spin projection over several axes, making each of them an element of reality for the previous definitions,

However, in Quantum Mechanics the spin of a particle along a direction is not compatible with the one along another direction, indeed the Pauli operators, which are associated with spin, don't commute. Hence, for Heisenberg's principle, it is not possible to know with arbitrary precision the value of the spin along different directions. Therefore, assuming local realism and the completeness of the theory, EPR showed that two physical quantities with non-commuting operators can be simultaneous reality elements. This contradicts Quantum Mechanics foundations, and it is why the authors concluded that the quantum mechanical description of Nature isn't complete [107], since abandoning local realism was inconceivable for them. Hence, at the end of the discussion, they claimed that quantum theory should be replaced with a theory in which new additional degrees of freedom, called *hidden variables*, would allow to describe reality in a completely and deterministically manner.

A few months after the publication of the EPR article, Bohr attempted to defend the completeness of the theory [406]. Its theoretical argumentation relies on the ambiguity of the reality criterion proposed by EPR, pointing out the impossibility of distinguishing between the elements of physical reality and their interaction with the measuring instruments. In this way declaring that is not only impossible to determine the value of incompatible quantities at the same time, but they can be defined only in an ambiguous way. Excluding in this way the possibility of knowing them with certainty and without perturbing the system.

A more practical approach to rule out the conclusion reached by EPR was proposed in 1964 by Bell [106], showing that not the completeness of the theory but its local description should be questioned and that any theory based on local hidden variable could not account for the correlations emerging when measuring an entangled quantum state.

Thus, the EPR paradox highlighted for the first time, using entangled states, the non-local character of Quantum Mechanics.

A.2 Bell's theorem and quantum nonlocality

Bell's theorem represents a central step in the debate on the completeness of Quantum Mechanics and the existence of Local Hidden Variable (LHV) models [106]. In particular, Bell demonstrated that the EPR proposal of completing Quantum

Mechanics with LHV models is impossible, proving the inconsistency of every LHV model with Quantum Mechanics predictions. In his argumentation, Bell derived a set of inequalities for the correlation of quantum observables that enable an experimental test of the theories. Every LHV model must satisfy these inequalities, while they are violated by Quantum Mechanics.

We now describe the Bell inequality formulation proposed by Clauser, Horne, Shimony and Holt in 1969 [407], called CHSH inequality, which is suitable to be tested in experimental scenarios. Let's consider the experimental scenario reported in Fig. A.1, here two subsystems are generated from the same source (S) and then divided between two parties, Alice a) and Bob b), that will perform measurements on them. We assume that the correlations measured by the two observers are due to a common hidden variable Λ.

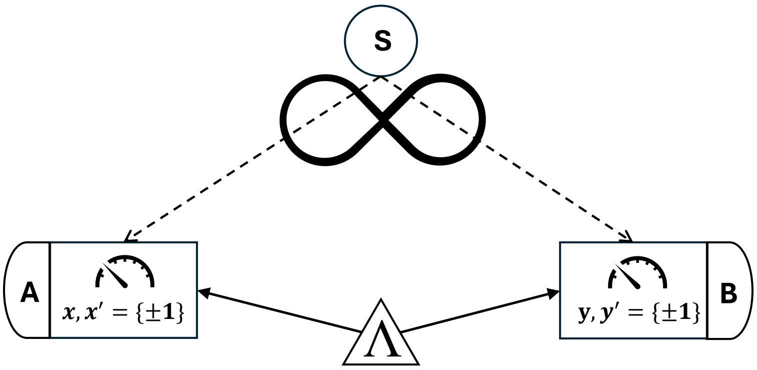

Figure A.1. Bell Scenario. A source (S) generates two subsystems that are divided between two parties, Alice (A) and Bob (B), that are separated by a space-like distance. Each of them chooses to perform a dichotomous measurement, respectively x, x' or y, y'. A LHV provides that the correlation in the measurement can be classically explained through a hidden and local variable Λ.

Suppose that each observer performs a dichotomous measurement. i.e. measurement with results $\{-1, 1\}$ such as the spin projection along an axis. Defined $\{a, b\}$ the measurement results at each station for a specific choice x or y of measured observables, and taken $\mu(\lambda)$ as the continuous and normalized distribution of the values λ that the hidden value Λ can assume. The correlation between the measurement outcomes can be written as:

$$\begin{aligned}\langle A_x B_y \rangle &= \sum_{a,b} \int_\lambda ab\, p(a,b|x,y,\lambda)\mu(\lambda)d\lambda \\ &= \sum_{a,b} \int_\lambda ab\, p(a|x,\lambda)p(b|y,\lambda)\mu(\lambda)d\lambda\end{aligned} \tag{A.2}$$

where in the second line we have made use of the locality assumption, for which the measurement outcome in Alice's system cannot depend on the measurement choice made in Bob's one, and vice versa.

Considering also another set of measurements x' and y' respectively for Alice and Bob, we can define a linear combination of correlations between the outcomes and can demonstrate that *any* LHV respects the following bound [407]:

$$|S| = |\langle A_x B_y \rangle - \langle A_x B_{y'} \rangle + \langle A_{x'} B_y \rangle + \langle A_{x'} B_{y'} \rangle| \leq 2 \tag{A.3}$$

This is the CHSH inequality, and the main reason for which LHV respects this inequality is the locality assumption [408].

The inequality A.3 can be instead violated by quantum entangled systems by appropriately choosing the state and the measurement set. For instance, taking the Bell state $|\Psi^-\rangle$ (see Eq. 1.23) and choosing as measurement observables the Pauli operators $\{A_x = \sigma_x, A'_x = \sigma_z\}$ for Alice and their combination $\left\{B_y = -(\sigma_x + \sigma_z)/\sqrt{2}, B_{y'} = (\sigma_z - \sigma_x)/\sqrt{2}\right\}$ for Bob (the matrix expression of Pauli operators can be found in Section 1.2.1), we have that:

$$S_{mq} = 2\sqrt{2} > 2 \tag{A.4}$$

This violation showcases how it is possible to find systems for which quantum mechanic predictions differ from the one made using *any* local hidden variable theory. Hence, even if LHV can reproduce part of the prediction of Quantum Mechanics, they cannot completely account for all of them. In particular, the value $2\sqrt{2}$ is the maximum obtainable in Quantum Mechanics representing an upper bound called *Tsirelson bound* [409], which is reached by maximally entangled states.

It is worth noting that Bell's theorem and the inequality violation do not establish the validity of Quantum Mechanics over hidden variable theories, but they rule out the local causality principle that had been placed as one of the assumptions of the EPR paradox. Therefore, any hidden variable model that wants to complete the quantum theory should be intrinsically nonlocal, in terms of local causality. This kind of nonlocality is compatible with special relativity, indeed it is not possible to transmit information in a superluminal way exploiting entanglement [108].

A.2.1 Loopholes in experimental tests of Bell's inequality

It is conceptually clear how to theoretically violate Bell's inequality, however performing it experimentally requires more caution, and additional assumptions are usually made. Even if Bell's theorem doesn't give a specific indication about the experimental setup, being in this sense essentially *device-independent*, it is needed to exactly reproduce the causal structure pictured in Fig. A.1. This implies that we should not allow Alice and Bob to have hidden communication and that we need to collect sufficient statistics, to eliminate possible fake violations. Indeed, experimental imperfections when not accounted for and resolved allow the LHV models to violate Bell's inequality. Such imperfections are called *loopholes*, here we give examples of the most important ones:

- **Locality Loophole:** This loophole regards the possibility that a hidden variable could communicate the choice and/or the results of measurements between a station and the other, in this way emulating the quantum behavior. To avoid this possibility the two measurement stations are separated by a space-like distance. In this way, from special relativity, no hidden signal could link the two apparatus. The first experiment closing this loophole was the pioneering work of Alain Aspect in 1982 [23].
- **Measurement Independence Loophole:** This loophole is connected to the free will in the choice of the system under investigation and the measurement set decided to use to test its entanglement. This can be closed only under reasonable assumptions, since we cannot exclude the existence in an arbitrary past of a common cause under the choice of the state and the measurement stages. In practice, we can close it by increasing the likelihood of this independence. To do so several methods have been used, for instance relying on

random number generation based on quantum effects [410, 411] or exploiting the human free-will [412].

- **Detection Loophole:** This loophole is connected to the limited efficiency of the detector used while performing the measurement. Since in practice, this is always lower than 100%, some particles are detected and some others not, producing an alteration in the statistics. For instance, we can think that the only particles measured are the ones that violate the Bell's inequality. The assumption that we can make is called *fair sample assumption*, which states that the detected events are a representative fraction of the total. However, also without this assumption, LHV can be ruled out if the efficiency of our detectors is greater than a certain threshold η_{min}. For instance, for maximally entangled state and CHSH inequality it is possible to show that $\eta_{min} = 2\sqrt{2} - 2 \sim 82.8\%$ [108]. The violation of Bell inequalities closing detection loophole was realized in different experiments [413–415]

Recently, strong evidence of Bell nonlocality has been demonstrated by experimental results obtained within setups capable of closing all the relevant loopholes *simultaneously* [416–418].

Appendix B

Off-axis Digital Holography: Hermite-Gaussian modes, phase matching function and quantum imaging

In Section 4.1, we described the spatial structure of the photon pairs generated through SPDC in a nonlinear crystal. In particular, working in the image plane of the crystal, in which the observed correlations can be described using the thin crystal approximation (see Eq. 4.7), we focused our attention on the produced biphoton states when the input pump beam is a LG mode. Then we studied the conservation of the OAM and the entanglement in this degree of freedom.

Here, instead, we analyze the case in which we use different modulations for the entering beam. Specifically, we start by using the SLM to shape $\mathcal{E}_p$ as an HG mode (see Eq. 2.59) and therefore we can expand the output beam in the same basis:

$$|\Psi\rangle = \sum_{m_i,n_i}^{m_s,n_s} K_{m_i,n_i}^{m_s,n_s} \, |m_i, n_i\rangle \otimes |m_s, n_s\rangle \tag{B.1}$$

Where:

$$\begin{aligned} K_{m_i,m_i}^{m_s,n_s} &= (\langle m_i, n_i| \otimes \langle m_s, n_s|) \, |\Psi\rangle = \\ &= \mathcal{N} \iint \mathcal{E}(x,y) HG^*_{m_i,n_i}(x,y) HG^*_{m_s,n_s}(x,y) dx \, dy. \end{aligned} \tag{B.2}$$

In this case, we have that the spatial modes parity is conserved [419]. In particular, we have the conservation laws:

$$n_p = \mathrm{mod}(n_i + n_s, 2) \quad \text{and} \quad m_p = \mathrm{mod}(m_i + m_s, 2) \tag{B.3}$$

These can be derived from the coefficients of the expansion reported in Eq. B.2. Indeed, since $HG_{m_p,n_p}(x,y) := \langle x,y|m_p,n_p\rangle \propto \exp\Big(-(x^2+y^2)/w_p^2\Big) H_{m_p}(x/w_p) H_{n_p}(y/w_p)$ where $H_m(x)$ is the Hermite polynomial of order m, we can decompose the pump beam as $\mathcal{E}(x,y) = F_x(x)\, F_y(y)$ where F_x and F_y are even or odd functions of x and y. Therefore, we have that $K_{m_i,m_i}^{m_s,n_s} = I_{F_x} \times I_{F_y}$, where:

$$I_{F_\xi} := \sqrt{\mathcal{N}} \int_{-\infty}^{\infty} e^{-2(\frac{\xi}{w_p})^2} F_\xi(\xi) h_{l_i}\left(\frac{\xi}{w_p}\right) h_{l_s}\left(\frac{\xi}{w_p}\right) d\xi \tag{B.4}$$

with $l = m, n$ for $\xi = x, y$, respectively. The product $h_{l_i}\left(\frac{\xi}{w_p}\right) h_{l_s}\left(\frac{\xi}{w_p}\right)$ is even/odd if $l_i + l_s$ is even/odd. Thus, the integral is zero if the parity of F_ξ is different than the parity of $l_i + l_s$, hence the conservation laws of Eq. B.3.

We investigated this property for 3 different HG input modes, the results for the reconstructed biphoton states are reported in Fig. B.1. It shows the amplitudes and phases retrieved with the digital off-axis holography together with the estimated fidelities, and from the chessboard-like correlation patterns we can verify the parity conservation of the SPDC process.

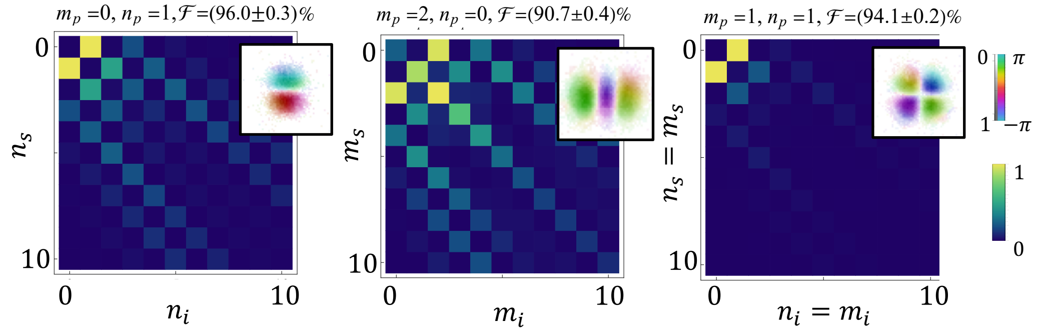
m_p =0, n_p =1,$\mathcal{F}$=(96.0±0.3)%
m_p =2, n_p =0, $\mathcal{F}$=(90.7±0.4)%
m_p =1, n_p =1, $\mathcal{F}$=(94.1±0.2)%

Figure B.1. Hermite-Gaussian modes correlations. When pumping the BBO crystal with $\mathcal{E}_p(x, y) = \mathrm{HG}_{m,n}(x, y)$ we observe biphoton correlations in the basis of HG modes which highlight the parity conservation of the SPDC process. Insets show the reconstructed biphoton fields from which the correlations have been extracted. Upon each plot, the Fidelity between the retrieved field and the theoretical one in the thin crystal approximation is reported. The errors are calculated by considering a Poissonian statistic on the measured counts.

So far, working in the image plane of the crystal, we have considered only the sharp correlation given by the thin crystal approximation. Therefore, we restricted to consider only the effects of the pump beam on the spatial structure of the generated pairs. However, in a generic plane, we have to consider also the effect of the phase matching function, with the state description given by Eqs. 4.3-4.6. To investigate this situation, we took a measurement moving the camera away from the image plane of the crystal, the collected image is reported in Fig. B.2-a. Where, we see how the transverse spatial correlations are broader than the one reported in Fig. 4.2 and that without any postselection the coincidences image does not show any interference. However, when we look at the coincidence image after selecting diagonal spatial correlations, we obtain the marginal $\int d\mathbf{X}_s \, \mathcal{C}(\mathbf{X}_i, \mathbf{X}_s)\delta(\mathbf{X}_s - \mathbf{X}_i) = |\mathcal{E}(\mathbf{X}_i)|^2 |\phi(0)|^2$. In our case $\mathcal{E} = \mathcal{E}_p + \mathcal{E}_{\text{ref}}$ so we see the interference between reference and unknown pump beam (see Fig. B.2-b). From this pattern, using the proposed method, one can reconstruct the pump field contribution to the SPDC state, as shown in Fig. B.2-c. Anyway, this gives just a partial description of the state, for the complete one we need to characterize also the phase-matching contribution. The latter can be retrieved by extracting $\int d\mathbf{X}_s \, \mathcal{C}(\mathbf{X}_i, \mathbf{X}_s)\delta(\mathbf{X}_i + \mathbf{X}_s) = |\mathcal{E}(0)|^2 |\phi(\mathbf{X}_i)|^2$, that is the anticorrelations, as shown in Fig. B.2-d.

It is worth noticing that, since the phase-matching functions of reference and unknown state are identical, we only have access to the absolute value of this contribution. Therefore, to retrieve also the phase term required for the complete description in a generic plane, we need to exploit other methods. For instance, one can extract the phase-matching contribution at different planes and infer its phase by a Gerchberg–Saxton algorithm [420]. Since we focused on the state produced in

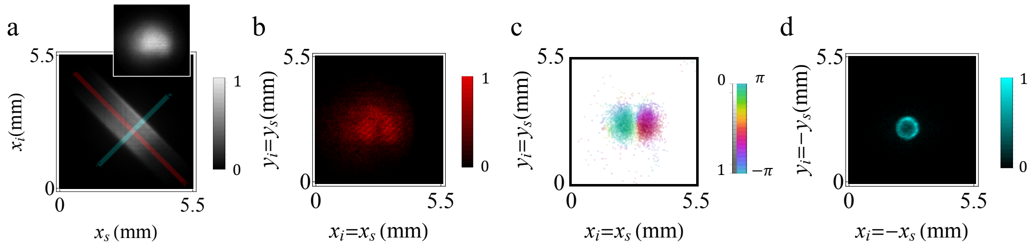

Figure B.2. SPDC state reconstruction at an intermediate plane. a) When moving the camera 10 cm away from the crystal image plane, the spatial correlations are broader respect to the one observed in that plane (See Fig. 4.2). The image obtained after postselecting only on temporal coincidence (shown in the inset) does not exhibit any interference as in the crystal image plane. The red and cyan bands in **a)** indicate the 2-pixel wide regions selected to analyze coincidence images obtained after selecting spatially correlated and anticorrelated photons, respectively. These images are shown, respectively, in panels **b)** and **d)**. The correlation image b) shows again the interference between the unknown and reference pump fields, allowing us to reconstruct the former with off-axis digital holography, as showed in panel **c)**. In **d)**, the anti-correlation image is shown, displaying the characteristic cone shape of the phase-matching function.

the image plane of the crystal, we did not investigate further this approach in our work.

Finally, figure B.3 shows an example of the potential applications of biphoton digital holography. The unknown pump beam can carry information about an image or be scattered by a three-dimensional object. The information about the scatterer is transferred to the SPDC state and can be retrieved through our technique (Fig. B.3-b). We show this in the case of off-axis holography, which can present limitations for complex structures due to the limited camera resolution. These limitations are not related to our proposal and can be improved by employing other approaches, e.g. on-axis phase-shifting digital holography [238].

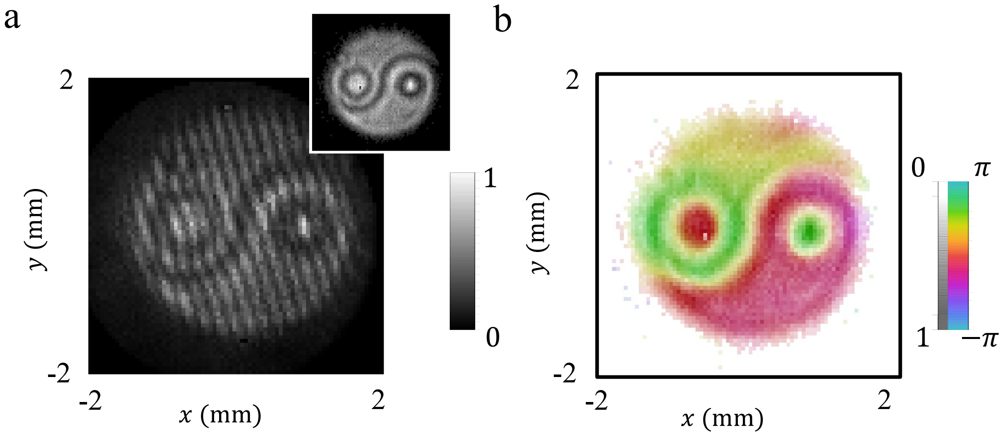

Figure B.3. Image reconstruction. a) Coincidence image of interference between a reference SPDC state and a state obtained by a pump beam with the shape of a Ying and Yang symbol (shown in the inset). The inset scale is the same as in the main plot. **b)** Reconstructed amplitude and phase structure of the image imprinted on the unknown pump.

Appendix C

Fresnel integrals for the refined theoretical propagation model

In this appendix, we report the solution of the Fresnel integrals for the q-plate action when entering the device with a Laguerre-Gaussian mode. In particular, we concentrate on the radial indexes $p = \{0, 1, 2, 3\}$ that have been used during the thesis work.

We have that the Fresnel integral for a q-plate placed in z' and an input Laguerre-Gaussian beam with Rayleigh range z_0 is:

$$\begin{aligned} E_{out}(\rho, \phi, \xi) = \frac{i\ e^{-ik(z-z') \pm i2\alpha_0}}{\pi\,(\xi - \xi')} \int_0^{2\pi} d\phi' \int_0^{\infty} d\rho' LG_{p,m}(\rho', \phi', \xi') \times \\ \times\ e^{\pm i2q\phi'}\ e^{\left\{\frac{-i}{\xi-\xi'}\left[\rho^2+\rho'^2-2\rho\rho'\cos(\phi-\phi')\right]\right\}} \end{aligned} \tag{C.1}$$

where we have introduced the adimensional cylindrical coordinates $\rho = \sqrt{x^2 + y^2}/W_0$, $\rho' = \sqrt{x'^2 + y'^2}/W_0$, $\xi = z/z_0$, $\xi' = z'/z_0$, and the sign ± depends upon the field polarization. Before reporting the results of this integral for the values of p and m relevant to the model developed in this thesis, imposing z_i as the distance between the i-th q-plate and the $(i-1)$-th, we define the parameters and variables for the n-th q-plate as follows:

$$\xi_i = \frac{z_i}{z_0} \tag{C.2}$$

$$\tilde{\xi}_{(n)} = \sum_{i=1}^{n} \xi_i \tag{C.3}$$

$$R_n^2 = \frac{\rho^2}{1 - i\,\tilde{\xi}_{(n)}} \tag{C.4}$$

$$Z_n = \frac{\xi}{1 - i\,\tilde{\xi}_{(n)}} \tag{C.5}$$

$$c_{1n} = \frac{1 - i\,\tilde{\xi}_{(n-1)}}{1 - i\,\tilde{\xi}_{(n)}} \tag{C.6}$$

$$c_{2n} = \frac{i + \tilde{\xi}_{(n-1)} - \xi_n}{i + \tilde{\xi}_{(n)}} \tag{C.7}$$

Thus, we have, posing $\alpha_0 = 0$ and neglecting the phase term $e^{ik(z-z')}$, the following results of the integral (C.1) for the n-th q-plate of a succession of q-plates and for different values of the p, m indices of the Laguerre-Gaussian modes in input to the device:

- Laguerre-Gaussian mode with $p = 0$ and an arbitrary m:

$$\hat{QP}\ LG_{0,m}\,|L/R\rangle = (c_{1n})^{|m|/2+1}\ HyGG_{|m|-|m\pm 2q|,\ m\pm 2q}(R_n, \phi, Z_n)\,|R/L\rangle \tag{C.8}$$

- Laguerre-Gaussian mode with $p = 01$ and an arbitrary m:

$$\begin{aligned}\hat{QP}\ LG_{1,m}\,|L/R\rangle = {} & ((c_{1n})^{|m|/2+1}\ c_{2n}\ \sqrt{|m|+1}\ HyGG_{|m|-|m\pm 2q|,\ m\pm 2q}(R_n, \phi, Z_n) + \\ & - (c_{1n})^{|m|/2+2}\sqrt{|m|+2}\ HyGG_{|m|-|m\pm 2q|+2,\ m\pm 2q}(R_n, \phi, Z_n))\,|R/L\rangle\end{aligned} \tag{C.9}$$

- Laguerre-Gaussian mode with $p = 2$ and an arbitrary m:

$$\begin{aligned}\hat{QP}\ LG_{2,m}\,|L/R\rangle = {} & ((c_{1n})^{|m|/2+1}\ (c_{2n})^2\ \sqrt{\frac{(|m|+2)(|m|+1)}{2}}\ HyGG_{|m|-|m\pm 2q|,\ m\pm 2q}(R_n, \phi, Z_n) + \\ & - (c_{1n})^{|m|/2+2}\ c_{2n}\ \sqrt{2}\ (|m|+2)\ HyGG_{|m|-|m\pm 2q|+2,\ m\pm 2q}(R_n, \phi, Z_n) + \\ & (c_{1n})^{|m|/2+3}\ \sqrt{\frac{(|m|+4)(|m|+3)}{2}}\ HyGG_{|m|-|m\pm 2q|+4,\ m\pm 2q}(R_n, \phi, Z_n))\,|R/L\rangle\end{aligned} \tag{C.10}$$

- Laguerre-Gaussian mode with $p = 3$ and an arbitrary m:

$$\begin{aligned}& \hat{QP}\ LG_{3,m}\,|L/R\rangle = \\ & = ((c_{1n})^{|m|/2+1}\ (c_{2n})^3\ \sqrt{\frac{(|m|+3)(|m|+2)(|m|+1)}{6}}\ HyGG_{|m|-|m\pm 2q|,\ m\pm 2q}(R_n, \phi, Z_n) + \\ & - (c_{1n})^{|m|/2+2}\ (c_{2n})^2\ (|m|+2)\sqrt{\frac{3(|m|+3)}{2}}\ HyGG_{|m|-|m\pm 2q|+2,\ m\pm 2q}(R_n, \phi, Z_n) + \\ & (c_{1n})^{|m|/2+3}\ c_{2n}\ (|m|+3)\sqrt{\frac{3(|m|+4)}{2}}\ HyGG_{|m|-|m\pm 2q|+4,\ m\pm 2q}(R_n, \phi, Z_n) + \\ & - (c_{1n})^{|m|/2+4}\ \sqrt{\frac{(|m|+6)(|m|+5)(|m|+4)}{6}}\ HyGG_{|m|-|m\pm 2q|+6,\ m\pm 2q}(R_n, \phi, Z_n))\,|R/L\rangle\end{aligned} \tag{C.11}$$

Appendix D

Fidelity and efficiency results for the refined theoretical HyGG model

In this appendix, we reported explicitly the values obtained while studying the performances of the holographic technique when the holograms are programmed using the refined description discussed in Section 6.1.1. In particular, we engineered 14 states: the elements of the computational basis ($|m\rangle = \{|-5\rangle, |-3\rangle, |-1\rangle, |1\rangle, |3\rangle, |5\rangle\}$), coherent superpositions of the extreme sites of the walker ($\frac{|5\rangle+e^{i\beta}|-5\rangle}{\sqrt{2}}$ where $\beta \in [0, \pi/2, \pi, 3\pi/2]$) and the elements of the Quantum Fourier basis ($\frac{1}{\sqrt{6}}\sum_{j=1}^{6} e^{\frac{i\pi jk}{3}}|j\rangle$ where $|j\rangle \in \{|-5\rangle, |-3\rangle, |-1\rangle, |1\rangle, |3\rangle, |5\rangle\}$ and $k = 1, 2, 3, 6$).

The results for the measured fidelities of these states are reported in Tab. D.1, while in Tab. D.2 are collected the coupling efficiencies to a SMF for the same states.

State	LG model	HyGG model
$\vert -1\rangle$	0.9832 ± 0.0019	0.9864 ± 0.0013
$\vert 1\rangle$	0.9806 ± 0.0021	0.9857 ± 0.0012
$\vert 3\rangle$	0.9793 ± 0.0036	0.9904 ± 0.0011
$\vert -3\rangle$	0.9686 ± 0.0059	0.9761 ± 0.0024
$\vert -5\rangle$	0.9876 ± 0.0017	0.9900 ± 0.0013
$\vert 5\rangle$	0.9873 ± 0.0018	0.9955 ± 0.0007
$\frac{1}{\sqrt{2}}(\vert -5\rangle + \vert 5\rangle)$	0.9675 ± 0.0050	0.9874 ± 0.0021
$\frac{1}{\sqrt{2}}(\vert -5\rangle - \vert 5\rangle)$	0.9829 ± 0.0039	0.9929 ± 0.0006
$\frac{1}{\sqrt{2}}(\vert -5\rangle - i\,\vert 5\rangle)$	0.9622 ± 0.0038	0.9768 ± 0.0021
$\frac{1}{\sqrt{2}}(\vert -5\rangle + i\,\vert 5\rangle)$	0.9780 ± 0.0022	0.9900 ± 0.0015
QFT_1	0.9620 ± 0.0034	0.9832 ± 0.0024
QFT_2	0.9308 ± 0.0039	0.9657 ± 0.0027
QFT_3	0.9165 ± 0.0058	0.9727 ± 0.0029
QFT_6	0.9525 ± 0.0057	0.9707 ± 0.0037
Average value	0.9671 ± 0.0010	0.9831 ± 0.0005

Table D.1. Fidelity values. The table shows the values of the fidelity for the engineered states. In the second and third column we report the values obtained with the holograms generated with the LG and the HyGG model, respectively.

State	η_{LG}	η_{HyGG}	$\eta_{\mathrm{HyGG}}/\eta_{\mathrm{LG}}$	D
$\|-1\rangle$	0.0951 ± 0.0036	0.1175 ± 0.0044	1.235 ± 0.064	1.096
$\|1\rangle$	0.0835 ± 0.0031	0.0931 ± 0.0034	1.116 ± 0.058	1.096
$\|3\rangle$	0.0387 ± 0.0014	0.0770 ± 0.0029	1.99 ± 0.10	1.739
$\|-3\rangle$	0.0448 ± 0.0017	0.0918 ± 0.0034	2.05 ± 0.11	1.739
$\|-5\rangle$	0.01873 ± 0.00069	0.05397 ± 0.0020	2.88 ± 0.15	3.12
$\|5\rangle$	0.01609 ± 0.00059	0.0492 ± 0.0018	3.06 ± 0.16	3.12
$\frac{1}{\sqrt{2}}(\|-5\rangle + \|5\rangle)$	0.00445 ± 0.00016	0.01121 ± 0.00041	2.52 ± 0.13	3.12
$\frac{1}{\sqrt{2}}(\|-5\rangle - \|5\rangle)$	0.00362 ± 0.00013	0.01104 ± 0.00041	3.05 ± 0.16	3.12
$\frac{1}{\sqrt{2}}(\|-5\rangle - i\,\|5\rangle)$	0.00613 ± 0.00022	0.01232 ± 0.00045	2.01 ± 0.11	3.12
$\frac{1}{\sqrt{2}}(\|-5\rangle + i\,\|5\rangle)$	0.00456 ± 0.00017	0.01091 ± 0.00040	2.38 ± 0.13	3.12
QFT_1	0.01380 ± 0.00051	0.02642 ± 0.00098	1.91 ± 0.10	2.138
QFT_2	0.01158 ± 0.00043	0.02210 ± 0.00081	1.91 ± 0.10	2.093
QFT_3	0.01221 ± 0.00045	0.0276 ± 0.0010	2.26 ± 0.12	2.066
QFT_4	0.02631 ± 0.00097	0.0368 ± 0.0014	1.400 ± 0.073	2.317

Table D.2. Coupling efficiency values. In the table we report the coupling efficiencies for each hologram programmed both with the LG model (η_{LG}) and with the HyGG model (η_{HyGG}). In the third column we report the ratios between η_{HyGG} and η_{LG}. These ratios are compared with the theoretically predicted quantity $D = \frac{|\langle\Phi_{\mathrm{HyGG}}|\Phi_{\mathrm{exp}}\rangle|^2}{|\langle\Phi_{\mathrm{LG}}|\Phi_{\mathrm{exp}}\rangle|^2}$, where $\Phi_{exp} = \Phi_{\mathrm{HyGG}}(w_0^{\mathrm{exp}})$ and w_0^{exp} is the experimental beam waist.

Appendix E

Optimization of the QW in the measurement frames formalism

As we discussed in Section 7.2, our experimental reconstruction method can be described using the formalism of measurment frames [381], by introducing the dual frame canonical operators associated with the effective POVM $\tilde{\boldsymbol{\mu}}$. In our specific case, we use wave-plates, characterized by the parameters $\zeta, \theta, \phi \in \mathbb{R}$, and q-plates $S(\alpha, \delta) = \mathrm{QP}(\alpha, \delta)$, with $\alpha, \delta \in \mathbb{R}$, to experimentally implement the QW dynamics. Therefore, the canonical estimator are given by:

$$\tilde{\mu}_b = V^\dagger (|\psi\rangle\langle\psi| \otimes \mu_b) V. \tag{E.1}$$

where V is the Qw evolution and $|\psi\rangle$ is the polarization state onto which we project at the end. From the variance expression of Eq. 7.13, we have that finding an optimal estimation strategy then amounts to finding the experimental parameters for which the isometry V and projection $|\psi\rangle$ minimize $\mathrm{Tr}(F^{-1})$.

To further simplify our modelization, we can include the projection on the polarization state inside the evolution V by defining the linear operator $\tilde{V} \equiv (\langle\psi| \otimes I_{\mathrm{OAM}})V$. The latter has the following explicit expression:

$$\tilde{V} = \frac{1}{\sqrt{2}} \begin{pmatrix} 0 & e^{2i\alpha_1+2i\alpha_2-i\zeta-i\phi}\sin(\eta)\cos(\theta_p) \\ -ie^{2i\alpha_2-i\zeta-i\phi}\sin(\eta)\cos(\theta_p) & ie^{2i\alpha_2+i\zeta-i\phi}\cos(\eta)\cos(\theta_p) \\ -e^{-2i\alpha_1+2i\alpha_2+i\zeta-i\phi}\cos(\eta)\cos(\theta_p) & -e^{2i\alpha_1-2i\alpha_2-i\zeta+i\phi_p+i\phi}\cos(\eta)\sin(\theta_p) \\ ie^{-2i\alpha_2-i\zeta+i\phi_p+i\phi}\cos(\eta)\sin(\theta_p) & ie^{-2i\alpha_2+i\zeta+i\phi_p+i\phi}\sin(\eta)\sin(\theta_p) \\ -e^{-2i\alpha_1-2i\alpha_2+i\zeta+i\phi_p+i\phi}\sin(\eta)\sin(\theta_p) & 0 \end{pmatrix} \tag{E.2}$$

where the polarization projection is characterized by the angles θ_p, ϕ_p via $|\psi\rangle = \cos(\theta_p)|0\rangle + \sin(\theta_p)e^{i\phi_p}|1\rangle$.

From $\tilde{V}$ we compute the five operators in $\tilde{\boldsymbol{\mu}}$, which read

$$\tilde{\mu}_1 = \tfrac{1}{2}\begin{pmatrix} 0 & 0 \\ 0 & S_\eta^2 C_{\theta_p}^2 \end{pmatrix}, \qquad \tilde{\mu}_2 = \tfrac{1}{2}\begin{pmatrix} S_\eta^2 S_{\theta_p}^2 & 0 \\ 0 & 0 \end{pmatrix}, \qquad \tilde{\mu}_3 = \tfrac{1}{2}\begin{pmatrix} S_\eta^2 C_{\theta_p}^2 & -\frac{e^{-2i\zeta}}{2} S_{2\eta} C_{\theta_p}^2 \\ -\frac{e^{2i\zeta}}{2} S_{2\eta} C_{\theta_p}^2 & C_\eta^2 C_{\theta_p}^2 \end{pmatrix}, \tag{E.3}$$
$$\tilde{\mu}_4 = \tfrac{1}{2}\begin{pmatrix} C_\eta^2 C_{\theta_p}^2 & \frac{e^{-2i\nu}}{2} C_\eta^2 S_{2\theta_p} \\ \frac{e^{2i\nu}}{2} C_\eta^2 S_{2\theta_p} & C_\eta^2 S_{\theta_p}^2 \end{pmatrix}, \qquad \tilde{\mu}_5 = \tfrac{1}{2}\begin{pmatrix} C_\eta^2 S_{\theta_p}^2 & \frac{e^{-2i\zeta}}{2} S_{2\eta} S_{\theta_p}^2 \\ \frac{e^{2i\zeta}}{2} S_{2\eta} S_{\theta_p}^2 & S_\eta^2 S_{\theta_p}^2 \end{pmatrix}$$

where we introduced the auxiliary variable $\nu = 4\alpha_1 - 4\alpha_2 - 2\zeta + \phi_p + 2\phi$ for notational brevity, and used the shorthand notation $C_\alpha \equiv \cos(\alpha)$, $S_\alpha \equiv \sin(\alpha)$. From these, we compute the frame superoperator F of Eqs. 7.12, obtaining:

$$F = \frac{1}{2}\begin{pmatrix} 2 & C_\eta^2 C_\nu S_{2\theta_p} - C_{2\zeta} S_{2\eta} C_{2\theta_p} & C_\eta^2 S_\nu S_{2\theta_p} - S_{2\zeta} S_{2\eta} C_{2\theta_p} & 0 \\ C_\eta^2 C_\nu S_{2\theta_p} - C_{2\zeta} S_{2\eta} C_{2\theta_p} & C_\eta^2 C_\nu^2 S_{2\theta_p}^2 + C_{2\zeta}^2 S_{2\eta}^2 & \frac{1}{2}\left(C_\eta^2 S_{2\nu} S_{2\theta_p}^2 + S_{4\zeta} S_{2\eta}^2\right) & \frac{1}{2}\left(C_\eta^2 C_\nu S_{4\theta_p} + C_{2\zeta} S_{4\eta}\right) \\ C_\eta^2 S_\nu S_{2\theta_p} - S_{2\zeta} S_{2\eta} C_{2\theta_p} & \frac{1}{2}\left(C_\eta^2 S_{2\nu} S_{2\theta_p}^2 + S_{4\zeta} S_{2\eta}^2\right) & C_\eta^2 S_\nu^2 S_{2\theta_p}^2 + S_{2\zeta}^2 S_{2\eta}^2 & \frac{1}{2}\left(C_\eta^2 S_\nu S_{4\theta_p} + S_{2\zeta} S_{4\eta}\right) \\ 0 & \frac{1}{2}\left(C_\eta^2 C_\nu S_{4\theta_p} + C_{2\zeta} S_{4\eta}\right) & \frac{1}{2}\left(C_\eta^2 S_\nu S_{4\theta_p} + S_{2\zeta} S_{4\eta}\right) & C_{2\eta}^2 + C_\eta^2 C_{2\theta_p}^2 + S_\eta^2 \end{pmatrix} \tag{E.4}$$

Finally, we find the optimal values of the parameters reported in Section 7.2 by numerically minimizing $\mathrm{Tr}(F^{-1})$. In Fig. E.1 we show the variation of $\mathrm{Tr}(F^{-1})$ around the optimal value when varying each parameter individually, to assess the sensitivity of the averaged reconstruction MSE with respect to small parameter changes.

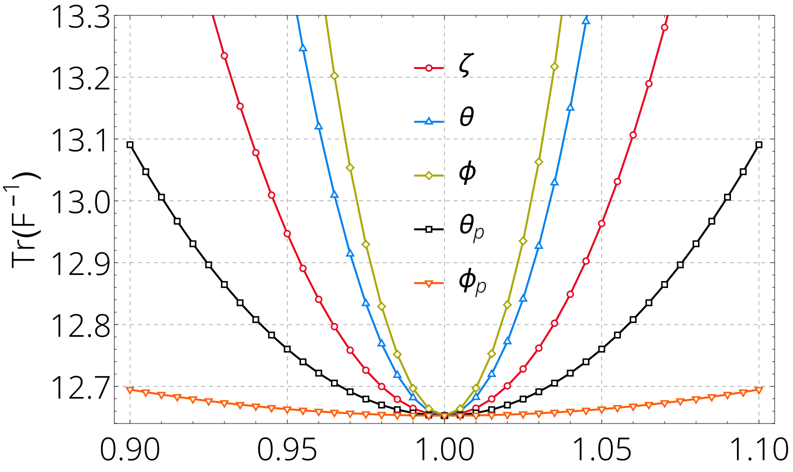

Figure E.1. Smoothness of reconstruction variance We show the average estimation variance with respect to small variations of individual parameters characterizing the experimental apparatus. Each parameter is perturbed independently, leaving all the other parameters fixed at their optimal value. This showcases how different parameters affect the overall estimation accuracies in possibly different ways.

Acronyms

APD **A**valance **P**hotodiode **D**etector

BBO **B**arium **BO**rate

BS **B**eam **S**plitter

CHSH **C**lauser **H**orne **S**himony **H**olt

CCD **C**harge-**C**oupled **D**evice

CNN **C**onvolutional **N**eural **N**etwork

CTQW **C**ontinuos-**T**ime-**Q**uantum **W**alk

DQCA **D**irac **Q**uantum **C**ellular **A**utomaton

DTQW **D**iscrete-**T**ime-**Q**uantum **W**alk

ELM **E**xtreme **L**earning **M**achine

EPR **E**instein **P**odolsky **R**osen

FSS **F**ine-**S**tructure **S**plitting

GMM **G**eneralized **G**ellmann **M**atrices

HG **H**ermite-**G**aussian

HyGG **Hy**per**G**eometric-**G**aussian

HWP **H**alf **W**ave **P**late

HOM **H**ong-**O**u-**M**andel

LG **L**aguerre-**G**aussian

MSE **M**ean **S**quared **E**rror

MSRSM **M**etric **S**tochastic **R**esponse **S**urface **M**ethod

MUBs **M**utually **U**nbiased **B**ases

NN **N**eural **N**etwork

OAM **O**rbital **A**ngular **M**omentum

PBS **P**olarizing **B**eam **S**plitter

PPKTP **P**eriodically **P**oled **P**otassium **T**itanyl **P**hosphate

PCA **P**rincipal **C**omponent **A**nalysis

POVMs **P**ositive **O**perator **V**alued **M**easurements

QELM **Q**uantum **E**xtreme **L**earning **M**achine

QCA **Q**uantum **C**ellular **A**utomaton

QD **Q**uantum **D**ot

QW **Q**uantum **W**alk

QWP **Q**uarter **W**ave **P**late

RBF **R**adial **B**asis **F**unction

SAM **S**pin **A**ngular **M**omentum

SPDC **S**pontaneous **P**arametric **D**owwn **C**onversion

SLM **S**patial **L**ight **M**odulator

SMF **S**ingle **M**ode **F**iber

STOC **S**pin-**T**o-**O**rbital **C**onversion

VVB **V**ector **V**ortex **B**eam

Bibliography

1. Nielsen, M. A. & Chuang, I. L. Quantum computation and quantum information. *Phys. Today* **54,** 60 (2001).
2. Benenti, G., Casati, G. & Strini, G. *Principles of quantum computation and information-volume I: Basic concepts* (World scientific, 2004).
3. Benenti, G., Casati, G. & Strini, G. *Principles Of Quantum Computation And Information - Volume Ii: Basic Tools And Special Topics* ISBN: 9789814365550. `https://books.google.it/books?id=Its7DQAAQBAJ` (World Scientific Publishing Company, 2007).
4. Shor, P. W. Polynomial-time algorithms for prime factorization and discrete logarithms on a quantum computer. *SIAM review* **41,** 303–332 (1999).
5. Grover, L. K. *A fast quantum mechanical algorithm for database search* in *Proceedings of the twenty-eighth annual ACM symposium on Theory of computing* (1996), 212–219.
6. Aaronson, S. & Arkhipov, A. *The computational complexity of linear optics* in *Proceedings of the forty-third annual ACM symposium on Theory of computing* (2011), 333–342.
7. Bennett, C. & Brassard, G. Quantum cryptography: Public key distribution and coin tossing. *Proceedings of the IEEE International Conference on Computers, Systems, and Signal Processing* **560,** 7–11 (Jan. 1984).
8. Bechmann-Pasquinucci, H. & Peres, A. Quantum Cryptography with 3-State Systems. *Phys. Rev. Lett.* **85,** 3313. ISSN: 1079-7114. `http://dx.doi.org/10.1103/physrevlett.85.3313` (2000).
9. Bechmann-Pasquinucci, H. & Tittel, W. Quantum cryptography using larger alphabets. *Phys. Rev. A* **61,** 062308. `https://link.aps.org/doi/10.1103/PhysRevA.61.062308` (6 May 2000).
10. Cerf, N. J. *et al.* Security of Quantum Key Distribution Using d-Level Systems. *Phys. Rev. Lett.* **88,** 127902. ISSN: 1079-7114. `http://dx.doi.org/10.1103/physrevlett.88.127902` (Feb. 2002).
11. Durt, T. *et al.* Security of quantum key distributions with entangled qudits. *Phys. Rev. A* **69,** 032313. ISSN: 2469-9934. `http://dx.doi.org/10.1103/physreva.69.032313` (Apr. 2004).
12. Wang, Y. *et al.* Qudits and high-dimensional quantum computing. *Frontiers in Physics* **8,** 589504 (2020).
13. Genovese, M. & Traina, P. Review on qudits production and their application to quantum communication and studies on local realism. *Advanced Science Letters* **1,** 153–160 (2008).

14. Ringbauer, M. *et al.* A universal qudit quantum processor with trapped ions. *Nature Physics* **18,** 1053–1057 (2022).
15. Shlyakhov, A. *et al.* Quantum metrology with a transmon qutrit. *Physical Review A* **97,** 022115 (2018).
16. Michael, M. H. *et al.* New class of quantum error-correcting codes for a bosonic mode. *Physical Review X* **6,** 031006. ISSN: 21603308. `http://arxiv.org/abs/1602.00008%20http://dx.doi.org/10.1103/PhysRevX.6.031006%20https://link.aps.org/doi/10.1103/PhysRevX.6.031006` (Jan. 2016).
17. Chuang, I. L., Leung, D. W. & Yamamoto, Y. Bosonic quantum codes for amplitude damping. *Phys. Rev. A* **56,** 1114–1125. ISSN: 1050-2947. `https://link.aps.org/doi/10.1103/PhysRevA.56.1114` (Aug. 1997).
18. Duclos-Cianci, G. & Poulin, D. Kitaev's Z d -code threshold estimates. *Phys. Rev. A* **87,** 062338. ISSN: 1050-2947. `https://link.aps.org/doi/10.1103/PhysRevA.87.062338` (June 2013).
19. Campbell, E. T. Enhanced Fault-Tolerant Quantum Computing in d -Level Systems. *Phys. Rev. Lett.* **113,** 230501. ISSN: 0031-9007. `https://link.aps.org/doi/10.1103/PhysRevLett.113.230501` (Dec. 2014).
20. Campbell, E. T., Anwar, H. & Browne, D. E. Magic-state distillation in all prime dimensions using quantum reed-muller codes. *Physical Review X* **2,** 041021 (2012).
21. Flamini, F., Spagnolo, N. & Sciarrino, F. Photonic quantum information processing: a review. *Reports on Progress in Physics* **82,** 016001. `https://doi.org/10.1088/1361-6633/aad5b2` (Nov. 2018).
22. Planck, M. On the law of distribution of energy in the normal spectrum. *Annalen der physik* **4,** 1 (1901).
23. Aspect, A., Dalibard, J. & Roger, G. Experimental test of Bell's inequalities using time-varying analyzers. *Physical review letters* **49,** 1804 (1982).
24. Allen, L. *et al.* Orbital angular momentum of light and the transformation of Laguerre-Gaussian laser modes. *Physical review A* **45,** 8185 (1992).
25. Erhard, M. *et al.* Twisted photons: new quantum perspectives in high dimensions. *Light: Science & Applications* **7,** 17146 (2018).
26. Rubinsztein-Dunlop, H. *et al.* Roadmap on structured light. *Journal of Optics* **19,** 013001 (Nov. 2016).
27. Sit, A. *et al.* High-dimensional intracity quantum cryptography with structured photons. *Optica* **4,** 1006–1010 (2017).
28. Hufnagel, F. *et al.* Characterization of an underwater channel for quantum communications in the Ottawa River. *Optics express* **27,** 26346–26354 (2019).
29. Cimini, V. *et al.* Experimental metrology beyond the standard quantum limit for a wide resources range. *npj Quantum Information* **9,** 20 (2023).
30. Polino, E. *et al.* Photonic quantum metrology. *AVS Quantum Science* **2,** 024703 (2020).
31. Krenn, M. *et al.* Generation and confirmation of a (100 x 100)-dimensional entangled quantum system. *Proceedings of the National Academy of Sciences* **111,** 6243–6247. ISSN: 0027-8424. `http://dx.doi.org/10.1073/pnas.1402365111` (2014).

32. Wang, X.-L. *et al.* Quantum teleportation of multiple degrees of freedom of a single photon. *Nature* **518,** 516 (2015).

33. Mirhosseini, M. *et al.* High-dimensional quantum cryptography with twisted light. *New Journal of Physics* **17,** 033033 (2015).

34. Krenn, M. *et al.* Twisted photon entanglement through turbulent air across Vienna. *Proceedings of the National Academy of Sciences* **112,** 14197–14201 (2015).

35. Ralph, T., Resch, K. & Gilchrist, A. Efficient Toffoli gates using qudits. *Physical Review A* **75,** 022313 (2007).

36. Lanyon, B. P. *et al.* Simplifying quantum logic using higher-dimensional Hilbert spaces. *Nature Physics* **5,** 134–140. ISSN: 1745-2473. `http://www.nature.com/articles/nphys1150` (Feb. 2009).

37. Cardano, F. *et al.* Quantum walks and wavepacket dynamics on a lattice with twisted photons. *Science Advances* **1,** e1500087 (2015).

38. D'Ambrosio, V. *et al.* Photonic polarization gears for ultra-sensitive angular measurements. *Nat. Comm.* **4,** 2432. `https://www.nature.com/articles/ncomms3432` (2013).

39. Fickler, R. *et al.* Quantum Entanglement of High Angular Momenta. *Science* **338,** 640. `https://doi.org/10.1126/science.1227193` (2012).

40. Bouchard, F. *et al.* Quantum cryptography with twisted photons through an outdoor underwater channel. *Optics express* **26,** 22563–22573 (2018).

41. Bouchard, F. *et al.* Experimental investigation of high-dimensional quantum key distribution protocols with twisted photons. *Quantum* **2,** 111 (2018).

42. Zhan, Q. Cylindrical vector beams: from mathematical concepts to applications. *Advances in Optics and Photonics* **1,** 1–57. `http://aop.osa.org/abstract.cfm?URI=aop-1-1-1` (Jan. 2009).

43. Fürhapter, S. *et al.* Spiral phase contrast imaging in microscopy. *Optics Express* **13,** 689–694 (2005).

44. Tamburini, F. *et al.* Overcoming the Rayleigh criterion limit with optical vortices. *Phys. Rev. Lett.* **97,** 163903 (2006).

45. Gibson, G. *et al.* Free-space information transfer using light beams carrying orbital angular momentum. *Optics express* **12,** 5448–5456 (2004).

46. Willner, A. E. *et al.* Optical communications using orbital angular momentum beams. *Advances in Optics and Photonics* **7,** 66 (Mar. 2015).

47. Krenn, M. *et al.* Communication with spatially modulated light through turbulent air across Vienna. *New Journal of Physics* **16,** 113028 (2014).

48. Krenn, M. *et al.* Twisted light transmission over 143 km. *Proceedings of the National Academy of Sciences* **113,** 13648–13653 (2016).

49. Bolduc, E. *et al.* Exact solution to simultaneous intensity and phase encryption with a single phase-only hologram. *Optics letters* **38,** 3546–3549 (2013).

50. Genevet, P. *et al.* Holographic detection of the orbital angular momentum of light with plasmonic photodiodes. *Nat. Comm.* **3,** 1278 (2012).

51. Marrucci, L., Manzo, C. & Paparo, D. Optical spin-to-orbital angular momentum conversion in inhomogeneous anisotropic media. *Phys. Rev. Lett.* **96,** 163905 (2006).

52. Marrucci, L. *et al.* Spin-to-orbital conversion of the angular momentum of light and its classical and quantum applications. *Journal of Optics* **13,** 064001 (2011).

53. Karimi, E. *et al.* Light propagation in a birefringent plate with topological charge. *Optics letters* **34,** 1225–1227 (2009).

54. Walborn, S. P. *et al.* Spatial correlations in parametric down-conversion. *Physics Reports* **495,** 87–139 (2010).

55. Torres, J., Alexandrescu, A. & Torner, L. Quantum spiral bandwidth of entangled two-photon states. *Physical Review A* **68,** 050301 (2003).

56. Agnew, M. *et al.* Tomography of the quantum state of photons entangled in high dimensions. *Physical Review A* **84,** 062101 (2011).

57. Dada, A. C. *et al.* Experimental high-dimensional two-photon entanglement and violations of generalized Bell inequalities. *Nature Physics* **7,** 677–680. ISSN: 1745-2473. `http://www.nature.com/articles/nphys1996` (Sept. 2011).

58. Thew, R. *et al.* Qudit quantum-state tomography. *Physical Review A* **66,** 012303 (2002).

59. Zia, D. *et al.* Interferometric imaging of amplitude and phase of spatial biphoton states. *Nature Photonics,* 1–8 (2023).

60. Brassard, G. *et al.* Limitations on practical quantum cryptography. *Physical review letters* **85,** 1330 (2000).

61. Lütkenhaus, N. Security against individual attacks for realistic quantum key distribution. *Physical Review A* **61,** 052304 (2000).

62. Suprano, A. *et al.* Orbital angular momentum based intra-and interparticle entangled states generated via a quantum dot source. *Advanced Photonics* **5,** 046008–046008 (2023).

63. Venegas-Andraca, S. Quantum walks: a comprehensive review. *Quantum Information Processing* **11,** 1015–1106. ISSN: 1570-0755. `http://dx.doi.org/10.1007/s11128-012-0432-5` (Dec. 2012).

64. Innocenti, L. *et al.* Quantum state engineering using one-dimensional discrete-time quantum walks. *Phys. Rev. A* **96,** 062326. `https://link.aps.org/doi/10.1103/PhysRevA.96.062326` (6 Dec. 2017).

65. Giordani, T. *et al.* Experimental Engineering of Arbitrary Qudit States with Discrete-Time Quantum Walks. *Phys. Rev. Lett.* **122,** 020503. `https://link.aps.org/doi/10.1103/PhysRevLett.122.020503` (2 Jan. 2019).

66. Suprano, A. *et al.* Dynamical learning of a photonics quantum-state engineering process. *Advanced Photonics* **3,** 066002 (2021).

67. Leach, J. *et al.* Measuring the orbital angular momentum of a single photon. *Phys. Rev. Lett.* **88,** 257901 (2002).

68. Slussarenko, S. *et al.* The polarizing Sagnac interferometer: a tool for light orbital angular momentum sorting and spin-orbit photon processing. *Optics Express* **18,** 27205–27216 (2010).

69. Malik, M. *et al.* Direct measurement of a 27-dimensional orbital-angular-momentum state vector. *Nature communications* **5,** 1–7 (2014).

70. Suprano, A. *et al.* Enhanced detection techniques of orbital angular momentum states in the classical and quantum regimes. *New Journal of Physics* **23,** 073014. `https://doi.org/10.1088/1367-2630/ac0c53` (July 2021).

71. Zia, D. *et al.* Regression of high-dimensional angular momentum states of light. *Physical Review Research* **5,** 013142 (2023).

72. Wittek, P. *Quantum machine learning: what quantum computing means to data mining* (Academic Press, 2014).

73. Schuld, M., Sinayskiy, I. & Petruccione, F. An introduction to quantum machine learning. *Contemporary Physics* **56,** 172–185. ISSN: 0010-7514. `http://www.tandfonline.com/doi/full/10.1080/00107514.2014.964942` (Apr. 2015).

74. Biamonte, J. *et al.* Quantum machine learning. *Nature* **549,** 195–202. ISSN: 0028-0836. `http://www.nature.com/doifinder/10.1038/nature23474` (Sept. 2017).

75. Useche, D. H. *et al.* Quantum measurement classification with qudits. *Quantum Information Processing* **21,** 1–12 (2022).

76. Roca-Jerat, S., Román-Roche, J. & Zueco, D. Qudit Machine Learning. *arXiv preprint arXiv:2308.16230* (2023).

77. Suprano, A. *et al.* Experimental Property Reconstruction in a Photonic Quantum Extreme Learning Machine. *Physical Review Letters* **132,** 160802 (2024).

78. DAriano, G. M. The quantum field as a quantum computer. *Physics Letters A* **376,** 697–702. ISSN: 0375-9601. `https://www.sciencedirect.com/science/article/pii/S0375960111014836` (2012).

79. Bisio, A., D'Ariano, G. M. & Tosini, A. Quantum field as a quantum cellular automaton: The Dirac free evolution in one dimension. *Annals of Physics* **354,** 244–264. ISSN: 0003-4916. `https://www.sciencedirect.com/science/article/pii/S0003491614003546` (2015).

80. D'Ariano, G. M. & Perinotti, P. Derivation of the Dirac equation from principles of information processing. *Phys. Rev. A* **90,** 062106. `https://link.aps.org/doi/10.1103/PhysRevA.90.062106` (6 Dec. 2014).

81. Gerritsma, R. *et al.* Quantum simulation of the Dirac equation. *Nature* **463,** 68–71 (2010).

82. Schumacher, B. & Werner, R. F. Reversible quantum cellular automata. *arXiv preprint quant-ph/0405174* (2004).

83. Gross, D. *et al.* Index theory of one dimensional quantum walks and cellular automata. *Communications in Mathematical Physics* **310,** 419–454 (2012).

84. Arrighi, P., Nesme, V. & Werner, R. Unitarity plus causality implies localizability. *Journal of Computer and System Sciences* **77,** 372–378 (2011).

85. Farrelly, T. A review of quantum cellular automata. *Quantum* **4,** 368 (2020).

86. Freedman, M. & Hastings, M. B. Classification of quantum cellular automata. *Communications in Mathematical Physics* **376,** 1171–1222 (2020).

87. Watrous, J. *On one-dimensional quantum cellular automata* in *Proceedings of IEEE 36th Annual Foundations of Computer Science* (1995), 528–537.

88. Raussendorf, R. Quantum cellular automaton for universal quantum computation. *Phys. Rev. A* **72,** 022301. `https://link.aps.org/doi/10.1103/PhysRevA.72.022301` (2 Aug. 2005).

89. Vollbrecht, K. G. H. & Cirac, J. I. Reversible universal quantum computation within translation-invariant systems. *Phys. Rev. A* **73,** 012324. `https://link.aps.org/doi/10.1103/PhysRevA.73.012324` (1 Jan. 2006).
90. Mallick, A. & Chandrashekar, C. Dirac cellular automaton from split-step quantum walk. *Scientific reports* **6,** 1–13 (2016).
91. Bisio, A., D'Ariano, G. M. & Tosini, A. Dirac quantum cellular automaton in one dimension: Zitterbewegung and scattering from potential. *Physical Review A* **88,** 032301 (2013).
92. Schrödinger, E. *Über die kräftefreie Bewegung in der relativistischen Quantenmechanik* (Akademie der wissenschaften in kommission bei W. de Gruyter u. Company, 1930).
93. Harrow, A. W. & Montanaro, A. Quantum computational supremacy. *Nature* **549,** 203–209 (2017).
94. Cozzolino, D. *et al.* High-dimensional quantum communication: benefits, progress, and future challenges. *Advanced Quantum Technologies* **2,** 1900038 (2019).
95. DiVincenzo, D. P. Quantum computation. *Science* **270,** 255–261 (1995).
96. Zhong, H.-S. *et al.* Quantum computational advantage using photons. *Science* **370,** 1460–1463 (2020).
97. Giovannetti, V., Lloyd, S. & Maccone, L. Advances in quantum metrology. *Nature photonics* **5,** 222–229 (2011).
98. Gisin, N. *et al.* Quantum cryptography. *Reviews of modern physics* **74,** 145 (2002).
99. Bennett, C. H. *et al.* Experimental quantum cryptography. *Journal of cryptology* **5,** 3–28 (1992).
100. Heisenberg, W. Über den anschaulichen Inhalt der quantentheoretischen Kinematik und Mechanik. *Zeitschrift für Physik* **43,** 172–198. ISSN: 0044-3328. `https://doi.org/10.1007/BF01397280` (Mar. 1927).
101. Bell, J. S. *Speakable and unspeakable in quantum mechanics: Collected papers on quantum philosophy* (Cambridge university press, 2004).
102. Greenberger, D., Hentschel, K. & Weinert, F. *Compendium of quantum physics: concepts, experiments, history and philosophy* (Springer Science & Business Media, 2009).
103. Maudlin, T. *Philosophy of Physics: Quantum Theory* (Princeton University Press, Princeton, 2019).
104. James, D. F. *et al.* Measurement of qubits. *Physical Review A* **64,** 052312 (2001).
105. Fiurášek, J. Maximum-likelihood estimation of quantum measurement. *Physical Review A* **64,** 024102 (2001).
106. Bell, J. S. On the einstein podolsky rosen paradox. *Physics Physique Fizika* **1,** 195 (1964).
107. Einstein, A., Podolsky, B. & Rosen, N. Can quantum-mechanical description of physical reality be considered complete? *Physical review* **47,** 777 (1935).
108. Brunner, N. *et al.* Bell nonlocality. *Reviews of Modern Physics* **86,** 419. ISSN: 1539-0756. `http://dx.doi.org/10.1103/revmodphys.86.419` (2014).

109. Horodecki, R. *et al.* Quantum entanglement. *Reviews of Modern Physics* **81,** 865. ISSN: 1539-0756. `http://dx.doi.org/10.1103/revmodphys.81.865` (Sept. 2009).

110. Aharonov, Y., Davidovich, L. & Zagury, N. Quantum random walks. *Phys. Rev. A* **48,** 1687–1690. ISSN: 1050-2947. `http://dx.doi.org/10.1103/physreva.48.1687` (1993).

111. Xia, F. *et al.* Random walks: A review of algorithms and applications. *IEEE Transactions on Emerging Topics in Computational Intelligence* **4,** 95–107 (2019).

112. Childs, A. M. Universal computation by quantum walk. *Phys. Rev. Lett.* **102,** 180501 (2009).

113. Lovett, N. B. *et al.* Universal quantum computation using the discrete-time quantum walk. *Physical Review A* **81,** 042330. ISSN: 1094-1622. `http://dx.doi.org/10.1103/PhysRevA.81.042330` (Apr. 2010).

114. Childs, A. M. & Goldstone, J. Spatial search by quantum walk. *Physical Review A* **70,** 022314 (2004).

115. Santha, M. *Quantum walk based search algorithms* in *International Conference on Theory and Applications of Models of Computation* (2008), 31–46.

116. Aspuru-Guzik, A. & Walther, P. Photonic quantum simulators. *Nature physics* **8,** 285–291 (2012).

117. Zhang, W.-W. *et al.* Decomposition of split-step quantum walks for simulating Majorana modes and edge states. *Physical Review A* **95,** 052351 (2017).

118. Kitagawa, T. *et al.* Observation of topologically protected bound states in photonic quantum walks. *Nature Communications* **3,** 882. ISSN: 2041-1733. `http://dx.doi.org/10.1038/ncomms1872` (Dec. 2012).

119. Vlachou, C. *et al.* Quantum walk public-key cryptographic system. *International Journal of Quantum Information* **13,** 1550050 (2015).

120. Vlachou, C. *et al.* Quantum key distribution with quantum walks. *Quantum Information Processing* **17,** 1–37 (2018).

121. Majury, H. *et al.* Robust quantum state engineering through coherent localization in biased-coin quantum walks. *EPJ Quant. Tech.* **5,** 1 (2018).

122. Ambainis, A. Quantum walks and their algorithmic applications. *International Journal of Quantum Information* **1,** 507–518 (2003).

123. Chandrashekar, C. M., Srikanth, R. & Laflamme, R. Optimizing the discrete time quantum walk using a SU(2) coin. *Phys. Rev. A* **77,** 032326. ISSN: 2469-9934. `http://dx.doi.org/10.1103/physreva.77.032326` (Aug. 2008).

124. Jozsa, R. Fidelity for mixed quantum states. *Journal of modern optics* **41,** 2315–2323 (1994).

125. Newton, I. An hypothesis explaining the properties of light. *The History of the Royal Society* **3,** 247–305 (1757).

126. Huygens, C. *Treatise on Light: In which are Explained the Causes of that which Occurs in Reflexion, & in Refraction. And Particularly in the Strange Refraction of Iceland Crystal* (MacMillan and Company, limited, 1912).

127. Jackson, J. D. *Classical electrodynamics* 1999.

128. Poynting, J. H. On the transfer of energy in the electromagnetic field. *Philosophical Transactions of the Royal Society of London,* 343–361 (1884).
129. Poynting, J. H. The wave motion of a revolving shaft, and a suggestion as to the angular momentum in a beam of circularly polarised light. *Proceedings of the Royal Society of London. Series A, Containing Papers of a Mathematical and Physical Character* **82,** 560–567 (1909).
130. Beth, R. A. Mechanical detection and measurement of the angular momentum of light. *Physical Review* **50,** 115 (1936).
131. He, H. *et al.* Direct observation of transfer of angular momentum to absorptive particles from a laser beam with a phase singularity. *Physical review letters* **75,** 826 (1995).
132. García-Ripoll, J. J., Zoller, P. & Cirac, J. I. Quantum information processing with cold atoms and trapped ions. *Journal of Physics B: Atomic, Molecular and Optical Physics* **38,** S567 (2005).
133. Arute, F. *et al.* Quantum supremacy using a programmable superconducting processor. *Nature* **574,** 505–510 (2019).
134. Pan, J.-W. *et al.* Experimental entanglement swapping: entangling photons that never interacted. *Physical review letters* **80,** 3891 (1998).
135. Boschi, D. *et al.* Experimental realization of teleporting an unknown pure quantum state via dual classical and Einstein-Podolsky-Rosen channels. *Physical Review Letters* **80,** 1121 (1998).
136. Loudon, R. *The quantum theory of light* ISBN: 0198511302 (Clarendon Press Oxford, 1973).
137. Darwin, C. G. Notes on the theory of radiation. *Proceedings of the Royal Society of London. Series A, Containing Papers of a Mathematical and Physical Character* **136,** 36–52 (1932).
138. Beth, R. A. Mechanical Detection and Measurement of the Angular Momentum of Light. *Phys. Rev.* **50,** 115–125. `https://link.aps.org/doi/10.1103/PhysRev.50.115` (2 July 1936).
139. Bialynicki-Birula, I. & Bialynicka-Birula, Z. Canonical separation of angular momentum of light into its orbital and spin parts. *Journal of Optics-nouvelle Revue D Optique - J OPT* **13** (May 2011).
140. Cohen-Tannoudji, C., Dupont-Roc, J. & Grynberg, G. *Photons and atoms-introduction to quantum electrodynamics* (1997).
141. Humblet, J. Sur le moment d'impulsion d'une onde electromagnetique. *Physica* **10,** 585–603 (1943).
142. Van Enk, S. & Nienhuis, G. Commutation rules and eigenvalues of spin and orbital angular momentum of radiation fields. *Journal of Modern Optics* **41,** 963–963 (1994).
143. Van Enk, S. & Nienhuis, G. Spin and orbital angular momentum of photons. *Europhysics Letters* **25,** 497 (1994).
144. Barnett, S. M. Rotation of electromagnetic fields and the nature of optical angular momentum. *Journal of modern optics* **57,** 1339–1343 (2010).
145. Allen, L., Barnett, S. & Padgett, M. *Optical Angular Momentum* `http://eprints.gla.ac.uk/65877/` (Institute of Physics Publishing, Bristol, UK, Mar. 2003).

146. Saleh, B. & Teich, M. *Fundamentals of photonics; 2nd ed.* `https://cds.cern.ch/record/1084451` (Wiley, New York, NY, 2007).
147. Da Silva, B. P. *et al.* Machine-learning recognition of light orbital-angular-momentum superpositions. *Phys. Rev. A* **103,** 063704. `https://link.aps.org/doi/10.1103/PhysRevA.103.063704` (6 June 2021).
148. Lavery, M. P. *et al.* Free-space propagation of high-dimensional structured optical fields in an urban environment. *Science Advances* **3,** e1700552 (2017).
149. Beijersbergen, M. W. *et al.* Astigmatic laser mode converters and transfer of orbital angular momentum. *Optics Communications* **96,** 123–132 (1993).
150. Karimi, E. *et al.* Hypergeometric-Gaussian modes. *Optics letters* **32,** 3053–3055. `http://ol.osa.org/abstract.cfm?URI=ol-32-21-3053` (Nov. 2007).
151. Karimi, E. Generation and manipulation of laser beams carrying orbital angular momentum for classical and quantum information applications. *Universita degli Studi di Napoli Federico II,* 1–8 (2009).
152. Heckenberg, N. *et al.* Laser beams with phase singularities. *Optical and quantum electronics* **24,** S951–S962 (1992).
153. D'Errico, A. *et al.* Measuring the complex orbital angular momentum spectrum and spatial mode decomposition of structured light beams. *Optica* **4,** 1350–1357 (2017).
154. D'Errico, A. *et al.* Full-mode characterization of correlated photon pairs generated in spontaneous downconversion. *Optics Letters* **46,** 2388–2391 (2021).
155. Shu, W. *et al.* Propagation model for vector beams generated by metasurfaces. *Optics express* **24,** 21177–21189 (2016).
156. Eisaman, M. D. *et al.* Invited review article: Single-photon sources and detectors. *Review of scientific instruments* **82,** 071101 (2011).
157. Kwiat, P. G. *et al.* New high-intensity source of polarization-entangled photon pairs. *Physical Review Letters* **75,** 4337 (1995).
158. Ansari, V. *et al.* Tailoring nonlinear processes for quantum optics with pulsed temporal-mode encodings. *Optica* **5,** 534–550 (2018).
159. Mair, A. *et al.* Entanglement of the orbital angular momentum states of photons. *Nature* **412,** 313 (2001).
160. Atzeni, S. *et al.* Integrated sources of entangled photons at the telecom wavelength in femtosecond-laser-written circuits. *Optica* **5,** 311–314 (2018).
161. Rarity, J. *et al.* Photonic crystal fiber source of correlated photon pairs. *Optics express* **13,** 534–544 (2005).
162. Silverstone, J. W. *et al.* On-chip quantum interference between silicon photon-pair sources. *Nature Photonics* **8,** 104–108 (2014).
163. Somaschi, N. *et al.* Near-optimal single-photon sources in the solid state. *Nature Photonics* **10,** 340–345 (2016).
164. Lodahl, P. Quantum-dot based photonic quantum networks. *Quantum Science and Technology* **3,** 013001 (2017).
165. Wang, H. *et al.* Towards optimal single-photon sources from polarized microcavities. *Nature Photonics* **13,** 770–775 (2019).
166. Uppu, R. *et al.* Scalable integrated single-photon source. *Science advances* **6,** eabc8268 (2020).

167. Tomm, N. *et al.* A bright and fast source of coherent single photons. *Nature Nanotechnology* **16,** 399–403 (2021).
168. Boyd, R. W., Gaeta, A. L. & Giese, E. in *Springer Handbook of Atomic, Molecular, and Optical Physics* 1097–1110 (Springer, 2008).
169. Franken, e. P. *et al.* Generation of optical harmonics. *Physical review letters* **7,** 118 (1961).
170. De Martini, F. & Sciarrino, F. Non-linear parametric processes in quantum information. *Progress in quantum electronics* **29,** 165–256 (2005).
171. Walls, D. & Milburn, G. *Quantum Optics* ISBN: 9783540285731. `https://books.google.it/books?id=LiWsc3Nlf0kC` (Springer Berlin Heidelberg, 2008).
172. Armstrong, J. *et al.* Interactions between light waves in a nonlinear dielectric. *Physical review* **127,** 1918 (1962).
173. Hum, D. S. & Fejer, M. M. Quasi-phasematching. *Comptes Rendus Physique* **8,** 180–198 (2007).
174. Kim, T., Fiorentino, M. & Wong, F. N. Phase-stable source of polarization-entangled photons using a polarization Sagnac interferometer. *Physical Review A* **73,** 012316 (2006).
175. Fedrizzi, A. *et al.* A wavelength-tunable fiber-coupled source of narrowband entangled photons. *Optics Express* **15,** 15377–15386 (2007).
176. Lodahl, P., Mahmoodian, S. & Stobbe, S. Interfacing single photons and single quantum dots with photonic nanostructures. *Reviews of Modern Physics* **87,** 347 (2015).
177. De Buy Wenniger, I. M. *Impact of photon-number coherence on the performance and energetics of quantum optics protocols* PhD thesis (Université Paris-Saclay, 2023).
178. Seguin, R. *et al.* Size-dependent fine-structure splitting in self-organized InAs/GaAs quantum dots. *Physical review letters* **95,** 257402 (2005).
179. Thomas, S. *et al.* Bright polarized single-photon source based on a linear dipole. *Physical review letters* **126,** 233601 (2021).
180. Purcell, E. M., Torrey, H. C. & Pound, R. V. Resonance absorption by nuclear magnetic moments in a solid. *Physical review* **69,** 37 (1946).
181. Barth, A. M. *et al.* Fast and selective phonon-assisted state preparation of a quantum dot by adiabatic undressing. *Physical Review B* **94,** 045306 (2016).
182. Cosacchi, M. *et al.* Emission-frequency separated high quality single-photon sources enabled by phonons. *Physical Review Letters* **123,** 017403 (2019).
183. Huber, D. *et al.* Highly indistinguishable and strongly entangled photons from symmetric GaAs quantum dots. *Nature communications* **8,** 15506 (2017).
184. Li, J.-P. *et al.* Multiphoton Graph States from a Solid-State Single-Photon Source. *ACS Photonics* **7,** 1603–1610 (2020).
185. Istrati, D. *et al.* Sequential generation of linear cluster states from a single photon emitter. *Nature Communications* **11,** 5501. ISSN: 2041-1723. `https://doi.org/10.1038/s41467-020-19341-4` (2020).
186. Li, J.-P. *et al.* Heralded Nondestructive Quantum Entangling Gate with Single-Photon Sources. *Phys. Rev. Lett.* **126,** 140501. `https://link.aps.org/doi/10.1103/PhysRevLett.126.140501` (14 Apr. 2021).

187. Dousse, A. *et al.* Ultrabright source of entangled photon pairs. *Nature* **466,** 217–220. `https://doi.org/10.1038/nature09148` (2010).

188. Quandela Products Chatalogue `https://www.quandela.com/wp-content/uploads/2023/01/Quandela-Product-Catalogue-2023-.pdf`.

189. Durt, T. *et al.* On mutually unbiased bases. *International journal of quantum information* **8,** 535–640 (2010).

190. Fowles, G. R. *Introduction to modern optics* (Courier Corporation, 1989).

191. O'brien, J. L. Optical quantum computing. *Science* **318,** 1567–1570 (2007).

192. Poincare, H. *Théorie mathématique de la lumière: Leçons professées pendant le 1er semestre 1891-1892. II.* `https://books.google.it/books?id=SS1lOAEACAAJ` (Gauthier-Villars, 1892).

193. Milione, G. *et al.* Higher-Order Poincaré Sphere, Stokes Parameters, and the Angular Momentum of Light. *Phys. Rev. Lett.* **107,** 053601. `https://link.aps.org/doi/10.1103/PhysRevLett.107.053601` (5 July 2011).

194. Beijersbergen, M. *et al.* Helical-wavefront laser beams produced with a spiral phaseplate. *Optics Communications* **112,** 321–327 (1994).

195. Nagali, E. *et al.* Quantum Information Transfer from Spin to Orbital Angular Momentum of Photons. *Phys. Rev. Lett.* **103,** 013601 (1 June 2009).

196. Nagali, E. *et al.* Optimal quantum cloning of orbital angular momentum photon qubits through Hong–Ou–Mandel coalescence. *Nature Photonics* **3,** 720–723. ISSN: 1749-4893. `https://doi.org/10.1038/nphoton.2009.214` (Dec. 2009).

197. Vallone, G. *et al.* Free-Space Quantum Key Distribution by Rotation-Invariant Twisted Photons. *Phys. Rev. Lett.* **113,** 060503. `https://link.aps.org/doi/10.1103/PhysRevLett.11` (2014).

198. Nagali, E. *et al.* Experimental generation and characterization of single-photon hybrid ququarts based on polarization and orbital angular momentum encoding. *Phys. Rev. A* **81,** 052317. `https://link.aps.org/doi/10.1103/PhysRevA.81.052317` (5 May 2010).

199. Hamamtsu. Phase spatial light modulato lcos-slm.

200. Kirk, J. P. & Jones, A. L. Phase-only complex-valued spatial filter. *JOSA* **61,** 1023–1028 (1971).

201. Heckenberg, N. *et al.* Generation of optical phase singularities by computer-generated holograms. *Optics letters* **17,** 221–223 (1992).

202. Qassim, H. *et al.* Limitations to the determination of a Laguerre-Gauss spectrum via projective, phase-flattening measurement. *J. Opt. Soc. Am. B* **31,** A20–A23. `http://josab.osa.org/abstract.cfm?URI=josab-31-6-A20` (June 2014).

203. Sarker, I. H. Machine learning: Algorithms, real-world applications and research directions. *SN computer science* **2,** 160 (2021).

204. He, K. *et al.* *Deep residual learning for image recognition* in *Proceedings of the IEEE conference on computer vision and pattern recognition* (2016), 770–778.

205. Deng, L. & Li, X. Machine learning paradigms for speech recognition: An overview. *IEEE Transactions on Audio, Speech, and Language Processing* **21,** 1060–1089 (2013).

206. Agresti, I. *et al.* Pattern recognition techniques for boson sampling validation. *Phys. Rev. X* **9,** 011013. `https://link.aps.org/doi/10.1103/PhysRevX.9.011013` (1 Jan. 2019).
207. Lumino, A. *et al.* Experimental phase estimation enhanced by machine learning. *Physical Review Applied* **10,** 044033 (2018).
208. Rocchetto, A. *et al.* Learning hard quantum distributions with variational autoencoders. *npj Quantum Information* **4,** 1–7 (2018).
209. Santagati, R. *et al.* Witnessing eigenstates for quantum simulation of Hamiltonian spectra. *Science advances* **4,** eaap9646 (2018).
210. Melnikov, A. A., Sekatski, P. & Sangouard, N. Setting Up Experimental Bell Tests with Reinforcement Learning. *Phys. Rev. Lett.* **125,** 160401. `https://link.aps.org/doi/10.1103/PhysRevLett.125.160401` (16 Oct. 2020).
211. Melnikov, A. A. *et al.* Active learning machine learns to create new quantum experiments. *Proceedings of the National Academy of Sciences* **115,** 1221–1226 (2018).
212. Ruiz-Gonzalez, C. *et al.* Digital discovery of 100 diverse quantum experiments with PyTheus. *Quantum* **7,** 1204 (2023).
213. Costa, A. & Nannicini, G. RBFOpt: an open-source library for black-box optimization with costly function evaluations. *Mathematical Programming Computation* **10.** ISSN: 597–629. `https://doi.org/10.1007/s12532-018-0144-7` (Dec. 2018).
214. Nannicini, G. On the implementation of a global optimization method for mixed-variable problems. *Open Journal of Mathematical Optimization* **2,** 1–25 (2021).
215. Intriligator, M. D. *Mathematical optimization and economic theory* (SIAM, 2002).
216. Snyman, J. A., Wilke, D. N., *et al. Practical mathematical optimization* (Springer, 2005).
217. Guerreschi, G. G. & Smelyanskiy, M. Practical optimization for hybrid quantum-classical algorithms. *arXiv preprint arXiv:1701.01450* (2017).
218. Bonet-Monroig, X. *et al.* Performance comparison of optimization methods on variational quantum algorithms. *Physical Review A* **107,** 032407 (2023).
219. Gutmann, H.-M. A Radial Basis Function Method for Global Optimization. *Journal of Global Optimization* **19.** ISSN: 1573-2916. `https://doi.org/10.1023/A:1011255519438` (Mar. 2001).
220. Regis, R. & Shoemaker, C. A Stochastic Radial Basis Function Method for the Global Optimization of Expensive Functions. *INFORMS Journal on Computing* **19,** 497–509 (Nov. 2007).
221. RBFOpt Documentation `https://rbfopt.readthedocs.io/en/latest/index.html`.
222. The source code of the RBFOpt algorithm `https://github.com/coin-or/rbfopt`.
223. Mitchell, T. *Machine Learning* ISBN: 9780071154673. `https://books.google.it/books?id=EoYBngEACAAJ` (McGraw-Hill, 1997).
224. Shalev-Shwartz, S. & Ben-David, S. *Understanding machine learning: From theory to algorithms* (Cambridge university press, 2014).

225. Jolliffe, I. T. & Cadima, J. Principal component analysis: a review and recent developments. *Philosophical Transactions of the Royal Society A: Mathematical, Physical and Engineering Sciences* **374,** 20150202 (2016).
226. Ruder, S. An overview of gradient descent optimization algorithms. *arXiv preprint arXiv:1609.04747* (2016).
227. Gunning, D. *et al.* XAI—Explainable artificial intelligence. *Science robotics* **4,** eaay7120 (2019).
228. Russakovsky, O. *et al.* ImageNet Large Scale Visual Recognition Challenge. *International Journal of Computer Vision (IJCV)* **115,** 211–252 (2015).
229. Schroff, F., Kalenichenko, D. & Philbin, J. *Facenet: A unified embedding for face recognition and clustering* in *Proceedings of the IEEE conference on computer vision and pattern recognition* (2015), 815–823.
230. Canziani, A., Paszke, A. & Culurciello, E. An analysis of deep neural network models for practical applications. *arXiv preprint arXiv:1605.07678* (2016).
231. Huang, G.-B., Zhu, Q.-Y. & Siew, C.-K. *Extreme learning machine: a new learning scheme of feedforward neural networks* in *2004 IEEE international joint conference on neural networks (IEEE Cat. No. 04CH37541)* **2** (2004), 985–990.
232. Huang, G.-B., Zhu, Q.-Y. & Siew, C.-K. Extreme learning machine: theory and applications. *Neurocomputing* **70,** 489–501 (2006).
233. Schrauwen, B., Verstraeten, D. & Van Campenhout, J. *An overview of reservoir computing: theory, applications and implementations* in *Proceedings of the 15th european symposium on artificial neural networks. p. 471-482 2007* (2007), 471–482.
234. Lukoševičius, M. & Jaeger, H. Reservoir computing approaches to recurrent neural network training. *Computer science review* **3,** 127–149 (2009).
235. Tanaka, G. *et al.* Recent advances in physical reservoir computing: A review. *Neural Networks* **115,** 100–123 (2019).
236. Moore, E. H. On the reciprocal of the general algebraic matrix. *Bulletin of the american mathematical society* **26,** 294–295 (1920).
237. Penrose, R. *A generalized inverse for matrices* in *Mathematical proceedings of the Cambridge philosophical society* **51** (1955), 406–413.
238. Yamaguchi, I. Phase-Shifting Digital Holography: Principles and applications. *Digital holography and three-dimensional display: principles and applications,* 145–171 (2006).
239. Verrier, N. & Atlan, M. Off-axis digital hologram reconstruction: some practical considerations. *Applied optics* **50,** H136–H146 (2011).
240. Chen, B. *et al.* Bright solid-state sources for single photons with orbital angular momentum. *Nature Nanotechnology* **16,** 302–307 (2021).
241. Monken, C. H., Ribeiro, P. S. & Pádua, S. Transfer of angular spectrum and image formation in spontaneous parametric down-conversion. *Physical Review A* **57,** 3123 (1998).
242. Valencia, N. H. *et al.* Entangled ripples and twists of light: radial and azimuthal Laguerre–Gaussian mode entanglement. *Journal of optics* **23,** 104001 (2021).
243. Fisher-Levine, M. & Nomerotski, A. TimepixCam: a fast optical imager with time-stamping. *Journal of Instrumentation* **11,** C03016 (2016).

244. Zhang, Y. *et al.* High speed imaging of spectral-temporal correlations in Hong-Ou-Mandel interference. *Optics Express* **29,** 28217–28227 (2021).

245. Gao, X. *et al.* High-speed imaging of spatiotemporal correlations in Hong-Ou-Mandel interference. *Optics Express* **30,** 19456–19464 (2022).

246. Zhang, Y. *et al.* Ray tracing with quantum correlated photons to image a three-dimensional scene. *Physical Review A* **105,** L011701 (2022).

247. Karimi, E. *et al.* Radial quantum number of Laguerre-Gauss modes. *Phys. Rev. A* **89,** 063813. `https://link.aps.org/doi/10.1103/PhysRevA.89.063813` (6 June 2014).

248. Zhang, D. *et al.* Violation of a Bell inequality in two-dimensional state spaces for radial quantum number. *Physical Review A* **98,** 042134 (2018).

249. Vallone, G. Role of beam waist in Laguerre–Gauss expansion of vortex beams. *Optics letters* **42,** 1097–1100 (2017).

250. Ollivier, H. *et al.* Hong-ou-mandel interference with imperfect single photon sources. *Physical Review Letters* **126,** 063602 (2021).

251. Thomas, S. E. *et al.* Bright Polarized Single-Photon Source Based on a Linear Dipole. *Phys. Rev. Lett.* **126,** 233601. `https://link.aps.org/doi/10.1103/PhysRevLett.126.233601` (23 June 2021).

252. Hong, C.-K., Ou, Z.-Y. & Mandel, L. Measurement of subpicosecond time intervals between two photons by interference. *Physical review letters* **59,** 2044 (1987).

253. Ndagano, B. & Forbes, A. Entanglement distillation by Hong-Ou-Mandel interference with orbital angular momentum states. *APL Photonics* **4,** 016103 (2019).

254. Anderson, B. E. *et al.* Accurate and Robust Unitary Transformations of a High-Dimensional Quantum System. *Phys. Rev. Lett.* **114,** 240401. ISSN: 0031-9007. `https://link.aps.org/doi/10.1103/PhysRevLett.114.240401` (June 2015).

255. Hofheinz, M. *et al.* Synthesizing arbitrary quantum states in a superconducting resonator. *Nature* **459,** 546–549. ISSN: 0028-0836. `http://www.nature.com/articles/nature08005` (May 2009).

256. Rosenblum, S. *et al.* A CNOT gate between multiphoton qubits encoded in two cavities. *Nature Comm.* **9,** 652 (2018).

257. Neeley, M. *et al.* Emulation of a quantum spin with a superconducting phase qudit. *Science* **325,** 722–5 (2009).

258. Kempe, J. Quantum random walks: An introductory overview. *Contemporary Physics* **44,** 307–327. ISSN: 0010-7514. `http://www.tandfonline.com/doi/abs/10.1080/00107151031000110776` (July 2003).

259. Zähringer, F. *et al.* Realization of a Quantum Walk with One and Two Trapped Ions. *Phys. Rev. Lett.* **104,** 100503. ISSN: 0031-9007. `https://link.aps.org/doi/10.1103/PhysRevLett.104.100503` (Mar. 2010).

260. Leibfried, D. *et al.* Experimental Determination of the Motional Quantum State of a Trapped Atom. *Phys. Rev. Lett.* **77,** 4281–4285. ISSN: 0031-9007. `https://link.aps.org/doi/10.1103/PhysRevLett.77.4281` (Nov. 1996).

261. Côté, R. *et al.* Quantum random walk with Rydberg atoms in an optical lattice. *New Journal of Physics* **8,** 156. ISSN: 1367-2630. `https://doi.org/10.1088/1367-2630/8/8/156` (June 2006).

262. Perets, H. B. *et al.* Realization of Quantum Walks with Negligible Decoherence in Waveguide Lattices. *Phys. Rev. Lett.* **100,** 170506 (2008).
263. Peruzzo, A. *et al.* Quantum Walks of Correlated Photons. *Science* **329,** 1500–1503. ISSN: 0036-8075. `http://dx.doi.org/10.1126/science.1193515` (Oct. 2010).
264. Broome, M. A. *et al.* Discrete Single-Photon Quantum Walks with Tunable Decoherence. *Phys. Rev. Lett.* **104,** 153602. ISSN: 1079-7114. `http://dx.doi.org/10.1103/physrevlett.104.153602` (Oct. 2010).
265. Schreiber, A. *et al.* Photons walking the line: A quantum walk with adjustable coin operations. *Phys. Rev. Lett.* **104,** 050502. ISSN: 0031-9007. `https://link.aps.org/doi/10.1103/PhysRevLett.104.050502` (Feb. 2010).
266. Sansoni, L. *et al.* Two-Particle Bosonic-Fermionic Quantum Walk via Integrated Photonics. *Phys. Rev. Lett.* **108,** 010502. ISSN: 1079-7114. `http://dx.doi.org/10.1103/physrevlett.108.010502` (Dec. 2012).
267. Boutari, J. *et al.* Large scale quantum walks by means of optical fiber cavities. *Journal of Optics* **18,** 094007. ISSN: 2040-8978. `http://dx.doi.org/10.1088/2040-8978/18/9/094007` (2016).
268. Caruso, F. *et al.* Fast escape of a quantum walker from an integrated photonic maze. *Nature Communications* **7,** 11682. ISSN: 2041-1733. `http://dx.doi.org/10.1038/ncomms11682` (2016).
269. White, S. J. *et al.* A robust approach for time-bin encoded photonic quantum information protocols. *arXiv preprint arXiv:2404.16106* (2024).
270. Imany, P. *et al.* Probing quantum walks through coherent control of high-dimensionally entangled photons. *Science advances* **6,** eaba8066 (2020).
271. Zhang, P. *et al.* Implementation of one-dimensional quantum walks on spin-orbital angular momentum space of photons. *Phys. Rev. A* **81,** 052322. ISSN: 2469-9934. `http://dx.doi.org/10.1103/physreva.81.052322` (Oct. 2010).
272. Cardano, F. *et al.* Detection of Zak phases and topological invariants in a chiral quantum walk of twisted photons. *Nat. Comm.* **8,** 15516. `https://www.nature.com/articles/ncomms15516` (2017).
273. Cardano, F. *et al.* Statistical moments of quantum-walk dynamics reveal topological quantum transitions. *Nat. Comm.* **7,** 11439 (2016).
274. Li, J., Zhang, M. & Wang, D. Adaptive Demodulator Using Machine Learning for Orbital Angular Momentum Shift Keying. *IEEE Photonics Technology Letters* **29,** 1455–1458. `https://ieeexplore.ieee.org/stamp/stamp.jsp?arnumber=7976374` (2017).
275. Arrazola, J. M. *et al.* Machine learning method for state preparation and gate synthesis on photonic quantum computers. *Quantum Science and Technology* **4,** 024004 (2019).
276. Yue, F. *et al.* Vector vortex beam generation with a single plasmonic metasurface. *ACS photonics* **3,** 1558–1563. `https://doi.org/10.1021/acsphotonics.6b00392` (2016).
277. Giordani, T. *et al.* Machine learning-based classification of vector vortex beams. *Physical review letters* **124,** 160401 (2020).

278. Mackeprang, J., Dasari, D. B. R. & Wrachtrup, J. A reinforcement learning approach for quantum state engineering. *Quantum Machine Intelligence* **2.** ISSN: 2524-4914. `https://doi.org/10.1007/s42484-020-00016-8` (May 2020).
279. Wang, J. Advances in communications using optical vortices. *Photonics Research* **4,** B14–B28 (2016).
280. Rambhatla, K. *et al.* Adaptive phase estimation through a genetic algorithm. *Physical Review Research* **2,** 033078 (2020).
281. Ren, Y. *et al.* Genetic-algorithm-based deep neural networks for highly efficient photonic device design. *Photon. Res.* **9,** B247–B252. `http://www.osapublishing.org/prj/abstract.cfm?URI=prj-9-6-B247` (June 2021).
282. Bharti, K. *et al.* Machine learning meets quantum foundations: A brief survey. *AVS Quantum Science* **2,** 034101 (2020).
283. Goyal, S. K. *et al.* Implementing Quantum Walks Using Orbital Angular Momentum of Classical Light. *Phys. Rev. Lett.* **110,** 263602. ISSN: 1079-7114. `http://dx.doi.org/10.1103/physrevlett.110.263602` (2013).
284. Powell, M. J. D. The theory of radial basis function approximation in 1990. *Advances in numerical analysis* **II,** 105–210. `https://ci.nii.ac.jp/naid/10008965650/en/` (1992).
285. Powell, M. J. D. *Recent research at Cambridge on radial basis functions* in *New Developments in Approximation Theory* (eds Müller, M. W. *et al.*) (Birkhäuser Basel, Basel, 1999), 215–232. ISBN: 978-3-0348-8696-3.
286. Buhmann, M. D. *Radial Basis Functions: Theory and Implementations* (Cambridge University Press, 2003).
287. Powell, M. J. D. An efficient method for finding the minimum of a function of several variables without calculating derivatives. *The Computer Journal* **7,** 155–162. ISSN: 0010-4620. eprint: `https://academic.oup.com/comjnl/article-pdf/7/2/155/959784/070155.pdf`. `https://doi.org/10.1093/comjnl/7.2.155` (Jan. 1964).
288. Brod, D. J. *et al.* Photonic implementation of boson sampling: a review. *Advanced Photonics* **1,** 034001 (2019).
289. Hoch, F. *et al.* Boson Sampling in a reconfigurable continuously-coupled 3D photonic circuit. arXiv: `2106.08260 [quant-ph]` (2021).
290. Cimini, V. *et al.* Calibration of Multiparameter Sensors via Machine Learning at the Single-Photon Level. *Physical Review Applied* **15,** 044003 (2021).
291. Pan, J.-W. *et al.* Multiphoton entanglement and interferometry. *Reviews of Modern Physics* **84,** 777 (2012).
292. Giordani, T. *et al.* Entanglement transfer, accumulation and retrieval via quantum-walk-based qubit–qudit dynamics. *New Journal of Physics* **23,** 023012 (2021).
293. Sztul, H. & Alfano, R. Double-slit interference with Laguerre-Gaussian beams. *Optics letters* **31,** 999–1001 (2006).
294. Lavery, M. P. *et al.* Robust interferometer for the routing of light beams carrying orbital angular momentum. *New Journal of Physics* **13,** 093014 (2011).

295. Berkhout, G. C. & Beijersbergen, M. W. Method for probing the orbital angular momentum of optical vortices in electromagnetic waves from astronomical objects. *Physical review letters* **101,** 100801 (2008).
296. Ferreira, Q. S. *et al.* Fraunhofer diffraction of light with orbital angular momentum by a slit. *Optics letters* **36,** 3106–3108 (2011).
297. Mazilu, M. *et al.* Simultaneous determination of the constituent azimuthal and radial mode indices for light fields possessing orbital angular momentum. *Applied Physics Letters* **100,** 231115 (2012).
298. Mourka, A. *et al.* Visualization of the birth of an optical vortex using diffraction from a triangular aperture. *Optics express* **19,** 5760–5771 (2011).
299. Hickmann, J. *et al.* Unveiling a truncated optical lattice associated with a triangular aperture using light's orbital angular momentum. *Physical review letters* **105,** 053904 (2010).
300. Vaity, P., Banerji, J. & Singh, R. Measuring the topological charge of an optical vortex by using a tilted convex lens. *Physics Letters A* **377,** 1154–1156. ISSN: 0375-9601. `https://www.sciencedirect.com/science/article/pii/S0375960113001953` (2013).
301. Harris, M. *et al.* Laser modes with helical wave fronts. *Physical Review A* **49,** 3119 (1994).
302. Padgett, M. *et al.* An experiment to observe the intensity and phase structure of Laguerre–Gaussian laser modes. *American Journal of Physics* **64,** 77–82 (1996).
303. Fu, S. *et al.* Universal orbital angular momentum spectrum analyzer for beams. *PhotoniX* **1,** 1–12 (2020).
304. Ariyawansa, A., Figueroa, E. J. & Brown, T. G. Amplitude and phase sorting of orbital angular momentum states at low light levels. *Optica* **8,** 147–155 (2021).
305. Courtial, J. *et al.* Rotational frequency shift of a light beam. *Physical review letters* **81,** 4828 (1998).
306. Vasnetsov, M. *et al.* Observation of the orbital angular momentum spectrum of a light beam. *Optics letters* **28,** 2285–2287 (2003).
307. Zhou, H.-L. *et al.* Orbital angular momentum complex spectrum analyzer for vortex light based on the rotational Doppler effect. *Light: Science & Applications* **6,** e16251–e16251 (2017).
308. Karimi, E. *et al.* Time-division multiplexing of the orbital angular momentum of light. *Optics letters* **37,** 127–129 (2012).
309. Jin, J. *et al.* Generation and detection of orbital angular momentum via metasurface. *Scientific reports* **6,** 24286 (2016).
310. Devlin, R. C. *et al.* Arbitrary spin-to–orbital angular momentum conversion of light. *Science* **358,** 896–901 (2017).
311. Deng, Z.-L. *et al.* Diatomic metasurface for vectorial holography. *Nano letters* **18,** 2885–2892 (2018).
312. Guo, Y. *et al.* Spin-decoupled metasurface for simultaneous detection of spin and orbital angular momenta via momentum transformation. *Light: Science & Applications* **10,** 1–12 (2021).

313. Gao, Y. *et al.* Nonlinear holographic all-dielectric metasurfaces. *Nano letters* **18,** 8054–8061 (2018).

314. Allen, B. *et al.* Experimental evaluation of 3D printed spiral phase plates for enabling an orbital angular momentum multiplexed radio system. *Royal Society open science* **6,** 191419 (2019).

315. Forbes, A., Dudley, A. & McLaren, M. Creation and detection of optical modes with spatial light modulators. *Advances in Optics and Photonics* **8,** 200–227 (2016).

316. Bouchard, F. *et al.* Measuring azimuthal and radial modes of photons. *Optics express* **26,** 31925–31941. `http://www.opticsexpress.org/abstract.cfm?URI=oe-26-24-31925` (2018).

317. Kaiser, T. *et al.* Complete modal decomposition for optical fibers using CGH-based correlation filters. *Optics express* **17,** 9347–9356 (2009).

318. Schulze, C. *et al.* Measurement of the orbital angular momentum density of light by modal decomposition. *New Journal of Physics* **15,** 073025 (2013).

319. D'Ambrosio, V. *et al.* Test of mutually unbiased bases for six-dimensional photonic quantum systems. *Scientific reports* **3,** 1–7 (2013).

320. Pachava, S., Dixit, A. & Srinivasan, B. Modal decomposition of Laguerre Gaussian beams with different radial orders using optical correlation technique. *Optics Express* **27,** 13182–13193 (2019).

321. Krenn, M. *et al.* Orbital angular momentum of photons and the entanglement of Laguerre–Gaussian modes. *Philosophical Transactions of the Royal Society A: Mathematical, Physical and Engineering Sciences* **375,** 20150442 (2017).

322. Zhang, L.-F. *et al.* Recognition of orbital-angular-momentum modes with different topological charges and their unknown superpositions via machine learning. *Physical Review A* **104,** 053525 (2021).

323. Doster, T. & Watnik, A. T. Machine learning approach to OAM beam demultiplexing via convolutional neural networks. *Applied optics* **56,** 3386–3396 (2017).

324. Park, S. R. *et al.* De-multiplexing vortex modes in optical communications using transport-based pattern recognition. *Optics express* **26,** 4004–4022. `http://www.opticsexpress.org/abstract.cfm?URI=oe-26-4-4004` (Feb. 2018).

325. Na, Y. & Ko, D.-K. Deep-learning-based high-resolution recognition of fractional-spatial-mode-encoded data for free-space optical communications. *Scientific Reports* **11,** 1–11 (2021).

326. Wang, H. *et al.* Deep-learning-based recognition of multi-singularity structured light. *Nanophotonics* **11,** 779–786 (2022).

327. Raskatla, V., Badavath, P. S. & Kumar, V. Convolutional networks for speckle-based orbital angular momentum modes classification. *Optical Engineering* **61,** 036114 (2022).

328. Maurer, C. *et al.* Tailoring of arbitrary optical vector beams. *New J. Phys.* **9,** 78. `http://stacks.iop.org/1367-2630/9/i=3/a=078` (2007).

329. Lohani, S. *et al.* On the use of deep neural networks in optical communications. *Appl. Opt.* **57,** 4180–4190. `http://ao.osa.org/abstract.cfm?URI=ao-57-15-4180` (May 2018).

330. Liu, J. *et al.* Deep learning based atmospheric turbulence compensation for orbital angular momentum beam distortion and communication. *Optics express* **27,** 16671–16688 (2019).

331. Li, J. *et al.* Joint atmospheric turbulence detection and adaptive demodulation technique using the CNN for the OAM-FSO communication. *Optics express* **26,** 10494–10508 (2018).

332. Neary, P. L. *et al.* Machine learning-based signal degradation models for attenuated underwater optical communication OAM beams. *Optics Communications* **474,** 126058. ISSN: 0030-4018. `http://www.sciencedirect.com/science/article/pii/S0030401820304752` (2020).

333. Xie, G. *et al.* Phase correction for a distorted orbital angular momentum beam using a Zernike polynomials-based stochastic-parallel-gradient-descent algorithm. *Optics letters* **40,** 1197–1200. `http://ol.osa.org/abstract.cfm?URI=ol-40-7-1197` (Apr. 2015).

334. Lohani, S. & Glasser, R. T. Turbulence correction with artificial neural networks. *Optics letters* **43,** 2611–2614 (2018).

335. Bhusal, N. *et al.* Spatial Mode Correction of Single Photons using Machine Learning. *arXiv.* eprint: `2006.07760` (2020).

336. Zhan, H. *et al.* Experimental analysis of adaptive optics correction methods on the beam carrying orbital angular momentum mode through oceanic turbulence. *Optik* **240,** 166990 (2021).

337. Avramov-Zamurovic, S. *et al.* Machine learning-aided classification of beams carrying orbital angular momentum propagated in highly turbid water. *JOSA A* **37,** 1662–1672 (2020).

338. Cox, M. A. *et al.* Interferometric orbital angular momentum mode detection in turbulence with deep learning. *Applied Optics* **61,** D1–D6 (2022).

339. Teo, Y. S. *et al.* Benchmarking quantum tomography completeness and fidelity with machine learning. *New Journal of Physics* **23,** 103021 (2021).

340. Bertlmann, R. A. & Krammer, P. Bloch vectors for qudits. *Journal of Physics A: Mathematical and Theoretical* **41,** 235303 (2008).

341. Pedregosa, F. *et al.* Scikit-learn: Machine learning in Python. *the Journal of machine Learning research* **12,** 2825–2830 (2011).

342. Gradshteyn, I. S. & Ryzhik, I. M. *Table of integrals, series, and products* (Academic press, 2014).

343. Hall, D. G. Vector-beam solutions of Maxwell's wave equation. *Optics letters* **21,** 9–11 (1996).

344. Cardano, F. & Marrucci, L. Spin-Orbit photonics. *Nature Photonics* **9,** 776. `https://doi.org/10.1038/nphoton.2015.232` (2015).

345. D'Ambrosio, V. *et al.* Complete experimental toolbox for alignment-free quantum communication. *Nature Communications* **3** (Jan. 2012).

346. Kozawa, Y., Matsunaga, D. & Sato, S. Superresolution imaging via superoscillation focusing of a radially polarized beam. *Optica* **5,** 86–92 (2018).

347. Suprano, A. *et al.* Propagation of structured light through tissue-mimicking phantoms. *Optics Express* **28,** 35427–35437 (2020).

348. Berg-Johansen, S. *et al.* Classically entangled optical beams for high-speed kinematic sensing. *Optica* **2,** 864–868 (2015).

349. Cozzolino, D. *et al.* Orbital Angular Momentum States Enabling Fiber-based High-dimensional Quantum Communication. *Phys. Rev. Appl.* **11,** 064058 (6 June 2019).

350. Cozzolino, D. *et al.* Air-core fiber distribution of hybrid vector vortex-polarization entangled states. *Advanced Photonics* **1,** 046005. `https://doi.org/10.1117/1.AP.1.4.046005` (2019).

351. Snyder, A. W., Love, J. D., *et al. Optical waveguide theory* (Chapman and hall London, 1983).

352. Milione, G., Sztul, H. & Alfano, R. *Stokes polarimetry of a hybrid vector beam from a spun elliptical core optical fiber* in *Complex Light and Optical Forces IV* **7613** (2010), 38–42.

353. Chen, M. L., Jiang, L. J. & Sha, W. E. Orbital angular momentum generation and detection by geometric-phase based metasurfaces. *Applied Sciences* **8,** 362 (2018).

354. Cai, X. *et al.* Integrated compact optical vortex beam emitters. *Science* **338,** 363–366 (2012).

355. Liu, J. *et al.* Direct fiber vector eigenmode multiplexing transmission seeded by integrated optical vortex emitters. *Light: Science & Applications* **7,** 17148–17148 (2018).

356. D'Ambrosio, V. *et al.* Arbitrary, direct and deterministic manipulation of vector beams via electrically-tuned q-plates. *Scientific Reports* **5,** 7840 (2015).

357. Chollet, F. *et al. Keras* `https://keras.io`. 2015.

358. Martín Abadi *et al. TensorFlow: Large-Scale Machine Learning on Heterogeneous Systems* Software available from tensorflow.org. 2015. `https://www.tensorflow.org/`.

359. Torlai, G. *et al.* Neural-network quantum state tomography. *Nature Physics* **14,** 447–450 (2018).

360. Carrasquilla, J. *et al.* Reconstructing quantum states with generative models. *Nat. Mach. Intell.* **1,** 155 (2019).

361. Lohani, S. *et al.* On the experimental feasibility of quantum state reconstruction via machine learning. *IEEE Transactions on Quantum Engineering* **2,** 1–10 (2021).

362. Ma, H. *et al.* A comparative study on how neural networks enhance quantum state tomography. *arXiv preprint arXiv:2111.09504* (2021).

363. Palmieri, A. M. *et al.* Experimental neural network enhanced quantum tomography. *npj Quantum Information* **6,** 1–5 (2020).

364. Ahmed, S. *et al.* Quantum state tomography with conditional generative adversarial networks. *Physical Review Letters* **127,** 140502 (2021).

365. Gross, D. *et al.* Quantum state tomography via compressed sensing. *Physical review letters* **105,** 150401 (2010).

366. Abdi, H. & Williams, L. J. Principal component analysis. *Wiley interdisciplinary reviews: computational statistics* **2,** 433–459 (2010).

367. Giordani, T. *et al.* Experimental statistical signature of many-body quantum interference. *Nature Photonics* **12,** 173–178 (2018).

368. Flamini, F., Spagnolo, N. & Sciarrino, F. Visual assessment of multi-photon interference. *Quantum Science and Technology* **4,** 024008 (2019).

369. Canabarro, A., Brito, S. & Chaves, R. Machine Learning Nonlocal Correlations. *Phys. Rev. Lett.* **122,** 200401. `https://link.aps.org/doi/10.1103/PhysRevLett.122.200401` (20 May 2019).

370. Ma, Y.-C. & Yung, M.-H. Transforming Bell's inequalities into state classifiers with machine learning. *npj Quantum Information* **4,** 1–10 (2018).

371. Cimini, V. *et al.* Calibration of Quantum Sensors by Neural Networks. *Phys. Rev. Lett.* **123,** 230502. `https://link.aps.org/doi/10.1103/PhysRevLett.123.230502` (23 Dec. 2019).

372. Angelatos, G., Khan, S. A. & Türeci, H. E. Reservoir computing approach to quantum state measurement. *Physical Review X* **11,** 041062 (2021).

373. Lloyd, S., Mohseni, M. & Rebentrost, P. Quantum algorithms for supervised and unsupervised machine learning. *arXiv preprint arXiv:1307.0411* (2013).

374. Rebentrost, P., Mohseni, M. & Lloyd, S. Quantum support vector machine for big data classification. *Physical review letters* **113,** 130503 (2014).

375. Ghosh, S. *et al.* Quantum reservoir processing. *npj Quantum Information* **5.** ISSN: 2056-6387. `http://dx.doi.org/10.1038/s41534-019-0149-8` (Apr. 2019).

376. Mujal, P. *et al.* Opportunities in quantum reservoir computing and extreme learning machines. *Advanced Quantum Technologies* **4,** 2100027 (2021).

377. Innocenti, L. *et al.* Potential and limitations of quantum extreme learning machines. *Communications Physics* **6,** 118 (2023).

378. Wiebe, N., Kapoor, A. & Svore, K. M. Quantum deep learning. *arXiv preprint arXiv:1412.3489* (2014).

379. Purushothaman, G. & Karayiannis, N. B. Quantum neural networks (QNNs): inherently fuzzy feedforward neural networks. *IEEE Transactions on neural networks* **8,** 679–693 (1997).

380. Abbas, A. *et al.* The power of quantum neural networks. *Nature Computational Science* **1,** 403–409 (2021).

381. Innocenti, L. *et al.* Shadow tomography on measurement frames. *arXiv preprint arXiv:2301.13229* (2023).

382. Haah, J. *et al. Sample-optimal tomography of quantum states* in *Proceedings of the forty-eighth annual ACM symposium on Theory of Computing* (2016), 913–925.

383. Zhu, H. & Englert, B.-G. Quantum state tomography with fully symmetric measurements and product measurements. *Physical Review A* **84,** 022327 (2011).

384. Scott, A. J. Tight informationally complete quantum measurements. *Journal of Physics A: Mathematical and General* **39,** 13507 (2006).

385. Bisio, A. *et al.* Optimal quantum tomography. *IEEE Journal of Selected Topics in Quantum Electronics* **15,** 1646–1660 (2009).

386. Neumann, J. v. Theory of self-reproducing automata. *Edited by Arthur W. Burks* (1966).

387. Cook, M. *et al.* Universality in elementary cellular automata. *Complex systems* **15,** 1–40 (2004).

388. Feynman, R. P. in *Feynman and computation* 133–153 (CRC Press, 2018).

389. Arrighi, P. & Grattage, J. The quantum game of life. *Physics World* **25,** 23–26. https://doi.org/10.1088/2058-7058/25/06/37 (June 2012).

390. Po, H. C. *et al.* Chiral Floquet Phases of Many-Body Localized Bosons. *Phys. Rev. X* **6,** 041070. https://link.aps.org/doi/10.1103/PhysRevX.6.041070 (4 Dec. 2016).

391. Fidkowski, L. *et al.* Interacting invariants for Floquet phases of fermions in two dimensions. *Phys. Rev. B* **99,** 085115. https://link.aps.org/doi/10.1103/PhysRevB.99.085115 (8 Feb. 2019).

392. Osborne, T. J. Efficient Approximation of the Dynamics of One-Dimensional Quantum Spin Systems. *Phys. Rev. Lett.* **97,** 157202. https://link.aps.org/doi/10.1103/PhysRevLett.97.157202 (15 Oct. 2006).

393. Di Molfetta, G., Brachet, M. & Debbasch, F. Quantum walks as massless Dirac fermions in curved space-time. *Phys. Rev. A* **88,** 042301. https://link.aps.org/doi/10.1103/PhysRevA.88.042301 (4 Oct. 2013).

394. Cedzich, C. *et al.* Propagation of Quantum Walks in Electric Fields. *Phys. Rev. Lett.* **111,** 160601. https://link.aps.org/doi/10.1103/PhysRevLett.111.160601 (16 Oct. 2013).

395. Di Molfetta, G., Brachet, M. & Debbasch, F. Quantum walks in artificial electric and gravitational fields. *Physica A: Statistical Mechanics and its Applications* **397,** 157–168. ISSN: 0378-4371. https://www.sciencedirect.com/science/article/pii/S0378437113011059 (2014).

396. D'Ariano, G. M. *et al.* Discrete Feynman propagator for the Weyl quantum walk in 2 1 dimensions. *EPL (Europhysics Letters)* **109,** 40012. https://doi.org/10.1209/0295-5075/109/40012 (Feb. 2015).

397. Bisio, A., Mosco, N. & Perinotti, P. Scattering and perturbation theory for discrete-time dynamics. *Physical Review Letters* **126,** 250503 (2021).

398. Suprano, A. *et al.* Photonic cellular automaton simulation of relativistic quantum fields: observation of Zitterbewegung. *arXiv preprint arXiv:2402.07672* (2024).

399. Bisio, A., D'Ariano, G. M. & Perinotti, P. Quantum cellular automaton theory of light. *Annals of Physics* **368,** 177–190 (2016).

400. Thaller, B. *The dirac equation* (Springer Science & Business Media, 2013).

401. David, G. & Cserti, J. General theory of Zitterbewegung. *Physical Review B* **81,** 121417 (2010).

402. Cedzich, C. *et al.* Quantum walks in external gauge fields. *Journal of Mathematical Physics* **60,** 012107 (2019).

403. Arrighi, P., Facchini, S. & Forets, M. Quantum walking in curved spacetime. *Quantum Information Processing* **15,** 3467–3486 (2016).

404. Mallick, A. *et al.* Simulating Dirac Hamiltonian in curved space-time by split-step quantum walk. *Journal of Physics Communications* **3,** 015012 (2019).

405. Bohm, D. & Aharonov, Y. Discussion of experimental proof for the paradox of Einstein, Rosen, and Podolsky. *Physical Review* **108,** 1070 (1957).

406. Bohr, N. Can quantum-mechanical description of physical reality be considered complete? *Physical review* **48,** 696 (1935).

407. Clauser, J. F. *et al.* Proposed experiment to test local hidden-variable theories. *Physical review letters* **23,** 880 (1969).

408. Bell, J. S. *et al. John S. Bell on the foundations of quantum mechanics* (World Scientific, 2001).

409. Cirel'son, B. S. Quantum generalizations of Bell's inequality. *Letters in Mathematical Physics* **4,** 93–100. ISSN: 1573-0530. `https://doi.org/10.1007/BF00417500` (Mar. 1980).

410. Weihs, G. *et al.* Violation of Bell's inequality under strict Einstein locality conditions. *Physical Review Letters* **81,** 5039 (1998).

411. Scheidl, T. *et al.* Violation of local realism with freedom of choice. *Proceedings of the National Academy of Sciences* **107,** 19708–19713 (2010).

412. Challenging local realism with human choices. *Nature* **557,** 212–216 (2018).

413. Rowe, M. A. *et al.* Experimental violation of a Bell's inequality with efficient detection. *Nature* **409,** 791–794 (2001).

414. Giustina, M. *et al.* Bell violation using entangled photons without the fair-sampling assumption. *Nature* **497,** 227–230 (2013).

415. Christensen, B. G. *et al.* Detection-loophole-free test of quantum nonlocality, and applications. *Physical review letters* **111,** 130406 (2013).

416. Hensen, B. *et al.* Loophole-free Bell inequality violation using electron spins separated by 1.3 kilometres. *Nature* **526,** 682–686 (2015).

417. Giustina, M. *et al.* Significant-loophole-free test of Bell's theorem with entangled photons. *Physical review letters* **115,** 250401 (2015).

418. Shalm, L. K. *et al.* Strong loophole-free test of local realism. *Physical review letters* **115,** 250402 (2015).

419. Walborn, S., Pádua, S. & Monken, C. Conservation and entanglement of Hermite-Gaussian modes in parametric down-conversion. *Physical Review A* **71,** 053812 (2005).

420. Gerhberg, R. & Saxton, W. A practical algorithm for the determination of phase from image and diffraction plane picture. *Optik* **35,** 237–246 (1972).